Multi-scale investigation of fire behaviour of a seat and a wall panel from European railway transport system

Anycée Camillo

THESE

Pour l'obtention du Grade de
DOCTEUR DE L'ECOLE NATIONALE SUPERIEURE DE MECANIQUE ET D'AEROTECHNIQUE
(Diplôme National - Arrêté du 7 août 2006)

Ecole Doctorale :
Sciences et Ingénierie en Matériaux, Mécanique, Energétique et Aéronautique
Secteur de recherche : **Fluide, Thermique et Combustion**

Presentée par

Anycée CAMILLO

****

Etude multi-echelle du comportement au feu d'un siège et d'une paroi types issus d'un système de transport ferroviaire européen

Multi-scale investigation of fire behaviour of a seat and a wall panel from European railway transport system

****

Directeur de thèse Thomas ROGAUME - Institut P_{PRIME} - Université de Poitiers
Co-encadrant de thèse Eric GUILLAUME - LNE

Thèse soutenue le 24 Avril 2013
devant la Commission d'Examen :

- Jury -

Président	Pr VAN HEES P.	Professeur, *LTH - Université de Lund (Sweden)*
Rapporteurs	Pr BOULET P.	Professeur, *LEMTA - Université de Lorraine*
	Pr PORTERIE B.	Professeur, *IUSTI - Université d'Aix-Marseille*
Examinateurs	Dr RICHARD F.	Maître de Conférence, *Institut P' - Université de Poitiers*
	Dr ROGAUME T.	HDR, Maître de Conférence, *Institut P' - Université de Poitiers*
	Mr GUILLAUME E.	Responsable R&D - Direction des Essais, *LNE - Trappes*
	Mr SAINRAT A.	Expert - Transfeu, *LNE - Trappes*

To Hung and my parents,
this work will not exist without you.

Acknowledgement

Results of this work would not be the same without the support of many people, mentioned below.

This thesis has been performed with CIFRE financial support and conducted in the framework of the European Transfeu project. I would like to thank all Transfeu partners: Alstom, Ansaldobreda, BRE Global, Bombardier, CEN/DIN FSF, Currenta, DeutscheBahn, Exova Warringtonfire, Instytut Kolejnictwa, LSFire, RATP, Siemens, SNCF, SP Technical Research Institute of Sweden, Tecnalia, TRENITALIA, UNIFE, University of Wuppertal and VTT Technical Research Centre of Finland. I would like to thank in particular Maria Hjolman (SP) and Silvio Messa (LSFire) for their warm welcome in their laboratory.

Thanks to my jury, Pascal Boulet, Bernard Porterie and Patrick Van Hees who have accepted to read carefully and ask interesting questions about this work during the defence. Thanks to Franck Richard for his advice and discussions about fire modelling. It is always a pleasure to get your opinion.

I offer to Thomas Rogaume and Eric Guillaume, my sincere thanks for their continual support during these three years. You make a very complementary team of supervisors, the best possible. Thanks for your advice, discussions and trust.

I thank my LNE supervisors, Noelle Pedespan, Valerie Rumbau and then Sophie Thiefry for their advice during these three years.

I would like to thank people from the Fire department at LNE who actively participated in this research: Alain Sainrat, Franck Didieux, Laurent Saragoza, Damien Lesenechal and Alexandre Allard. Thanks for your time and for answering all my questions. I would like to thank in particular Damien Marquis for his continual support and our interesting discussion about fire science.

I would like to thank all my colleagues who answered all my questions with enthusiasm: Mickael Deabreu, Aymeric Raguideau, Carine Chivas, Melinda Ayraut, Bruno Rochat, Virginie Barbosa, Lucas Bustamente Valancia, Luc Noblanc, Frederic Delagos and also Talal Fateh, Jocelyn Luche, Benjamin Batiot and Etienne Mathis. Thank you for your support and your good mood. In addition, I wish in addition the best to the two PhD students Marta and Fabien.

I would like to thank warmly my family and especially my mum, my dad and my sister for their encouragement throughout my studies years. Needless to say, I would like to thank all my friends who supported me during these three years: Mimi, Ninise, Julie, Marjo and Alex, Hosni, Omar, Dany, Antoine, Julie, Fabien, Pauline, Charles, Catherine, JM and also my basket-ball team, Myriam, Elo, Anne-lise, Coco, Alex, Maud, Sophie and Camille. Thank you my friends for all the excellent parties we had.

Finally, I would like to thank my lover, Hung. During these three years, he was here for me at each moment, both good and bad. This work is also yours.

Contents

Context

The first railway steam locomotive was born in England at the beginning of the nineteenth century as the outcome of a competition organised by Liverpool and Manchester Railway. In 1829, Mr Robert Stephenson won the competition with his steam locomotive, named "the Rocket". At that time, the railway steam locomotive was used to transport merchandise. In 1837, Louis-Philippe the 1^{st} launched the first railway line between Paris and St Germain (19 km), especially designed for passengers. In 1863, the first subway was introduced in London from Farrington Street to Paddington. In 1883, the famous Orient express was opened as a long-distance passenger train. The railway locomotive went from Paris to Istanbul. It was the most luxurious train in Europe. It was equipped with a restaurant, a living room and sleeping coaches. It travelled 3,186 km in three days. In 1900, the first electric subway was opened in Paris. Then, the railway rolling stock network increased in Europe. In the seventies, the French high speed train reached the speed of 318 km/h and the last steam locomotives were removed from the French railway network. In 2007, the French high speed train achieved a new speed record: 574,8 km/h.(SNCF group (2012))

This dazzling railway innovation implied that a lot of passengers were transported in a small space. A recent statistic study from 2004 to 2011 (Eurostat (2012)) reported the number of fires occurring in the coach, and also the number of victims (casualties and people killed) involved in train fires in Europe (figures 1). The histograms can be analysed in terms of occurrence (number of fire) and severity (number of victims). These data were collected according to EU Regulation 91/2003. However, data sources may be not homogeneous for all countries. Moreover, Barnett (2005) and White (2010) have concluded that although large passenger train fires are infrequent, they may have extreme consequences. In reality, when a fire occurs on a passenger coach, the most important thing is to protect people from fire effects in a such confined space (high number of people by square meter). Fire effects are defined as the smoke, the radiative heat flux and the temperature. They strongly depend on the quantity and nature of the fuel, and also on fire conditions (Purser *et al.* (2010)). The probable quantity of fuel can come from the products located inside the passenger coach, either proper to the coach or to passengers (luggage, laptops,...). The latter can not be controlled in terms of type and quantity because it is function of each passenger inside the coach.

However, the quantity and nature of each product related to the coach is supposed to be known, such as the railway seat, the floor, the ceiling and the panel inside the coach. The regulation principle is to avoid a good reaction-to-fire of each coach product in order to prevent the fire from spreading into the coach.

Regulations and standards: fire safety in passengers railway

In France, during the sixties and the seventies, the use of plastic materials increased in railway coaches. Furthermore, because of malevolencies in the coach, a group was formed, called "Groupe de Travail Matériaux" (GTM) (Guillaume (2010)). The missions of this group was to define material fire test methods, set material fire characteristics and improve railway coach materials fire performance (Guillaume (2010)). In 1980, two documents ($10-3000960$ and $10-5084838$) were published, which dealt with reaction-

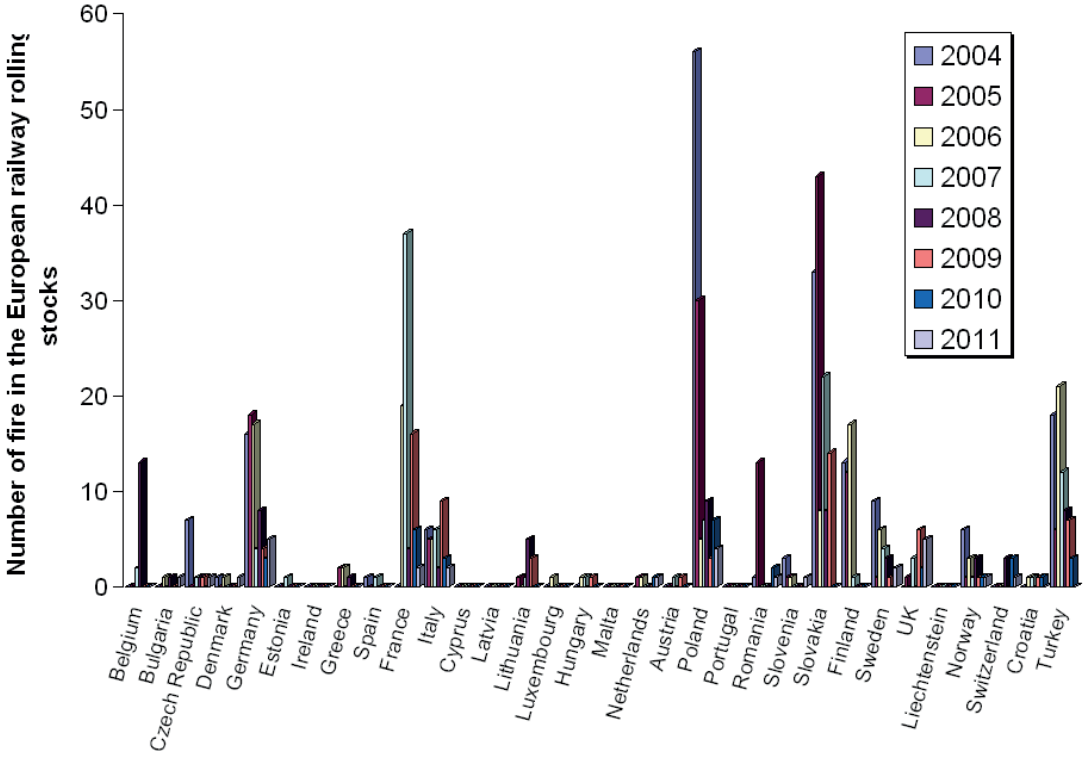

a/ Number of fires in the European railway rolling stocks from 2004 to 2011.

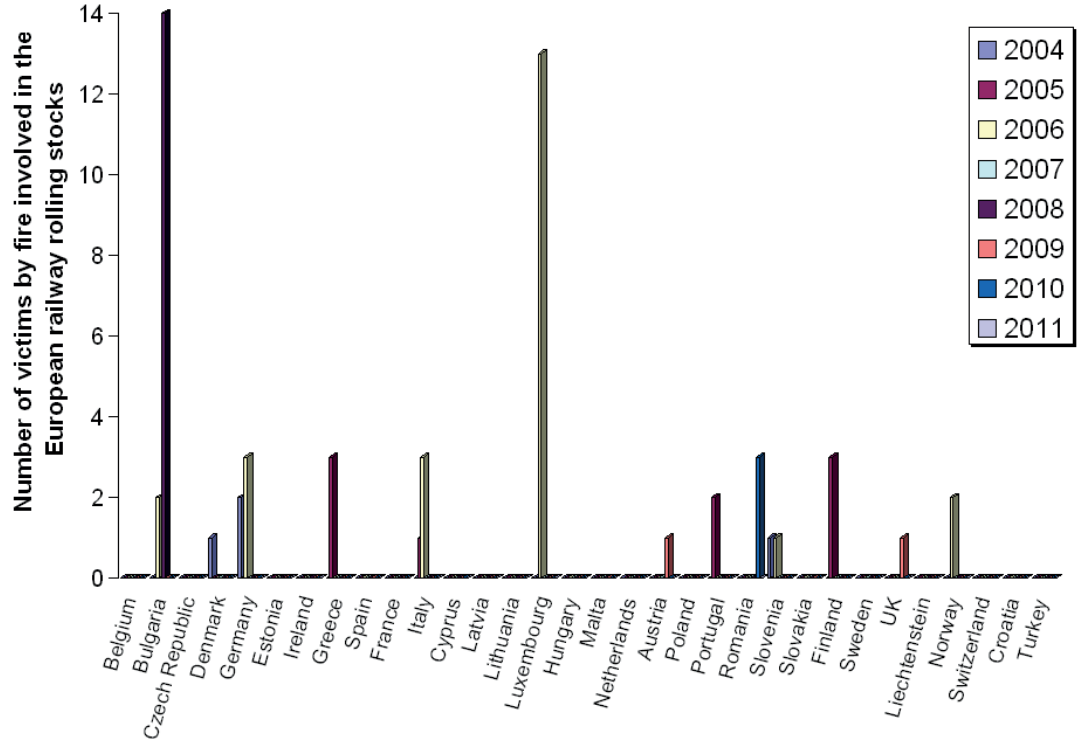

b/ Number of victims by fire involved in the European railway rolling stocks from 2004 to 2011.

Figure 1: Statistic data from 2004 to 2011, Eurostat (2012).

to-fire of material present in the passenger coach. In 1988 and 1989, standards NF F 16-101 (1988), NF F 16-102 (1992) and NF F 16-103 (1989) replaced these two documents. These standards prescribe the materials choice policy to apply to the railway rolling stock according to the reaction-to-fire classification (classification M and I) and a smoke classification (classification F) (Mandatory for SNCF and RATP). These standards have been mandatory since the decree of July 1st, 2004 (Arrêté (2004)).

In England, in 1999, standard BS 6853 (1999) presented the materials criteria applied to the railway rolling stock. This standard explains all fire tests methods for each material or product and each associated criteria classification. For Italy, Germany and the United States, standards UNI CEI 11170-3 (2005), DIN 5510-2 (2009) and NFPA 130 (2010) also present respectively fire tests methods to follow for each product. As the French and English standards, they are related to a material fire classification. All details about these standards are available in references Guillaume (2010). For all countries, during the sixties and the seventies, when there was no proper national standard, safety level of railway materials fire behaviour was regulated by the international standard UIC 564-2. This system corresponded to the minimum safety level.

In 1991, the first work of the future European standard began and related to fire risk management applied to the railway network. European Commission started a research program, called FIRESTARR, in order to establish tests methods for material selection at European level. In 2008, European directive 2008/57/CE, related to the interoperability of the high speed European railway system, was published (European Directive 2008/57/EC (2008)). It sets the essential requirements for the European railway system and defines seven sub-systems:

- Infrastructure
- Energy
- Control-command and signalling
- Rolling stock
- Traffic operation and management
- Maintenance
- Telematics applications for passenger and freight services.

A Technical Specification Interoperability (TSI) is associated to each sub-system. A TSI is identified as a law. The TSI "High Speed" defined the requirements linked to fire safety in the rolling stock (TSI 2008/232/EC (2008) and TSI 2011/291/EC (2011))). The TSI requires the application of the national (France, UK, Italy, Germany and Poland) fire safety standard (described in the previous paragraph) until the publication of the future European standard. In November 2012, this European standard (FprEN 45545-2 (2012)) was approved as Technical Specification by the European Committee for Standardisation (CEN). Part 2 of the European standard is required in the TSI high speed. This European fire safety railway standard will be published in a few months (May 2013) in order to harmonize requirements for the railway transport network in Europe. A transition period of 3 years is required. This standard takes into account fire behaviour characteristics of

the different products, depending on their usage, the operation category and the type of train vehicle. However, if one requirement is not met for a coach product, then the fire safety level and safety objectives of EU Directive and TSI can be assessed with a new approach: fire safety engineering study. The objective of this approach is to prove that the design scenario of the coach reaches fire safety levels according to several fire scenarios (CEN/TS 45545-1 (2009)). Fire safety engineering study through experimental tests on real scale is possible but very expensive. Thus, a fire safety assessment via numerical fire models can be planned. The European Railway Agency (ERA) plays a key role in promoting interoperability and harmonising technical standards. ERA also evaluates fire safety engineering methods.

In parallel with these prescriptive requirements for railway material, several countries have studied railway materials or products fire behaviour present in the coach through different fire research projects. The next paragraphs summarize the major fire research projects objectives and results.

Fire research program on passenger railway

In 1975, the fire research project, named Fire hazard evaluation of the interior of Washington metropolitan area transit authority (Materials cars), conducted a series of fire tests to assess potential fire and smoke hazards represented by various materials incorporated in new metro cars (Braun (1975)). The full-scale tests results showed that the materials failed to satisfy their end-conditions.

In 1978, the National Bureau of Standard (now "NIST"), conducted a fire hazard evaluation of the Bay Area Rapid Transit (BART) metro system in San Francisco in California (Braun (1978)). The objective of this study was to check whether any design details of the materials present in the metro car could spread fire. They concluded that the polyamide or the vinyl covering the seats had to be replaced because they represented important hazard. Moreover, they recommended the use of intumescing coating on walls or ceilings to improve fire behaviour and the installation of a fire detection system. Six years later (Peacock and Braun (1984)), the National Bureau of Standard conducted fire tests on Amtrak Passenger Rail Vehicle Interiors. The aim was to assess the burning behaviour of the interior of passenger rail vehicles. They established that small scale test results could not be used directly to predict large scale behaviour. Finally, they specified that a small number of full-scale tests should be performed to determine a set of acceptable materials for a given design scenario of the studied vehicle. This could be followed by a set of small scale tests to assess alternative material. Then, materials, which had equal or better fire performance than the material tested in the full-scale test could then be substituted without further full scale tests.

In 1990, SP laboratory in Sweden led a project on fires in buses and trains (Goransson and Lundqvist (1990)). Research involved a large-scale experiment to estimate the ignitability and heat release rate of a variety of interior materials from buses and trains.

Between 1995 and 2004, the NIST (Peacock and Braun (1999), Peacock *et al.* (2002)

and Peacock *et al.* (2004)) conducted a project named "Fire Safety of Passengers Trains". They proposed an alternative approach based on heat release rate test methods incorporated with fire modelling and fire hazard analysis. Assessing potential hazards under real fire conditions could provide a more credible and cost effective approach to predict fire performance of passenger trains materials. The project was divided into three phases. The first one was focused on the evaluation of passenger train interior materials using cone calorimeter test data (ISO 5660-2 (2012)) for fire modelling. The second stage consisted in performing large scale tests. Input data from cone calorimeter tests and large-scale tests were used in a zone model developed by the NIST. For this study, the CFAST zone model of the fire model HAZARD I was used. Then, the Available Safety Egress Time (ASET) was compared to the Required Safety Egress Time (RSET) for a given design fire scenario. Concerning the third phase, a set of real scale tests of a full size railway car was performed. These tests data were compared with the data obtained from large scale and cone calorimeter tests. Moreover, a good match between measured and modelled ASET was obtained, but White (2010) reported that model assumptions and inputs were not explicitly stated and it was not clear whether model inputs were iteratively modified to achieve a good match.

In 2001, the FIRESTARR (Fire STAndardisation Research of Railway vehicles, "Contract SMT4-CT97-2164") project assisted the work of the CEN, the European Standardisation committee. The objectives of this project were to select suitable tests methods and tests conditions to assess fire performance of materials and propose a classification for railway materials for future European standard (FprEN 45545-2 (2012)). The working group focused on the development of the prescriptive requirements of individual railway interior products based on the small and large scale tests (Briggs *et al.* (2001)a, Briggs *et al.* (2001)b and Le Tallec *et al.* (2001)).

In 2004, full-scale experiments on a railway passenger car were performed by the Commonwealth Scientific and Industrial Research Organization (CSIRO). The project aimed to investigate the fire size of railway products from different ignition sources and to understand passenger rail products fire behaviour and fire spread (White and Dowling (2004)). The main conclusions were as follows:

- The combination design of the seat and the wall lining are important factors during fire growth (Chiam (2005)).
- Fire safety interest is focused on the use of the heat release rate measurement to assess the material fire performance (Chiam (2005)).
- The measured data from the cone calorimeter test can provide useful data for computer modelling.

In 2005, Chiam (2005) objectives were to identify credible fire scenarios, evaluate the materials reaction-to-fire, derive material thermo-physical properties from cone calorimeter tests and predict the heat release rate of this test. Analytical methods were used to predict the heat release rate. However, a new computational fluid dynamic (CFD) code (FDS, Version 4) was used to predict the heat release rate on the cone calorimeter scale. Two different methods to simulate the heat release rate were tested proper to FDS. For

both FDS methods, the prediction failed: the input data derived from the cone calorimeter tests were not suitable to predict directly heat release rate at lower heat flux. A combination of derived and fitted data function of the exposure heat flux was required to reproduce the heat release rate. White (2010) obtained the same conclusion as Chiam (2005).

Hostikka and McGrattan (2001) showed that the CFD model failed to predict the heat release rate at low heat flux exposure through a pyrolysis model. They reported that this could be due to the errors in the heat transfer solutions and thermal properties. Furthermore, they added that the absence of some physical phenomena, such as surface reactions and internal mass transfer, may also affect the results.

In 2008, Capote modelled fire development in a passenger train compartment with FDS (Version 4) from the bench and the full scale tests performed during FIRESTARR project (Capote *et al.* (2008)). The method involved the use of data from cone calorimeter tests (ISO 5660-1 (2002)). They concluded that the FDS heat release rate response was influenced by the heat flow, and the ignition temperature from cone calorimeter tests.

In 2012, Hu *et al.* (2012) used a CFD model called SMARTFIRE (Version 4.1) to predict the heat release rate. They also required two ignition parameters criteria: ignition temperature and flame spread rate derived from small scale tests. They achieved a good correlation before the flashover for a small fire compartment. However, they highlighted that the flame spread rate measurement was function of the experimental small scale conditions. They suggested that the flame spread rate could be modelled with more fundamental spread models involving a pyrolysis mechanism.

Transfeu project

Between 2009 and 2012, the Transport Fire Safety Engineering in the European Union (Transfeu) project was founded in this context, and supported by the European Commission through the Seventh Framework programme. Transfeu consortium is composed of 21 partners: Fire Tests and Research Laboratories, standardization and Regulation bodies, train builders and train operators (figure 2). LNE (French National laboratory of testing and metrology) is the coordinator of the project. Transfeu is divided into two main objectives. The first one is related to fire tests and especially gases toxicity, and the second to fire modelling. On the one hand, Transfeu objectives are to develop a new dynamic method of measurement of toxic effluents from the combustion of railway materials. Transfeu members performed prescriptive tests on materials in order to improve the future European railway standard (FprEN 45545-2 (2012)). On the other hand, Transfeu aims to develop a fire safety engineering methodology in order to predict the impact of fire during passenger evacuation. The available and required safe egress time (ASET and RSET) are calculated with a fire modelling tool. In the future, these research results could be applied to other surface transportation services, such as ships and buses. The project is divided in seven workpackages:

- WP1: Transfeu management

- WP2: Fire tests for toxicity of fire effluents
- WP3: Development of a conventional pragmatic classification system for the toxicity of fire effluents released by products in trains
- WP4: Fire Safety Engineering Methodology for surface transportation
- WP5: Development of numerical simulation tools for fire performance, evacuation of people and decision tools for train design
- WP6: Validation of the conventional toxicity classification and the numerical simulation
- WP7: Exploitation, Dissemination and Contribution to standards

The author has actively participated in WP4, WP5 and WP6.

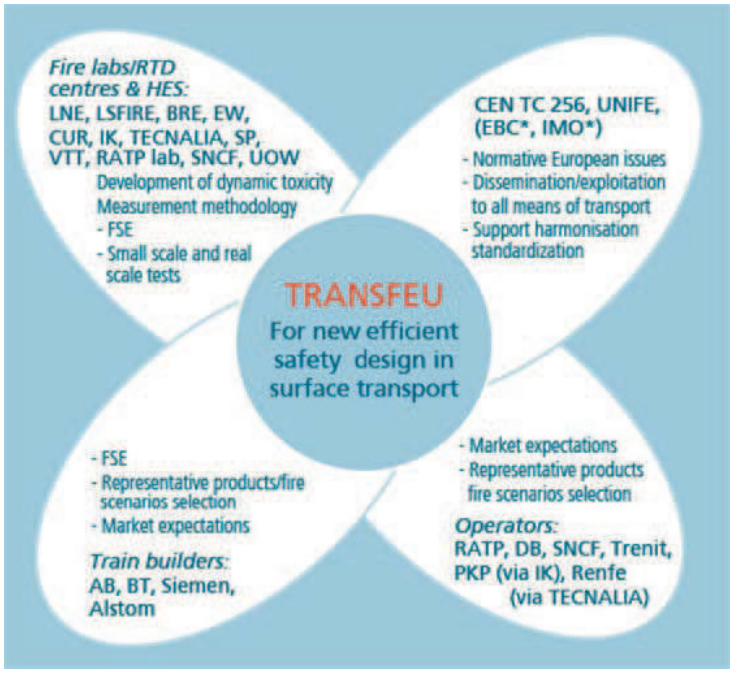

Figure 2: Transfeu partners

Over the last forty years, different fire tests, from small scale to large scale, were performed to understand the fire behaviour of the passenger train products, often seats and interior wall panel products. These tests have highlighted that the design of seat assemblies and wall linings are important factors in fire growth. Furthermore, according to these fire tests, it is important to remind that the quantity and nature of fire effluents (smoke, temperature and radiative heat flux) are linked to the fire development and type of products involved in fires. This strong combination between fire effluents and passenger train products as well as combustion conditions requires to understand the reaction-to-fire of train materials from small scale to large scale.

In the last decades, numerical fire computational fluid dynamics code was developed and applied on buildings, for example. The involved models in such CFD code are described

in this thesis. Currently, the employed method to simulate a large fire in a compartment depends on cone calorimeter data and on its exposure heat flux. Thus, there is a real need to determine train product fire growth, fire effluents impact on passengers of a design scenario, and independently on the fire source.

Considering the whole fire research projects, the main experimental fire characteristic is the heat release rate (HRR). The HRR is one of the fire data compared between experimental tests and numerical models. The aim of this comparison is to understand the ability of a fire CFD code to simulate a fire in a coach, in order to examine different coach designs. In this context, there are two possible ways to simulate a fire:

- The *prescribed* HRR (the mass flow of the fuel is set from experimental data).
- The *predicted* HRR (the mass flow of the fuel is modelled as function of temperature).

In the Transfeu project, these two simulation options are divided in three different approaches:

1. The prescribed HRR approach (the mass flow of the fuel is set only from the experimental cone calorimeter (ISO 5660-1 (2002)) data).
2. The controlled prescribed approach (the mass flow of the fuel is set from the experimental cone calorimeter (ISO 5660-1 (2002)) data and controlled by a thermal parameter).
3. The predicted HRR approach (the mass flow of the fuel is modelled by a pyrolysis model).

The principle is to understand the limits and advantages of each of these approaches. The application of each of them requires a multi-scale validation. These three methods are applied on two railway products involved in a hazardous coach design fire scenario.

In this project context, the author has performed and led the fire risk analysis and the multi-scale approach. Pyrolysis, combustion processes and gas generation have been studied experimentally and numerically on two different products, where other products have been analysed with less details by other partners. Only the most detailled modelling approach (the predicted HRR) is presented here. All full and real scale tests presented in this thesis were designed by a group of experts which included the author. Some experiments were conducted by the author and some other were realized by partners, under the supervision of the author.

Introduction

Fire safety is a main research field in railway transport system. Due to the high number of passengers by unit area in vehicles and delayed evacuation because of operation conditions, it is important that materials and products vehicles have good fire performances. These railway products such as seats, roof or wall panels must follow fire safety requirements according to train operation category and type of vehicle.

In this context, this thesis is incorporated within the framework of European research project, named Transfeu. The objective is to predict fire growth of a design fire scenario, considering the limits of the used numerical tool. This work is based on multi-scale investigations on a scenario, selected by a fire risk analysis. The fire behaviour of two products present in vehicle is studied (a seat and a wall panel). These two products have been chosen due to their positions in design fire scenario, close to the burner.

The seat studied is composed of three different elements: cushion, back and headrest. Each of them is made up of multilayer materials: cover, interliner and foam, framed by polycarbonate shell. The second studied product is an inner wall panel of train vehicle. It is a non-structural composite made of glass fibres and a polyester resin matrix. The composite surface is covered with a polyester gelcoat. In this way, this work is divided in six chapters.

The first chapter describes the selected design fire. The design fire scenario has been chosen according to a fire risk analysis, based on event trees method. The pre-selected scenario by Transfeu fire safety railway experts is compared with the whole possible scenarios. This scenario is characterised in term of fire source, detection, ventilation system, fire mitigation, type of vehicle, operation category, evacuation strategy and vehicle products. The composition of each studied product (seat and composite wall panel) is detailed on this chapter.

The multi-scale approach used in this work is based on reaction-to-fire understanding of these two products. The second chapter is the state of the art of occurred phenomena during experimental and numerical material reaction-to-fire. Before to simulate physical phenomena, it is essential to correctly understand pyrolysis, combustion processes and fire effluents generation. Moreover, it is important to distinguish the toxicity due to either a material or a scenario, since the toxicity is not a material characteristic but evolves with fire conditions. This chapter also describes toxic gases present in fire and their characteristics. Toxic gases generation is directly linked to material thermal decomposition. Thus, a presentation of each material thermal reaction mechanism is realised. Finally, this chapter makes an overview of pyrolysis modelling concept.

The third chapter describes the multi-scale approach. It is based on experimental and numerical material and product fire behaviour comparison, from raw matter to real scales. Each scale corresponds to a validation step of fire physical phenomena. Furthermore, the main physical models of the numerical tool used are detailed in this chapter. The numerical tool used is Fire Dynamics Simulator (FDS) version 5.5.3.

The fourth and the fifth chapters describe respectively the multi-scale results on rail-

way seat and composite wall panel. The comparisons are performed on different global physical data such as product mass loss, heat release rate, burnt surface area, toxic gas generation, and on local physical data like material surface and gas temperatures. The ability of FDS code to predict fire growth at real scale is examined taking into account experimental uncertainties, code limits and proposed alternative solutions.

The chapter six presents fire growth and toxic gases generation simulation results of the studied scenario. Important variations exist between experimental and numerical results related on carbon monoxide generation. A prescriptive approach of carbon monoxide release is proposed from finished product scale and based on experimental data, to improve these results.

The last part presents the general conclusion and future works from multi-scale results of the design fire scenario.

Chapter 1

Selection of Design Fire Scenario and associated products

Contents

The fire effluents impact on passengers during the running capability of a train might be estimated not only according to the type of products present in the coach but also to a given Design Fire Scenario (DFS). DFS typically defines the ignition and fire growth process, the fully developed stage and the decay stage, together with the environment and systems that will impact the course of the fire, until the safe evacuation of people. A fire risk analysis has been conducted in order to select some of the most hazardous DFS in order to study their fire safety performances.

The aim of this fire risk analysis is to compare a few selected DFS with the overall possible scenarios, hence the name: Relative Fire Risk Analysis. This analysis consists in finding all possible fire sequences, from fire outbreak through fire spread in the railway transport network (limited to fire outbreak in passenger areas). The chosen way to identify this succession of events is to use risk analysis tools, such as events trees. In support of this risk analysis and in harmony with requirements of risk analysis techniques, an

expert team was constituted by fire safety experts of train manufacturers, train operators and fire safety regulator. This team is called later Transfeu railway fire safety experts. In parallel to this risk analysis, two DFS have been identified by Transfeu railway fire safety experts, based on their relevance and feedback experience. Relative fire risk analysis results is a matrix of relative occurrence probabilities versus relative severities of each DFS. The risk level position of these two pre-selected DFS is compared with the others in the global matrix. Afterwards, a sensitivity analysis is developed in order to complete the relative fire risk analysis.

The selected hazard design fire scenario is then described accurately with all products. Afterwards, the reaction-to-fire of two products (a seat and a wall panel) have been chosen to be analysed through an experimental and numerical multi-scale study. Finally, the nature and thermal properties of each material are detailed.

1.1 Fire risk analysis applied to railway European transport - Relative approach

1.1.1 Risk analysis method

The risk analysis was firstly applied to power plants or chemical plants and then extended to all types of hazards, such as a blowing up, fire or a flooding. Table 1.1 represents some of the existing methods to carry out the risk analysis procedure. All of them use different ways to estimate qualitative and quantitative aspects. This estimation depends on the type of system and the level of knowledge related to this system. Some analysis such as HAZOP, PRA or Events analysis can be used only to qualify or describe the hazard system, while more sophisticated ones such as deterministic or probabilistic approaches can be employed to quantify the identified risk. Some of them start from causes, others from supposed consequences. The combination of both allows a complete overview from supposed causes to possible consequences.

Table 1.1: Risk analysis method.

Methods	**Analysis approach**	**Reference**
Hazard and operability studies (HAZOP)	Qualitative	Royer (2009)
Preliminary Risk Analysis (PRA)	Qualitative	Mortureux (2002)
Failure, Cause and Event Trees	Qualitative	Iddir (2009)
Failure Mode Effects Analysis (FMEA) and	Qualitative and Quantitative	EN 60812 (2006)
Failure Mode Effects Analysis and Criticality (FMEAC)	Qualitative and Quantitative	EN 60812 (2006)
Systemic Organized Method of Risk Analysis (MOSAR)	Qualitative	Perilhon (2002)
Deterministic Risk Analysis	Quantitative	Kirchsteiger (1999)
Probabilistic Risk Analysis	Quantitative	Kirchsteiger (1999)

For more information about risk analysis methods, the authors refer to the following texts: (Kirchsteiger (1999), Mortureux (2002), Perilhon (2002), EN 60812 (2006), ISO 16732-1 (2012), Royer (2009) and Iddir (2009). However, the relative fire risk analysis methodology of this thesis is composed of several known risk analysis methods combined together. Parts of the Preliminary Risk Analysis and the Event Trees methods are used

to identify all possible DFS for this system. An event tree is then used as a description of the temporal, causal sequences of events, built around a single initiating condition. Deterministic and Probabilistic Risk Analysis are used to complete the qualitative analysis and to assess relative occurrence probability and relative severity of each identified design fire scenario. Finally, a stochastic analysis is used to assess the sensitivity of this relative fire risk analysis.

1.1.2 The design fire scenario concept applied to train fire safety

This relative fire risk analysis is based on the design fire scenario concept. A design fire scenario represents a chronological chain of events from fire ignition to completion of the train evacuation for this case. Each event must be well identified and described according to the future European fire standard, used for train fire safety design (CEN/TS 45545-1 (2009)). Each event is conditioned by the pre-existing situation and events that already happened. The chronology of events, in figure 1.1, which affects fire dynamics is:

- Fire ignition source: it represents all possible fire sources inside a vehicle.
- Fire detection: when a fire occurs on a train, the automatic or manual detection/alarm is activated. In this study, the event of fire detection/alarm becomes always true, but time to detection depends on a set of possible events.
- Ventilation system: the ventilation system could be stopped when detection is activated in the European railway transport network, depending on train operation category according to CEN/TS 45545-1 (2009).
- Passive and Active fire protection: the passive and/or active fire protection are methods to mitigate fire spread or to bring the fire under control, according to CEN/TS 45545-6 (2009).
- Train stopping strategy: After detection is activated, the driver or the control center have to decide where the train has to be stopped in order to evacuate people safely. If this is an outdoor fire, the train could stop immediately, whereas in a tunnel, the train may have to continue running to bring passengers to a proper evacuation place, such as a station.
- Evacuation strategy: Once detection is activated and the fire localised, passengers make important decisions with the help of the train staff, in order to save their lives, depending on the train design. Some trains have relative safety places, such as adjacent vehicles: these allow passengers to be temporarily safe from fire effects before they reach an ultimate place of safety.

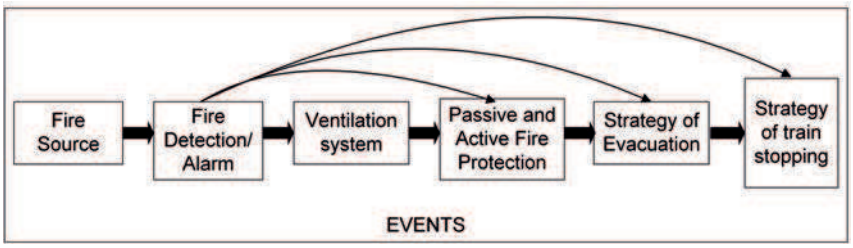

Figure 1.1: Concept of Design fire scenario

1.1.3 Methodology

The developed fire risk analysis is based on a complete and precise description of a large number of possible design fire scenarios. Figure 1.2 illustrates this methodology.

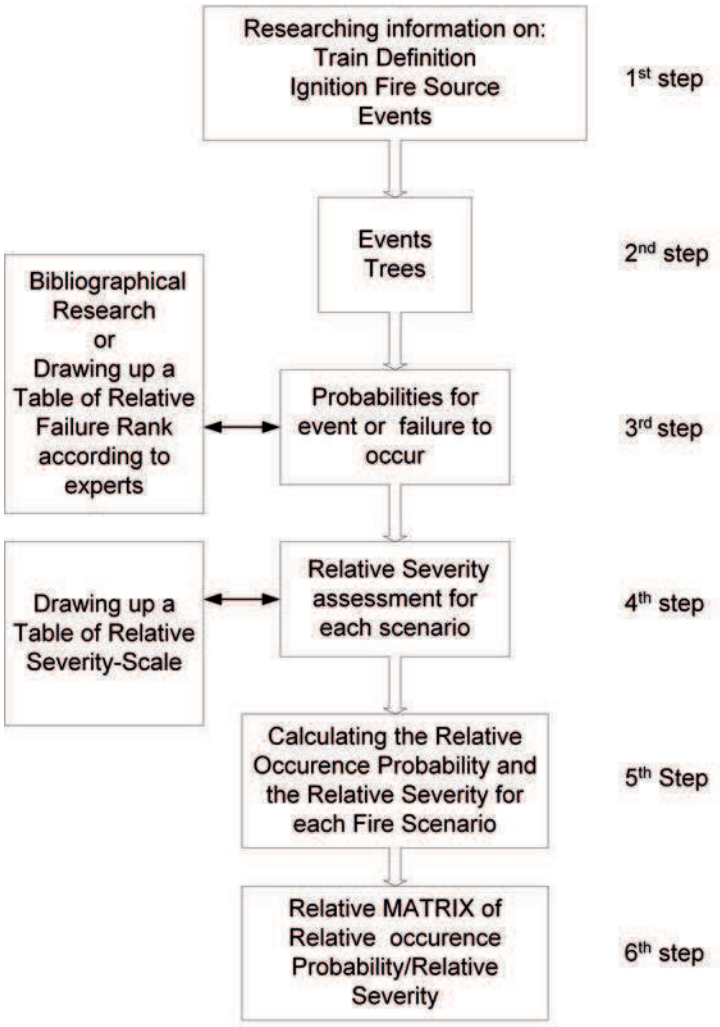

Figure 1.2: Methodology of the relative fire risk analysis

It is composed of 6 main steps. The first step is there to define the studied system,

such as the train vehicle and all design which can influence the fire source and growth. Then, for the second step, all these pieces of information are summarized in a general event tree that goes from the cause of the fire source to the evacuation strategy of passengers and staff. The corresponding general event tree can not be dealt with through a frontal analysis, because it includes too many branches.

To solve this issue, the general event tree is divided into sub-event trees that are then linked back to the whole tree. Moreover, each sub-event tree gives a number of several sub-scenarios. The third step enables to estimate the probability of each event or the probability of failure for each branch of each sub-event tree. The fourth step allows to assess each relative severity of each sub-DFS via a deterministic approach. The issue of a probability and severity assessment is explained in the next part. The fifth step is the calculation of the relative occurrence probability and relative severity of each DFS. Finally, the results of this risk analysis are expressed as a risk matrix where two pre-selected scenarios are highlighted.

In this risk analysis, the main tool used is the event tree. As defined in the introduction, an event tree is a succession of chronological events. As it is shown in the following figures, all branches are associated with an action corresponding to a probability. There are two kinds of probabilities:

- Probability of event: it is the probability that an event will occur. This probability is often unknown. Thus, It is assumed that an equiprobable distribution is appropriate. A sensitivity analysis using different kinds of distribution could be conceivable in the future.
- Probability of failure: it represents the probability of failure for a given system, i.e. that the event of a given system failure happens. These probabilities are obtained on the basis of literature. For example, the reliability of automatic alarm is assumed to be 0.999 (Initiating event frequency working group (2009)). However, it was difficult to find probabilities of failure regarding, for instance, the dysfunction of ventilation or the emergency lighting. The deterministic approach, based on table 1.2, is used to determine the probability of failure, when it is unknown, with the help of Transfeu railway fire safety experts.

Table 1.2: Failure frequency ratio corresponding to each event.

Event	**Failure frequency ratio**
Frequent	1 (reference)
Possible	10^{-1} to 10^{-2}
Rare	10^{-2} to 10^{-4}
Extremely rare	10^{-4} to 10^{-6}
Unlikely	10^{-6} to 10^{-8}
Highly unlikely	10^{-8}

Occurrence probability of sub-DFS is the product of each probability associated with each branch. It is important to note that small p means the probability of event or the probability of failure and a capital P means the relative occurrence probability of the sub fire scenario in each sub event tree. Assessing failure probability is often a tedious work. A sensitive analysis is then needed to assess the impact of probabilities uncertainties on the global result.

Each sub-scenario is also associated with a relative severity. As shown in Table 1.3, relative severities are obtained by a deterministic approach which takes into account the impact on train passengers in a fire case. For each sub-DFS obtained, a relative severity scale is assessed by the Transfeu railway fire safety experts.

Table 1.3: Relative severity scale table.

Severity scale	**Definition**	**Severity rank**
Minor	No particularly hazard for passengers and staff	1
Major	No safety hazard for passengers and staff	2
Critical	Hazard for passengers and staff	3
Very Critical	Very hazardous for passengers and staff life	4

Furthermore, each probability assessed for each main event is supposed to be independent. It means that the sum of each branch in each sub-event tree is equal to one. It is assumed that all actions are independent from the previous action in the sub-event tree. In the end, the global event tree gives 172,800 DFS, characterized by their relative occurrence probability and relative severity.

1.1.4 Event tree

1.1.4.1 The fire source sub-tree

According to two different references (Eurostat (2012) and Hudson (2001)), there are six principal kinds of fire origin in European trains nowadays, which are: arson, electrical, technical and mechanical defect, accidental and unknown (figure 1.3). The most common fire cause is arson. Each possible fire source in a vehicle is associated by an occurrence probability (P1 to P6) and a fire hazard status. Considering the low number of casualties and injuries for each fire source by year in the statistics, the fire hazard status of each fire source is estimated as function of the distance between the location of the fire source and the passengers in the train. The fire hazard status is also associated with a severity scale (table 1.4).

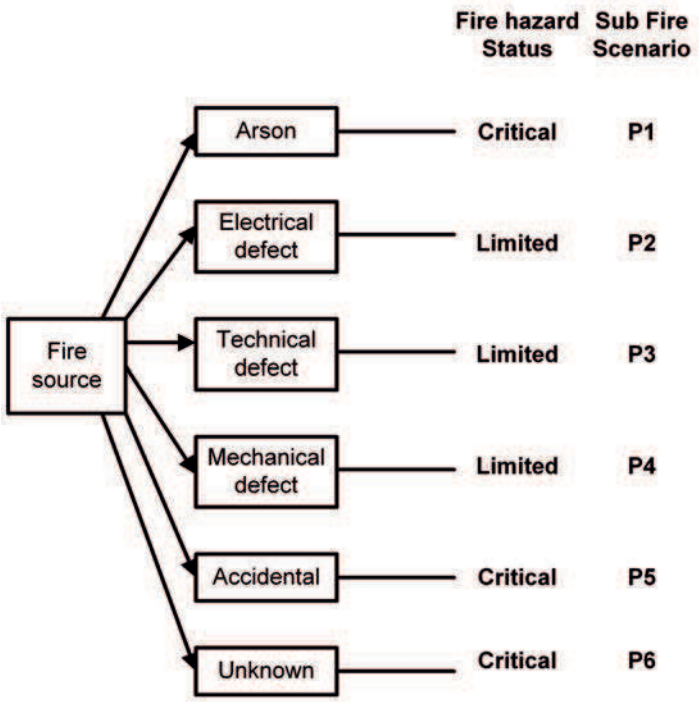

Figure 1.3: The fire source sub-tree

Table 1.4: Relative severity-scale of the fire source sub-scenario.

Fire Ignition Source	**Hazard status**	**Relative Severity-Scale**
Arson	Critical (passengers could be close to fire source)	Critical
Electrical defect	Limited (passengers are supposed to be far from fire source)	Minor
Technical defect	Limited (passengers are supposed to be far from fire source)	Minor
Mechanical defect	Limited (passengers are supposed to be far from fire source)	Minor
Accidental	Critical (passengers could be close to fire source)	Critical
Unknown	Critical (passengers could be close to fire source)	Critical

1.1.4.2 The detection/alarm sub-tree

This sub-tree is based on the following hypotheses, in accordance with the CEN/TS 45545-6 (2009) and Transfeu railway fire safety experts (Figure 1.4):

- Two different kinds of alarm exist: either manual or automatic;
- It is assumed that fire detection systematically occurs: fire is either detected by an automatic detection system or by passengers and staff. The case where there is no

witness at all of the fire is not considered in this study. However, the shorter the detection time is, the more safety of passengers and staff is preserved;

- Alarm systems may be subject to failure;
- If the automatic alarm is not working, someone triggers the manual alarm after a while;
- Higher is the number of passengers, the faster the manual alarm is supposed to be performed.

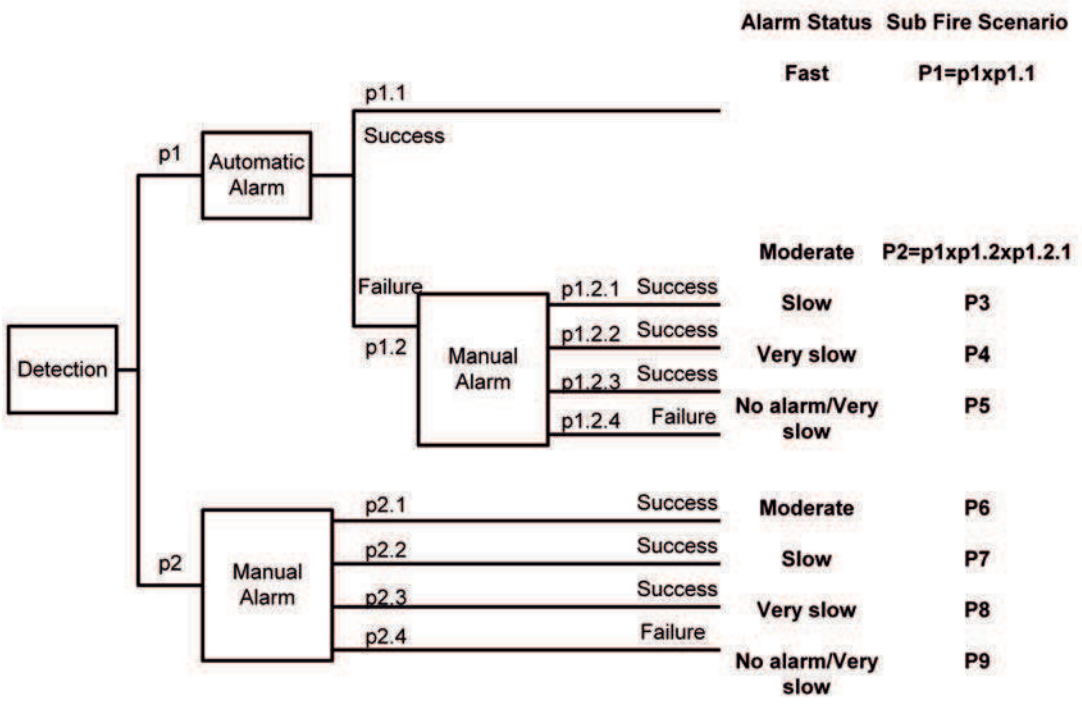

Figure 1.4: The fire detection sub-tree

Nine sub-design fire scenarios are found. *Success* and *failure* in the Detection/Alarm sub-tree correspond respectively to *triggered alarm* and *not triggered alarm.*

The column *Alarm triggering delay* is the relative delay between the moment when fire is detected (either automatically or manually) and when the alarm is set. The relative severity scale matches with the state of the scenario (table 1.5).

Table 1.5: Relative severity scale of the fire detection scenario sub-tree.

Status	Relative severity-scale
Fast	Minor
Moderate	Major
Slow	Critical
Very Slow	Very Critical

1.1.4.3 The ventilation system sub-tree

In accordance with the CEN/TS 45545-6 (2009), when fire detection is activated, air conditioning stops and the extraction system is maintained. Regarding the ventilation system, there are two possible sub-DFS (1.5).

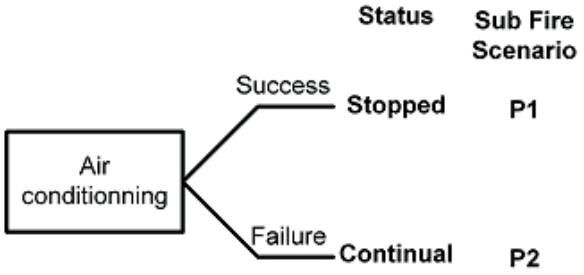

Figure 1.5: The ventilation sub-tree

If the ventilation system is not stopped, due to a failure of the stopping device, it provides fuel to the fire and a mix between air and smoke, leading to more serious consequences. For each status, a relative severity scale is given as an hypothesis in the following table 1.6.

Table 1.6: Relative severity-scale of the ventilation scenario sub-tree.

Status	Relative severity-scale
Stopped	Minor
Continual	Critical

1.1.4.4 The fire protection sub-tree

There are two kinds of fire protection (regarding trains): passive and active fire protection.

The Passive fire protection sub-tree

According to the CEN/TS 45545-6 (2009), fire barriers are ranked in the following way:

- The lowest performing barrier is E = Integrity.
- The next level of performance is E W = Integrity and Radiation transfer.
- The top level is E I = Integrity and Insulation requirement.

Passive fire protection structures such as fire barriers or fire doors are located in very specific places in the train. Passive fire protection is assumed to not be triggered. Thus, there is no probability of failure to its activation. Its probability of failure is therefore assumed to be null even if it may fail to fulfil its purpose if broken, damaged or unexpectedly affected by the fire. During a fire, there are two possible choices for the passive fire protection (figure 1.6): it is either present or it is not.

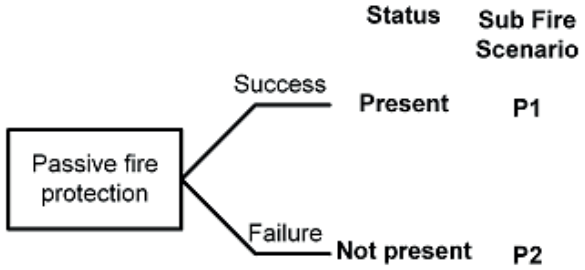

Figure 1.6: The Passive fire protection sub-tree

Two sub-scenarios are hypothesized for the passive fire protection event. Indeed, the event probability represents the event to have fire barrier between fire and passengers. Passive fire protection can delay fire spread and consequently passengers and staff can have more time to evacuate. If passive fire protection is present, people will face less serious consequences (table 1.7).

Table 1.7: Relative severity-scale of the passive fire protection scenario sub-tree.

Status	**Relative severity-scale**
Present	Minor
No present	Critical

The Active fire protection sub-tree

The active fire protection sub-tree is based on the following hypotheses, in compliance with CEN/TS 45545-6 (2009):

- There are two kinds of active fire protection: fixed fire fighting and mobile fire fighting;
- The active fire protection system features a probability of failure;
- Fire control is assumed to be faster with fixed fire fighting than with a hand extinguisher (due to human action);

- If automatic fixed fire fighting is not working, an extinguisher is used by passengers to maintain the fire under control. The authors made an assumption that at least one passenger or staff will try to extinguish the fire;
- There is a supposed 50% probability that the fire-fighting equipment efficiently controls the fire since its real efficiency is unknown.

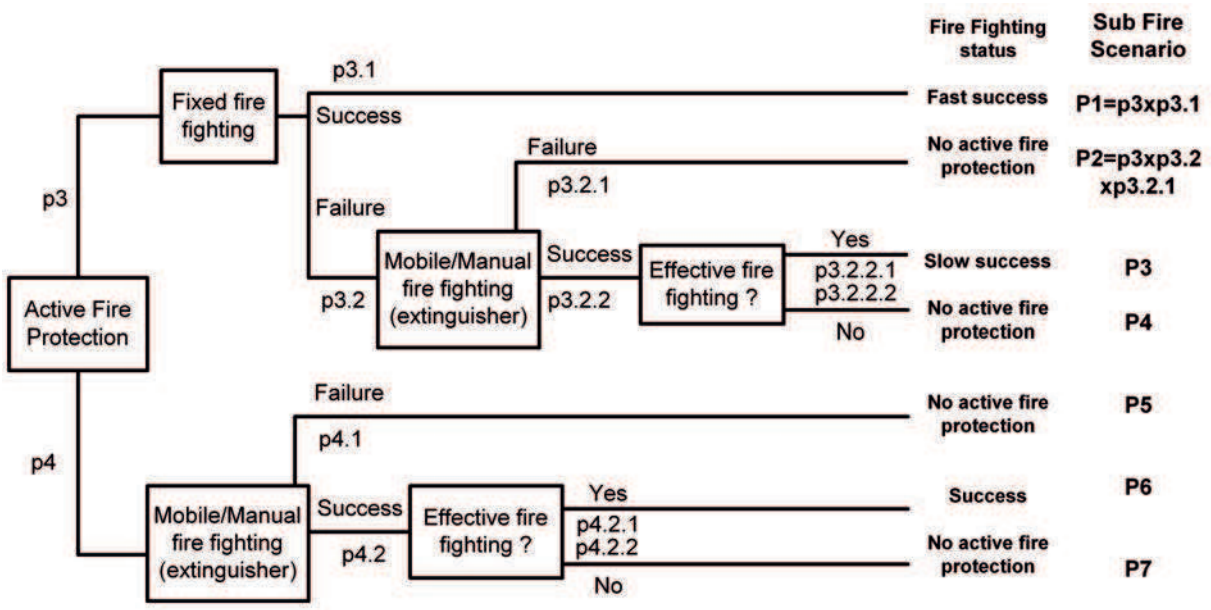

Figure 1.7: The Active fire protection sub-tree

Figure 1.7 shows there are seven possible sub-design fire scenarios. As indicated in the sub-tree, if fixed fire fighting fails, manual fire fighting is then the second option to put out the fire. Furthermore, putting out the fire in sub-scenario 1 shows faster results than in sub-scenario 3, due to the delay resulting of using an extinguisher (figure 1.7). Then, if the fire is not put out by an extinguisher, the result is *No active fire protection*. If the success is fast or slow, the severity scale will respectively be Minor and Major (table 1.8). However, if active fire protection is not working, the severity will be Critical (table 1.8).

Table 1.8: Relative severity-scale of the passive fire protection scenario sub-tree.

Status	**Relative severity-scale**
Fast Success	Minor
Slow Success	Major
No active fire protection	Critical

1.1.4.5 The strategy of the train stopping sub-tree

The train-stopping strategy depends on the train environment (in a tunnel for instance) and the driver's decision. The driver's choice will be conditioned by the operation categories (OC) and design categories (DC) provided in CEN/TS 45545-1 (2009). The latter refers to the train type: an automatic train (without driver), a standard train, a double-deck train or a sleeping train. The European standard (CEN/TS 45545-1 (2009)) defines the OC as:

- OC1: Side evacuation to an ultimate safety place with a minimum delay
- OC2: Side evacuation to an ultimate safety place with a short period of time
- OC3: Side evacuation to an ultimate safety place with a long period of time
- OC4 : No side evacuation to an ultimate safety place with a short period of time

The train-stopping strategy sub-tree (figure 1.8), is based on the following hypotheses and parameters:

- The operation category
- If the train stops because of an engine failure due to fire, the probability that the train stops at the platform is assumed to be null.

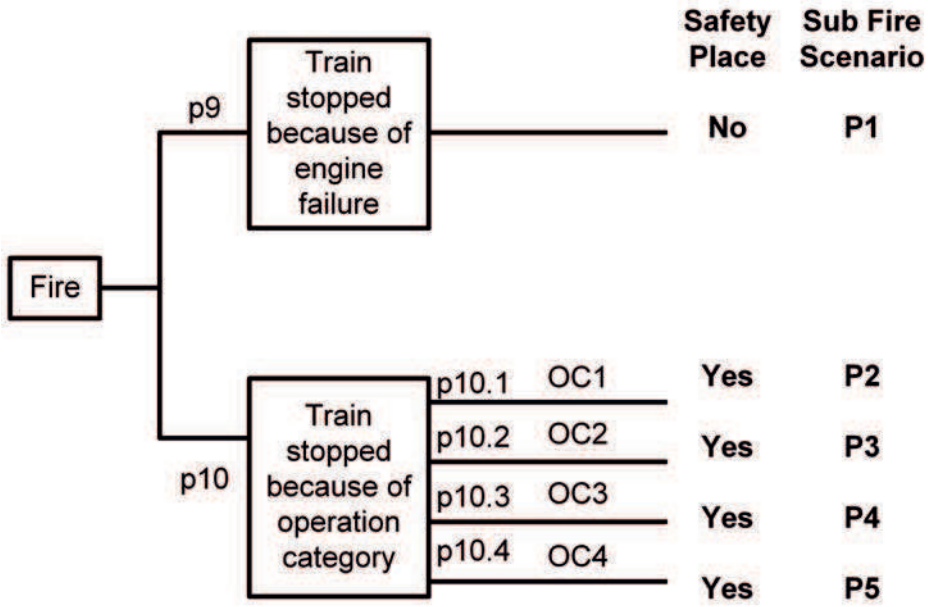

Figure 1.8: The strategy of the train stopping sub-tree

Five sub-design fire scenarios are possible. Probability P1 is the probability for a train to be subject to an engine failure that impairs the running capability. Probability p10 is the probability of stopping a train as a function of the operation category. Probabilities

p10.1, p10.2, p10.3 and p10.4 are deemed to be equivalent because the real frequency of the different train operation categories is unknown. The higher the index of the operation category is, the more difficult the evacuation of passengers is assumed to be. It is possible that the driver cannot comply with the procedure linked to the OC due to a problem in functional integrity, e.g. engine failure or energy breackdown. In this case, passengers may be located in different areas and may take more time to reach a safety place. In this situation, the sub-DFS does not respect the operation category (figure 1.8). Consequently, the considered sub-scenario becomes very dangerous for passengers, because its severity scale is very critical. The relative severity of the train-stopping strategy sub-tree is (table 1.9):

Table 1.9: Relative severity-scale of the train-stopping strategy sub-tree.

OC	**Status**	**Relative severity-scale**
1	Yes	Minor
2	Yes	Major
3	Yes	Critical
4	Yes	Very Critical
No	No	Very Critical

1.1.4.6 The evacuation strategy sub-tree

As shown in reference CEN/TS 45545-6 (2009), this tree (figure 1.9) depends on the train geometry and the following hypotheses:

- The probability of an emergency lighting failure;
- The possibility to have a relative safety place in the vehicle;
- The probability of failure of the automatic doors opening;
- The crowd effect (empty coach, half-full coach or full coach);
- The way to go to the ultimate safety place (through doors or windows).

Some trains have relative safety places, such as adjacent coaches: these allow passengers to temporarily be safe from fire effects before they reach an ultimate place of safety. Following Briggs (2010), an ultimate place of safety is a place away from the burning vehicle in which a person is protected from the effects of fire, e.g. evacuated trough a platform away from fire hazards.

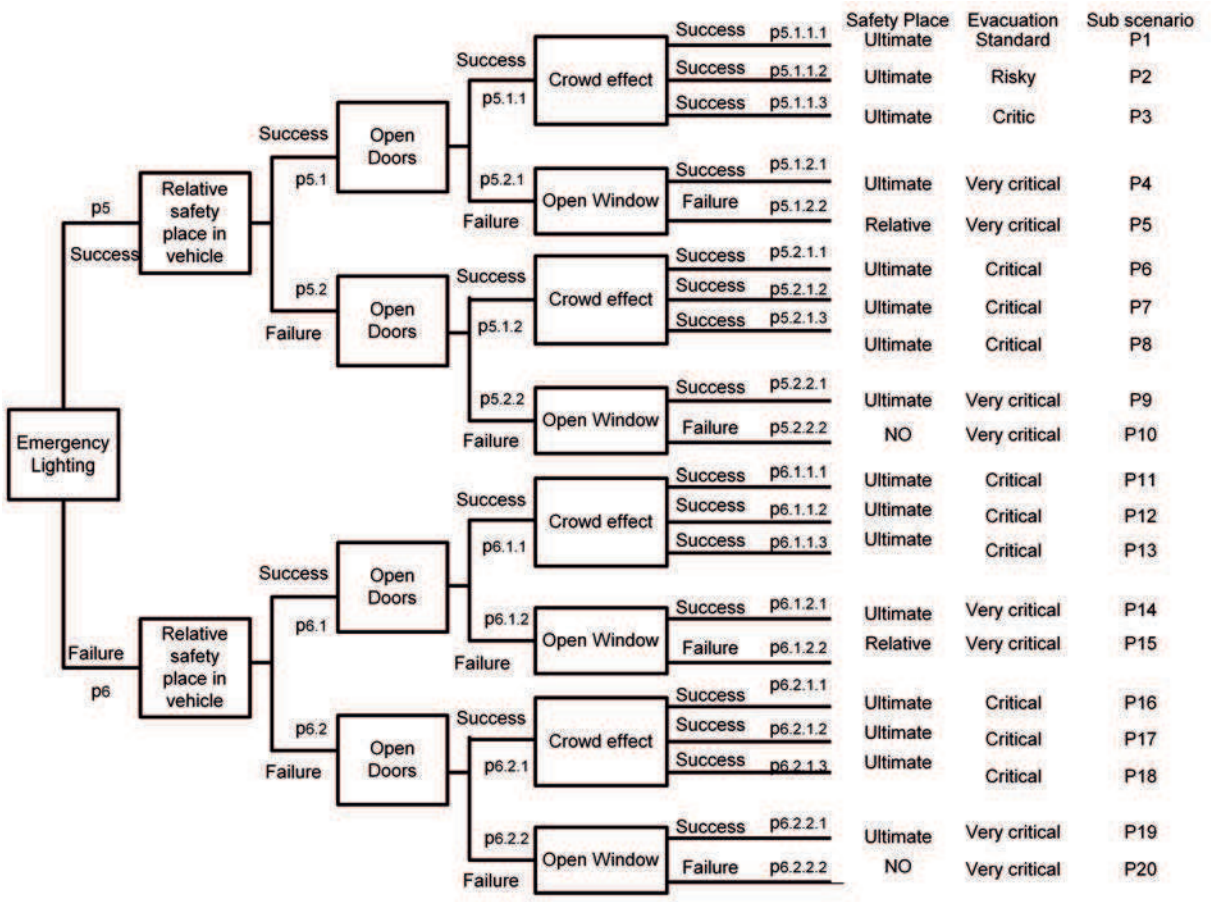

Figure 1.9: The evacuation strategy sub-tree

The relative severity scale depends on the assessment of Transfeu railway fire safety experts of and many evacuation criteria:

- The *Ultimate place of safety* is less dangerous than the *Relative* and *No safety place* for passengers evacuation.
- Emergency lighting is very important in case of evacuation. If it fails, passengers cannot go out in optimal safety conditions.
- The means to reach an ultimate or relative safety place, such as through a door or a window also matters. It is more hazardous to go out through a window than through a door.
- The density of presence: the more passengers there are, the more difficult it is to evacuate which represents higher hazard.

According to these sub-scenarios and *their safety evacuation results*, a relative severity scale and a relative severity number are assigned for each sub-DFS, table 1.10.

Table 1.10: Relative severity-scale of the evacuation strategy scenario sub-tree.

Status of Evacuation	**Relative severity-scale**
Standard	Minor
Risky	Major
Critical	Critical
Very critical	Very critical

1.1.5 The risk matrix

When all sub-event trees are built, the global event tree is obtained by chaining sub-event trees to one another, as events are supposed to be independent. Furthermore, the product of all probabilities for one pathway through the root to one leaf of the tree is the probability for a sub-scenario to occur ($P_{l,SDFS}$). A relative severity is also associated to each sub-scenario ($s_{l,SDFS}$). Then, the relative occurrence probability, the relative severity and the risk of each DFS are calculated with Eq 1.1, Eq 1.2 and Eq 1.3:

$$Q_{b,DFS} = \prod_{l=1}^{j} P_{l,SDFS} \tag{1.1}$$

$$S_{b,DFS} = \prod_{l=1}^{j} s_{l,SDFS} \tag{1.2}$$

$$R_{b,DFS} = Q_{b,DFS} \times S_{b,DFS} \tag{1.3}$$

Transfeu railway fire safety experts have chosen two hazardous predefined design fire scenarios, called 1A and 1B, based on their experiments feedback. They are described in table 1.11.

Table 1.11: Description of the pre-selected design fire scenarios 1A and 1B.

Event	**Scenario 1A**	**Scenario 1B**
Ignition source	Arson	Arson
Fire detection/alarm	Very Slow	Very Slow
Ventilation	Continual	Continual
Passive fire protection	Not present	Not present
Active fire protection	Not present	Not present
Design and Operation categories	Standard - OC1	Standard - OC2
Evacuation	Critical (Sub-scenario 3)	Critical (Sub-scenario 3)

The matching design category corresponds to a standard train and an operation category (OC) 1 and 2 (CEN/TS 45545-1 (2009)). Thus, according to equations 1.1 and 1.2, scenarios are characterized by their own relative occurrence probability (Q_{1A} and Q_{1B}) and

relative severity (S_{1A} and S_{1B}).

Figure 1.10 represents the relative matrix for standard trains and for operation category 1 to 4. Considering the bounds of the severity scales and the probabilities, and the multiplicative nature of the couple combinations, a logarithmic scale is used for a representation of data density.

The points scatter diagram corresponds to the 172,800 DFS (cross points), including scenarios 1A and 1B (respectively black triangular and black square points on figure 1.10). In addition, the more the DFS is placed on top of the graphic, the more the DFS has a high relative occurrence probability. The more the DFS is located on the right of the graphic, the more the consequences on people safety are critical. Considering the large number of possible fire scenarios (figure 1.10), the two scenarios 1A and 1B are placed on the right and on the top of the middle of the matrix. Thus, the consequences on people safety are very critical and these pre-selected scenarios show a great probability for happening (relative to the global matrix).

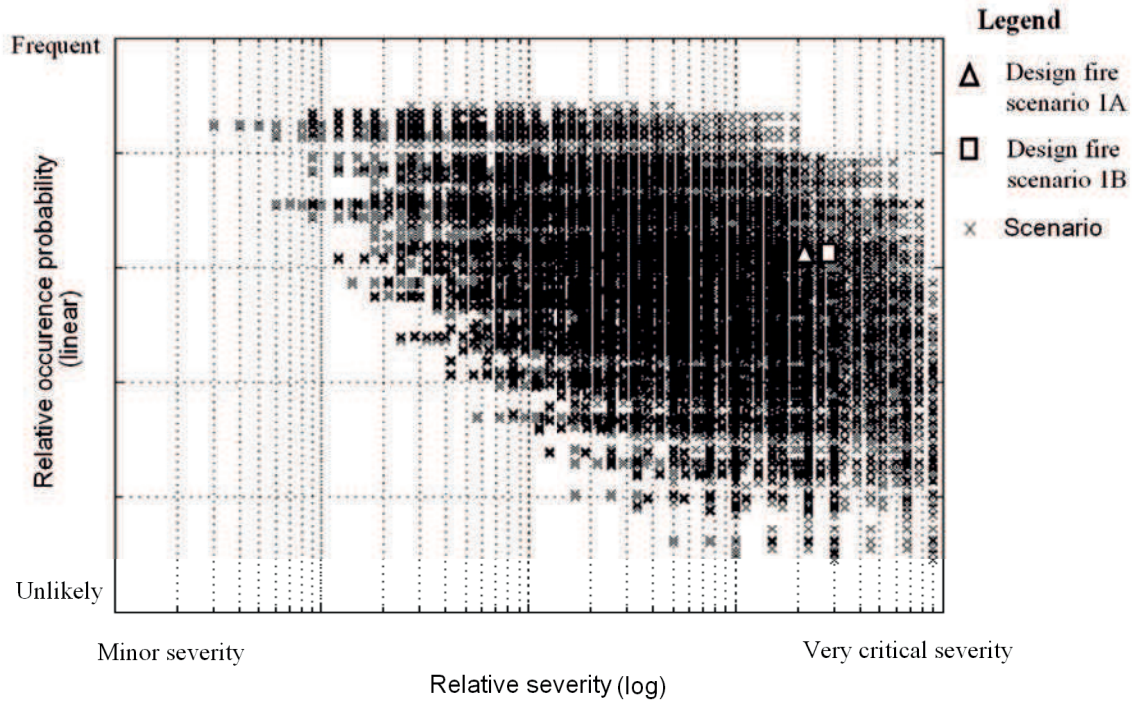

Figure 1.10: Relative risk matrix for standard train

Given the risk of each design fire scenario (Eq 1.3), a risk index is represented in order to compare the risk of the pre-selected scenarios 1A and 1B with the others (figure 1.11). The risk index is divided into five categories: *High risk*, *Serious risk*, *Moderate risk*, *Low risk* and *Negligible risk*. Regarding figure 1.11, the major part of possible DFS for standard trains features both a moderate and a serious risk. The DFS 1A and 1B are very

likely to happen and the consequences for passengers or staff are critical compared with the global matrix, i.e they have a *Serious risk*. Therefore, their selection by the experts team is relevant for the present detailed study.

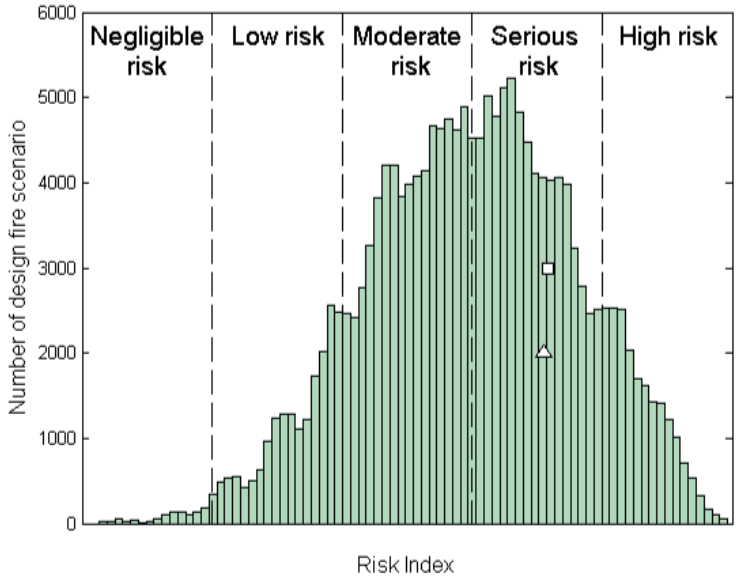

Figure 1.11: Risk index

Occurrence probabilities and severities used in this study are hypotheses and considered as relative. It is necessary to verify if those parameters can affect the results (the relative matrix) obtained with a sensitivity study.

1.1.6 Sensitivity analysis

1.1.6.1 Approach and hypothesis

For this fire risk analysis, the aim of the sensitivity analysis is to determine the weight of each event on the relative occurrence probability and on the relative severity of the two pre-selected design fire scenarios 1A and 1B. The estimation of the sensitivity indexes relies on the Monte Carlo simulations (ISO/CEI GUIDE 98-3/S1 (2008), ISO/CEI GUIDE 98-3 (2008) and Allard *et al.* (2011)). For each event, a probability distribution is assigned. Then, a M-sample ($\Omega = 100{,}000$ in this study) of these probability distributions is obtained using the Monte Carlo method. Application of the model (Eq 1.1 and Eq 1.1) leads to a M-sample for our quantities of interest: the relative occurrence probability and the relative severity of fire scenarios 1A and 1B. Crystal Ball software Version 7.2.1 is used to perform these calculations.

The principle of the Monte Carlo method is explained in figure 1.12. The four input data (ventilation, active fire protection, train-stopping strategy and evacuation strategy) are represented with their probability distributions, such as Uniform or Gaussian ones.

Input data are known (a lower bound and a upper bound in this case), a uniform distribution has been chosen.

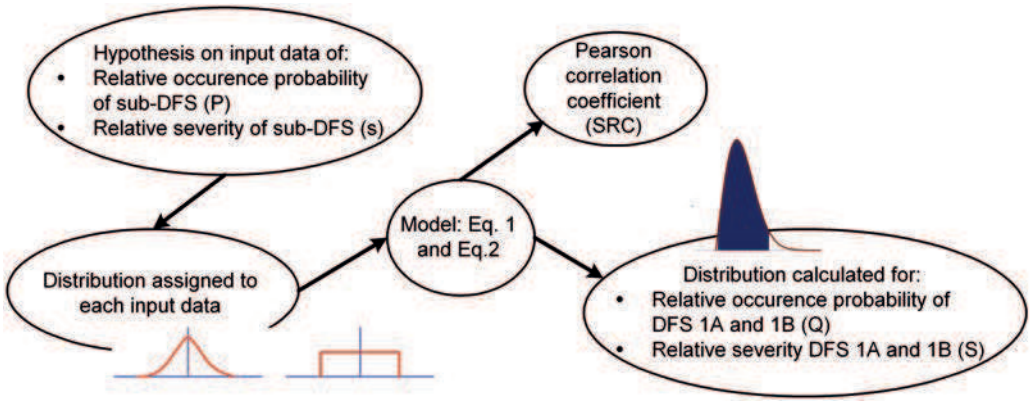

Figure 1.12: The principle of the Monte Carlo method

However, the sensitivity analysis of the relative occurrence probability of DFS 1A is calculated only with four discrete input values because only their uncertainties of occurrence probability are known and the two other input values are estimated to be constant. Consequently, the sensitivity analysis is assessed for four variables which are related to ventilation, active fire protection, train-stopping strategy and evacuation strategy. However an uncertainty is estimated for each relative severity of selected sub-scenarios. Then, for each chosen probability distribution, a 100,000-size sample of the input data is obtained through the pseudo-random congruential number generator implemented in Crystal Ball software. This leads to drawing up a histogram approximately representing the probability distribution of the output data.

According to references Collin and Anstett-Collin (2010) and Iooss (2011), the results of those simulations are probability distributions of the output data and the Standardized Regression Coefficient (SRC).

$$SRC = SRC(X_i, Y) = \beta\sqrt{(\frac{Var(X_i)}{Var(Y)})} \tag{1.4}$$

The SRC measures the linear influence of each input parameter on the variance of the output. But, if a second-order influence (interaction) between two inputs is significant, this quantity can not be used to identify it. Second-order Sobol coefficients (Eq 1.5) should then be used. The calculation of the first-order Sobol coefficient (Eq 1.6) is able to prove if the model is linear only if the Standardized Regression Coefficient is equal to this coefficient (SRC = S_i).

$$S_{ij} = \frac{V_{ij}(X)}{Var(Y)} \tag{1.5}$$

$$S_i = \frac{Var[E(Y|X_i)]}{Var(Y)} \tag{1.6}$$

References Collin and Anstett-Collin (2010) and Iooss (2011) explain more precisely the definition of equations 1.5 and 1.6. Furthermore, it is possible to calculate the total Sobol coefficient, S_{Ti} (Eq 1.7), in which all influences of all order implying the input parameter X_i are taken into account. If the first-order Sobol coefficient is equal to the total Sobol coefficient, there is no interaction between input parameters.

$$S_{Ti} = 1 - \frac{Var[E(Y|X_{\sim i})]}{Var(Y)} \tag{1.7}$$

1.1.6.2 Results

Results of the sensitivity analysis carried out in scenario 1A on relative occurrence probability and relative severity are in figures 1.13.

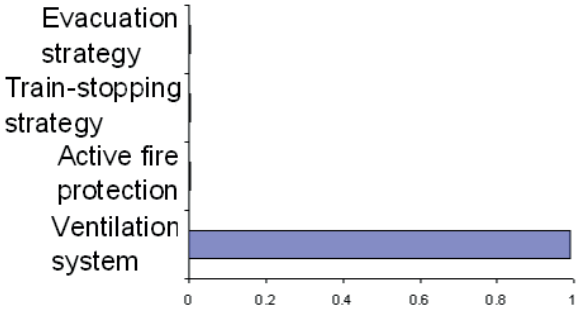

a/ Sensitivity analysis results on occurrence probability of each event, same graphic for SRC, S_i and S_{Ti} calculation.

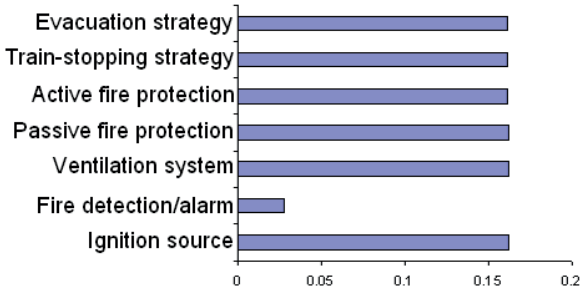

b/ Sensitivity analysis on relative severity of each event, SRC calculation.

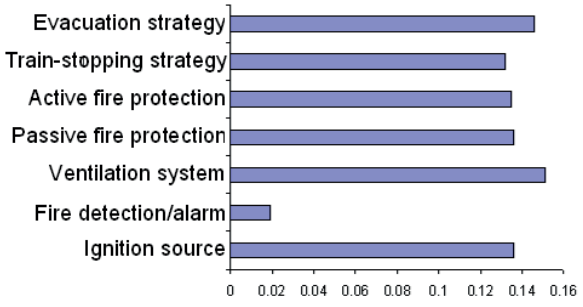

c/ Sensitivity analysis on relative severity of each event, S_i calculation.

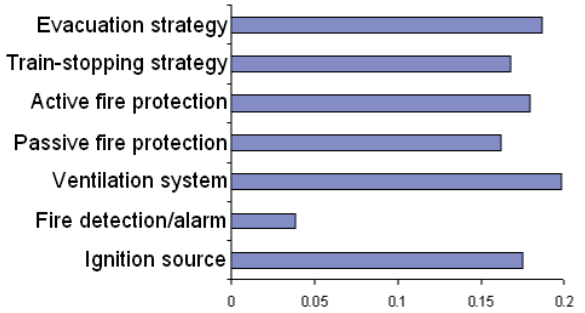

d/ Sensitivity analysis on relative severity of each event, S_{Ti} calculation.

Figure 1.13: Sensitivity analysis results on occurrence probability and on relative severity of each event.

The ventilation system has the most influence on the scenario 1A occurrence probability among these four represented events. According to figure 15a, each SRC is approximately equal to each S_i and S_{Ti}. These results mean that the model of occurrence probability considered here is linear and that there is no interaction between each variables (related on the used models, Eq 1.1 and Eq 1.2).

The sensitivity analysis results of the SRC on relative severity (figure 1.13b) shows that all events have the same impact on the severity in scenario 1A except the fire detection/alarm event. Moreover, there is a small difference between each SRC and S_i values (figure 1.13b and 1.13c).

The sum of each S_i values and each S_{Ti} values is respectively lower than 1 and higher than 1. This difference proves that there are interactions between variables. Then, the second-order Sobol coefficient (Eq1.5) is calculated for the severity model (Eq1.2) in order to quantify the interaction effects. Each S_{ij} is equal to about 0.01. There is the same small interaction between each couple of variables.

This sensitivity study has also allowed to estimate the probability and severity uncertainties for scenario 1A in the global matrix base on the Monte-Carlo simulations approach. The scenario 1A is still a hazardous scenario compared to the global matrix considering these uncertainties.

1.1.7 Conclusion

Risk analysis is one of the first part of the fire safety engineering methodology (ISO 23932 (2009)). Its objective is to select the most hazardous scenarios in order to study their fire safety performances. A design fire scenario goes from fire outbreak to the completion of people evacuation. The developed methodology of a fire risk analysis used different tools such as event trees or probability distribution. This methodology consists in:

- Describing the railway transport network, the ignition source and the events that may affect the propagation of fire;
- Estimating the input parameters: the relative probability and the relative severity scale. For each event, the occurrence probability and severity are assumed to be independent from each other;
- Building the matrix of relative occurrence probability/relative severity for each type of train.

On the basis of the risk matrix for a standard train, both pre-selected scenarios (1A and 1B), defined by railway fire safety experts, have a high relative occurrence probability as well as a high relative severity compared with the other DFS. The sensitivity analysis is essential because the probability and severity data used are very difficult to obtain due to the rarity of these kinds of events, nowadays, in the railways European transport network.

1.2 Studied Design Fire Scenario

1.2.1 Choice of the studied scenario

The LNE was in charge to study the design fire scenario 1A according to the Transfeu project. Consequently, the studied scenario of this thesis is scenario 1A.

The scenario 1A consists in an arson fire source in a train coach. The studied vehicle type is a standard single coach (reference: Matériel Suburbain 61, figure 1.14).

Figure 1.14: The studied coach of scenario 1A

It has four doors on each side. There is no possible evacuation through an other vehicle. The number of passengers is 75. The air conditioning is continuously injected by the ceiling. Either passive or active fire protection are used during the fire mitigation in this scenario. The fire source is a propane sand diffusion burner. The burner is applied during 10 minutes: 75 kW during 2 minutes and then 150 kW during 8 minutes. This square burner has the following dimensions: length 0.305 m x width 0.305 m x height 0.30 m (ISO 9705 (2006)). The burner is located where a luggage can be placed under normal operation conditions, on the floor close to the seats and the wall deep down of the coach. The design fire scenario is composed of seats, wall panel, strips, ceiling, floor and partition (figure 1.15).

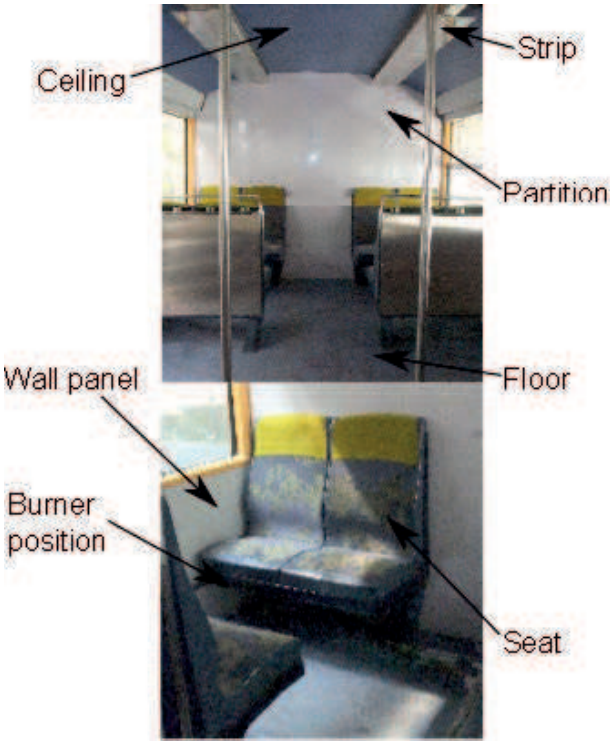

Figure 1.15: The products position of the design fire scenario 1A

At t_0 ($t = 0s$), the burner starts to ignites until 75 kW and all doors are closed. After 40 seconds ($t = 40s$), three doors open on the same side as the burner. At t_{120}, the second phase of the burner (150 kW) begins until t_{600}. The scenario stops when products have self-extinguish (less than two minutes after the burner stop).

The seat and wall panel are potentially the two products which are going to participate to the fire due to their positions with the burner.

1.2.2 Associated studied products

Reaction-to-fire of panel and seat products of an European railway vehicle are studied in the present work. The panel is a hand-laminated glass fibres/polyester/mineral fillers composite, while the seat is composed of a multilayer material:

- a cover: wool, viscose and aramide polymers.
- an interliner: aramide polymers.
- a foam: mixture of polyurethane and melamine foam.

1.2.2.1 Wall panel: Glass reinforced polyester (GRP) composite

The non-structural composite is composed of glass fibre and a resin matrix. The composite surface is covered with a polyester gelcoat. The total thickness of the GRP composite is 4.8 mm.

Gelcoat
Gelcoat is a thinner surface material (0.5 to 0.8 mm) located on the visible surface of the GRP composite. It is composed of a resin (polyester resin) and some additives, such as pigment and mineral charges (like flame retardants, ATH (aluminium trihydroxide). The mineral fillers thermal properties are presented in table 1.12.

Matrix
The resin matrix is composed of 46% of unsaturated polyester and 29% ATH used as flame retardant. Unsaturated polyesters are obtained by the reaction of a dicarboxylic acid (hydroxy-acid functional group) with saturated or unsaturated diol. The elementary raw composition of the unsaturated polyester is $C_1H_{1,039}O_{0,2}$. Properties of ATH and polyester are presented in table 1.12.

Reinforcement
Composite reinforcement are either organic or mineral fibres. Their role is to improve the mechanical behaviour of the composite, depending on their texture and geometry. Different architectures of reinforcement exist, such as:

- Discontinuous random-oriented fibre: fibres are randomly dispersed in the composite (named masts).
- Non-continuous fibre: fibres are all oriented in the same direction. They have very well axial mechanical properties.

- Tissue fibres (knitted): fibres are twisted and oriented according to two directions.

All orientations and textures advantages and inconvenients are detailed in Marquis (2007) and in Marquis (2010) thesis. The composite studied in this thesis has discontinuous random oriented glass fibre. Properties of glass fibres are presented in table 1.12. It should be remind that temperature dependent properties are difficult to obtain.

Table 1.12: Material properties of the wall panel, Powell *et al.* (1966)[a], Kakac *et al.* (1985)[b], Almaz Optics (1993)[c], Accuratus (2002)[d], Lattimer and Ouellette (2006)[e], Mouritz and Gibson (2006)[f], Capote *et al.* (2008)[h], Drysdale (2011)[g], Marquis *et al.* (2012)[h]

Properties	**Units**	**Mineral filler**[a,c]**(TiO_2)**	**ATH**[d,f]	**Polyester**[e,h]	**Glass fibres**[b]	**GRP**[g,h]
ρ	$kg.m^{-3}$	3300	2460	1189	2600	1690
Cp	$kJ.kg^{-1}.K^{-1}$	0.7	0.9	1.3	0.9	1.465
λ	$W.m^{-1}.K^{-1}$	8.4-3.3 (27-927°C)	18-35	0.16	1	0.586
$T_{decomposition}$	°C		220 − 350	350 − 450		
$T_{ignition}$	°C					375
$\Delta H_{reaction}$	$kJ.kg^{-1}$					1750

1.2.2.2 Seat: Multilayer materials

The seat is made of multi-layer materials, composed of a cover, an interliner and a foam, surrounded and shielded by a shell. A picture of a multi layer seat material is presented on figure 1.16.

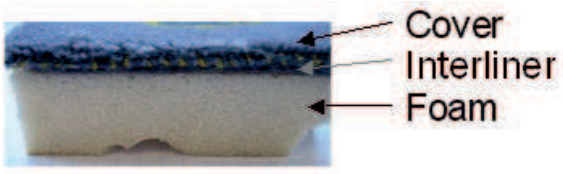

Figure 1.16: Picture of the multilayer seat materials for the cone calorimeter test.

The thickness of the cover, the interliner and the foam are respectively 3, 2.5 and 25 mm.
Seat cover
The seat cover is composed of three different materials in the following proportions:

- 70% of wool
- 20% of polyamide
- 10% of viscose

Wool is a natural animal protein and belongs to the keratin family. It is a complex and heterogeneous material. Its structure is composed of fibres. Several authors (Rippon (1992) and Höcker (2002) have studied the morphology of the wool fibre as presented in the following figure 1.17 (Salpin (2008)).

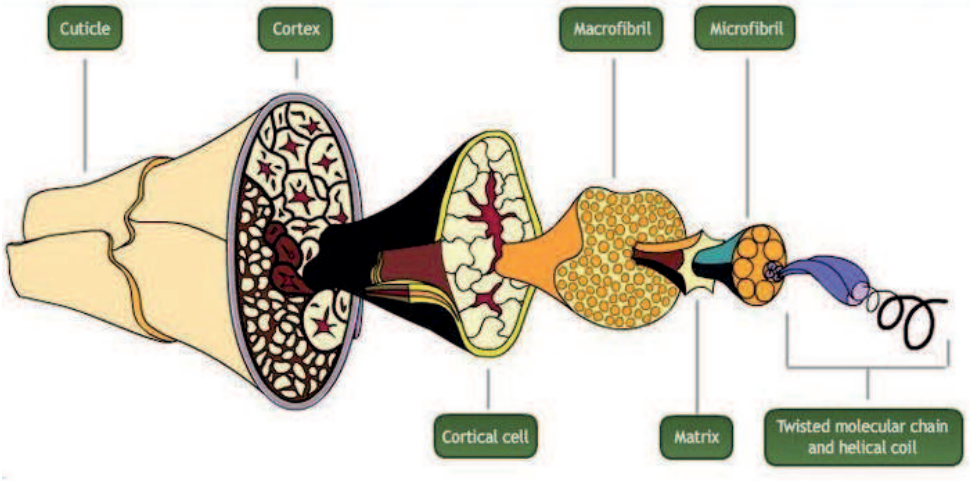

Figure 1.17: Schema of a wool fibre Biotechnology learning hub (2005)

The diameter of the fibre is around 20 μm. The fibre is composed of two kinds of cells, the cuticle and the fibrous cells. The cortex, which represents 85% of the mass of the fibre cells, is surrounded by the cuticle. The cortex contains cortical cells. A long filament, called macro-fibrils, are inside the cortical cells. They are made up of bundles of even thinner filaments, named micro-fibrils, surrounded by a matrix. Moreover, within the twisted molecular chain, there are protein chains that are coiled as a helical shape. Several type of bonds are observed, such as:

1. disulphured bridge,
2. covalent bond,
3. ionic bond bridge,
4. hydrogen bond,
5. hydrophobic interaction.

The viscose is an artificial fibre. The viscose is made up from wood cellulose with chemical (reaction with sodium hydroxide and then carbon disulphide) and physical (regeneration by extrusion and stretching) processings.

Polyamide is also present in the seat interliner. It is introduced in the next part.

Seat interliner

The second layer of the seat product is an aromatic polyamide or aramide. The aramide structure unit is composed of amide functions from the amine and carboxylic acid functions (1.18).

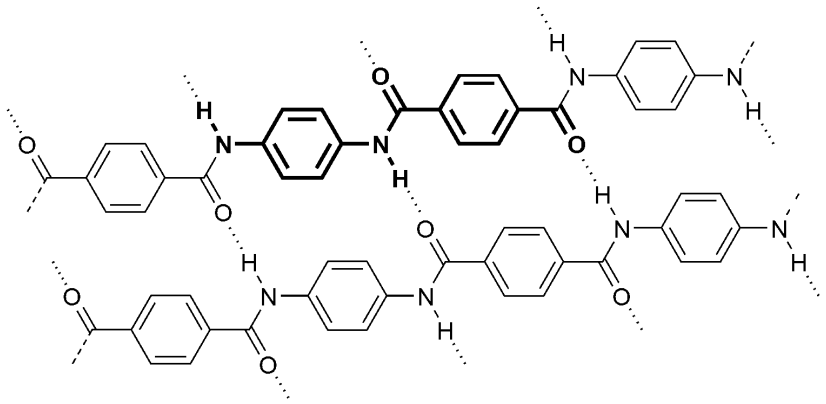

Figure 1.18: Structural unit of an aramide polymer

The aramide is known for its good heat resistance and good mechanical properties. It is possible that seat interliner is also constituted of polyimide.

Seat foam

The foam of the seat is a mixture of flexible polyurethane (PU) and melamine foam. This foam behaves as a thermoplastic. Polyurethanes are produced by the polyaddition reaction of a polyisocyanate with a polyalcohol (polyol) in the presence of a catalyst and other additives. The elementary composition of this PU foam is $C_1H_{1,732}O_{0,268}N_{0,185}$. The addition of the melamine in the polyurethane foam has a fire retardant effect. The melamine is prepared from triazine or cyanamid.

Table 1.13 summarizes the magnitude order of seat materials properties.

Table 1.13: Material properties of the seat, Mc Adams (1961)[a], ISO 10456 (2007)[b], Horrocks and Kandola (2004)[c], Bustamante Valencia (2009)[d]

Properties	**Units**	**Wool**[b,c]	**Viscose**[a,c]	**Aramide fibre**[c]	**Polyurethane foam**[c,d]
ρ	$kg.m^{-3}$	$135-330$	$200-400$	1400	$30-80$
Cp	$kJ.kg^{-1}.K^{-1}$	1		1.2	1.4
λ	$W.m^{-1}.K^{-1}$	0.15		$0.2-0.4$	$0.03-0.085$
$T_{decomposition}$	°C	245	350	410	$200-300$
$T_{ignition}$	°C	500	600	420	350
$\Delta H_{combustion}$	$MJ.kg^{-1}$	27	19	30	$25-30$

Chapter 2

Reaction-to-fire of polymers and conditions of fire effluents generation: The State of the Art

Contents

As argued with the fire risk analysis, a design fire scenario has been selected as probably hazardous for passengers. The fuel sources are the seat and the lining (internal wall panel). Most of these products, present inside a train vehicle, are composed of natural or synthetic polymers. A polymer is a large macromolecule composed of repeating structural units. For instance, the ester is the structural unit of the polyester (PE) polymer.

It is essential to understand the polymer fire behaviour (reaction-to-fire and fire resistance) because of the widespread use of those materials in the train vehicle and in other applications. This thesis deals only with the polymer reaction-to-fire. The best way to

understand the reaction-to-fire is to study the condensed phase (fuel source) heated by an external heat source and the gas phase (products combustion reaction) from the raw matter to the real scale, in order to simulate several different fire scenarios.

Moreover, according to their thermal behaviour, polymer can be divided in two groups: thermoplastic and thermoset (char-forming) polymer. Most of the studied polymer in the thesis behave as char-forming polymers.

The state of the art of reaction-to-fire of the polymer material is divided in three parts: the first one develops the polymer reaction-to-fire. The second one shows the reaction mechanisms during thermal decomposition of products studied. The third presents an overview of the pyrolysis modelling.

2.1 Reaction-to-fire of polymer and generation of toxic gases effluents

2.1.1 Thermal decomposition of polymers

2.1.1.1 Definitions

According to the standard ISO 13943 (2011):

- The thermal decomposition is *the process whereby the action of heat or elevated temperature on an item causes changes to the chemical composition.*
- The thermal degradation is *the process whereby the heat or elevated temperature on an item causes a deterioration of one or more properties (physical, mechanical or electrical for example).*
- The pyrolysis is *the chemical decomposition of a substance by the action of heat in absence or in presence of oxygen.*

These two thermal behaviours can exist at the same time in presence or not of oxygen. The state of the art focuses on the thermal decomposition or pyrolysis of char-forming polymer. The pyrolysis process is fundamental to understand because it gives the quantity of gaseous fuel produced for a given material available for the combustion reaction. The gases products and the heat release rate stem from the combustion are directly proportional to the quantity of fuel. Gases products from the combustion can also be toxic gases. Toxic gases are by extension proportional to the quantity of fuel released by the pyrolysis of a material.

Thermal decomposition is the first step and the continuous step that occurs during the combustion processes. When a polymer is heated by an external heat source, both chemical and physical processes happen. These processes are detailed in the figure 2.1 (Di Blasi (1993)). During the chemical processes, the condensed phase decomposes in char and volatile gases. Whereas, during the physical processes, such heat transfer and pressure gradient lead to the surface regression or to the shrinkage of the polymer, for instance.

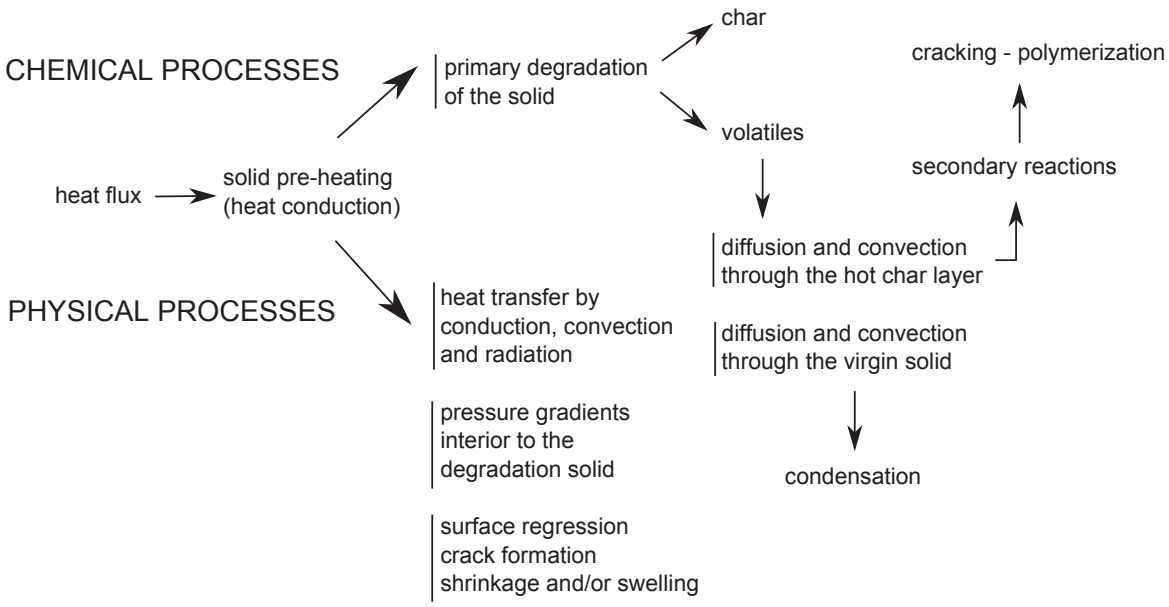

Figure 2.1: Chemical and physical processes of char-forming material, Di Blasi (1993)

2.1.1.2 Chemical processes

The chemical processes correspond to the rupture of chemical bonds. It should be divided in two processes: thermal decomposition linked to temperature action and thermo-oxidative decomposition related to both oxygen and temperature. Many authors reported four chemical mechanisms during thermal decomposition in the condensed phase of a polymer (Rocaboy (1972), Kashiwagi (1994), Wilkie and Mckinney (2004) and Hirschler and Morgan (2008)):

- The random chain scission: chain scissions happen at randomly place in the main polymer chain (or backbone).
- The end-chain scission or unzipped: monomer molecule is disconnected from the end of the backbone polymer.
- The chain-stripping: side-chain removed from the backbone polymer.
- The cross-linking: chemical bonds formed between polymer chains.

In case of chain scissions, small molecular weights are volatilized, as potential combustible gases. During this kind of oxidative decomposition, Bolland (1946), Bolland and Gee (1946)a and Bolland and Gee (1946)b proposed a general mechanism of radical chain reactions: initiation, propagation, branching and termination steps.

Chain scissions mechanisms generally occur in thermoplastic polymer, such as the PMMA, whereas the cross-linking mechanism sparks off the formation of high molecular weight chain, such as char.

2.1.1.3 Physical processes

When polymer is heated, the physical processes happen for both thermoplastic and thermoset polymers at the surface and/or in-depth. Physical processes can be defined as a change of state from solid to gas phase. Other physical processes happen at the polymer surface or in-depth: swelling, shrinkage, cracking, and char formation. These polymer physical changes may depend on the cross linking bonds which happen during the chemical processes and the presence or not of flame retardant in the polymer. These physical changes may have an influence on the pyrolysis and the combustion of the materials. For example, the char formation on the material surface implies a decreasing of the gaseous fuel diffusion.

2.1.1.4 Parametric influence on the thermal decomposition polymer

The thermogravimetric analyser (*TGA*) has been commonly used for several years now, to understand the thermal decomposition rate of a condensed phase of a material. The principle of TGA is to put few milligrams of material in a crucible inside a furnace under air or nitrogen atmosphere. The measurement of the sample mass and temperature is recorded as a function of time and of temperature into the furnace. The heating protocol can be divided in two classes (Bustamante Valencia (2009)):

1. Isothermal condition: the temperature remains constant inside the furnace.
2. Dynamic temperature condition: the furnace can follow a linear heating rate, i.e. the furnace temperature evolves from the ambient temperature to a chosen temperature, during a defined time period.

Several authors report that the mass loss rate of a material during a TGA test is dependent on the heating rate, the material temperature and the atmosphere conditions (Di Blasi (1999), Jiang (2006), Bustamante Valencia (2009), Marquis (2010), Fateh (2011)).These following authors have studied three different materials: foam, polyester and laminated wood. Figures 2.2 a to c show the mass loss rate results from TGA tests at different heating rates in air and nitrogen atmospheres for different fuels, as examples.

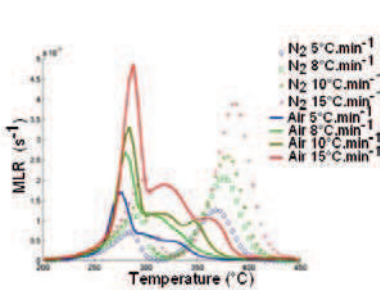

a/ Foam polyurethane mass loss rate from TGA test, Bustamante Valencia (2009)

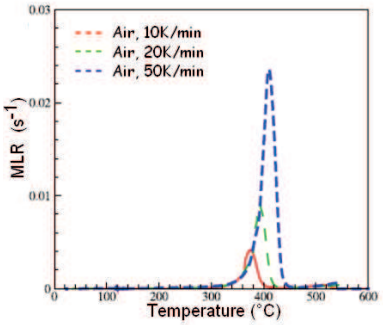

b/ Polyester mass loss rate from TGA test, Marquis (2010)

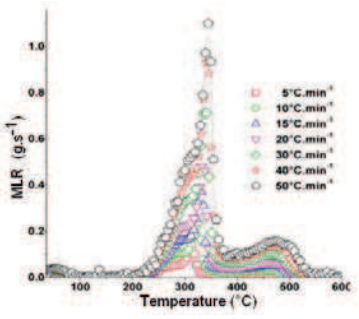

c/ Laminated wood mass loss rate from TGA test (under air atmosphere), Fateh (2011)

Figure 2.2: Mass loss rate during thermal decomposition of different materials

Generally, it is assumed that one peak of the mass loss rate is associated to one global reaction of a reactive A to a product B for a range of temperature. However, in reality, a lot of concomitant reactions happen. It is important to note that the temperature of a peak is dependent of the nature of the polymer itself: i.e. the presence or not of a flame retardant can change the kinetic of the mass loss rate of the material condensed phase.

Moreover, according to the previous figures 2.2, the heating rate has an influence on the mass loss rate for each type of material. Higher is the heating rate, and bigger is the deviation of the mass loss rate to the high temperature. Jiang (2006) confirmed this observation with several TGA tests on different materials (cotton and PU foam) from $5K/min$ up to $200K/min$. Furthermore Mehrabian *et al.* (2012) have studied the effect of thermal decomposition conditions on the heating rate applied to biomass particles. They showed that the temperature *lateral shift might be attributed to the residence time in the sample, i.e. since a higher heating rate means shorter exposure to a certain temperature, the sample needs to reach higher temperature to have enough time for completion of the overall decomposition.* Generally, heating rates values, applied to this domain, go from $5K/min$ to $50K/min$. It is important to remind that for this thermal decomposition study, the objective is not to reproduce the heating gradient observed during fire but to separate as well as it is possible each global (main) reaction.

Marquis (2010) reported that, during the TGA test, a temperature gradient inside the material may arise when the heating rate is close to $100K/min$. Hence, the theoretical conditions of the TGA test suppose that the material should present the same temperature on its surface and in-depth. Thus, at $5K/min$, the material temperature is supposed homogeneous, i.e. the recorded surface temperature might be equal to the intern temperature.

The third parameter which affect thermal decomposition of the condensed phase is the atmospheric condition: i.e. either air or nitrogen atmosphere. Bolland (1946), Bolland and Gee (1946)a, Bolland and Gee (1946)b and later Bustamante Valencia (2009) reported that the presence of oxygen *accelerates the breakdown of molecules at relatively lower temperatures.* In addition, it is known that the presence of alveolus inside the material has an acceleration impact on the oxygen and fuel diffusion. The presence of oxygen has also an effect on the char-forming polymer material (Marquis (2010)). The influence of oxygen on thermal decomposition is strongly dependent on the kind of material used. The ambient ventilation into the furnace (or the gas flow rate) may also have an impact on the material decomposition kinetic. It should be interesting to study this influence for the same heating rate and during dynamic temperature condition.

2.1.2 Combustion processes of polymers material: general principles

The combustion processes are summarized in the following figure 2.3. This diagram completes the one proposed by Marquis (2010) in his PhD thesis.

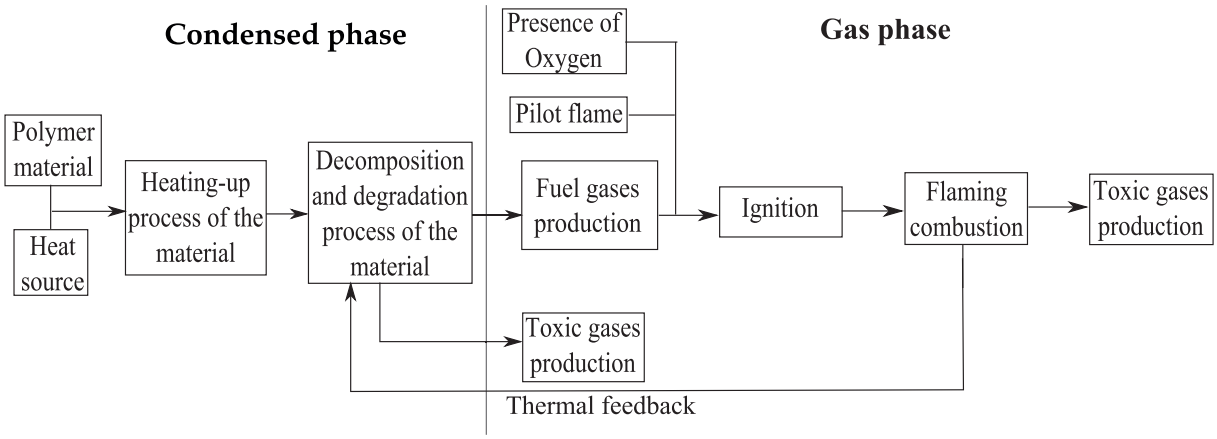

Figure 2.3: General combustion processes at ambient conditions

2.1.2.1 Heating-up process

During the heating-up process, the polymer material temperature increases in depth with time when it is exposed to an external heat source. The material heating-up process depends on the thermal diffusivity and effusivity properties, as well as the absorption conditions of the surface material exposed, the material thickness and the material boundaries conditions (Torero (2008)). Thermal diffusivity characterizes the ability of a material to transfer temperature inside the material. Whereas, the thermal effusivity corresponds to the ability of the material to exchange thermal energy with its surroundings.

2.1.2.2 Ignition and combustion processes

Following the heating up and thermal decomposition processes, a mixture of gaseous fuel is present above the exposed heated surface of the material. In presence of oxygen above the exposed material surface and if the gaseous fuel mixture reaches the lower flammability limit (LFL), the fuel reacts with oxygen to reach flash point conditions (Drysdale (2011)b). However, due to the complex nature of the gaseous fuel mixture from a material and the dynamic evolution of the thermodynamic conditions (temperature and pressure) of the mixture, the LFL of the fuel mixture can not be assessed. Moreover, when the quantity and the concentration of the gaseous fuel flow is suitable, a flame is visible above the condensed phase material surface. Nevertheless, the activation of the fuel and oxygen reaction is feasible only in presence of a certain energy. This one can result either from the exothermic gaseous oxidation reaction itself (the ignition is known as auto-ignition) or from an external source (the ignition is known as piloted). The ignition temperature and ignition delay time are both properties of the ignition process.

This oxidation reaction is called combustion and takes place in the gas phase. In fact, the complete combustion reactions group together elementary chemical equations. Initiation, branching and termination reactions exist during combustion reactions. Reaction involves the presence of highly reactive molecular atoms and free radical ($H^{\bullet}$ or $OH^{\bullet}$). They have a short existence into the flame. The mechanism of combustion reaction of the methane

is complex even if molecule reagent (CH_4) is known, unlike the pyrolysis products of realistic materials. Pyrolysis products from the material thermal decomposition are difficult to qualify and to quantify. It is illusory to try to describe the chemical kinetic of the complete combustion of the pyrolysis products. In this thesis, details of combustion chemical kinetic are not taken into account but only a set of global reactions.

The combustion is a sum of exothermic reactions. The heat of combustion of a reaction in the gas phase can be expressed by the sum of the products heats of formation minus the heat of formation of reactants and according to the stoechiometry of the reaction. A method was developed to calculate the heat release rate (or HRR), which describes the reaction-to-fire of a material. The concept assumes that the heat of combustion is constant during the combustion when it is expressed according to the consumption of oxygen. Several expressions of HRR are detailed in Thornton (1917) and Hugett (1980) pieces of work. The visual representation of combustion can be a flame. There are two kinds of flame: diffusion and pre-mixed flames. In the case of solid burning, a diffusion flame is generally observed because the fuel and air are initially separated and combustion occurs in the zone where the gases mix. Corlett (1974) classifies the natural diffusion flame in accordance with the fuel bed diameter. The higher is the fuel bed diameter ($\geq 0.3\ m$), the more the fire plume (flame shape) becomes intermittent and turbulent.

2.1.2.3 Fire spread process over a solid product

The fire spread process over a solid corresponds to the surface pyrolysis front movement along the material surface. The fire spread principle is heating-up and decomposing the virgin surface material to obtain the pyrolysis products. Then, pyrolysis products are mixed with oxygen and combustion could occur in the phase gas. The radiative heat flux from the flame, the heat of conduction into the material and the heat of convection from the gas phase allow the flame front movement progress. According to Drysdale (2011), there are two kinds of fire spread mode:

- The counter-current spread, where the air flow is opposed to the flame front direction.
- The concurrent spread, where the air flow and the front flame are set in the same direction.

Additionally, the fire spread mode is concurrent when the fire spread over a vertical panel is upward. As reported by Friedman (1977), the rate of flame spread over a combustible depends on many factors, described in the following table (2.1).

It is not an intrinsic property of the material, but a scenario dependent factor. For example, material and products factors, such as thermal and radiative properties (conductivity, specific heat, density and emissivity) can influence the heating-up process of the product and then, increase or decrease the flame spread. Moreover, Magee and McAlevy (1971) have shown the influence of the surface orientation. They demonstrated that higher is the inclination angle and faster the flame spreads. The geometry of the scenario has also an impact on the flame spread rate and notably with the presence of edges, mounting and fixing parts.

Table 2.1: Factors affecting the rate of flame spread over a solid.

Chemical factors	**Physical factors**	**Environmental factors**
Composition of fuel	Initial temperature	Composition of atmosphere
Presence of retardants	Surface orientation	Pressure of atmosphere
	Direction of propagation	Temperature
	Thickness	Imposed incident heat flux
	Thermal capacity	Air velocity
	Thermal conductivity	
	Density	
	Geometry (Mounting and fixing)	
	Continuity	

Concerning the environmental factors, the composition of the atmosphere and the air velocity can affect the mixing combustion reaction in the gas phase and thus reduce or raise the flame spread. Moreover, backing conditions (insulated or exposed for example) of the products can also influence the thermal budget into the product and consequently changes the flame spread.

The next section explains the nature of toxicants and the factors which can affect the toxic gases generation.

2.1.3 Generation of fire effluents

2.1.3.1 Acute toxic effect

When a fire happens, the estimation of occupants tenability involves their ability to perform cognitive and motor-skill function at an acceptable level (ISO 13571 (2012)). Concerning the fire safety domain, this acceptable level is exceeded when incapacity criteria are reached. These criteria correspond to the toxic gases from the combustion processes, the smoke opacity and the radiative and temperature from the smoke and fire. As argued by Levin (2006) and Hall (2008), people die more by the smoke inhalation than by burns in building. Guillaume (2012) reported that the survival time for a person in a fire is inversely proportional to toxic gases concentration and also depends on the individual response ability of pollutants. Smoke is a mixture of gases and aerosols, including suspended particles, created by combustion and pyrolysis during a fire (ISO 13943 (2011)). Aerosols or particles are not studied in this thesis, which is only focused on the gaseous emissions. This part focusses only on the acute toxic effect.

Fire effluents contain a mixture of complete combustion products (carbon dioxide) and incomplete ones. These later are composed of partially oxidised products (carbon monoxide and aldehyds), fuel decomposition products (aliphatic or aromatic hydrocarbon) and other relatively stable molecules (hydrogen halides and hydrogen cyanide) (figure 2.4).

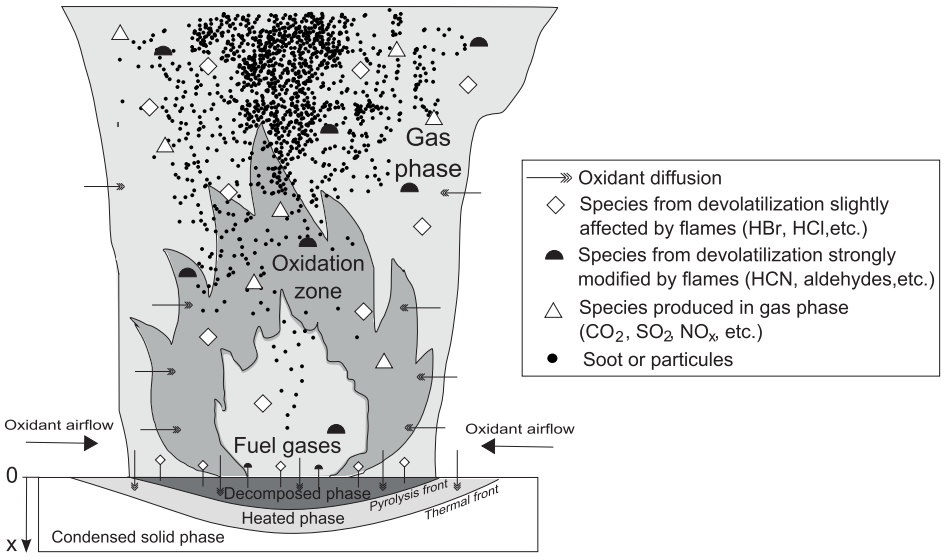

Figure 2.4: Toxic gases generation from fire stages

Products from the incomplete combustion can be divided in two classes regarding their acute toxicity effect according to Hull and Stec (2010):

1. Asphyxiant gases: carbon monoxide and hydrogen cyanide
2. Irritant gases: hydrogen halides, nitrogen oxide, sulphur dioxide, formaldehyde and acrolein.

Considering the asphyxiant gases, Hartzell (1987), Purser (2008) and then Guillaume (2012) explained the toxicity effect of carbon monoxide and hydrogen cyanide: the asphyxia by carbon monoxide results from the conversion of the hemoglobin into carboxyhemoglobin instead of oxyhemoglobin. This conversion implies a decrease of oxygen level in body tissues. Guillaume (2012) added that the carbon monoxide is responsible of 90% of deaths linked to the gases inhalation, during a fire. Afterwards, for the hydrogen cyanide effect, it results the inhibition of the utilization of oxygen by a mechanism with ions cyanide and enzyme in body cells. Hartzell (1987) quoted that the hydrogen cyanide is approximately twenty times more toxic than carbon monoxide.

Hartzell (2001) and then Purser (2008) introduced the concept of the "exposure dose" for asphyxiant gases. Asphyxiant effect associated with an exposure to fire may impact the safe escape of occupants. Asphyxiant toxicity is function of both concentration gases and duration of exposure to smoke and fire. Additionally to carbon monoxide and hydrogen cyanide, carbon dioxide concentration in fire causes people to hyperventilate and thereby raises the quantity of inhaled toxic gases (Hartzell (1987), Purser (2008) and Guillaume (2012)).

As regards to irritants gases, Guillaume (2012) summarized irritant gases in two groups: inorganic acids (hydrogen halides, nitrogen oxide and sulphur dioxide) and organic compounds such as, formaldehyde, acrolein and acetaldehyde). Purser (2008) averted further

irritant gases like, for example, toluene diisocyanate (from polyurethane foam decomposition), crotonaldehyde, phenol, styrene and ammonia. Irritants gases effects are eyes, nose, lung and throat irritation. These irritations depends on the irritant gases concentration.

Furthermore, the combustion reactions consume oxygen of air and thereby the oxygen concentration can be strongly reduced in a confined space. Guillaume (2012) reported the principal effect of the oxygen concentration reducing on people: incapacity effect observed around 15 to 16% (Volumetric yield of oxygen in atmosphere), irreversible injuries at 12% and death occurs within five to eight minutes when the volumetric yield in the atmosphere is 6% .

2.1.3.2 Toxic gases sources

As reported by several authors (Guillaume and Chivas (2008) and Purser *et al.* (2010)), the composition of gases effluents from a fire depends on:

- The material composition.
- The fire conditions: in particular the local concentration of oxygen, the temperature, the exposed incident heat flux level received on product surface, the residence time in high temperature regions, the nature and the possible interactions of the other gases.

Indeed, the toxic gases related to the nature of materials are presented in table 2.2. The first and the second columns of source material are respectively summarized by Stec (2010) and Kaplan *et al.* (1984) references.

Table 2.2: Major toxic gases and material source from pyrolysis and combustion.

Gases	**Materials sources, Stec (2010)**	**Materials sources, Kaplan *et al.* (1984)**
Carbon Monoxide	Most combustible material	Not specified
Carbon Dioxide	Most combustible material	Not specified
Acrolein	Cellulosic materials, PE, PP, wood, cotton, paper, ABS and PS	Pyrolysis of polyolefins and cellulosics at lower temperature ($\sim 400\ ^{\circ}C$)
Formaldehyde	Polyoxymethylene and PP	Not specified
Hydrogen cyanide	Nitrogen containing polymer, wool and silk	Combustion of wool, silk, polyacrylonitrile, polyamide, PU and paper
Nitrogen dioxide	PAN, ABS and nylon	Fabric, cellulose nitrate and celluloid
Hydrogen chloride	PVC and materials with halogenated flame retardant	Combustion of PVC and some fire Combustion of PVC and some fire retardant treated material
Hydrogen bromide	Materials with halogenated flame retardant	Retardant material containing bromide
Hydrogen fluoride	PTFE, PVF and fluorinated compounds	Combustion of fluorinated resins or films
Sulphur dioxide	Sulphur containing materials and wool	Materials containing sulphur

For each toxic gas, the materials sources are the same between the two references. Carbon dioxide and carbon monoxide come from the most combustible materials. Acrolein arises from cellulosic material and polyolefins (PE, PP). Formaldehyde is released by polyoxymethylene and PP polymers. Hydrogen cyanide and sulphur dioxide come from respectively nitrogen-containing materials and sulphur-containing materials, such as wool. Nitrogen dioxide arises from celullose nitrate polymer. Finally, hydrogen halides are released from halides-containing material. This retardant effect will be explained in the next part.

The toxic potential is defined as the nature and the quantity of gas by surface unit or mass unit of a burnt material for a given fire condition. Thus, the toxic potential of material depends on the material itself and the given combustion model. Nevertheless, the toxic potential of a scenario depends on multi materials or products and the evolution of fire conditions in a given environment.

2.1.3.3 Estimation of gaseous emission generation

During a fire scenario, the gaseous emissions are quite complex to describe. However, as previously reported, the impact of a fire and its gaseous emissions on the environment is very important and more than 70% of the deaths during a fire are due to the toxicity of the smokes (Hall (2008). It is very important to determine the toxic gases effluents generation and migration, especially in a railway vehicle. The yield of production of gaseous emissions during a disaster are classically done by two different approaches

- One based on normative (ISO 19706 (2011), ISO 19703 (2010)) and abacus approaches found in several handbooks (Tewarson (2008) and Wang *et al.* (2011): This approach is the most employed since it is the simplest. Nevertheless, it is based on the generalization of the fire, proposing a yield of formation of each pollutant simply considering the nature of the combustible and sometime two or three general conditions of ventilations. Thus, this approach is very rough, since it is well known that the formation of the gaseous species are very influenced by the fire local conditions, such as the temperature, the oxygen concentration and the residence time. In the normative and the abacus approaches, fire conditions represent the different fire stages met during a real fire, from non-flaming to well-ventilated flaming and under-ventilated flaming stages. These classes are detailed in the table 1 of the ISO 19706 (2011), Huggett (1989) and Purser *et al.* (2010) references. Moreover, each fire stage can be characterized by the incident heat flux received by the material, the fuel surface temperature, the oxygen concentration near the flame and the volumetric ratio between carbon monoxide and carbon dioxide ($[CO]/[CO_2]$). For example, concerning the thermo-oxidative decomposition stage, the fuel surface temperature is between 300 $°C$ and 600$°C$ with a volumetric ($[CO]/[CO_2]$) ratio close to zero. The factors of the well-ventilated flaming stage are the same as the thermo-oxidative decomposition stage except the volumic ($[CO]/[CO_2]$) ratio which is around 0.05 (ISO 19706 (2011)).

- One based on the kinetic characterization of the different gaseous species, taking into account the real characteristics of the fire (figure 2.4). This approach is more accu-

rate, but it is very complex and requires a lot of calculation time and experiments. For instance, gases molecules (as free radicals of fuel molecules) and toxic gases (as free radicals then stable molecule, for example HCl and HBr) are released from the solid phase and become the gas phase during thermal decomposition process (figure 2.4). Those toxic gases (as HCl and HBr) are slightly affected by the flame when material ignites. Moreover, when ignition temperature and pressure conditions are reached, combustible/fuel gases react with oxygen (combustion reaction) and some toxic gases (as aldehydes and HCN) are strongly modified by the flame (Marquis *et al.* (2011)) (figure 2.4). During flaming stages, some toxic gases are also produced, such as carbon dioxide, sulphur dioxide and nitrogen dioxide (figure 2.4).
Additionally, as reported by the reference Rogaume (2010), carbon monoxide can come:

- from the solid thermolysis or thermo-oxydative decomposition stages,
- from oxidation reaction of hydrocarbon (well and under-ventilated flaming stages),
- from char oxidation (smouldering stage).

Andzi Barhe (2004) reported the mechanism of CO formation from hydrocarbon oxidation. He highlighted also that the CO formation from CH_4 is function of the increase of temperature. Thus, it is possible that the CO concentration evolves from the bottom to the high of the flame.

To conclude, toxicity is not a material characteristic. The estimation of the impact of the gas toxicity on people may be assessed for a given design fire scenario.

In railway transport domain, materials are often filled with flame retardant molecules in order to improve the product reaction-to-fire.

2.1.4 Fire retardants effects

There are many kinds of flame retardants with different actions to reduce the combustion process (Chivas *et al.* (2009) and Nikolaeva and Karki (2011)). According to several authors, Hull and Stec (2009), Brossas (1999) and Bourbigot and Le Bras (2004), there are present initially in the solid phase. Under an external heat source, the combustion process is changed by physical or/and chemical actions. Some fire retardants and their actions are described below (Hull and Stec (2009), Brossas (1999), Bourbigot and Le Bras (2004)):

- **Halogens** (**X**): C-C bond dissociation energy of polymer is around 347 kJ/mol (Wichman (2003)). C-X (with $X = Cl$ or Br) bond dissociation energy is lower than C-C bond. Consequently, the released free radicals, as Cl and Br, play an inhibitor role when the combustion starts, and reduce the combustion process. Indeed, the bond C-X breaks with the heat action (reaction 2.1). Then, a hydrogen halide salt is generated by an hydrocarbon (reaction 2.2). Next, highly reactive $H^\bullet$ or $OH^\bullet$ react with hydrogen halide and are replaced with lower energy $X^\bullet$ radical (reactions 2.3 and 2.4). This later radical leaves the flame without further reaction or to

be regenerated by reaction with a hydrocarbon (reaction 2.2). Another important effect is that the removal of $H^\bullet$ or $OH^\bullet$ stops the conversion of carbon monoxide to carbon dioxide (reaction 2.5). Consequently, the combustion process is reduced but the carbon monoxide generation is encouraged.

$$C - Cl \longrightarrow 3Cl^\bullet \tag{2.1}$$

$$Cl^\bullet + RH^\bullet \longrightarrow 3R^\bullet + HCl \tag{2.2}$$

$$HCl + H^\bullet \longrightarrow 3H_2 + Cl^\bullet \tag{2.3}$$

$$HCl + OH^\bullet \longrightarrow 3H_2O + Cl^\bullet \tag{2.4}$$

$$CO + OH^\bullet \longrightarrow 3CO_2 + H^\bullet \tag{2.5}$$

The effectiveness of halogen retardant takes place in gas phase but releases hydrogen halides, which have an irritant effect in smoke.

- **Halogens and Antimony**: Reaction between halogens acid and antimony oxide produces antimony oxyhalogens, heavier than halogens acid. Thus, they remain longer in flame. It has the same gas action than halogens.
- **Inorganic fillers**: Their actions are physical and chemical. For example, the aluminium hydroxide (or ATH) decomposes between $80°C$ to $300°C$ with an endothermic energy of 1150 kJ/kg (Brossas (1999)). This endothermic reaction cools the gaseous mixture. Moreover, products of this thermal decomposition are water and a residue of alumina. Consequently, released water dilutes combustible radicals in the flame and residue of alumina forms a crust with char. This mixing crust above the polymer strongly decreases the formation of radicals (Hull and Stec (2009) and Brossas (1999)).
- **Phosphorous compounds**: They favour the formation of a char layer on polymer surface by reticulation or cross linking reactions. This char layer behaves as a physical barrier between the source of heat and the virgin polymer material (Hirschler and Morgan (2008)).
- **Intumescent agents**: Under thermal attack, intumescent agents blow up and form an alveolar layer above the material. This protective layer has a low conductivity and reduces the combustible gases diffusion velocity.
- **Melamine and melamine salts**: The polyurethane foam is often produced with melamine in the United Kingdom due to its action in gas phase. Melamine is a nitrogen based compound. Troitzsch (2007) reported that Melamine is transformed into cross-linked structures like melam, melem and melon by condensation reactions and stepwise loss of ammonia. The quantity of nitrogen released dilutes fuel gases and oxygen into the flame (Bourbigot and Le Bras (2004)).

2.2 Reaction mechanisms (paths) of studied materials during thermal decomposition

The material reaction-to-fire depends on the nature of the material, the exposed incident heat flux and surrounding factors. Before being able to grasp the influence of the two later parameters, it is important to have a good understanding of the studied material. This knowledge allows to model the potential available gaseous fuel quantity in order to estimate in fine the quantity of toxic gases for a given scenario. The gaseous fuel emission is controlled by the evolution of the thermal decomposition phenomena. Consequently, it is essential to study the decomposition key steps of each involved material in fire, which are related on the reaction mechanism. Each reaction mechanism is proper to each material. It can be composed of concomitant and/or parallel heterogeneous reactions. This information is often deduced from a thermogravimetric analysis test (TGA) coupled with FTIR spectrometer. The TGA response corresponds to the evolution of the material mass loss function of the sample temperature.

2.2.1 Glass reinforced polyester composite

The thermal decomposition of each component of the composite and then of the entirely composite is reviewed in this section.

Polyester

In 2008, Kandare *et al.* (2008) studied the effect of flame-retardant on the thermal decomposition of polyester resin. They performed TGA tests under air atmosphere at $10K/min$ of unmodified and flame retardant polyester resin. The TGA was coupled with non-dispersive infrared gas analyser to determine the evolution of carbon monoxide and carbon dioxide concentrations and with an electrochemical cell oxygen sensor in order to know the consumption of oxygen. According to TGA and gases analysers responses, Kandare *et al.* (2008) reported that decomposition of polyester resin occurred in three stages:

- The first stage (120-275$°C$) showing 8% mass loss attributed to the loss of water via dehydration ;
- The second stage (275-460$°C$) showing 80% mass loss attributed to the rupture of the polyester and polystyrene chains to form a primary char with the evolution of styrene, phthalic anhydride, CO and CO_2 ;
- The third stage (460-600$°C$) contributing 8% mass loss attributed to the char oxidation stage. 4% of residual char remains into the crucible at 800 $°C$.

Moreover, according also to these experimental results, Kandare *et al.* (2008) declared that the first stage of mass loss is independent of oxygen consumption consistent with dehydration. This reaction mechanism is summarized in the table 2.3.

Table 2.3: Thermal decomposition mechanism of polyester, Kandare *et al.* (2008)

Temperature	**Solid reagent**		**Solid product**		**Gas product**
120 - 275°C	Polyester	$\longrightarrow$		+	H_2O
275 - 400°C	Polyester + O_2	$\longrightarrow$	Char	+	CO_2, C_8H_8, $C_8H_4O_3$, CO
460 - 600°C	Char + O_2	$\longrightarrow$	Residue	+	CO_2 and CO

At the same time period, Lautenberger *et al.* (2008) studied the decomposition of unsaturated brominated polyester resin with TGA test under air and nitrogen atmosphere at 5 K/min, 10 K/min, 30 K/min and 50 K/min. Based on these results, they concluded that three primary reactions occur. The reaction mechanism is reported in the table 2.4.

Table 2.4: Thermal decomposition mechanism of unsaturated brominated polyester, Lautenberger *et al.* (2008)

Solid reagent		**Solid product**		**Gas product**
Resin	$\longrightarrow$	β-resin	+	gas
β-resin	$\longrightarrow$	Char	+	gas
Char	$\longrightarrow$		+	gas

Moreover, Lautenberger *et al.* (2008) added that around 20% of the mass loss from the resin corresponded to the first reaction and around 70% from the second one (β resin). This reaction mechanism is very close to the mechanism proposed by Kandare *et al.* (2008).

In 2012, Marquis *et al.* (2012) studied also the thermal decomposition of glass reinforced unsaturated polyester composite with TGA, under air and nitrogen atmosphere at 10 K/min, 20 K/min and 50 K/min, coupled with a FTIR spectrometer. Marquis *et al.* (2012) proposed a four-step reaction mechanism, showed in table 2.5.

Table 2.5: Thermal decomposition mechanism of polyester, Marquis (2010)

Type of reaction	**Solid reagent**		**Solid product**		**Gas product**
Thermolysis	Polyester	$\rightarrow$	Char	+	$[Y_k + CO_2 + H_2O + HCOH + CH_4]$
Thermo oxydation	Polyester + O_2	$\rightarrow$	Tar	+	$[Y_k + CO_2 + H_2O + HCOH + CH_4]$
Thermo oxydation	Tar + O_2	$\rightarrow$	Char	+	$[Y_k + CO_2 + H_2O + HCOH + CH_4 + CO + NO + HCl]$
Thermo oxydation	Char + O_2	$\rightarrow$	Residue	+	$[CO_2 + H_2O + CO + NO + HCl]$

$Y_k = C_8H_6O_4 + CH_3CH_2CHO + C_8H_8$: Main track species

$C_8H_6O_4$: Isophtalic acid

CH_3CH_2CHO : Propionaldehyde

C_8H_8 : Styrene

This thermal decomposition mechanism is more detailed than the two first ones and especially for the gas phase level. As argued by Marquis (2010), the first reaction does not depend on the oxygen concentration.
Indeed, unlike the two previous mechanisms, Marquis *et al.* (2012) separate the thermolysis and the thermo-oxidative reactions. Moreover, the second reaction is divided in two successive reactions compared to the two first proposed reaction mechanisms.

Aluminium Trihydrate (ATH)
Cerin-Delaval (2010) has studied the thermal behaviour of a ATH with a thermogravimetric analyser in nitrogen atmosphere at $10K/min$. The result is presented in figure 2.5 and shows that the decomposition temperature range of ATH is between 200 and 300$°C$.

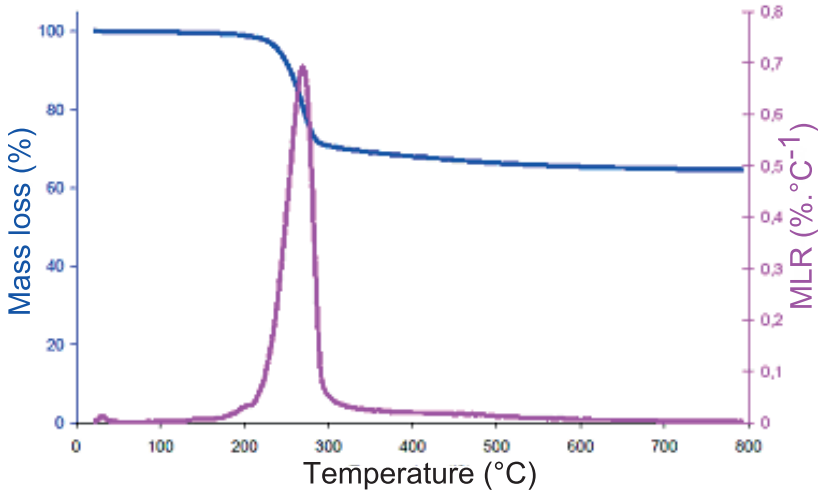

Figure 2.5: Result of ATH decomposition from thermogravimietric analyser

As also reported by Cerin-Delaval (2010), ATH required 1127 $kJ.kg^{-1}$ of energy to decompose in aluminium oxide and water:

$$Al(OH)_3 \longrightarrow Al_2O_3 + 3H_2O$$

Water is released in gas phase, and aluminium oxide remains in solid phase. This explains the remaining mass after the reaction, as shown on figure 2.5.

Glass fibres
Glass fibres are the most widely used fibres to reinforce composite. Glass fibres are chemically inert in fire and retain chemical and physical stability at high temperature and high heat flux (Mouritz and Gibson (2006)). It exists several types of glass fibres, such as:

- E-glass: remains unaffected by fire until around 830$°C$ and melts around 1070$°C$.
- S-glass: has superior high temperature properties than the E-glass. The softening and melting temperatures are respectively 1050$°C$ and 1500$°C$.

Marquis (2007) reported details about glass fibres. The type of glass used in the studied composite is unknown.

Composite

A composite is a combination of materials. It is important to understand the thermal decomposition of the interaction between the resin polyester matrix and the glass reinforcement. Figure 2.6 describes the thermal decomposition of the composite, according to Mouritz and Gibson (2006) and Marquis and Guillaume (2011).

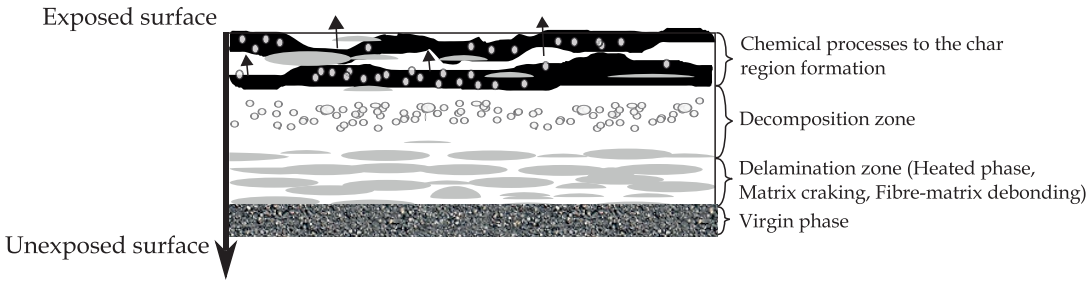

Figure 2.6: Thermal decomposition of a glass reinforced polymer composite - material scale

When the composite is exposed to an external heat source, chemical processes of the polyester begin in the resin matrix. Small molecular weight fragments from the decomposing polyester chain vaporize while the *char* zone is formed by cross-linking mechanism in the solid phase. Below the char zone, there is a thin region named the decomposition zone. Inside this region, the molecular bonds cracking begins but strongly slows down due to the above char formation. Moreover, the molecular fragments are too heavy to vaporize in the gas phase through the char zone. Then, below the decomposition zone, there is the delamination region. Delamination is *the separation of fibres plies which depend on the architecture of fibre* (Marquis and Guillaume (2011)). Delamination is caused by the pressure exerted by the trapped gases onto the soft complaint matrix (Marquis and Guillaume (2011)). This phenomenon is present for the knitted glass fibres but less visible for the mast reinforcement. With increasing the exposure time or the heat intensity, the char and the decomposed regions move towards the unexposed side of the composite. Furthermore, delamination and char zones, as well as the aluminium oxide residue, have a shield effect between the external heat source and the virgin condensed composite phase. These zones decrease the rate of the thermal decomposition.

Then, according to this description of the composite decomposition, an essential point is to understand the influence of the components decomposition in relation with each other. Lautenberger *et al.* (2008) proposed to model the composite as a successive of a set of components: alternatively 100% polyester resin, 100% glass or a mixture of 50% of resin and 50% of glass. While Marquis (2010) used an equivalent reaction mechanism for the glass-polyester layer of its studied composite.

2.2.2 Seat: Multilayer polymers materials

Thermal decomposition of wool, aramide and polyurethane foam are discussed in this section. Unfortunately, thermal decomposition of viscose is not described in this thesis, because too few information was found. Considering that viscose is obtained from wood cellulose, a brief description of cellulose thermal decomposition is done.

Wool

When wool is heated at around $162°C$, some cross-linking of amino acids occur (Hirschler and Morgan (2008)). Between $162°C$ and $292°C$, the disulphide bond in the amino acid cystine is cleaved with carbon disulphide and carbon dioxide being evolved (Hirschler and Morgan (2008)). Then, large quantity of hydrogen cyanide, benzene, toluene and carbon oxides are released at higher temperature ($600°C$ and $925°C$) (table 2.6).

Table 2.6: Thermal decomposition mechanism of wool, Hirschler and Morgan (2008)

Temperature	**Solid reagent**		**Solid product**		**Gas product**
$162°C$	Wool	$\longrightarrow$	Amino acids		
162 - $292°C$	Amino acids	$\longrightarrow$	Char/Residue	+	CO_2 and CS_2
600 - $925°C$	Char/Residue	$\longrightarrow$			$CO_x, C_6H_6, C_7H_8, HCN$

Moreover, according to Flambard *et al.* (2005) the wool melts and then forms a char layer. Theses decomposition mechanisms are confirmed by Popescu *et al.* (1995) (table 2.7).

Table 2.7: Thermal decomposition mechanism of wool, Popescu *et al.* (1995)

Type of reaction	**Solid reagent**		**Solid product**		**Gas product**
Thermolysis ($200 - 400°C$)	Amino acids	$\longrightarrow$	Pyrolysis products	+	CO, NH_3, H_2S
Thermo-oxidative ($450 - 600°C$)	Pyrolysis products	$\longrightarrow$	Char	+	CO_2 and oxidative products

Cellulose

The main component of the cellulose is the D-glucose. A complete overview of the cellulose decomposition mechanism is reviewed in Fateh (2011) thesis. The main reactions mechanism of the cellulose decomposition is performed in 3 steps. Before $300°C$, the cellulose polymer starts to decompose into a new polymer, as α-cellulose, carbon oxide and water are released in the gas phase. Then, after $300°C$, α-cellulose is decomposed in char and tar (known as levoglucosane) and released gases. Finally, the tar and char are oxidised in water, acetic acid, formic acid, phenol and other gases.

Aramide

Aramide polymers have a good thermal stability in air until $452°C$ (Hirschler and Morgan (2008)). Horrocks (1996) reviewed the thermal decomposition of an aramide polymer. He confirmed that the aramide polymer has a stable thermal behaviour until 375-400$°C$. Above this temperature, the aramide decomposes in char and releases few combustible volatiles gases. According to Hirschler and Morgan (2008), major gases released at low temperature are water and carbon oxides. At higher temperature, carbon monoxide, benzene, hydrogen cyanide, toluene and benzonitrile are formed. Around $550°C$, hydrogen and ammonia are produced. The high quantity of nitrogen compound released has a flame inhibitor effect in the gas phase due to the cooling action of combustible gases. The aramide reaction mechanism is summarized in table 2.8.

Table 2.8: Thermal decomposition mechanism of aramide

Range of temperature	**Solid reagent**		**Solid product**		**Gas product**
$(\sim 375°C)$	Aramide	$\longrightarrow$	α-Aramide	+	CO_x and H_20
$(375 - 450°C)$	α-Aramide	$\longrightarrow$	Char	+	CO, HCN, C_6H_6, C_7H_8 and C_7H_5N
$(\sim 550°C)$	α-Aramide	$\longrightarrow$	Residue	+	NH_3 and H_2

As it is known, interliner is often a mixture of aramide and polyimide polymers. According to Chern *et al.* (2009), polyimide is thermally stable up to $450°C$. Under nitrogen atmosphere at $10K/min$, it loses around 40% of it virgin mass in one step. Under air atmosphere, polyimide decomposes completely between 450 and $650°C$ in two majors steps.

Seat Foam

The foam of the seat is a mix of polyurethane and melamine foam.
Thermal decomposition of polyurethane (PU) foam is well known and widespread studied (Ravey and Pearce (1997), Hirschler and Morgan (2008), Bustamante Valencia (2009)). A table summarising of the the PU foam thermal decomposition mechanisms is available in Bustamante Valencia (2009) thesis. According to Hirschler and Morgan (2008), isocyanate molecule vaporizes and liquid polyol remains to further decomposes. Major products are: nitrogen oxide, nitrile, toluene diisocyanate (TDI), hydrogen cyanide and carbon monoxide. Bustamante Valencia (2009) reported the three independent steps of the PU foam decomposition mechanisms:

1. Dissociation to isocyanate and polyol.
2. Dissociation to primary amine, olefin and carbon dioxide.
3. Elimination of carbon dioxide, leading to formation of a secondary amine.

Then, he validated the model presented in figure 2.7 for the decomposition of a flexible polyether polyurethane foam used in furniture.

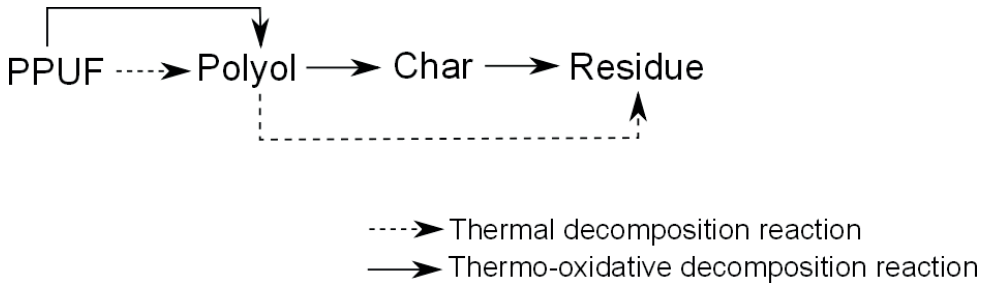

Figure 2.7: Thermal decomposition of the polyether polyurethane foam, Bustamante Valencia (2009)

The flexible PU foam behaves as a thermoplastic. Polyol turned into liquid state has an important influence on the reaction-to-fire, i.e. the flexible PU foam is placed into the seat between interliner, air and the shell. In this case, polyol remains in the shell or it might flow outside of the shell, down to the floor.

The addition of melamine in the polyurethane foam has a flame retardant effect. The melamine is formed from triazine or cyanamid. Costa *et al.* (1990), Crews (1992) and Troitzsch (2007) have studied the thermal decomposition mechanism of the melamine: the decompostion starts from successive elimination of ammonia and leads to the formation of *melam*, *melem* and finally *melon* (figure 2.8). Cerin-Delaval (2010) added that the melamine plays a role in the condensed phase and in the gas phase. Two processes are identified: an endothermic sublimation and then a condensation and decomposition in the condensed phase into melam, melem and finally melon, which are thermally stable compounds (figure 2.8)

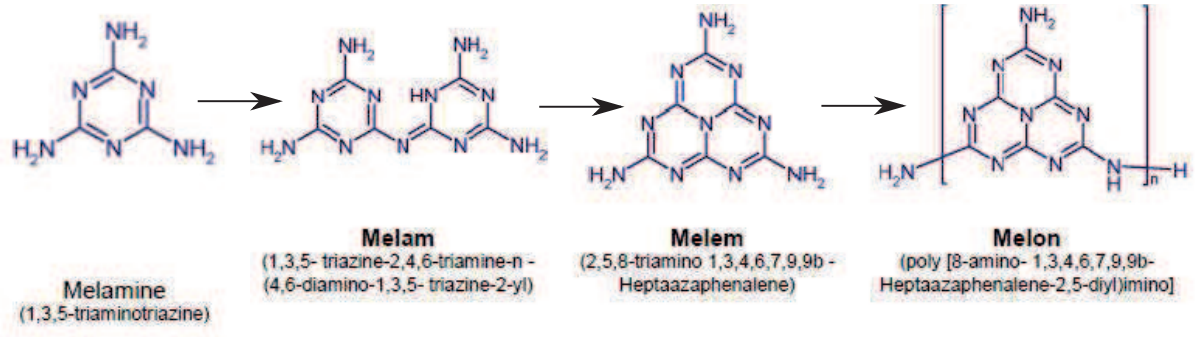

Figure 2.8: Thermal decomposition of the melamine compound, Troitzsch (2007)

In the gas phase, the releasing of molecular nitrogen dilutes the potential combustible gases.

2.3 Pyrolysis modelling of a polymer material

As it is known, the material pyrolysis process is complex because physical and chemical phenomena occur at the same place and time. *Oxygen and fuel concentrations will be controlled by the local permeability and by production-consumption rates, thus indirectly by the temperature* (Torero (2008)) in the condensed phase. The objective of the pyrolysis modelling is to predict the fuel mass flow production of the condensed phase independently from surroundings factors. Moreover, at macro scale, the fuel mass production is controlled by the condensed phase temperature and atmospheric conditions.

The main aim of this part is to explain the different key steps of the pyrolysis model for a given material:

- The reaction mechanism.
- The mathematical model and associated hypothesis.
- The optimisation resolution of the pyrolysis parameters (supposed as unique for a given material).
- The various pyrolysis codes available.

2.3.1 Concept of pyrolysis modelling

Bustamante Valencia (2009) reported that thermal decomposition studies began at the end of the nineteen century with van t'Hoff (1884), Arrhenius (1889), Wilhelmy (1891),Guldberg (1899) and Lewis (1905). More specifically, the Arrhenius relation states that the rate of a chemical reaction is dependent on the temperature through the expression of the constant rate k:

$$k = A.exp\left(\frac{-E_a}{RT}\right) \tag{2.6}$$

Usually, the Arrhenius relation is used for chemical reactions that take place in the gas phase. However, the Arrhenius relation has been proposed to model the reaction rate of the solid phase thermal decomposition in 1981 by Rogers and Ohlemiller (1981). Many authors have then worked with this relation to describe the pyrolysis modelling, for instance Rein (2005), Torero (2008) and recently Matala *et al.* (2012).

The methodology to model thermal decomposition at matter scale (of few milligrams of material) is referenced and applied in Bustamante Valencia (2009) and in Marquis *et al.* (2012). The principle is to perform TGA experiments of the tested material, then to define reaction mechanism of thermal decomposition at matter scale. Finally, the aim is to find pyrolysis parameters suitable to a thermal decomposition model.

Marquis *et al.* (2012) coupled the TGA test with a Fourier Transformed Infra-red spectrometer. This technique gives information about the solid phase decomposition and the gases released: in fact, each peak of the material mass loss rate is assumed as one decomposition reaction during a given temperature period. Then, gases measured during this

given temperature period can complete the reaction definition and precise their chemical nature.

Several tests are realised at different low heating rates in order to verify if the decomposition kinetic is the same for each heating rate. These tests are also carried out under air and nitrogen atmospheres. A simplified reaction mechanism is done for each atmosphere due to the oxygen impact on thermal decomposition (see section 1.5).

Kinetic studies of the simplified reaction mechanisms can be classified into three mains approaches (Di Blasi (1999)):

1. The global model, also called the Lumped Parameter Approach (LPA): It considers that the material is homogeneous and represents one compound. For example, according to Shafizadeh (1977) the wood decomposes in *tar*, *char* and *gases*. This approach is used on the interliner material of the studied seat.
2. The model by constituent: this approach takes into account the decomposition of each main constituent of the material. In the case of wood material, it is mainly composed of cellulose, hemicellulose and lignin. This kind of model is used on the glass reinforced polyester composite, the cover and the foam materials of the studied seat.
3. The multi-reaction model: this technique is based on the functional groups paths. This model is not used in this thesis because it requires a complete and accurate gas phase analysis.

Generally, approaches 1 or 2 are chosen to represent thermal decomposition from TGA tests measurements. This choice depends on the knowledge of the material and the mass loss rate kinetic during the matter decomposition. An important hypothesis of a simplified reaction mechanism is that each peak of the mass loss rate vector is associated to one global reaction. The following step is used to mathematically model the thermal decomposition mass in relying on the material simplified reaction mechanism.

For example, considering a two-steps reaction mechanism of a material A (table 2.9):

Table 2.9: Example of a two-steps reaction mechanism of a material A

Solid reagent		**Solid product**		**Gas product**
A_α	$\longrightarrow$	$Y_{r,\alpha\beta}$ Char	+	$Y_{g,\alpha\beta}$ Fuel
Char	$\longrightarrow$	$Y_{r,ch\gamma}$ Residue	+	$Y_{g,h\gamma}$ Fuel

$Y_{r,\alpha\beta}$ represents the residual mass fraction of the *Char* solid product from the component α of the material A of the reaction β. $Y_{g,\alpha\beta}$ represents the gas mass fraction of Fuel gas product from the component Char of the material A of the reaction β. $Y_{r,ch\gamma}$ and $Y_{g,h\gamma}$ are respectively the residual and the gas mass fraction of the Residue and the Fuel from the Char component of the material A for the reaction γ. It is assumed that

$Y_{r,\alpha\beta} + Y_{g,\alpha\beta} = 1$ and $Y_{r,ch\gamma} + Y_{g,h\gamma} = 1$.

The pyrolysis model is based on an heterogeneous (solid/gas phase) reaction mechanism. The reaction mechanism can be one-step (only one reaction or one group of reaction) or multi-steps mechanism (several concomitant or parallel reactions). At raw matter scale, the hypothesis of the pyrolysis model are:

- local thermal equilibrium between the solid and the volatiles,
- no physical change of the condensed phase,
- no volume change of the condensed phase,
- no gas diffusion into the condensed phase,
- no porosity effect,
- the condensed phase is homogeneous and isotropic.

The evolution of the local density of the material A component is the difference between the production rate of the product component and the consumption rate of the reagent component:

$$\frac{d}{dt}\left(\frac{\rho_{s,\alpha}}{\rho_{s,o}}\right) = -\dot{\omega}_{\alpha\beta} \tag{2.7}$$

$$\frac{d}{dt}\left(\frac{\rho_{s,ch}}{\rho_{s,o}}\right) = Y_{r,\alpha\beta}\dot{\omega}_{\alpha\beta} - \dot{\omega}_{ch\gamma} \tag{2.8}$$

$$\frac{d}{dt}\left(\frac{\rho_{s,R}}{\rho_{s,o}}\right) = Y_{r,ch\gamma}\dot{\omega}_{ch\gamma} \tag{2.9}$$

The total local density evolution is the sum of each component (α, *Char* and R).

$$\frac{d}{dt}\left(\frac{\rho_{s,tot}}{\rho_{s,o}}\right) = \frac{d}{dt}\left(\frac{\rho_{s,\alpha}}{\rho_{s,o}}\right) + \frac{d}{dt}\left(\frac{\rho_{s,ch}}{\rho_{s,o}}\right) + \frac{d}{dt}\left(\frac{\rho_{s,R}}{\rho_{s,o}}\right) \tag{2.10}$$

Then, by combining equations 2.7, 2.8, 2.9 and 2.10:

$$\frac{d}{dt}\left(\frac{\rho_{s,tot}}{\rho_{s,o}}\right) = \left(Y_{r,\alpha\beta} - 1\right)\dot{\omega}_{\alpha\beta} + \left(Y_{r,ch\gamma} - 1\right)\dot{\omega}_{ch\gamma} \tag{2.11}$$

Generally and according to Guillaume (2013), the total density rate of the material is defined with equations 2.12, 2.13 and 2.15 knowing that N and W are respectively the total number of the reactions i and compounds j in the solid phase (Bustamante Valencia (2009)):

$$\frac{d}{dt}\left(\frac{\rho_{s,i}}{\rho_{s,o}}\right) = \sum_{i=1}^{N} Y_{r_i}\dot{\omega}_i - \sum_{i=1}^{N}\dot{\omega}_i \tag{2.12}$$

with

$$\dot{\omega}_i = k_i f(\delta)_j \tag{2.13}$$

and

$$k_i = A_i exp\left(\frac{-E_{a,i}}{RT}\right) \tag{2.14}$$

and

$$\frac{d}{dt}\left(\frac{\rho_{tot,s}}{\rho_{s,o}}\right) = \sum_{j=1}^{W} \frac{d}{dt}\left(\frac{\rho_{j,s}}{\rho_{s,o}}\right) \tag{2.15}$$

The function $f(\delta)$ is called differential conversion function. This one is detailed in references Bustamante Valencia (2009) and Guillaume (2013). In this function, δ is the degree of conversion of the species j of the reaction i:

$$\delta = \frac{m_j - m_{j,f}}{m_{j,0} - m_{j,f}} \tag{2.16}$$

Where, m_j, $m_{j,f}$ and $m_{j,0}$ are respectively the mass of species j at each time step, the final mass of the species j and the initial mass of the species j.

2.3.2 Overview of pyrolysis codes

The model of thermal decomposition taking place during the solid phase relies on several hypothesis. Some of them are:

- each reaction is complete.
- the solid, liquid and gas/vapour phases are in local thermal equilibrium.

This approach of the general pyrolysis model is widely used in the current pyrolysis and/or fire code with some differences. For some years now, the most widely used pyrolysis and/or fire code to model the pyrolysis of a condensed material have been GPYRO (Generalized pyrolysis model for combustible solids, Lautenberger and Fernandez-Pello (2009)), ThermaKin (Stoliarov and Lyon (2008)), FDS (Fire Dynamics Simulator, Version 5.5, McGrattan *et al.* (2010)) and FireFoam (Krisnamoorthy *et al.* (2009) and Chaos *et al.* (2010)).

GPYRO and ThermaKin are specific to the modelling of the pyrolysis into the condensed phase.Yet, FDS and FireFoam are more general fire CFD code where pyrolysis of the solid is a boundary condition for gas phase. The main hypotheses on the pyrolysis model of each pyrolysis code are presented in the table 2.10.

Table 2.10: Major assumptions of the pyolysis model of different codes

Parameter	**GPYRO**	**ThermaKin**	**FDS**	**FireFoam**
Differential conversion function	several $f(\delta)$	$f(\delta) = Y_j^{ni}$	$f(\delta) = Y_j^{ni}$	$f(\delta) = (1-\delta)$
reaction mechanism	Multi-steps	Multi-steps	Multi-steps	Single
Atmosphere conditions	Y_{O_2}	No Y_{O_2}	No Y_{O_2}	No Y_{O_2}
Type of flow distribution into the material	Temperature, species and pressure	Temperature, species and pressure	Temperature	?
Volume of the material	Evolution of the material volume	Evolution of the material volume	No Evolution of the material volume	Evolution of the material volume
Porosity	Porosity effect	Porosity effect	No Porosity effect	Porosity effect
Resolution	Coupled with Optimization tool	No optimization tool	No optimization tool	Coupled with Optimization tool

Many kinds of differential conversion functions are available in GPYRO. The GPYRO user can chose one of these differential conversion functions, which are the more adapted to the reaction mechanism of the material. FDS and ThermaKin use only one possible differential conversion function, which is $f(\delta) = \left(\frac{m_j}{m_{j,0}}\right)^{ni} = Y_j^{ni}$ where Y_j is the mass fraction of species j of the reaction i. The $m_{j,f}$ is assumed equal to zero, i.e. reagent decomposes.

Concerning FireFoam, the differential conversion function can be associated only to a first order reaction , such as $f(\delta) = (1-\delta)$. Furthermore, a material reaction mechanism can have a multi-step reaction for GPYRO, ThermaKin and FDS while only a single reaction is possible for the FireFoam code. The local mass fraction of oxygen is taken into account in the pyrolysis model only for GPYRO. It means that only GPYRO can take into account oxidative pyrolysis reaction. Moreover, GPYRO and ThermaKin couple the pyrolysis model with a diffusion and transport of gas flow models into the condensed phase. These codes also allow the evolution of the volume of the material in order to take

into account the charring material or intumescent coating. The porosity effect applied to the material is also considered for the modelling of porous media. At the same time, FDS models allow to assume that the condensed phase volume is constant during calculation time and that gases are transported from the surface of the solid where they were generated. Snegirev *et al.* (2012) presented a pyrolysis model to predict pyrolysis od composite material. This pyrolysis model is close to GPYRO model.

The whole of this thesis is based on the simulation from the material scale to the real fire scenario. Many physical phenomena are present during these multi-scale simulations: pyrolysis, combustion, transport and turbulence in both solid and gas phases. FDS and FireFoam are designed to represent these fire phenomena. However, only a single reaction can be modelled into the pyrolysis model of FireFoam. The pyrolysis of train materials requires more than one single reaction. Moreover, the Transfeu partners choose to use FDS. Thus, FDS version 5.5 is used along this thesis from the material scale to the real scale.

2.3.3 Optimization algorithm for the pyrolysis parameters estimation

One of the great challenges in the fire community is to estimate the unknown parameters (pyrolysis parameters) of this pyrolysis model (2.12, 2.13 and 2.15):

- the kinetic parameter (A, E_a and n) associated to each reaction
- the residual mass fraction for each reaction (Y_r)

Two kinds of methods exist to find these parameters:

- a direct (isoconvertional) method,
- an indirect method

Bustamante Valencia (2009) and Guillaume (2013) described these two kinds of methods.

The direct method or the isoconvertional approach allows to obtain the evolution of the activation energy function of the reaction rate without taking into account the reaction mechanism. This method is based on a graphic resolution. The reader is invited to look at these references Lautenberger *et al.* (2008), Matala *et al.* (2012) and Guillaume (2013) for more information. The advantage of this technique is that it takes few minutes to obtain a set of parameters. This approach is simple to apply when the decomposition reaction is unique or when all reaction are correctly separated. However, it is not the case of the thermal decomposition of the studied wall panel and seat. Thus, this approach cannot be used here.

The principle of the indirect method is to optimize each reaction pyrolysis parameters in order to provide a near-optimal agreement between the numerical pyrolysis model predictions and the experimental measurements from TGA test. The optimization tool role is to randomly try a set of unknown pyrolysis parameters to the corresponding pyrolysis model. Additionally, an optimization algorithm is used to compare the experimental and

the optimized mass loss rate in order to obtain the best result.
To this end, the optimization algorithm is globally composed of:

- a pyrolysis model corresponding to the simplified reaction mechanism
- a randomly number generator, called an algorithm tool
- an optimization function.

Until 2004, the widely used optimization tool is the genetic algorithm (GA) (Rein (2005), Lautenberger (2007), Bustamante Valencia (2009) and Matala and Hostikka (2011)). However, Webster (2009) and Chaos (2010) recently developed other optimization algorithm tools, respectively the stochastic hill climber (SHC) and the shuffled complex evolution (SCE). Lautenberger and Fernandez-Pello (2011) have inserted three other optimization algorithms (SCE, SHC and GASA (Hybrid genetic algorithm/simulated annealing)) in addition to the GA into GPYRO in order to compare the performance of each optimization algorithm. Lautenberger and Fernandez-Pello (2011) concluded that the SCE is more efficient than the others. The GA principle is reminded in the methodology chapter.

FDS version 5.5 is not coupled with such sophisticated optimization algorithm. Thus, the pyrolysis parameters must to be estimated prior to use FDS as input data of the pyrolysis model. The GA is developed on Matlab according to the works of Houck and Joines (1996) and Bustamante Valencia (2009).

The GA looks for the best solution in the huge population of individuals. Generally, the best individual of a population survives to the next generation and then improves the solutions range of the next generations. In this thesis, like Bustamante Valencia (2009) and Marquis (2010), a fitness function (Eq 2.17) is used to compare experimental and modelling results. The higher the fitness function (ϕ) is, the more correct the optimization parameters are:

$$\phi = \sum_{\beta=0}^{c} \left[cos\left[\angle\left(\overrightarrow{x}, \overrightarrow{y}\right)\right] \left[\frac{\parallel \overrightarrow{x} - \overrightarrow{y} \parallel}{\parallel \overrightarrow{x} \parallel} \right]^{-1} \right]_{\beta} \tag{2.17}$$

The fitness function compares the phase between each curve (curve shape) and also the relative intensity difference (compared to the experimental one), simultaneously for all heating rates analysed.

Each estimated pyrolysis parameter, associated to each reaction and each material, is used as an input data to model the pyrolysis of materials.

2.3.4 Discussion about the kinetic parameter meaning

The Arrhenius relation is composed of three kinetic parameters:

- the activation energy
- the pre-exponential factor

- the order of the reaction.

This relation is used to characterize kinetic chemical reactions in the gas phase. It allows to model the variation of chemical reaction rate with the temperature. Indeed, this relation is applied on the molecular gas phase.

In the last few years, several articles and thesis (Rein (2005), Lautenberger (2007), Bustamante Valencia (2009), Marquis (2010) and Fateh (2011)) have relied on the Arrhenius relation to model the chemical reaction rate in the condensed phase during the thermal decomposition. However, simplified reaction mechanism applied on the condensed phase is not molecular mechanism but generalized one. In these terms, the physical meaning of kinetic parameter is arguable for a condensed phase reaction. These numerical kinetic parameters depend on the kind of material, the associated simplified reaction mechanism and the pyrolysis model. Thus, for a same material, the comparison of kinetic parameters during the mass thermal decomposition in the literature is complicated. Thermal decomposition and degradation both depend on the kind of material, the atmospheric conditions and the modelling hypotheses chosen by the user.

Chapter 3

Multi-scale approach (Testing scales and numerical tools)

Contents

3.1 Multi-scale tests and validation approach

Bustamante Valencia (2009) introduced the term of vertical integration of three scales (raw matter, material and finished scales). The principle is to measure or to estimate raw matter properties in order to provide input data for fire simulation and to predict the material thermal decomposition. Marquis (2010) completed the vertical integration concept with the reaction-to-fire study of a sandwich composite product and applied on upgrading five scales. The aim is to predict the pyrolysis and the fire spread processes of a product included in a real design fire scenario from the thermal decomposition of each studied material at raw matter to real scales. This approach comprises three phases: experiments on tests rigs of increasing scales, numerical simulation of these experiments and

comparisons with feedback corrective actions regarding input parameters used for simulation where necessary (figure 3.1) (ISO 16730 (2007)). These comparisons at increasing complexity allow to observe the ability of the model to reproduce realistic simulations and to better understand the fire phenomena at each scale (Marquis (2010) and Camillo *et al.* (2012)).

The product reaction-to-fire consists on understanding of the response of the product when it is exposed to an external heat source during a fire test (ISO 13943 (2011)). This product response can be characterized by the thermal decomposition and degradation, the ignition and combustion, the fire spread, and the generation and transport of gases released. One or several fire responses are potentially present at each scales. For example, the raw matter scale focuses more on the material thermal decomposition while the real scale groups together all fire responses including end-use characteristics such as mounting and fixing. This is why a multi-scale approach has been used during the present study. This one relies on the reaction-to-fire of railway products and especially on a seat and a wall panel. In this approach, the fire behaviour of railway products is studied from the raw matter scale to the real scale.

An other important challenge is to estimate the materials properties through fire tests or by literature, such as thermal properties and pyrolysis parameters, which are used as input data used for simulation. Once the product reaction-to-fire is validated at each scale, it is possible to change the design fire scenario and/or the fire scenario and to predict the fire responses.
Five scales are used and represented (3.1):

- The raw matter scale: a few milligramms of materials are heated in a TGA/DSC tests.
- The material scale: a few grams of materials are combination between materials are heated in a cone calorimeter (ISO 5660-1 (2002)) or in a smoke box (ISO 5659-2 (2012)) tests.
- The semi-finished product scale: a few kilograms of materials are heated in a end-use condition, such as ISO 21367 (2008) calorimeter.
- The finished or system scale: a few tens kilograms of products are heated in an open calorimeter test and mounted as final design (ISO 24473 (2006)).
- The real scale: a design fire scenario is studied in real conditions.

In this part, the interest of each scale is presented, then the description and limits of each scale of fire test and along with the numerical tools.

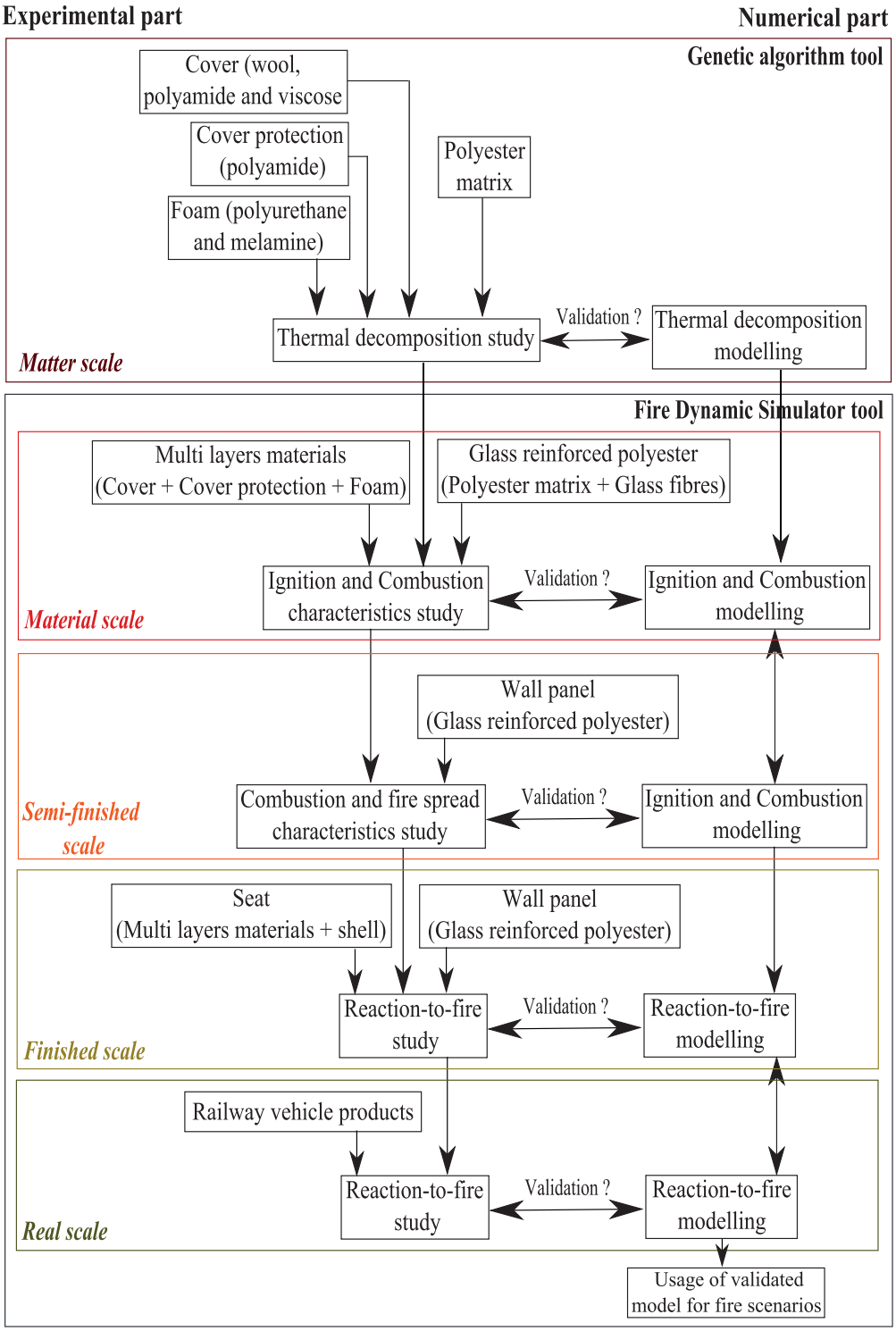

Figure 3.1: Multi scale approach

3.1.1 Raw matter scale

The aim of the raw matter scale is double:

- The analysis of polymer thermal decomposition (the assumptions of a simplified reactions mechanism for each studied material)
- The estimation of pyrolysis parameters (kinetic parameters and residual mass fraction) for each identified reaction.

TGA and DSC test

Matter scale tests are carried out from a Thermogravimetric Analysis (TGA) coupled with the Differential Scanning Calorimeter (DSC). The principle is to measure the reactivity of a few milligrams of material in function of the heating rate temperature to understand the thermal and oxidative decomposition of the polymer material. The measured data from a TGA test are the mass and temperature of the sample. The TGA tests conditions are:

- The material is thermally thin (the material temperature is homogeneous inside the crucible).
- the furnace temperature and the concentration of the gases vector are homogeneous around the tested sample.
- The gases diffusion is negligible inside the tested sample.
- The surrounding heat transfers are neglected.
- The solid and the gas phase are in thermodynamic equilibrium.
- The local pressure is low.
- The ambient atmosphere is either air or inert.
- The heating rate of the furnace is low enough in order to separate each global reaction during the decomposition.

DSC measures is the difference of heat flux between blank (ceramic, for instance) crucible and the sample one, obtained through a thermocouple probe or several thermocouples. This heat flux can be exothermic or endothermic during the physical transition of the material. As argued by Bustamante Valencia (2009), the DSC is designed to measure heat of reaction to a non-decomposing materials (like ceramic or metallic compounds). The major difficulty is to provide the baseline. Moreover, the DSC measurement is sensitive to the heterogeneity of the material as well as the open or close ceramic crucible. Thus, the heat of reaction obtained from the DSC measurement remains questionable for combustible materials. This physical quantity needs to be verified with literature value.
The results from TGA can be interpreted as an evolution of the mass loss and of the mass loss rate (MLR) function of the temperature increasing of the sample. One MLR peak for a given temperature range is supposed to represent a decomposition reaction. This reaction can be dependent or not on the oxygen concentration. The analysis of the MLR curve, the composition of the polymer and literature reviews allow to define a simplified reactions mechanism for the tested polymer material. As reported by Bustamante Valencia (2009), complementary analyses could be performed if the TGA were coupled to a

gas analyser. This study of gases evolved can confirm the simplified reaction mechanism proposed.

The pyrolysis parameters of each reaction for the tested polymer material are estimated with an inverse method according to the thermal decomposition model, the genetic algorithm tool, the fitness function and based on the proposed mechanism. Torero (2008) reported that the pyrolysis parameters are independent on the heating rate. This principle is summarized in figure 3.2.

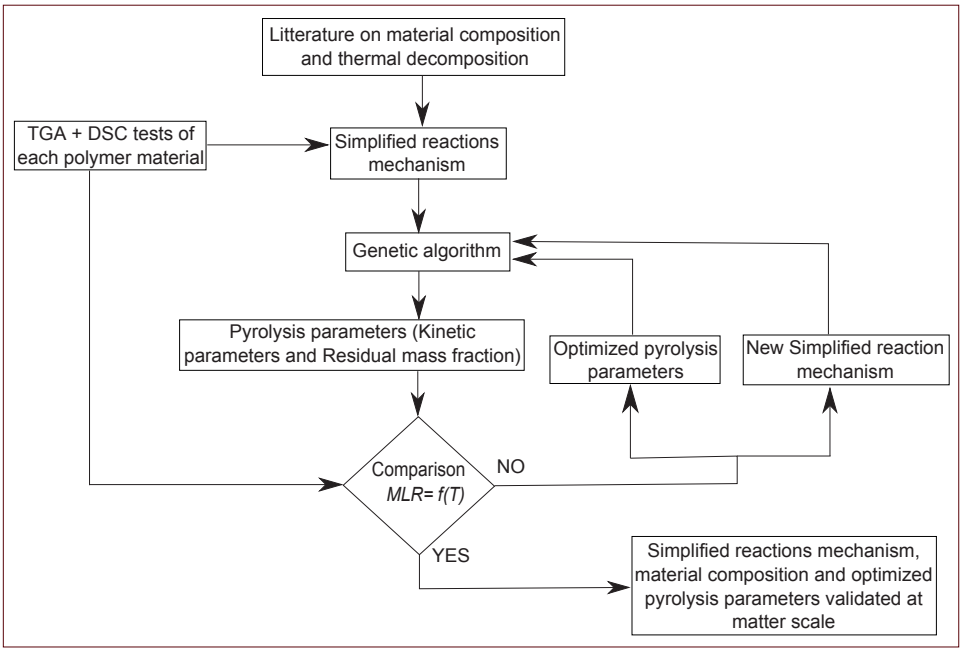

Figure 3.2: Matter scale approach (pyrolysis parameters estimation)

The objective of this modelling technique is to fit the best mass loss rate (MLR) to the numerical model with a certain pyrolysis parameters ranges. If the numerical mass loss rate does not fit either the parameter range or the simplified reaction mechanism, it must be changed. Afterwards, the pyrolysis parameters of each reaction are the input data of the next scale (material scale) simulation with a computational fluid dynamic tool.

3.1.2 Material scale

At the material scale, the reaction-to-fire is studied with the cone calorimeter and the smoke box. Both tests are detailed further.

Cone calorimeter test

Figure 3.3 presents a schema of the cone calorimeter test.

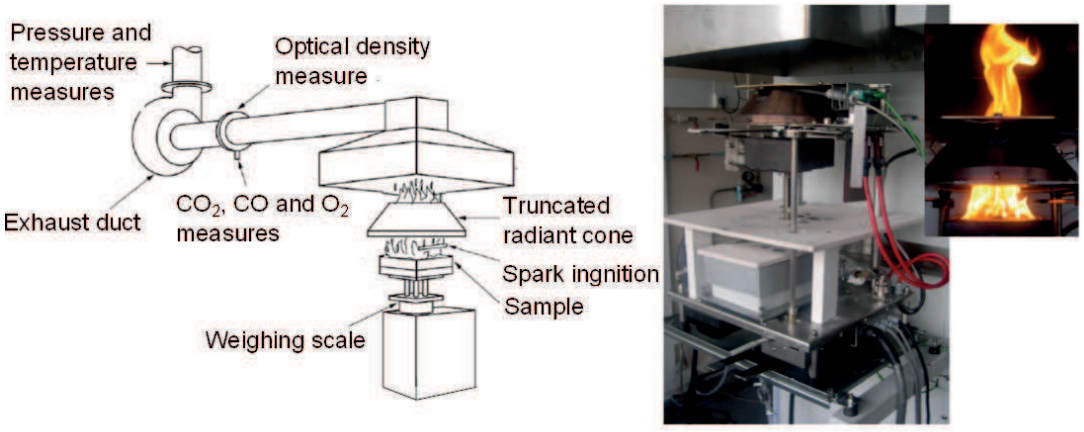

Figure 3.3: Schema of the cone calorimeter test (ISO 5660-1 (2002))

Like the previous scale, the cone calorimeter (ISO 5660-1 (2002)) scale has an experimental and a numerical objectives. Experimentally, the principle is to understand the behaviour of a material or several layers of a multilayer material when its surface is exposed to an external heat source. The test conditions are:

- The material is supposed homogeneous. The exposed material area is 10 x 10 cm.
- The $1D$ heat transfer is privileged.
- The system is open and supposed well-ventilated (the quantity of oxidant is higher than the fuel)
- The back condition of the tested material is fire blanket (silicate wool) to insure stability of the material inside the sample holder and especially to have a specific thermal condition on the back face.
- The conical radiant heater is placed 2.5 cm horizontally above the material. Moreover, the possible incident heat flux from the conical radiant source to the material surface goes from 0 up to 100 $kW.m^{-2}$.
- The piloted ignition is used with a spark plug.

The pyrolysis, ignition and combustion conditions are studied during the cone calorimeter test (ISO 5660-1 (2002)). A load cell is placed under the sample holder to record the material mass loss during the test. Then, an optical opacimeter is used in the duct to estimate the attenuation of a laser light. The concentration of oxygen, carbon monoxide, carbon dioxide and other gases are determined in the duct. Furthermore, the critical heat flux can be estimated with several tests. The critical heat flux is the lower heat flux received at the material surface to initiate and to maintain a combustion reaction. The indirect cone calorimeter measurements are:

- The thermal diffusivity through the Thermal Response Parameter and the critical heat flux.
- The heat release rate via an oxygen consumption calorimetry technique.

- The mass loss rate of the material.

To finish, the analysis of the cone calorimeter results is sensitive to the silicate wool used behind the tested material (Brown *et al.* (1988)). A more recent study has showed the thermal feedback effect with the replacement of the silicate wool by a aluminium plate (Carvel *et al.* (2011)).

Smoke box test

The figure 3.4 presents the schema of the smoke box.

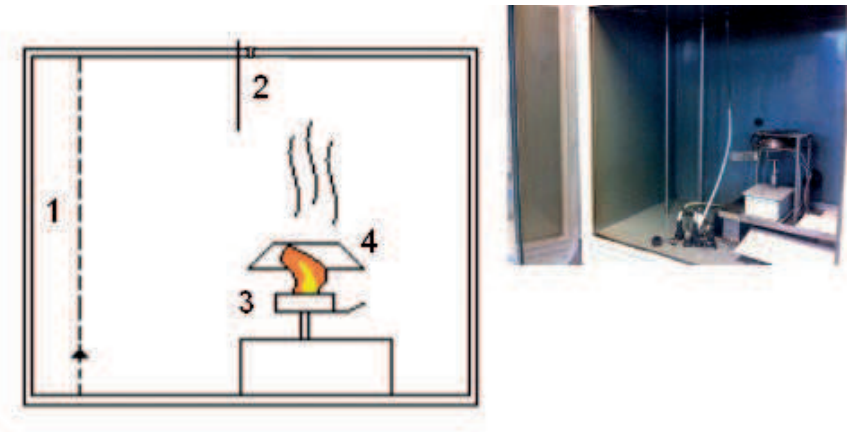

Figure 3.4: Schema of the smoke box test (ISO 5659-2 (2012)) with 1: optical density measure, 2: pressure measure, 3: sample and 4: truncated radiant cone.

The principle of the smoke box (ISO 5659-2 (2012)) is to measure the smoke production, via an optical density measure, from an exposed material surface under specific test conditions:

- The system or chamber is closed: the fire conditions evolve continuously in the box.
- The exposed material area is 7.5 x 7.5 cm.
- The horizontal position of the sample.
- The back condition of the tested material is fire blanket (silicate wool) to insure stability of the material inside the sample holder and especially to have a specific thermal condition on the back face.
- The incident heat flux from the conical radiant source to the material surface goes from 0 up to 100 $kW.m^{-2}$.
- The piloted ignition is used with or without pilot flame.

During the Smoke box test, the surface material is heated by a conical radiant heater. The pyrolysis and combustion gases remain into the box volume ($V = 0.51\ m^3$). The smoke opacity is measured with the attenuation of a white light beam passing through the smoke into the box. Moreover, the gases concentration from the material combustion can be analysed with a static point measurement through a gas analyser according to the

future CEN/TS 45545-2 (2009) standard. Transfeu has developed an alternative method to continuously measure the gases concentration. The interest of this test is to obtain the type and the quantity of gases released from the material.

The aim of the simulation at material scale is to predict the reaction-to-fire of the studied material. A good match between experimental and numerical data is obtained according to the limits of the models, the material input data and the experimental observations (figure 3.5).

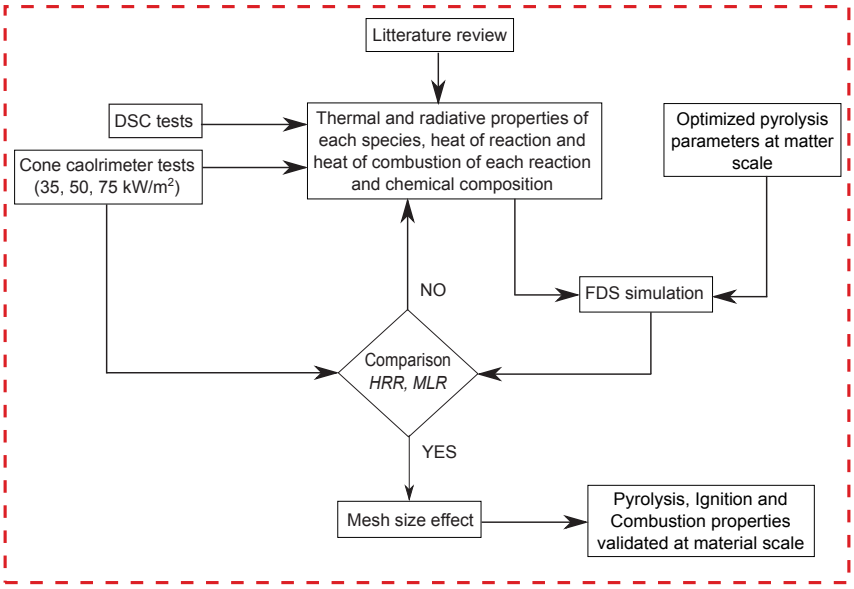

Figure 3.5: Material scale approach (Pyrolysis, Ignition and Combustion input data validation)

Thus, when the pyrolysis, ignition and combustion input data (thermal and radiative properties, pyrolysis parameters, heat of reaction, heat of combustion and the chemical composition) are confirmed at the material scale, the next step is to verify them at upper scale. This validation scale is complex due to the high number of input data and interlinked models to predict the pyrolysis, the ignition as well as the combustion. The most difficult input parameter to estimate is the heat of reaction associated with the pyrolysis model. Another difficulty is to experimentally and numerically understand the reaction-to-fire prediction of a multi layers materials.

3.1.3 Semi-finished product scale

Figure 3.6 presents the schema of the Medium Burning Item (MBI) test. MBI (ISO 21367 (2008)) test allows to study the reaction-to-fire and the fire spread only over a vertical product.

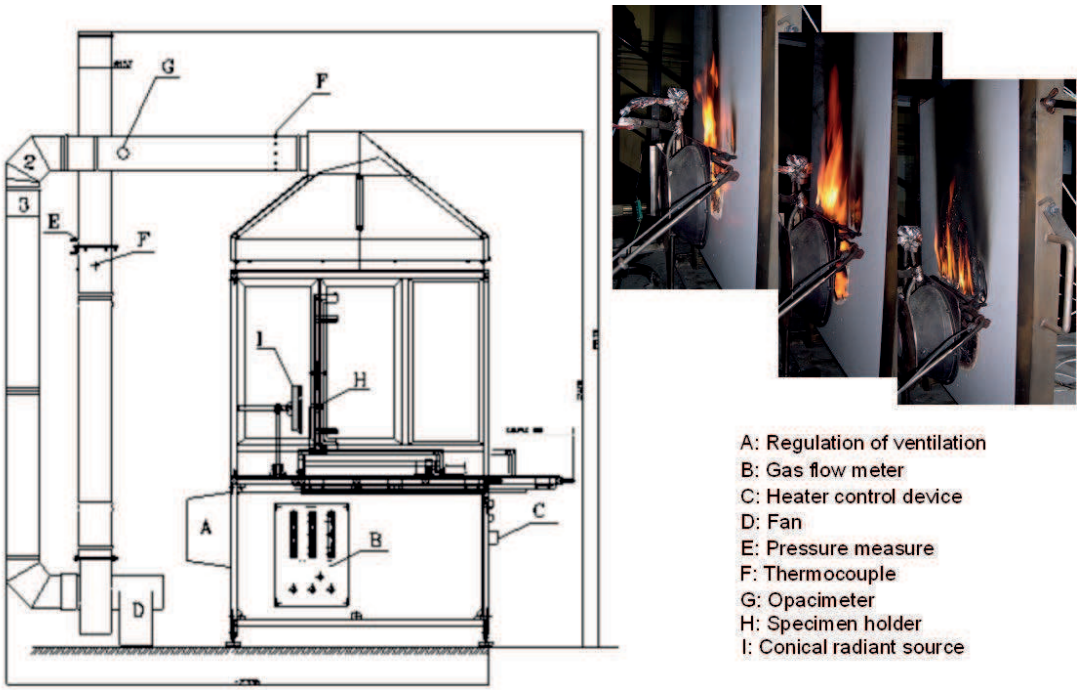

Figure 3.6: Schema of the Medium Burning Item test (ISO 21367 (2008)).

Then, for this study, only the wall panel is tested with MBI. The MBI test groups the same test conditions together as the cone calorimeter test excepted that:

- The product has not backing condition.
- A piloted flame.
- An exposed material area is 50×70 cm.
- The conical radiant heater is placed vertically at 50 mm from the material surface as shown in figure 3.6. Moreover, a vertical or lateral fire spread is possible.

The MBI simulation objective is to validate the ability of the Computational Fluid Dynamic code to predict the vertical and lateral flame spread for a vertically-oriented specimen and to confirm the material scale properties (figure 3.7). Experimental and numerical comparisons are based on heat release rate, total mass loss of the product, surface temperature and product burnt area.

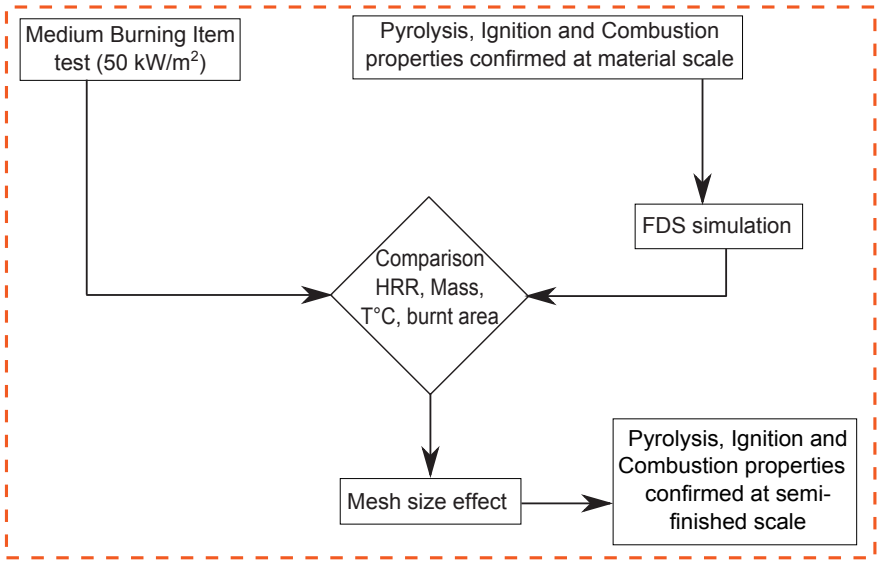

Figure 3.7: Semi-finished scale approach

3.1.4 Finished product or system scale

The fourth scale uses the open calorimetry test and represents the product in realistic condition, i.e. the configuration, the dimensions and the structural geometry of the product. The heat source, used in this work, is a propane burner while the previous scales used mainly a radiant source. The ignition source corresponds to a propane diffusion flame 75 kW during 2 minutes and then 150 kW during 8 minutes. For both products studied, the propane burner is placed on the floor close to the product, like a luggage position. Moreover, an internal train vehicle is represented by the presence of wall, ceiling and floor.

Concerning the wall panels test, panels were mounted as 1.5 m by 1.5 m walls in a steel frame in a corner configuration with a non-combustible ceiling and floor (3.8a). Behind the two tested wall panels, there is a 10 mm air gap, followed by 25 mm mineral wool and a 10 mm calcium silica board (on the back side). The propane burner is placed in the corner.

For the finished seat test, two non-combustible calcium silica panels were mounted as 1.5 m by 1.5 m, in a steel frame in a corner configuration with a non-combustible ceiling and floor (3.8b). The tested seat is arranged in the inner corner. The propane burner is located above the seat, close to the calcium silicate board.

For the two finished tests, the system is open and smoke is collected into the exhaust duct. Measurements of heat release rate, smoke production rate, gas production, weight loss and several temperatures are done. The aim of this scale is to test wall panel and seat in the end-use conditions, i.e. as a typical train vehicle, as well as to understand the fire spread on these product attacked by flame burner.

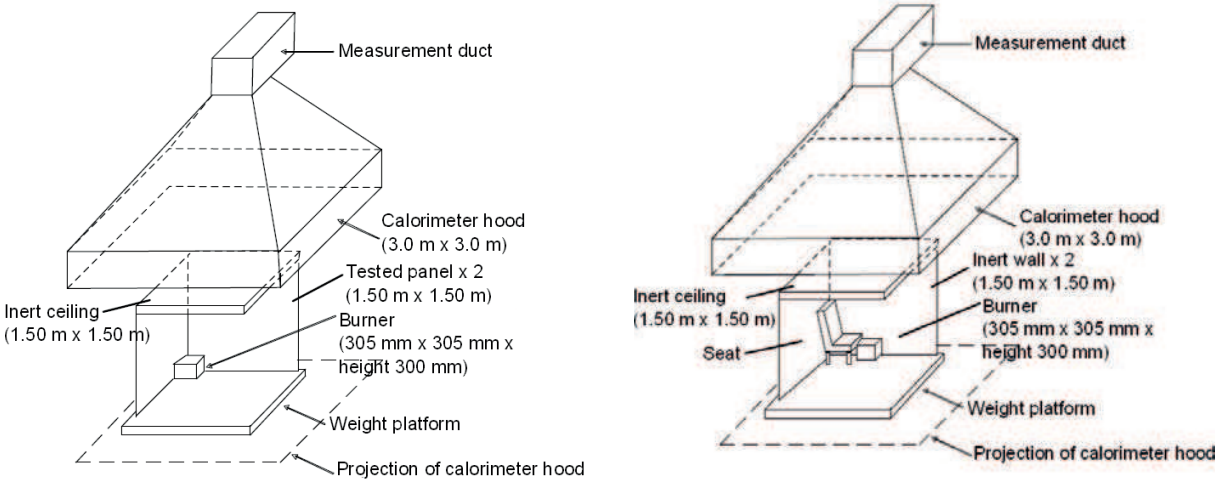

a/ Experimental view of the finished wall panel test set-up. *b/* Experimental view of the finished seat test set-up.

Figure 3.8: Experimental view of the finished product test set-up.

The finished scale simulation verifies the product reaction-to-fire taking into account the effect of mounting and fixing configuration (impact of the ceiling, the corner and joints) and then confirms numerical constants, numerical geometry and the mesh size (figure 3.9). Moreover, this scale allows to compare the total experimental and numerical generation of released gases from the propane burner and from the product itself.

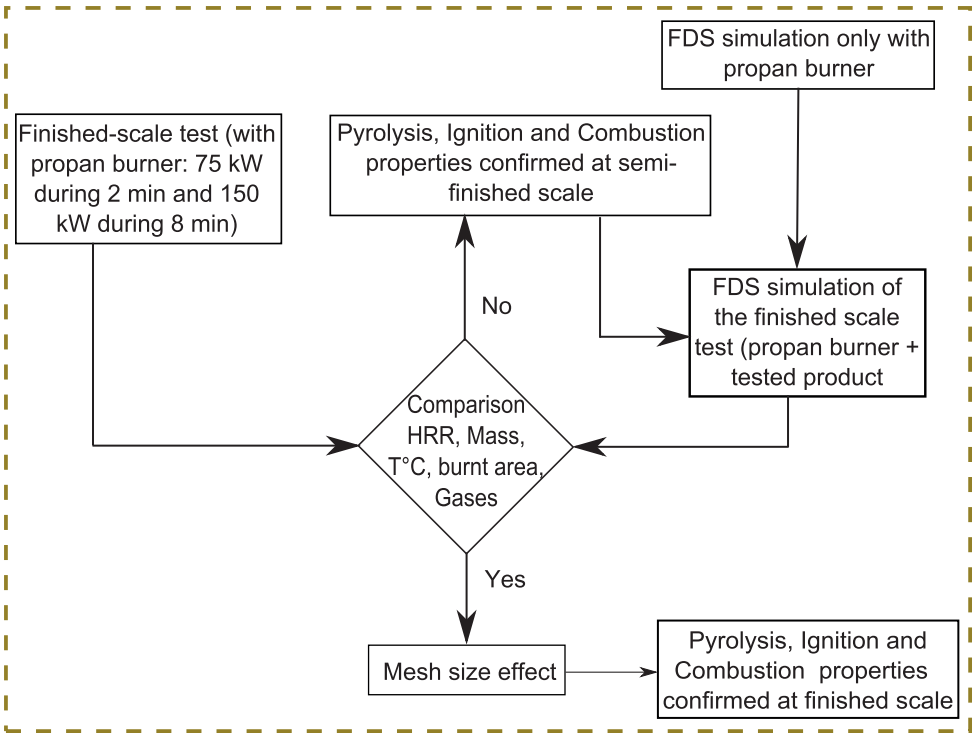

Figure 3.9: Finished product scale approach

An important point in this scale is the presence of two fuels (propane and tested product) compared to the previous scales, because products are heated by a propane diffusion flame. A flame can be characterized by its hight, its bed diameter and its heat release rate. It is then really important to model properly the burner flame in order to correctly reproduce the heat received by the tested samples.

3.1.5 Real scale

During Transfeu project, four tests are realised in two different realistic design vehicles (a single coach and a double deck coach). The design fire scenario was selected by the Transfeu consortium according to a fire risk analysis (Camillo *et al.* (2011)). During the fourth previous scales, a wall panel and a seat are separately studied. The studied design scenario has remained as:

- Fire source: propane burner (75 kW during 2 min and 150 kW during 8 min) located between two seats close to the wall panel.
- No fire detection.
- Ventilation system activated.
- No passive and active fire protection.
- Three doors open in the same side 40 s after the burner ignition.
- Involved products: seat, wall panel, floor, partition, ceiling and light diffuser.

Details of the selected design fire scenario are available on the Selection of Design Fire Scenario and associated products chapter. The aim of this real scale is to compare the experimental and the numerical fire growth and the toxic gases generation in order to confirm the abilities of the FDS code to simulate a such fire (figure 3.10). Then, the final objective of the real scale simulation is to assess the fire effects on the passengers during the evacuation.

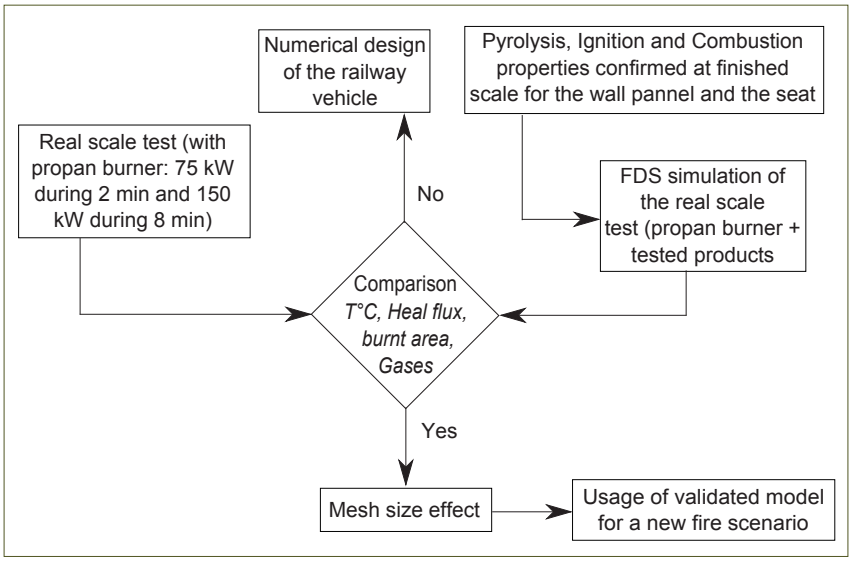

Figure 3.10: Real scale approach

Table 3.1: Summary table of multi-scale tests

Test	**Tested quantity**	**Direct measurements**	**Indirect measurements**	**Standard references**
TGA *DSC*	∼10 mg	Mass Temperature	MLR	ISO 11357-1, ISO 11357-5 ISO 11358-1, ISO 11358-2
Cone calorimeter	∼100 g	O_2, CO_2 and CO concentration, Mass, Temperature and Light transmittance	HRR, MLR, Optical density, T_{ig} and CHF	ISO $5660-1$ ISO $5660-2$
Smoke box	∼100 g	Light transmittance	Optical density	ISO $5659-2$
Medium burning item	∼1 kg	O_2, CO_2 and CO concentration, Mass, Temperature, Light transmittance and burnt area	HRR, Mass loss and Optical density	ISO 21367
Product system	∼10 kg	O_2, CO_2 and CO concentration, Mass, Temperature, Light transmittance and burnt area	HRR, MLR Optical density	ISO 24473
Real-scale test	$\geqslant$10 kg	O_2, CO_2 and CO concentration, Temperature, Light transmittance and burnt area	HRR, MLR Optical density	

The table 3.1.5 summarized the fire tests according to certain parameters: the tested material quantity, the direct and indirect measurements and the standard references.

3.1.6 Gas phase analysis

3.1.6.1 General notions

As for the condensed phase, the gas phase is difficult to study because of the nature and the quantity of the gases, which evolve quickly and their dependence on the type of material and the fire conditions. For instance, different fire conditions can be implied during the cone calorimeter and the smoke box tests. Furthermore, the choice of the sample position and the type of analyser are two of the main factors which can influence the gases measurements, according to the material tests configurations. Sampling can be either *extractive* or *in situ* (Fardell and Guillaume (2010)). *Extractive* analysis is when gases effluents are removed from the fire test for instantaneous or delayed analyses. It is opposed to the *in situ* sampling, where gases measurements are directly done into the flame (place of gases formation) or in smoke. In the context of fire safety, extractive methods are well developed (Fardell and Guillaume (2010)):

- Direct continous analysis:
  - from a non-dispersive infrared spectroscopy (NDIR) for carbon monoxide and carbon dioxide,
  - from a Fourier transform infrared spectroscopy (FTIR) for many inorganic and organic species,
  - from a paramagnetic analyser for oxygen.

- Indirect analysis from a gas chromatography (GC) or GC coupled with a mass spectrometer (GC-MS) for inorganic and organic species.
- Trapping by a liquid or by a solid (adsorbent or absorbent) followed by GC, ILC, HPLC or classical analytical chemistry.
- Collected in an inert bag by chemiluminescence method for oxides of nitrogen.

More infomation about sampling and analysis fire effluents are available in the ISO 19701 (2013) standard. The technique of FTIR analyser (ISO 19702 (2006)) is further detailed in the following section.

3.1.6.2 FTIR analyser

For some years now, one of the most widely used gases analyser has been on-line FTIR because it is capable to directly and quasi-continuously qualify and quantity many type of organic compounds. In this study, both the cone calorimeter and the smoke box tests have been coupled with a FTIR analyser. The sampling line between the fire test and the FTIR should respect specific tests conditions such as (Fardell and Guillaume (2010) and ISO 19702 (2006)):

- be inert to the analysed species,
- be heated at around 170°C to reduce condensation of analysed species,
- be as short as possible to minimise losses,
- have a high extract velocity to limit the residence time of analysed species into the sampling line.

The FTIR principle is summarized on figure 3.11.

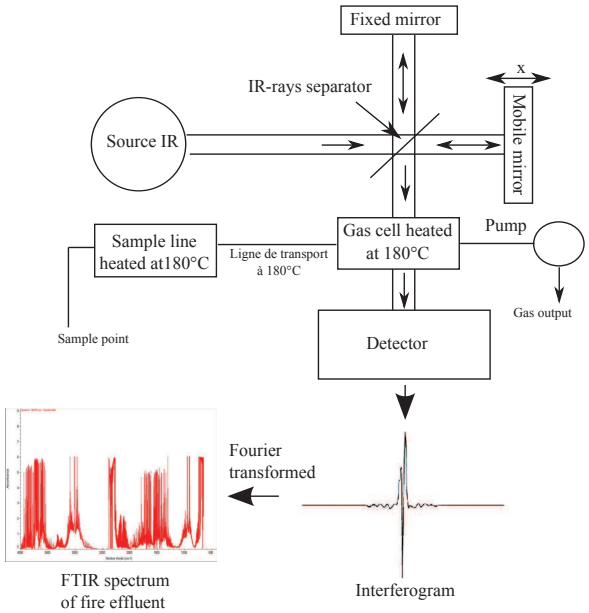

Figure 3.11: Principle of FTIR analyser

An infrared (IR) radiation is introduced in a gas cell (figure 3.11). In this study, this gas cell has an optical path of 10 m through a mirror system. The analysed species in the fire effluent absorb the IR radiation (650 up to 4000 cm^{-1}). The absorbed energy by species implies molecule vibrations. These vibrations can be translated by atomic rotations or bonds vibrations. Then, the IR rays (for which some wavelengths have been absorbed by gases species) go out from the gas cell through the interferometer. The role of the interferometer is to transform the IR rays in interferogram. This one is detected by a *Mercure-Cadmium-Telluride* detector. Finally, a FTIR spectrum is obtained by a Fourier Transformed operation of the interferogram every 4 seconds during the test time period, in this study. The spectrum is considered as the sign of the species of a given range wavelength. More details of FTIR principle are available on references Fardell and Guillaume (2010) and Stec *et al.* (2011).

The FTIR spectrum allows to qualify and quantify the gases studied(table 3.2) of the fire effluent.

Table 3.2: Range and quantitative analyses of gases from FTIR (with the gas cell heated at 180°C and an optical path of 10 m, MCT detector.

	Gases	Low limit [ppm]
CO	Carbon monoxide	2.7
CO_2	Carbon dioxide	62.2
H_2O	Water	21.1
HCl	Hydrogen chloride	4.1
HBr	Hydrogen bromide	4.7
HCN	Hydrogen cyanide	2.8
$HCOH$	Formaldehyde	19.8
NO	Nitrogen oxide	3.6
NO_2	Nitrogen dioxide	4
NH_3	Ammonia	0.3
N_2O	Nitrous oxide	10.7
SO_2	Sulfur dioxide	11.4

An example of FTIR spectrum is presented in figure 3.12.

The identification of gases species is based on the comparison of the unknown analysed spectrum with a library of known spectra. The difficulty of this method is when two species spectrum overlap each ones. The quantitative analysis requires a calibration spectra obtained from a previous range of calibrations tests of each studied species (Saragoza *et al.* (2009)). Another difficulty is to anticipate the concentration range of analysed fire species effluents.

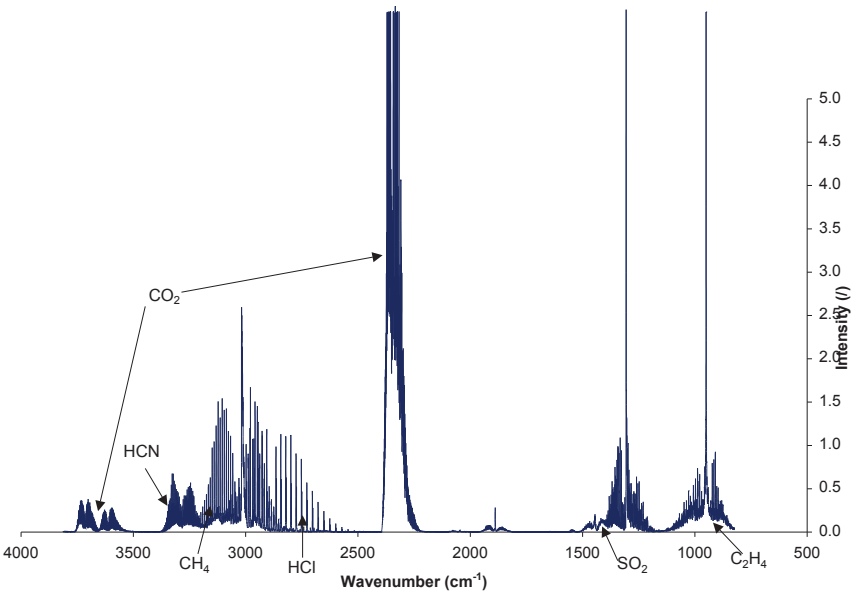

Figure 3.12: Example of a FTIR spectrum of a fire effluent

All tests from raw matter to real scale have been performed in the context of the Transfeu project. Concerning the studied seat and the wall panel products, tests have been conducted according to different European fire laboratories:

- Raw matter tests: Sveriges Tekniska Forskningsinstitut (SP) in Sweden
- Material tests: LSFire in Italy and Laboratoire National de métrologie et d'essais (LNE) in France
- Semi-finished tests: Laboratoire National de métrologie et d'essais (LNE) in France
- Finished tests: Sveriges Tekniska Forskningsinstitut (SP) in Sweden
- Real tests: RATP laboratory in France, Laboratoire National de métrologie et d'essais (LNE) in France, LSFire and Trenitalia in Italy.

3.2 Numerical tools

Two different tools are presented. The first one is intended to solve the thermal decomposition model and to estimate the pyrolysis parameters. The second one is designed to model the reaction-to-fire of a design fire scenario.

3.2.1 Numerical tool used at matter scale

Two main methods can be used to estimate the pyrolysis parameters linked to the thermal decomposition model (Guillaume (2013)):

- direct method (isoconverional) and
- indirect method.

Information about the direct method can be found in the literature section. In this thesis, the indirect method and especially the Genetic Algorithms, optimisation method is used to estimate the pyrolysis parameters.

3.2.1.1 Indirect method

The indirect method is a numerical optimisation method. For some years now, the fire community has used genetic algorithms (GA) as a numerical optimisation tool (Rein (2005), Lautenberger (2007), Bustamante Valencia (2009) and Matala and Hostikka (2011)). The GA is a tool that use the principles of Darwinian evolution to seek an optimal solution to a problem via a large number of adjustable parameters. These algorithms allow to estimate pyrolysis parameters for the raw matter scale (figure 3.13) according to the reaction mechanism of the raw matter decomposition and the thermal decomposition model. These pyrolysis parameters are used as input data to a reaction-to-fire model.

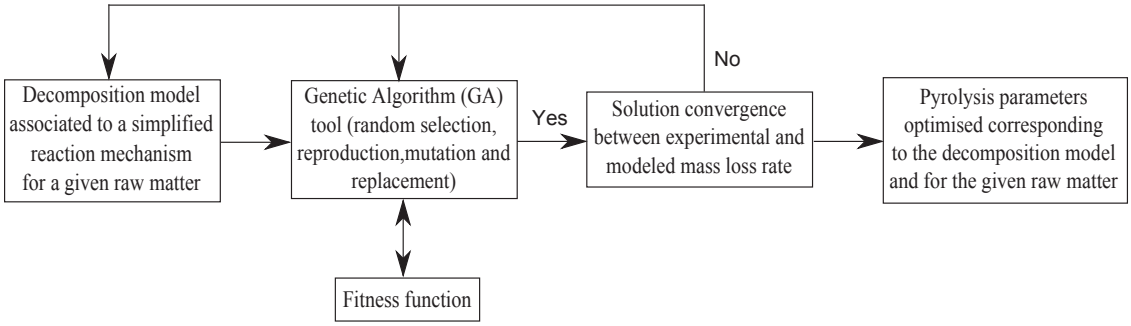

Figure 3.13: Numerical optimisation method

The GA are a pseudo-random number generator. An *individual* represents the set of parameters to optimise. The *population* is the entire group of candidates solution. The initial *population* corresponds to the first *generation*. First, the fitness function is evaluated for each *individual*. Then, the offspring of the first generation corresponds to the second generation. The following generations are obtained successively by a reproduction process through the GA and the fitness function. The higher fitness are selected for the reproduction process. This process is composed of the reproduction, the mutation and the replacement steps and more details are available in Lautenberger (2007).

It is important to note that the pyrolysis parameters optimisation is sensitive to the nature of the fitness function used.

3.2.1.2 Fitness function and comparison points approach

The fitness function can be defined as an analysis of a comparison between experimental points and modelled values. The method used is based on functional analysis study of Hilbert works in 1928 (Hilbert *et al.* (1928)). The following explanation comes from the

reference Peacock *et al.* (1999). The comparison of two time-dependent curves is more difficult than a single point. Each curve is represented as a multi-n-dimensional vectors noted (x_1,x_2,..., x_n) for n data. $\| \overrightarrow{x} \|$ norm defines the length of the vector $\overrightarrow{x}$. The distance between two vectors is the norm of the vectors difference, $\| \overrightarrow{x} - \overrightarrow{y} \|$. Moreover, the relative difference is noted as $\| \overrightarrow{x} - \overrightarrow{y} \| / \| \overrightarrow{x} \|$. In this study, the relative difference expresses the difference between experimental data ($\overrightarrow{x}$) and the model prediction ($\overrightarrow{y}$). Additionally, an other important vector comparison is the angle between two vectors. The inner product of two vectors is the product of the length of the two vectors and the cosine of the angle between them (Eq 3.1).

$$\langle \overrightarrow{x}, \overrightarrow{y} \rangle = \cos\left[\angle(\overrightarrow{x}, \overrightarrow{y})\right] \| \overrightarrow{x} \| \| \overrightarrow{y} \| \tag{3.1}$$

Finally, the fitness function applied in the GA method, in the present study, is presented in Eq 3.2.

$$\phi = \sum_{\beta=0}^{c} \left[cos\left[\angle\left(\overrightarrow{x}, \overrightarrow{y}\right)\right] \left[\frac{\| \overrightarrow{x} - \overrightarrow{y} \|}{\| \overrightarrow{x} \|} \right]^{-1} \right]_{\beta} \tag{3.2}$$

The fitness function is composed of a norm and an inner product. According to the equation 3.2, the principle is to maximise the ϕ value in order to minimise the relative shift between experimental and modelled curves.

A parametric study on different fitness functions was performed by LNE but the work is not published yet. This study tested three different fitness functions with the same parameter range and the same number of *population* and *generation*. All of the three fitness functions follow equation 3.2. The difference between each function is the mathematical expressions of the norm and the inner product. The norm and the inner product of the Euclidean fitness function, noted as $F1$, is presented in equation 3.3. This function puts the emphasis on the distance between two vectors.

$$F1 \left\{ \| \overrightarrow{x} \| = \left(\sum_{i=1}^{n} x_i^2 \right)^{1/2} ; \langle \overrightarrow{x}, \overrightarrow{y} \rangle = \sum_{i=1}^{n} x_i y_i \right. \tag{3.3}$$

The norm and the inner product of the Hellinger fitness function, noted $F2$, is presented in equation 3.4. This function puts the emphasis on the phase angle between two vectors.

$$F2 \left\{ \| \overrightarrow{x} \| = \left(\sum_{i=2}^{n} \left(\frac{x_i - x_{i-1}}{t_i - t_{i-1}} \right)^2 \right)^{1/2} ; \langle \overrightarrow{x}, \overrightarrow{y} \rangle = \sum_{i=2}^{n} \frac{(x_i - x_{i-1})(y_i - y_{i-1})}{(t_i - t_{i-1})^2} \right. \tag{3.4}$$

The norm and the inner product of the Hellinger and Euclidean fitness function, noted $F3$, is presented in equation 3.5. This function employs the norm of the Euclidean function and the sum of the inner products of the two previous functions. The advantages of both functions $F1$ and $F2$ are kept. However, the calculation time is longer than for $F1$ and $F2$ functions.

$$F3 \left\{ \| \overrightarrow{x} \| = \left(\sum_{i=1}^{n} x_i^2 \right)^{1/2} ; \langle \overrightarrow{x}, \overrightarrow{y} \rangle = \frac{1}{n} \sum_{i=1}^{n} x_i y_i + \frac{1}{n-1} \sum_{i=2}^{n} \frac{(x_i - x_{i-1})(y_i - y_{i-1})}{(t_i - t_{i-1})^2} \right. \tag{3.5}$$

The comparison of the best optimised solution of the mass loss rate is presented on figures 3.14.

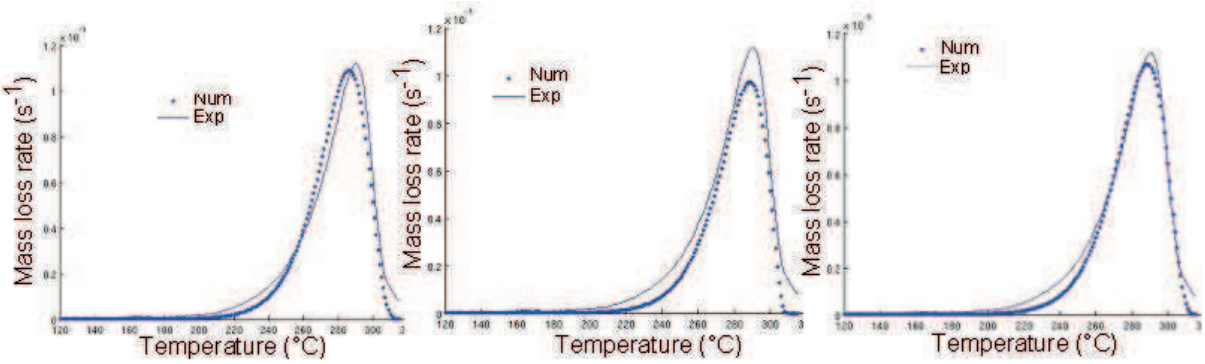

Figure 3.14: Optimised solution of the mass loss rate, from the left to the right: solution with $F1$, $F2$ and $F3$

Concerning results of function $F1$, it shows that the experimental and modelled intensity values of the MLR are similar but a difference of the phase angle is noteworthy. The inverse trend is observed on results obtained with function $F2$. The comparison from function $F3$ is the best one because the distance and the phase angle between the experimental and the modelled MLR values are very small. However, the calculation time for function $F3$ is longer than the one for function $F2$ and is itself longer than the one for function $F1$.

The fitness function $F1$ appears then to be the best compromise between the result accuracy and the computer time period calculation. Bustamante Valencia (2009) tested also two different fitness functions, the least square function and the first fitness function studied previously (F1). He reported also that the best optimized solution was obtained with the fitness function (F1). Moreover, research on sensitivity analysis on the thermal decomposition model are still in progress (Batiot *et al.* (2012)).

The FDS code validation implies a comparison between experimental measurements and numerical data from material to real scales. Considering these results on the fitness functions, the Euclidean function (F1) is used as a functional analysis comparison for all the results obtained at upper scales.

3.2.2 Reaction-to-fire modelling tool

Physical fire phenomena are very complex and often dependent on each other. The most encountered phenomena are the study of flow, the turbulence, the heat transfer (radiative, convective and conductive), the combustion and the pyrolysis processes. The modelling and the simulation of these phenomena are a great challenge because of the limitations due to the physics understanding and the power calculation available (Guillaume (2013)). Despite these limitations, it is now possible to simulate a fire according to several models adapted to different hypothesis. The whole models presented in this section are available in Fire Dynamic Simulator (FDS Version 5.5.3) but also in other numerical code, such as

OpenFoam (OpenFoam (2004)).

3.2.3 Conservative equations

Nowadays, the fire community uses a Computational Fluid Dynamic (CFD) where models are solved into a domain of a high number of control volumes (or called *meshes*). Each mesh is associated to several unknown physical quantities (density ρ, three components of the velocity $\overrightarrow{u}_{(x,y,z)}$, temperature T and pressure p). The goal is then to find a numerical solution, for each unsteady mesh, through the Navier Stokes equations. The Navier Stokes equations group together the conservation of momentum (Eq 3.8), the conservation of energy (Eq 3.9), the conservation of mass and species (Eq 3.6 and 3.7) and additional boundaries conditions. The FDS conservative equations are introduced below:

Continuity equation

$$\frac{\partial \rho}{\partial t} + \nabla \cdot \rho \overrightarrow{u} = 0 \tag{3.6}$$

Species conservation equation

$$\frac{\partial (\rho Y_i)}{\partial t} + \nabla \cdot \rho Y_i \overrightarrow{u} = \nabla \cdot \rho D_i \nabla Y_i + \dot{m}_i''' \tag{3.7}$$

Momentum conservation equation

$$\rho \left[\frac{\partial \overrightarrow{u}}{\partial t} + \left(\overrightarrow{u} \cdot \nabla \right) \overrightarrow{u} \right] + \nabla p = \rho \overrightarrow{g} + \overrightarrow{f} + \nabla \cdot \tau \tag{3.8}$$

Energy conservation equation

$$\rho \frac{Dh}{Dt} = \frac{\partial \left(\rho h \right)}{\partial t} + \nabla \cdot \left(\rho h \overrightarrow{u} \right) = \frac{Dp}{Dt} + \nabla \cdot \lambda \nabla T + \nabla \cdot \sum_{I=1}^{N} h_i \rho D_i \nabla Y_k - \nabla \cdot \overrightarrow{q_r} + \dot{Q}''' \tag{3.9}$$

A state equation id added to the Navier Stokes conservative equations, which assumes that mixed gases are perfect:

$$p = \rho \frac{R}{M} T \tag{3.10}$$

A finite difference technique is used to discretize the partial differential equations. Considering the involved flow momentum during the combustion process, the assumption of low Mach number of the Navier Stokes equations (developed by Rehm and Baum (1978)) is used in the CFD models (McGrattan *et al.* (2010)). The Low Mach number ($M = \mid \overrightarrow{u} \mid / c \ll 1$) considers that the flow momentums that is much smaller than the speed of sound. All spatial derivatives are approximated by a second-order central difference and the flow variables are updated using an explicit second-order Runge-Kutta schema. The numerical resolution of a low Mach number model first implies to calculate the divergence of the flow velocities and then to calculate the pressure perturbations through the divergence of the conservation of momentum.

The flow velocity for each given mesh is solved through the momentum conservation and the *Poisson* equations. Moreover, velocity perturbations inside the mesh can not be resolved directly, but they are filtered with a *sub-mesh* model. This *sub-mesh* model expresses the influence of flow velocity at the mesh scale on the flow velocity inside a mesh. The *sub-mesh* can be modelled with a Smagorinsky model through large eddy simulation (LES) model. This model resolves the velocity perturbations by taking into account several relations of the turbulent viscosity (μ_t). McGrattan *et al.* (2010) reported that the LES model weakness is the resolution of the fluid flow close to the solid side.

Furthermore, the stability condition of the numerical schemas must respect the Courant-Friedrichs-Lewy (CFL) condition, which asserts that the solution of the equations cannot be updated with a time step larger than the one allowing a parcel of fluid to cross a mesh McGrattan *et al.* (2010)). Another Von Neumann criteria exists only for small mesh size (smaller than 5 mm).

The resolution of the momentum conservation equation requires also the resolution of energy conservation via several models of heat transfers:

- The radiative transfer model in the gas phase,
- The convective transfer model in the gas phase,
- The conductive transfer model in the solid phase.

The radiative transfer is solved with the radiative transfer equation (RTE) through the use of a Finite Volume method (McGrattan *et al.* (2010)). A number of 100 angles is used to solve the RTE. The spectral dependence of the RTE can not be accurately calculated. Thus, the radiation spectrum is divided by N small number of spectral bands. This spectrum separation of N bands allows to estimate the absorption coefficient of the gas phase which is function of the gas phase composition, concentration and temperature. In this study, the grey gas model is used with $N = 1$.

The convective heat transfer corresponds to the maximum value of either natural or forced convective correlation (see McGrattan *et al.* (2010)).

The conductive heat transfer is obtained with an energy balance in one direction at the surface of the solid phase and the Fourier's law. The resolution of this energy balance requires boundaries conditions and the estimation of energy sources (via a radiative solid transfer, pyrolysis and combustion models). The next section details the pyrolysis and the combustion model implemented in FDS code.

3.2.4 Pyrolysis model

The quantity of energy released (3.11) from the solid phase during thermal decomposition and then the pyrolysis process is highly dependent of the normalised reaction rate ($\dot{\omega}_{\alpha\beta}$) of the material component α and the associated heat of reaction of β reaction ($H_{\dot{\omega},\alpha\beta}$).

Pyrolysis equation

$$\dot{q}_{pyr}^{'''}(x) = -\rho_{s0} \sum_{\alpha=1}^{N_m} \sum_{\beta=1}^{N_{r,\alpha}} \dot{\omega}_{\alpha\beta}(x) H_{\dot{\omega},\alpha\beta} \tag{3.11}$$

The major assumption concerning the solid is that its volume is constant during all the simulation period time. This hypothesis implies that only the material mass loss can evolves during the conductive heat transfer. The other assumptions of the pyrolysis model are:

- Instantaneous release of volatiles from solid to the gas phase,
- Local thermal equilibrium between the solid and the volatiles,
- No condensation of gaseous products,
- No porosity effects,
- No physical change of the solid phase.

The reaction rate model is expressed as the equation 3.12 and it relies on the Arrehnius law and the local mass yield of a component α:

Reaction rate equation

$$\dot{\omega}_{\alpha\beta} = \left(\frac{\rho_{s,\alpha}}{\rho_{s,0}}\right)^{n_{s,\alpha\beta}} A_{\alpha\beta} exp\left(-\frac{E_{a,\alpha\beta}}{RT_s}\right) \tag{3.12}$$

This equation is function of the number of reactions for each component present inside a material. The estimation of the sets of pyrolysis parameters are driven as explained in the previous section about the raw matter scale. The literature data are often used to estimate the heat of reaction. This material reaction rate is function of the available mass of fuel used in the combustion model.

3.2.5 Combustion model

The combustion model is based on the mixture fraction (Z) model. Z is as a linear combination of fuel and oxygen mass fractions. The mixture fraction is a function of space and time. It can be assumed that, upon mixing, the reaction of fuel and oxygen occurs rapidly and completely, the combustion process is referred to a *mixing-controlled*. Into a mesh, fuel and oxygen can not co-exist. At the two meshes isosurface and if the $Z(x,t) \geqslant Z_f$, the unique reaction occurs if conditions are favourable, i.e. if the oxygen volume fraction and the gas temperature are in the correct space according to the FDS technical User Guide, the reaction is allowed to take place (McGrattan *et al.* (2010)). At the flame surface, equations 3.13 are considered:

$$Z(x,t) = Z_f; Z_f = \frac{Y_{O_2}^{\infty}}{sY_F^I + Y_{O_2}^{\infty}}; s = \frac{\nu_{O_2} M_{O_2}}{\nu_{fuel} M_{fuel}} \tag{3.13}$$

The terms$Y_{O_2}^{\infty}$ and Y_F^I represent respectively the ambient mass fraction of oxygen and the fuel mass fraction onto the flow. Mass fractions of all species (such asCO_2 and CO) are related to the mixture fraction Z via a *state-relations*. However, it is assumed that the mass fractions of CO and soot are fixed. This *state-relations* is built according to the stoichiometry coefficient of the combustion reaction.

For instance, for an instantaneous propane combustion, the one-step combustion reaction is expressed as

$$CH_{2.67} + \nu_{O_2}O_2 + \nu_{N_2}N_2 \longrightarrow \nu_{CO_2}CO_2 + \nu_{H_2O}H_2O + \nu_{CO}CO + \nu_{C_{Soot}}C_{Soot} + \nu_{N_2}N_2$$

with
$\nu_{fuel} = 1$, $\nu_{O_2} = 1.636$, $\nu_{CO_2} = 0.968$, $\nu_{H_2O} = 1.333$, $\nu_{CO} = 0.003$, $\nu_{C_{Soot}} = 0.032$, $\nu_{N_2} = 13.611$
Thus, propane *state-relations* are obtained on figure 3.15 with the relation of mass fractions and the mixture fraction at the flame surface Z_f:

$$Y_k = \left[\frac{m_k}{m_{fuel}} \times \frac{m_{fuel}}{m_{air}}\right]_{st} = \frac{\nu_k M_k}{\nu_{fuel} M_{fuel}} \times \frac{\nu_{fuel} M_{fuel}}{\nu_{air} M_{air}} = \frac{\nu_k M_k}{\nu_{air} M_{air}} \tag{3.14}$$

and

$$s = \frac{\nu_{O_2} M_{O_2}}{\nu_{fuel} M_{fuel}} = \frac{1.636 \times 32}{1 \times 14.67} = 3.569$$

$$Z_f = \frac{0.23}{3.569 \times 1 + 0.23} = 0.060$$

The mixture fraction satisfies the conservation transport equation (the diffusivity coefficient is assumed the same for each species):

$$\frac{\partial (\rho Z)}{\partial t} + \nabla \cdot \rho Z u = \nabla \cdot \rho D \nabla Z \tag{3.15}$$

The one step combustion reaction is supposed to reproduce a fire in a large space (fire condition: fire well-ventilated). In order to reproduce the under-ventilated fire, where CO and soot have higher concentrations, a two steps combustion reaction is proposed in FDS:

$$C_x H_y O_z N_a X_b + \nu'_{O_2} O_2 \longrightarrow \nu_{H_2O} H_2O + \left(\nu_{CO} + \nu'_{CO}\right) CO + \nu_{C_{Soot}} C_{Soot} + \nu_{N_2} N_2 + \nu_X X$$

$$\nu'_{CO} \left(CO + \frac{1}{2} O_2 \longrightarrow CO_2\right)$$

The heat release rate in the gas phase is calculated with the production of fuel, the effective heat of combustion of the fuel and the turbulent diffusivity (link to the LES model).

Considering this combustion model, the main limit is that only one solid fuel is going to burn even if several types of solid fuels are present into the simulation. However, it is possible to take into account different effective heats of combustion of different fuels via the pyrolysis model. As a first step, only the one-step combustion reaction is used in this

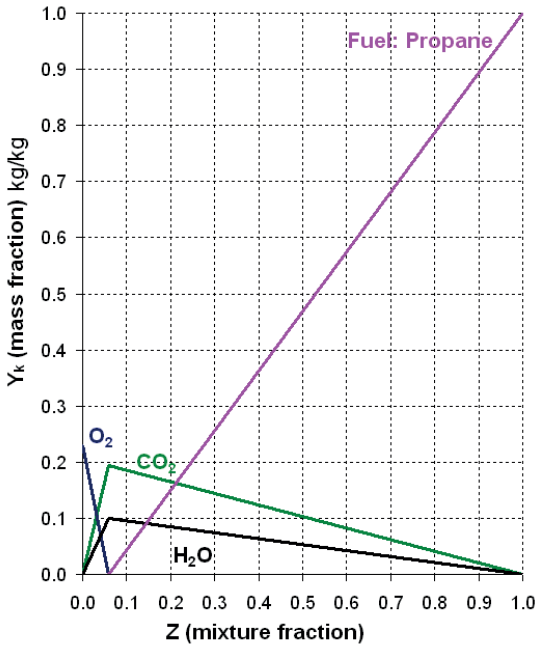

Figure 3.15: Propane state-relations

work.

Indeed, the total available fuel mass fraction is corrected by an effective heat of combustion ratio ($\frac{\triangle H_{c,material}}{\triangle H_{c,reaction}}$) just before to being multiplied by the effective heat of combustion of the fuel reaction. But the stoichiometry of the one step or the two-step combustion reactions still corresponds to one fuel.

The principal hypothesis of each model are summed up in table 3.3.

Table 3.3: Major models assumptions

Models	**Assumptions**
Navier Stokes equations	Low Mach number flow Second order accurate finite difference approximation Predictor/corrector method Poisson equation with a direct solver Large eddy simulation, Smagorinsky model
Combustion model	Diffusion flame Mixture fraction model Mixing controlled combustion Global (one step or two steps) combustion reaction Chemistry infinitely fast Choice of one fuel among the fire scenario
Radiative model	Radiative transfer equation Finite volume method Gray gases no dispersive (model at 1, 6 or 9 spectral bands) Usage of multiple number of solid angles
Pyrolysis model	Arrhenius relation Simple or multi-steps reaction mechanism Physical change of the solid phase not taken into account (melting, delamination...) No porosity effect
Boundaries	1D thermal transfer at each mesh surface Thermal properties dependent on temperature Heat transfer based on empiric correlations

The used numerical CFD tool (FDS) in this thesis is the same from the material up to the real scale. The general fire modelling code, Fire Dynamics Simulator (FDS) is widely used in the fire science and fire engineering communities. Furthermore its usage and its code are free. FDS is developed in partnership between NIST (USA) and VTT (Finland), (Transfeu partner). The version 5.5.3 was accepted, as a fire numerical tool, by all Transfeu partners.

Chapter 4

Multi-scale comparison results on railway seat

Contents

4.1 Raw matter scale

Before analysing the thermal decomposition of each layer of the railway seat composition, it is important to remind that the cover is a mix of wool, viscose and aramide, as well as the interliner which is also an aramide textile, and the foam is composed of polyurethane and melamine.

As already explained in the multi-scale approach chapter, the objective is to model the

mass loss rate of each component of the seat, via an indirect method, in order to optimise the pyrolysis parameters. This optimisation is based on the experimental mass loss rate data. That's why it is important to estimate the experiment uncertainties. In 1994, the decomposition of calciumoxalate monohydrate as a three-steps reaction has been investigated by thirteen laboratories using the TGA (Andersona *et al.* (1999)). The authors shown that the maximal relative mass loss deviation (or the reproducibility) equals up to 7% in nitrogen atmosphere and to 2% in air atmosphere.

4.1.1 Cover

The TGA results of the normalised mass loss and mass loss rate (MLR) of the cover under air and nitrogen atmospheres for two heating rates (5 and 10 K/min) are presented on figure 4.1.

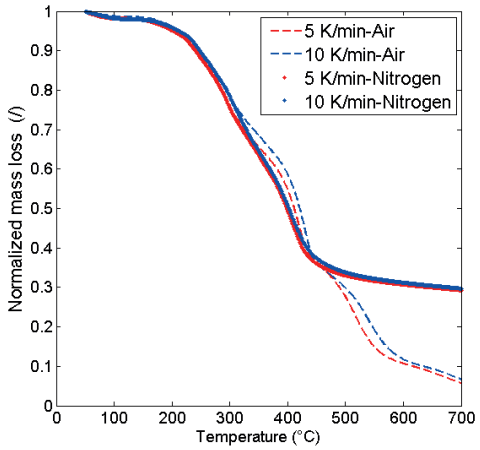

a/ Normalised mass loss results of the cover.

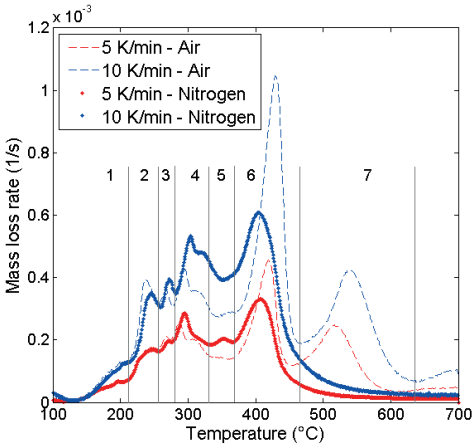

b/ Normalised mass loss rate results of the cover.

Figure 4.1: Thermal decomposition of the cover under air and nitrogen atmospheres for two different heating rates 5 and 10 K/min.

During a thermal analysis study at this scale, it is assumed that one peak of the mass loss rate corresponds to one reaction or group of reactions of the polymer (Torero (2008)). The thermal decomposition analysis of the cover is complex because many peaks and shoulders are identified under air and nitrogen atmospheres (figure 4.1 b). Each peak is not well separated from each others. This difficulty is linked to the number and the nature of the different compounds present in the cover material (wool, viscose and aramide).

Under nitrogen atmosphere, six peaks or shoulders are visually observed on figures 4.1 b. According to the literature part and figure 4.1 b, it is possible to define 6 reactions or groups:

- Between 120 and 220°C: the mass loss rate of the cover begins to increase and reaches a maximum around 200°C. This mass loss rate increase corresponds to a mass loss around 5% of the total mass. This mass loss until 200°C is associated to water dehydration.

- Between 220 and 280°C, the mass loss rate suddenly increases until around 240°C and then decreases. Around 10°C later, the mass loss rate raises to reach a peak at 260°C and then decreases. These two mass loss steps could involve a group of reactions: the wool is cleaved into several amino acids and then decomposes into a char.
- Between 280 and 330°C: the mass loss rate accelerates and reaches a peak at 290°C and then decreases slowly until 300°C. During this step, it is probable that the wool finishes to decompose. Moreover, the viscose composition is close to the cellulose. Thus, this step may be linked to the beginning of cellulose decomposition.
- Between 330 and 380°C: the mass loss rate is almost constant for this temperature range. This step can correspond to the end of the viscose decomposition. It should be reminded that the decomposition temperature is around 350°C (Horrocks and Kandola (2004)) for the viscose.
- Between 375 and 450°C: the mass loss rate increases until it reaches a peak at 400°C and then decreases until the end of decomposition. Within this temperature range, this step is characteristic of the aramide decomposition (formation of char) (Horrocks (1996)).

According to the figure 4.1b, for both atmospheres, the higher is the heating rate and the more the MLR intensity is visually observed. Furthermore, the same number of peaks or shoulders and the same kinetic are observed at 5 and 10K/min. 30% of the virgin mass remains in the crucible after thermal decomposition. The residual mass fraction at 700°C is five times more important under nitrogen than under air atmosphere.

Under air atmosphere, seven reactions are identified (4.1 b):

- Between 120 and 330°C: The mass loss rate increases and decreases suddenly and successively. Four peaks are visible, one for water dehydration and the last three for wool decomposition. The same steps are identified under nitrogen atmosphere. This part of the decomposition kinetic is not influenced by the presence of oxygen.
- Between 330 and 375°C: the mass loss rate remains constant but its intensity between this temperature range is higher under nitrogen atmosphere than under air atmosphere. Oxygen has an influence on viscose decomposition. This step is associated to viscose decomposition. The presence of oxygen could have an impact on viscose decomposition.
- Between 375 and 450°C: the mass loss rate suddenly increases until it reaches a peak around 405°C and then decreases until 450°C. The kinetic and the temperature peak are the same at 5 and 10K/min. This step corresponds to aramide decomposition (formation of char). Moreover, the peak temperature under air atmosphere (T=405°C) is lightly deviated to the high temperature compared with the peak temperature under nitrogen atmosphere (T=400°C). Furthermore, the intensity of the mass loss rate is higher under air atmosphere than under nitrogen atmosphere. Thus, the presence of oxygen has also an influence on aramide decomposition.

- Between 450 and 600°C: the mass loss rate increases until it reaches a peak around 550°C and then decreases until the end of decomposition. This last step does not happen under nitrogen atmosphere. This reaction is due to the charcoal oxidation. Moreover a shift to high temperatures is observed concerning the oxidation reaction (Mehrabian *et al.* (2012)). The oxygen diffusion may control the decomposition kinetic of the raw matter (Marquis (2010). Around 22% of the virgin mass corresponds to the char oxidation. Around 8% of the virgin mass remains into the crucible at 700°C.

For both atmospheres, the number of peaks and the kinetic of the MLR are similar, except for the last peak under air atmosphere (char oxidation).

It is important to remind that the final objective at this scale is to model the fuel mass production rate of the fuel available for combustion. In this sense, the first step of decomposition, that is to say water dehydration, is not taken into account. Thus, without the water dehydration step, five and six main steps are observed respectively under nitrogen and air atmosphere. The lumped parameter approach (LPA) has been chosen to represent the reaction mechanism of the cover (wool + viscose + aramide) because it is composed of three different polymers. According to the previous description of the MLR and the literature chapter on the cover decomposition (Hirschler and Morgan (2008), Horrocks (1996), Popescu *et al.* (1995) and Horrocks and Kandola (2004)), some steps are grouped to simplify the reaction mechanism. The TGA curves description allows to assess that each cover component decomposes regardless of the others in distinct temperature ranges. It is assumed that wool decomposes between 220 and 330°C, viscose between 330 and 380°C and aramide between 375 and 450°C.

In this context, the three first reactions, supposed to be link to the wool decomposition, are grouped to form the first global wool reaction or step between 220 and 330°C (first step, figure 4.2). This global step is not influenced by the presence of oxygen and formed a new intermediate species, named α - Cover (composed of modified wool, virgin viscose and virgin aramide). The second step is associated to the decomposition of α - Cover into β - Cover (figure 4.2) between 330 and 380°C. Due the few information on viscose and the TGA curves description, the second step is correlated to its decomposition. The new intermediate species β - Cover is composed of modified wool, modified viscose and virgin aramide. The next decomposition step corresponds to the formation of char from the species group β - Cover because of its temperature ranging between 375 and 450°C (figure 4.2). Under oxygen atmosphere, the species α - Cover is transformed into char because viscose decomposes in char after 300°C (Fateh (2011)). Moreover, the fifth step represents the formation of char from the β - Cover because polyamide and wool decompose into char within this temperature range (375 and 450°C). The last one is only present under air atmosphere: it is the oxidation of the char. To sum up, three and four global steps happen respectively under nitrogen and air atmosphere. This global reaction mechanism is summarized in the schema 4.2 and is translated in table 4.1 where $Y_{r,t/o,j}$ is the residual mass fraction of the product j of a thermal or a termo-oxidative decomposition reaction.

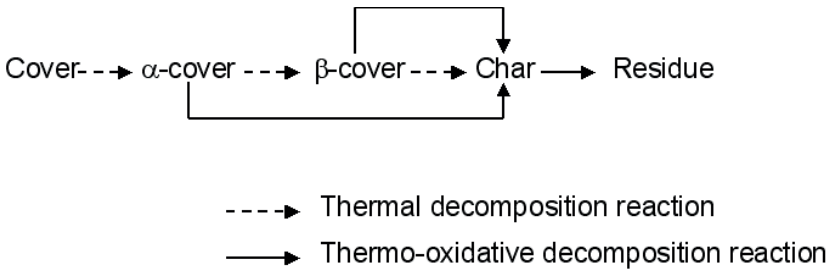

Figure 4.2: Reaction mechanism of the cover

Table 4.1: Reaction mechanism of thermal and thermo-oxidative decomposition of the seat cover.

Number of reaction	**Type of reaction**	**Reagents**		**Products**		
1	Thermal	Cover	$\rightarrow$	$Y_{r,t,c}$ α - Cover	+	$(1 - Y_{r,t,c})$ gases
2	Thermal	α - Cover	$\rightarrow$	$Y_{r,t,\alpha-c}$ β - Cover	+	$(1 - Y_{r,t,\alpha-c})$ gases
3	Thermal	β - Cover	$\rightarrow$	$Y_{r,t,\beta-c}$ Char	+	$(1 - Y_{r,t,\beta-c})$ gases
4	Thermo oxidative	α - Cover + O_2	$\rightarrow$	$Y_{r,o,\alpha-c}$ Char	+	$(1 - Y_{r,o,\alpha-c})$ gases
5	Thermo oxidative	β - Cover + O_2	$\rightarrow$	$Y_{r,o,\beta-c}$ Char	+	$(1 - Y_{r,o,\beta-c})$ gases
6	Thermo oxidative	Char + O_2	$\rightarrow$	$Y_{r,o,ch}$ Residue	+	$(1 - Y_{r,o,ch})$ gases

Thermal decomposition modelling follows the equations, explained in the literature part, and the previous reaction mechanism of the cover (table 4.1). The total normalised mass loss rate is the sum of each species normalised mass loss rate:

$$\frac{dY_{tot}}{dt} = \frac{dY_c}{dt} + \frac{dY_{\alpha-c}}{dt} + \frac{dY_{\beta-c}}{dt} + \frac{dY_{ch}}{dt} + \frac{dY_R}{dt} \tag{4.1}$$

where

$$\frac{dY_c}{dt} = -\dot{\omega}_1 \tag{4.2}$$

$$\frac{dY_{\alpha-c}}{dt} = Y_{r,t,c}\dot{\omega}_1 - \dot{\omega}_2 - \dot{\omega}_4 \tag{4.3}$$

$$\frac{dY_{\beta-c}}{dt} = Y_{r,t,\alpha-c}\dot{\omega}_2 - \dot{\omega}_3 - \dot{\omega}_5 \tag{4.4}$$

$$\frac{dY_{ch}}{dt} = Y_{r,t,\beta-c}\dot{\omega}_3 + Y_{r,o,\alpha-c}\dot{\omega}_4 + Y_{r,o,\beta-c}\dot{\omega}_5 - \dot{\omega}_6 \tag{4.5}$$

$$\frac{dY_R}{dt} = Y_{r,o,ch}\dot{\omega}_6 \tag{4.6}$$

Finally:

$$\frac{dY_{tot}}{dt} = \sum_{i=0}^{N} \left(Y_{r,i} - 1\right) \dot{\omega}_i \tag{4.7}$$

where

$$\left(\dot{\omega}_i\right) = f\left(\delta\right)^{n^i} A_i exp\left(\frac{-E_{a,i}}{RT}\right) Y_{O_2}^{\delta} \tag{4.8}$$

$$f\left(\delta\right)^{n^i} = \left(Y_j\left(t\right)\right)^{n^i} \tag{4.9}$$

with

$$\text{for thermal reaction } Y_{O_2}^{\delta} = 1 \tag{4.10}$$

$$\text{for thermo oxidative reaction } \begin{matrix} \left(Y_{O_2}^{\delta} = 0\right) \text{ under nitrogen atmosphere} \\ \left(Y_{O_2}^{\delta} = 0.23\right) \text{ under air atmosphere} \end{matrix} \tag{4.11}$$

The unknowns of this equation system, named pyrolysis parameters, are $\left(Y_{r,i}, n_i, A_i, E_{a,i}\right)_{i=1toN}$, with i the number of reactions, thus 24 parameters are unknowns in this case.

4.1.2 Interliner

The component of the interliner is an aramide - polyimide polymer. The TGA results of the normalised mass loss and mass loss rate of the cover under air and nitrogen atmospheres for two heating rates (5 and 10 K/min) are respectively presented in figure 4.3. The interliner remains thermally stable until $400°C$ and is located between the cover and the foam. Its main role is to protect the foam from the flame.
Under nitrogen atmosphere, the number of peaks and the kinetic of the mass loss rate are similar at 5 and 10 K/min. Three major steps are visually identified:

- Between 400 and $470°C$: the mass loss rate increases until it reaches a temperature peak around $440°C$ and then decreases. Within this temperature range, the aramide starts to decompose into carbon oxide and water vapour (Horrocks (1996) and Hirschler and Morgan (2008)).
- Between 470 and $560°C$: the mass loss rate is constant over this temperature period. The modified aramide still continues to decompose and to release gases (Hirschler and Morgan (2008)). In railway domain, it is also possible that the interliner is a mix of aramide and polyimide polymers. Polyimide is thermally stable until $500°C$ and then decomposes in one reaction under inert atmosphere (Chern *et al.* (2009)).

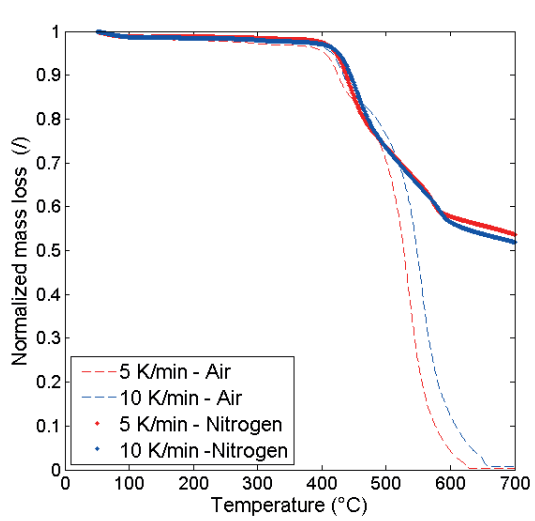

a/ Normalised mass loss results of the cover protection.

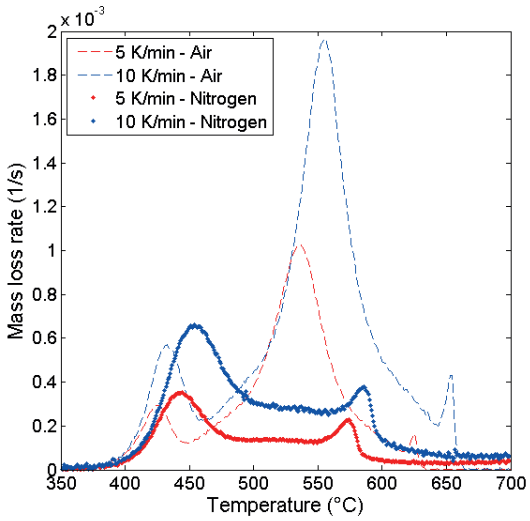

b/ Normalised mass loss rate results of the cover protection.

Figure 4.3: Thermal decomposition of the interliner under air and nitrogen atmospheres for two different heating rates 5 and 10 K/min.

- Between 560 and 590°C: a quick peak (a fast mass loss rate increase and decrease) happens at around 570°C. This short step can be associated to the formation of char and the release of ammonia and hydrogen (Hirschler and Morgan (2008)).

For both atmospheres, the higher are heating rates and the stronger the shift to high temperatures is going to be. An important difference between the two types of atmosphere is the residual mass yield at 700°C: it is 50% higher under nitrogen atmosphere than under air atmosphere.

Under air atmosphere, four major steps have been distinguished:

- Between 400 and 450°C, aramide polymer starts to decompose and release gases, such as water and carbon oxides (Horrocks (1996)) like under nitrogen atmosphere. However, compared to nitrogen atmosphere, the first decomposition reaction starts earlier: the oxygen presence may accelerate the reaction.
- Between 450 and 600°C: the mass loss rate slowly starts to raise around 500°C, then the mass loss rate accelerates suddenly until it reaches a peak around 540°C. After it reached the peak, the mass loss rate decreases quickly first and then more slowly. This two differences about the rate implies that two reactions may occur in parallel. The virgin aramide lost around 80% of its mass during these two concomitant reactions. The modified aramide is oxidized into char and releases gases. This step can be the result of the oxidation of the modified aramide and polyimide.
- Between 640 and 660°C: the mass loss rate suddenly increases and decreases. The maximum mass loss rate is reached around 650°C. This step corresponds to the char oxidation. The crucible is empty at the end of decomposition.

Moreover, shifts through high temperatures with increasing heating rate are visible in the figure 4.3b. This shift has been reported in literature (Torero (2008), Fateh (2011) and

Marquis *et al.* (2012) for instance).

In order to simplify the reaction mechanism, the LPA approach is also used here. To summarize, three and four steps are respectively identified under nitrogen and under oxygen atmosphere. Under nitrogen and oxygen atmosphere, the virgin cover is decomposes into an intermediate species, named α - Interliner and composed of a mixture of modified aramide and virgin polyimide (first step figure 4.4). Then, under nitrogen atmosphere, the second step is supposed to be the decomposition of α - Interliner into β - Interliner, according the TGA curves and the literature review on aramide and polyimide. This new intermediate species is associated to a modified aramide and polyimide polymers. The third step is assumed to be the formation of char at around $570°C$. Between 450 and $600°C$, under oxygen atmosphere, two steps are supposed to occur in parallel: the oxidation of the α - Interliner into β - Interliner and char (figure 4.4) Then, the last step under oxygen atmosphere is assumed to be the char oxidation.

The reaction mechanism of the interliner is presented in figure 4.4 according to previous explanations.

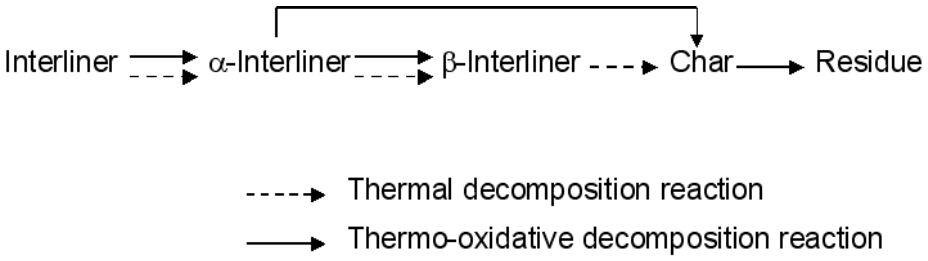

Figure 4.4: Reaction mechanism of the cover protection

This reaction mechanism is summarized in table 4.2.

Table 4.2: Reactions mechanism of the thermal and thermo oxidative decomposition of the cover protection of the seat.

Number of reaction	Type of reaction	Reagents		Products		
1	Thermal	Interliner	$\rightarrow$	$Y_{r,t,In}$ α - Interliner	+	$(1 - Y_{r,t,cp})$ gases
2	Thermal	α - Interliner	$\rightarrow$	$Y_{r,t,\alpha-In}$ β - Interliner	+	$(1 - Y_{r,t,\alpha-In})$ gases
3	Thermal	β - Interliner	$\rightarrow$	$Y_{r,t,\beta-In}$ Residue	+	$(1 - Y_{r,t,\beta-In})$ gases
4	Thermo oxidative	Interliner + O_2	$\rightarrow$	$Y_{r,o,cp}$ α - Interliner	+	$(1 - Y_{r,o,In})$ gases
5	Thermo oxidative	α - Interliner + O_2	$\rightarrow$	$Y_{r,o,\alpha-In}$ Char	+	$(1 - Y_{r,o,\alpha-In})$ gases
6	Thermo oxidative	β - Interliner + O_2	$\rightarrow$	$Y_{r,o,\beta-In}$ Char	+	$(1 - Y_{r,o,\beta-In})$ gases
7	Thermo oxidative	Char + O_2	$\rightarrow$	$Y_{r,o,ch}$ Residue	+	$(1 - Y_{r,o,ch})$ gases

The thermal decomposition model applied to the interliner follows the same equations as explained before (on the cover part): 5.8, 4.8, 5.10 and 4.11. A total of 28 unknowns parameters have to be optimized for the thermal decomposition model of the cover protection under air and nitrogen atmosphere.

4.1.3 Foam

The experimental mass loss and mass loss rate at two heating rates (5 and 10K/min) and under two different atmospheres (nitrogen and air) are showed respectively on figures 4.5a and 4.5b.

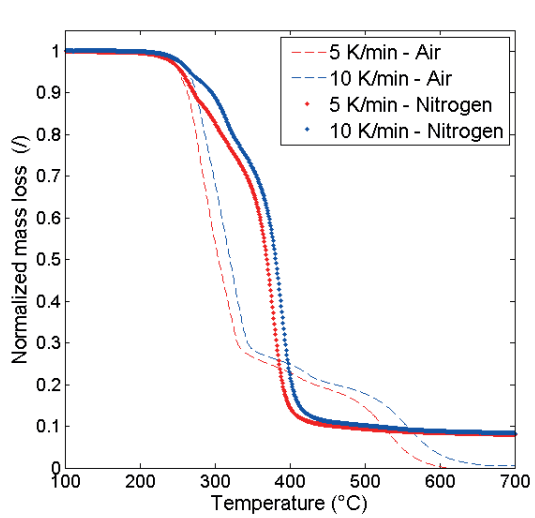

a/ Normalised mass loss results of the foam.

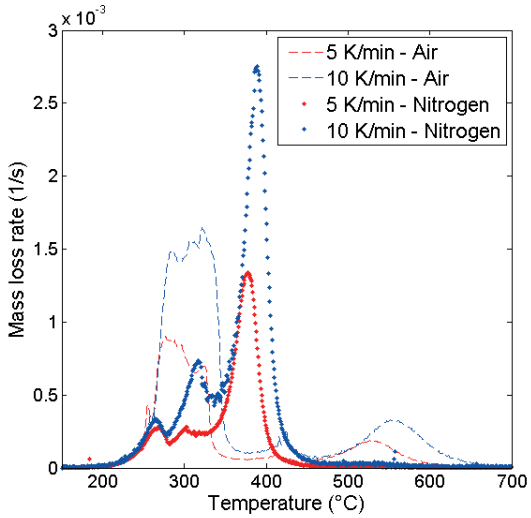

b/ Normalised mass loss rate results of the foam.

Figure 4.5: Thermal decomposition of the foam under air and nitrogen atmospheres for two different heating rates 5 and 10 K/min.

For each TGA atmosphere and for the both heating rates, their decomposition kinetic are very close. Concerning inert atmosphere, three major steps are identified because three peaks of MLR are present:

- Between 220 and 270°C: the mass loss rate begins to increase until it reaches a peak around 260°C and then decreases. Following the thermal reaction mechanism proposed by Konig *et al.* (2009), the melamine sublimates into derivatives melamine products such as melam, melem and melon. Moreover these successive reactions imply the release of ammonia as the following equation (figure 4.6):

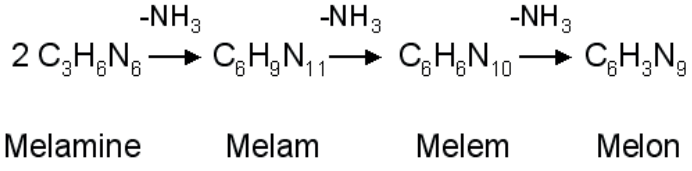

Figure 4.6: Decomposition mechanism of the melamine, Troitzsch (2007)

These successive reactions overlap during this step. Thus, as each melamine derivative product is not clearly distinguished in the figure 4.5, the author has chosen to group all melamine products into one unique reaction in the proposed reaction mechanism (figure 4.7).

- Between 270 and 320°C: the mass loss rate increases until it reaches a temperature peak around 305°C. This step is supposed to be the first reaction of the PU decomposition. The polyurethane dissociates to isocyanate and a condensed phase made of a mix of polyols (Bustamante Valencia (2009), Konig *et al.* (2009) and Rogaume *et al.* (2011)).
- Between 320 and 400°C: the mass loss rate increases until it reaches a temperature peak around 390°C and then decreases until the end of decomposition. This reaction is attributed to the decomposition of the remaining polyols chains (Bustamante Valencia (2009), Konig *et al.* (2009) and Rogaume *et al.* (2011)).

For both atmospheres, the higher are heating rates, the stronger the shift to high temperatures is going to be. Under air atmosphere, two global steps are observed:

- Between 220 and 320°C: the mass loss rate starts to increase until it reaches a stage around 100 °C and then decreases. The presence of this temperature stage shows that several reactions occur in parallel. Thus, it is supposed that the three reactions, that happen under nitrogen atmosphere, are concomitant (Konig *et al.* (2009)) under air atmosphere. The oxygen presence accelerates the sublimation of melamine, the dissociation of PU and finally the decomposition of polyols chains (Rogaume *et al.* (2011)) to form a charcoal.
- Between 500 and 650°C: the last step is the char oxidation.

As many PU thermal decomposition studies have been done, the proposed reaction mechanism uses the model of constituent approach. The reaction mechanism of this foam is summarized in figure 4.7 and table 4.3. It relates to the TGA results, the PU reaction mechanism from Bustamante Valencia (2009) and the foam decomposition mechanism studied by Konig *et al.* (2009). It is composed of three and four major steps respectively under nitrogen and air atmospheres.

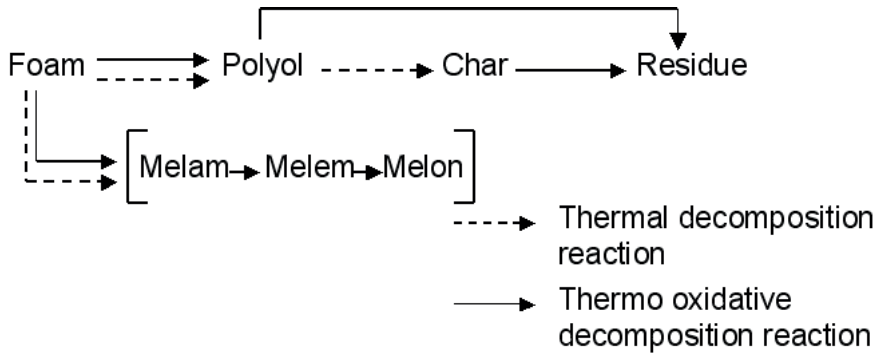

Figure 4.7: Reaction mechanism of the foam

The thermal decomposition model applied to the foam follows the same equations as explained before (on the cover part): 5.8, 4.8, 5.10 and 4.11. A total of 28 unknowns parameters have to be optimized for the thermal decomposition model of the foam under air and nitrogen atmosphere.

Table 4.3: Reaction mechanism of the thermal and thermo oxidative decomposition of the seat foam.

Number of reaction	Type of reaction	Reagents		Products		
1	Thermal	Foam	$\rightarrow$			$Y_{r,t,f1}$ Melon and NH_3
2	Thermal	Foam	$\rightarrow$	$Y_{r,t,f2}$ Polyol	+	$(1 - Y_{r,t,f2})$ Isocyanate
3	Thermal	Polyol	$\rightarrow$	$Y_{r,t,p}$ Residue	+	$(1 - Y_{r,t,p})$ gases
4	Thermo oxidative	Foam + O_2	$\rightarrow$			$Y_{r,o,f1}$ Melon and NH_3
5	Thermo oxidative	Foam + O_2	$\rightarrow$	$Y_{r,o,f2}$ Polyol	+	$(1 - Y_{r,o,f2})$ Isocyanate
6	Thermo oxidative	Polyol + O_2	$\rightarrow$	$Y_{r,o,p}$ Char	+	$(1 - Y_{r,o,p})$ gases
7	Thermo oxidative	Char + O_2	$\rightarrow$	$Y_{r,o,ch}$ Residue	+	$(1 - Y_{r,o,ch})$ gases

4.2 Simplification of the reaction mechanisms of each seat material

The objective of the pyrolysis modelling is to represent the mass loss rate of the end-use product. Pyrolysis model is the available source term producing for the combustion reaction.

Currently, concerning the TGA tests, several authors (Rein (2005), Rogaume *et al.* (2011) and Marquis *et al.* (2012)) reported the hypotheses of the thermal decomposition model:

- instantaneous release of volatiles from solid to the gas phase,
- local thermal equilibrium between the solid and the volatiles,
- no condensation of gaseous products,
- no porosity effects,
- no physical change of the solid phase (the solid volume material is constant),
- the pyrolysis is considered on material surface,
- the air and inert atmospheres are taken into account.

Furthermore, the ideal mass loss rate is function of the material temperature, the heating rate and the local oxygen mass fraction when the decomposition occurs (Eq 5.8, 4.8, 5.10 and 4.11):

$$MLR = f(T, \beta, Y_{O_2}) \tag{4.12}$$

Nevertheless, the reaction mechanism is proper to the material and independent of the heating rate and the local atmosphere. The second objective at raw matter scale is to estimate the pyrolysis parameters ($A_i, E_{a,i}, n^i$ and $Y_{r,i}$) of the thermal decomposition model. The associated pyrolysis parameters for each reaction are supposed to be unique and independent of the local atmosphere and heating rate. The pyrolysis parameters are also constant input data of the FDS pyrolysis model, used to simulate the reaction-to-fire at upper scales. The FDS pyrolysis model is based on the same hypotheses as the ideal

model described above,except that it considers only thermal decomposition or thermolysis reactions. In this sense, there is a need to adapt the thermal decomposition model (Eq 4.12) developed at raw matter scale to the FDS pyrolysis model used from the material to the real scales. Thus, the mathematical expression of the FDS pyrolysis model is almost the same as the raw matter model (Eq 5.8, 4.8, 5.10 and 4.11). The difference is that the term Y_{O_2} is not taken into account in the FDS pyrolysis model:

$$MLR = \frac{dY_{tot}}{dt} = \sum_{i=0}^{N} \left(Y_{r,i} - 1\right) \dot{\omega}_i \tag{4.13}$$

where

$$\left(\dot{\omega}_i\right) = \left(Y_j\left(t\right)\right)^{n^i} A_i exp\left(\frac{-E_{a,i}}{RT}\right) \tag{4.14}$$

The unknowns of these equations are the FDS pyrolysis parameters: $A_i, E_{a,i}, n^i$ and $Y_{r,i}$. Regarding the FDS pyrolysis model, the whole of the pyrolysis parameters can be optimized in order to represent the MLR either under nitrogen or under air atmosphere. The author has chosen to optimize the FDS pyrolysis parameters under air atmosphere because:

- Concerning the cover decomposition, the first reaction has the same kinetic under air and nitrogen atmosphere (no influence of the atmosphere).
- For all firsts oxidative reactions, the presence of oxygen accelerates the MLR and the raw matter releases more volatile fuels. In the sense of a conservative approach, the MLR under air atmosphere is chosen.
- Finally, under oxygen atmosphere, the MLR accounts always one more reaction than under nitrogen atmosphere: the charcoal oxidation. The pyrolysis model is applied on material, finished and real scales. All these scales happen under air atmosphere. Thus, an oxygen diffusion on material, at the place where pyrolysis occurs, is possible.

The estimation of pyrolysis parameters is performed only with the results of the MLR obtained under air atmosphere due to these previous reasons.

Moreover, it is illusory to think that a complete reaction mechanism of a raw matter is possible only with TGA tests. Nevertheless, it is possible to obtain a complex and global reaction mechanism which reproduces finely the reactions set and describes in the previous part. However, this approach implies the optimisation and the estimation of high number of parameters and properties at this scale and upper scales. Consequently, the aim is to simplify the number of reactions in order to reduce the number of parameters to optimize but in avoiding to increase the relative deviation on the MLR prediction.

4.2.1 Cover

A simple new reaction mechanism is defined under air atmosphere. Until $320°C$, the oxygen presence has not influenced the MLR (figure 4.1). Furthermore, the piloted ignition temperature of the seat product is estimated at around $370°C$. This temperature comes from a set of cone calorimeter tests with multi-layered seat materials (from the top surface to the bottom, the cover, the interliner and the foam). This temperature estimation arises from a surface thermal balance. Marquis (2010) summarizes the estimation method of the piloted ignition temperature of a thin or a thick material. Concerning the thick material, Tewarson (1994) proposed to link the material thermal properties to the ignition delay time. He showed that, for low external radiation ($<100kW.m^{-2}$), the ignition delay time t_{ig} is function of the incident heat flux density $\dot{q}_i''$:

$$\sqrt{\frac{1}{t_{ig}}} = \frac{\sqrt{\frac{\pi}{4}}(\dot{q}_i'' - \dot{q}_{min}'')}{TRP} = cte(\dot{q}_i'' - \dot{q}_{min}'') \tag{4.15}$$

Then, according to Janssens (1993), the minimal external radiation $\dot{q}_{min}''$ is evaluated with a graphic resolution of the transformed ignition delay time t_{ig}^n (with n=0.55) function of the external radiation $\dot{q}_i''$ (figure 4.8).

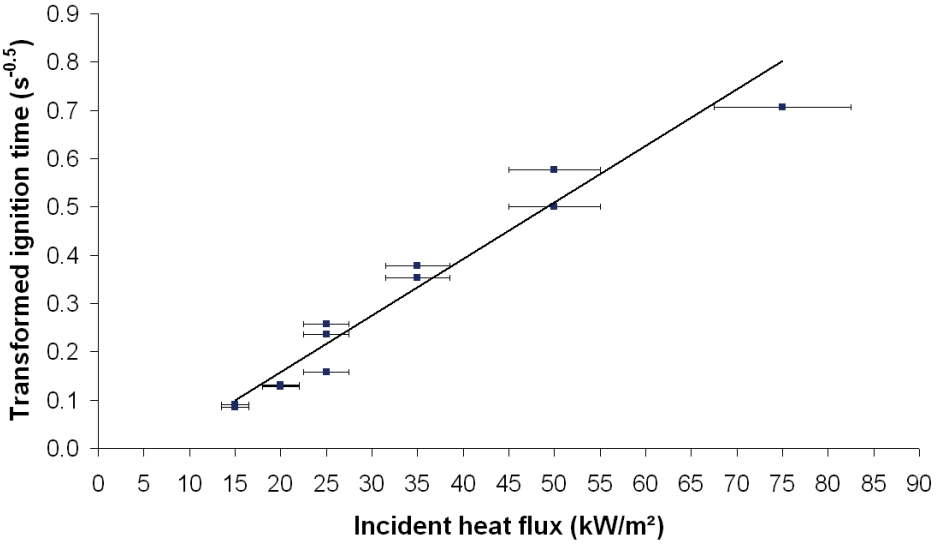

Figure 4.8: Relation between transformed ignition time and the incident heat flux of the seat materials (cover, interliner and foam)

The value of $\dot{q}_{min}''$ allows to estimate the material ignition temperature with an iterative process and its surface thermal balance:

$$\alpha_s \dot{q}_{min}'' = h_{cv}(T_{ig} - T_0) + \varepsilon\sigma\left(T_s^4(t) - T_\infty^4\right) \tag{4.16}$$

No ignition before $370°C$, the mass loss released from the cover does not participate to the combustion, e.g. does not produce combustible fuel (before this temperature). It is also

important to remind that when the fuel production begins in FDS, the fuel yield ($Y_f > 0$) is transported via the mixture fraction Z in gas phase. In this case where $\dot{Z}''' > Z_f$ at mesh interface, a quantity of heat is released. Consequently, the new reaction mechanism of the cover, showed in table 4.4, takes into account only the kinetic of the fuel production from $370°C$.

Table 4.4: Simplified reaction mechanism of the thermal oxidative decomposition of the cover of the seat.

Number of reaction	**Type of reaction**	**Reagents**		**Products**		
1	Thermo oxidative	γ - Cover + O_2	$\rightarrow$	$Y_{r,o,\gamma-c}$ Char	+	$(1 - Y_{r,o,\gamma-c})$ gases
2	Thermo oxidative	Char + O_2	$\rightarrow$	$Y_{r,o,ch}$ Residue	+	$(1 - Y_{r,o,ch})$ gases

Thus, pyrolysis parameters are estimated according to this new reaction mechanism. The input data are the experimental MLR and the initial following conditions:

$$\begin{cases} Y_{\gamma-c}\,(t=0) = 1 \\ Y_{ch}\,(t=0) = 0 \\ Y_R\,(t=0) = 0 \\ T\,(t=0) = 573K \end{cases} \tag{4.17}$$

The best optimisation is presented in figure 4.9 and the related pyrolysis parameters in table 4.5.

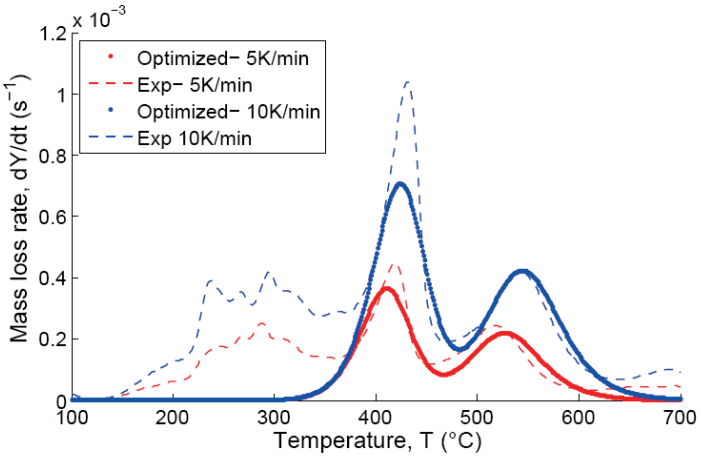

Figure 4.9: Experimental and optimized comparison of thermal decomposition at 5 and $10K/min$ for the estimation of the pyrolysis parameters of the cover material corresponding to the simplified reaction mechanism.

Table 4.5: Optimized pyrolysis parameters of the cover material

Reaction, *i*	A_i	$E_{a,i}$	n_i	$Y_{r,i}$	**Atmosphere**
	s^{-1}	$kJ.mol^{-1}$	/	$kg.kg^{-1}$	Air
1	$1.59.10^{12}$	191	1.51	0.71	Air
2	$2.76.10^{10}$	202	1.82	0.65	Air

The observed experimental and modelled phase angle is almost null concerning the reactions modelled between 350 and 650°C.

Whereas, the experimental and modelled deviation of the peak intensity of the first modelled reaction is higher at $10K/min$ than at $5K/min$. The peak intensity of the second modelled reaction between 450 and 650°C is closer to the experimental one for the both heating rate.

Table 4.6: Euclidean analysis on MLR for each heating rate

External radiant heat flux	**Euclidean relative deviation**	$cos(\Theta)$
K/min	%	
5	14	0.947
10	20	0.932

The relative deviation between the experimental and the modelled mass loss rate is presented in table 4.6 for each heating rate and between 350 and 650°C, according to the Euclidean comparison equation. The relative deviation is included between 14 and 20% and the $cos(\Theta)$ value is close to one. It should be reminded that the higher $cos(\Theta)$ result is close to one and the better is the phase angle between the two curves.

The deviation results seem sufficient to predict the MLR at this scale taking into account the simplification of the reaction mechanism and the experimental uncertainties (the repeatability, the TGA apparatus and the material heterogeneity). Thus, this reaction mechanism and the optimised pyrolysis parameter are used in the FDS pyrolsysis model at upper scale.

4.2.2 Interliner

During cone calorimeter tests of the seat materials under air atmosphere, the interliner plays a role of a thermal barrier between the foam and the combustion of the cover. Indeed, at the end of tests, a high quantity of interliner is still in the sample holder while the foam has partially disappeared (figure 4.10). It is important to keep in mind that during a TGA test, the quantity of the interliner residue that remains into the crucible is 50 % higher under nitrogen atmosphere than under air atmosphere (figure 4.3a).

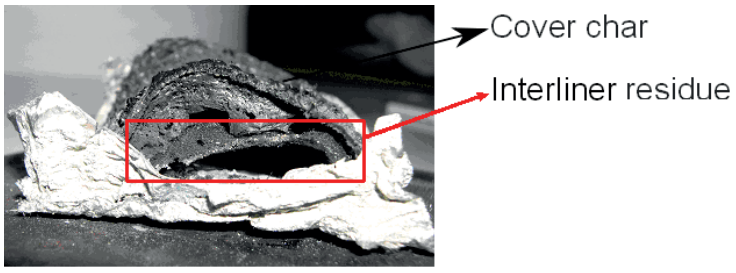

Figure 4.10: Picture of the seat materials after the cone calorimeter test.

In fact, the interliner layer is placed underneath the cover: it is possible that the cover or the cover-char formed layer plays the role of a thermal barrier between the external radiation and the interliner layer, as well as it prevents the diffusion of the potential interliner volatile fuels and then reduces the oxygen diffusion into the interliner surface. For these reasons, it is possible that the interliner thermal decomposition is closer to one under nitrogen atmosphere during the combustion of the global seat material. These observations of the reaction-to-fire of the interliner during the cone calorimeter tests and the TGA tests imply to keep the reaction mechanisms under nitrogen atmosphere for the interliner material during the combustion of the seat material. Thus, new reaction mechanism is presented in table 4.7.

Table 4.7: New reaction mechanism of the seat interliner thermal decomposition.

Number of reaction	**Type of reaction**	**Reagents**		**Products**		
1	Thermal	Interliner	$\rightarrow$	$Y_{r,t,in}$ α - Interliner	+	$(1 - Y_{r,t,cin})$ gases
2	Thermal	α - Interliner	$\rightarrow$	$Y_{r,t,\alpha-in}$ Char	+	$(1 - Y_{r,t,\alpha-in})$ gases
3	Thermal	Char	$\rightarrow$	$Y_{r,t,ch}$ Residue	+	$(1 - Y_{r,t,ch})$ gases

The pyrolysis parameters estimation is obtained from the FDS pyrolysis model (Eq5.8 and Eq5.9), the experimental interliner MLR under nitrogen atmosphere and the initial boundaries:

$$\begin{cases} Y_{cp}\,(t=0) = 1 \\ Y_{\alpha-cp}\,(t=0) = 0 \\ Y_{ch}\,(t=0) = 0 \\ Y_{R}\,(t=0) = 0 \\ T\,(t=0) = 623K \end{cases} \tag{4.18}$$

The mass loss rate comparison and the optimized pyrolysis parameters (under nitrogen atmosphere) are showed in figure 4.11 and in table 4.8 respectively.

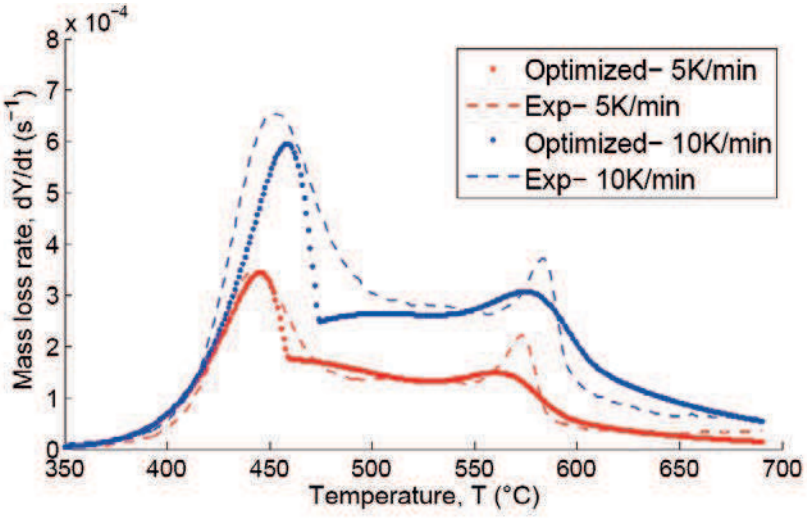

Figure 4.11: Experimental and optimized comparison of the interliner material thermal decomposition at 5 and 10 K/min corresponding to the simplified reaction mechanism.

Table 4.8: Optimized pyrolysis parameters of the interliner material

Reaction, *i*	A_i s^{-1}	$E_{a,i}$ $kJ.mol^{-1}$	n_i /	$Y_{r,i}$ $kg.kg^{-1}$	**Atmosphere**
1	$1.30.10^{12}$	198	0.60	0.87	Nitrogen
2	$3.66.10^{2}$	78	1.94	0.69	Nitrogen
3	$4.26.10^{16}$	303	1	0.91	Nitrogen

Visually, the morphology and MLR intensity of the model is in agreement with the experimental MLR, i.e. the three steps are modelled. Moreover, the relative deviation between the experimental and the modelled mass loss rate is presented in table 4.9 for each heating rate and between 350 and 650°C.

Table 4.9: Euclidean analysis on MLR for each heating rate

External radiant heat flux K/min	**Euclidean relative deviation** %	$cos(\Theta)$
5	5	0.987
10	15	0.982

The relative deviation is included between 5 and 15% and the $cos(\Theta)$ value is close to one. The deviation results seem sufficient to predict the MLR at this scale taking into account the simplification of the reaction mechanism and the experimental uncertainties (the repeatability, the TGA apparatus and the material heterogeneity). Thus, this reaction mechanism and the optimised pyrolysis parameter are used in the FDS pyrolsysis

model at upper scale.

4.2.3 Foam

Concerning the foam thermal decomposition, the reaction mechanism is reduced to two reactions under air atmosphere due to the presence of melamine (Konig *et al.* (2009)). Indeed, the presence of melamine and oxygen accelerates the three first reactions explained above. The new simplified reaction mechanism is presented in the table 4.10.

Table 4.10: New reaction mechanism of the thermal oxidative decomposition of the seat foam.

Number of reaction	Type of reaction	Reagents		Products		
1	Thermo oxidative	Foam + O_2	$\rightarrow$	$Y_{r,o,f}$ Char	+	$(1 - Y_{r,o,f})$ gases
2	Thermo oxidative	Char + O_2	$\rightarrow$	$Y_{r,o,ch}$ Residue	+	$(1 - Y_{r,o,\alpha-f})$ gases

The pyrolysis parameters estimation is obtained from the FDS pyrolysis model (Eq5.8 and Eq4.20), the experimental foam MLR under air atmosphere and the initial boundaries:

$$\begin{cases} Y_f\,(t=0) = 1 \\ Y_{ch}\,(t=0) = 0 \\ Y_R\,(t=0) = 0 \\ T\,(t=0) = 423K \end{cases} \tag{4.19}$$

The optimization mass loss rate and associated pyrolysis parameters are presented respectively in figure 4.12 and in table 4.11.

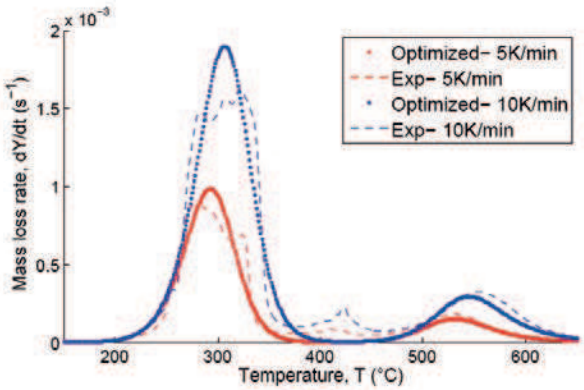

Figure 4.12: Experimental and optimized comparison of thermal decomposition at 5 and 10 K/min of the foam material corresponding to the simplified reaction mechanism.

Table 4.11: Optimized pyrolysis parameters of the foam material

Reaction, *i*	A_i s^{-1}	$E_{a,i}$ $kJ.mol^{-1}$	n_i /	$Y_{r,i}$ $kg.kg^{-1}$	**Atmosphere** Air
1	$2.53.10^9$	128	1.47	0.23	Air
2	$9.28.10^{14}$	254	2.40	0.28	Air

The two major decomposition steps of the foam are observed in figure 4.12 for both heating rates. The global experimental and modelled MLR peaks (or stage) intensities and the phase angle are respected. The relative deviation between the experimental and the modelled mass loss rate is presented in table 4.12 for each heating rate and between 350 and 650°C.

Table 4.12: Euclidean analysis on MLR for each heating rate

External radiant heat flux K/min	**Euclidean relative deviation** %	$cos(\Theta)$
5	1	0.978
10	1	0.976

The relative deviation is close to 1% and the $cos(\Theta)$ value is close to one. This results seem sufficient to predict the MLR at this scale considering the simplification of the reaction mechanism and the experimental uncertainties (the repeatability, the TGA apparatus and the material heterogeneity). Moreover, relative deviation is smaller than reproducibility.

To sum up, simplified sets of pyrolysis parameters are validated under air atmosphere for the cover and the foam. It was the opposite for the interliner, where simplified sets of pyrolysis parameters are validated under nitrogen atmosphere. These new parameters are supposed independent of the heating rate. These parameters are ones of the input data of the FDS pyrolysis model applied to the next scale: the material scale and then at upper scales.

4.3 Material scale

4.3.1 Experimental results

The tested seat sample is composed of a cover, an interliner and foam and was tested with the cone calorimeter at 5 different heat fluxes: 20, 25, 35, 50 and 75 $kW.m^{-2}$. The experimental heat release rate (HRR) of the multilayer seat materials at different heat flux are introduced in figures 4.13 a to e.

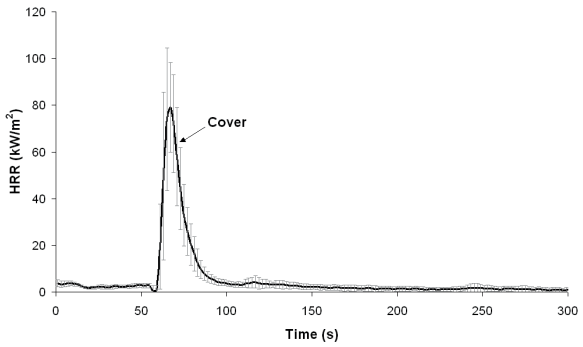

a/ Experimental HRR of the multilayer seat materials from an irradiance level of 20 $kW.m^{-2}$.

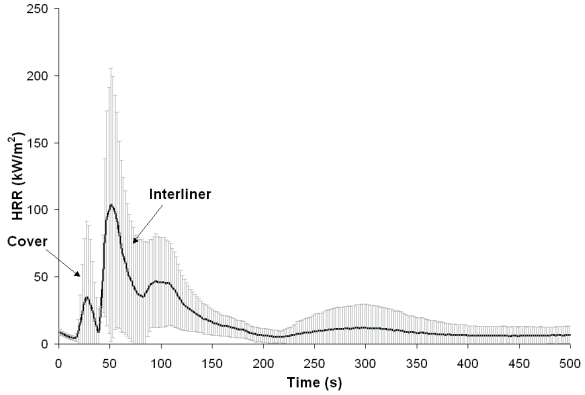

b/ Experimental HRR of the multilayer seat materials from an irradiance level of 25 $kW.m^{-2}$.

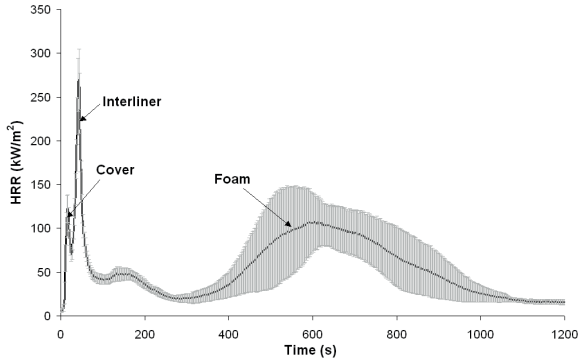

c/ Experimental HRR of the multilayer seat materials from an irradiance level of 35 $kW.m^{-2}$.

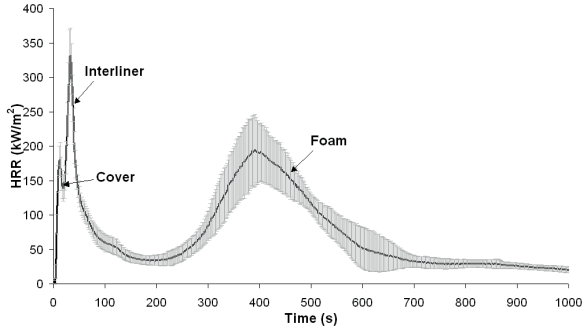

d/ Experimental HRR of the multilayer seat materials from an irradiance level of 50 $kW.m^{-2}$.

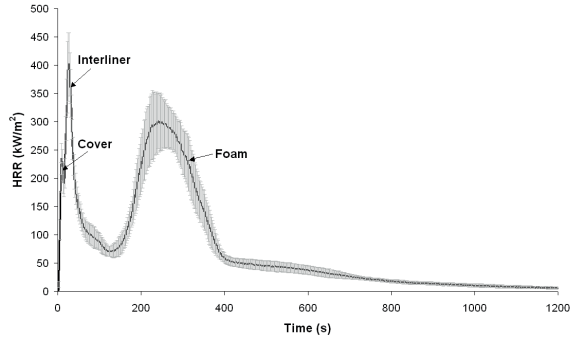

e/ Experimental HRR of the multilayer seat materials from the cone calorimeter test at 75 $kW.m^{-2}$.

Figure 4.13: Experimental HRR of the multilayer seat materials from the cone calorimeter test.

Uncertainties given here have been estimated according to *the guide to the expression of uncertainty in measurement* (NF ENV 13005 (1999)). It corresponds to the two standard deviations (repeatability and bench uncertainties) with a confidence level of 95% (Guillaume (xxxx)).

First, two different behaviours are observed, one at 20 and 25 and the second one at 35, 50 and 75 $kW.m^{-2}$. The first behaviour represents the reaction-to-fire of the first or to the two first layers (cover and interliner) seen by the presence of one or two HRR peaks (figures 4.13a and 4.13b). Indeed, the first HRR peak (at 20 and 25 $kW.m^{-2}$),

which reaches around $90kW.m^{-2}$, represents the heat released by the cover. Whereas, at $25kW.m^{-2}$, the cover and the interliner successively release heat. It should be noted that the second HRR peak could also correspond to a heat combination of interliner and cover. These two first HRR peaks are also visible on figure 4.13c, 4.13d and 4.13e corresponding to higher irradiance levels. Tests performed at 25 $kW.m^{-2}$ are not repeatable maybe because the combustible gases concentrations from the foam decomposition are close to their lower flammability limit.

Moreover, concerning these high irradiance levels (figures 4.13c, 4.13d and 4.13e), after these two first peaks, the HRR decreases (due to the thermal barrier effect of the cover and the interliner) and remains constant until another HRR peak starts. This last peak corresponds to the foam combustion. The higher is the irradiance level, the smaller is the delay between the second and the third HRR peaks and the higher is the repeatability between each test.

This behaviour is also confirmed by the results obtained on mass loss rate at 35, 50 and 75 $kW.m^{-2}$ (figures 4.14a, 4.14b and 4.14c) Indeed, two MLR peaks are detected

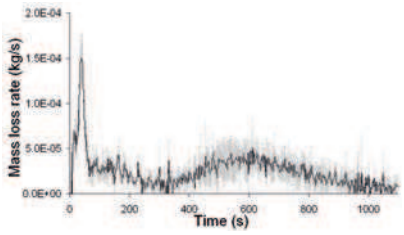

a/ Experimental MLR of the multilayer seat materials from an irradiance level of 35 $kW.m^{-2}$.

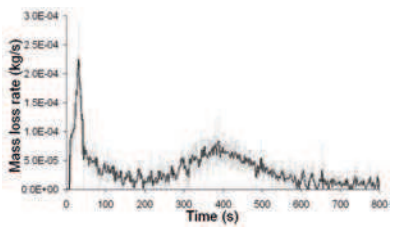

b/ Experimental MLR of the multilayer seat materials from an irradiance level of 50 $kW.m^{-2}$.

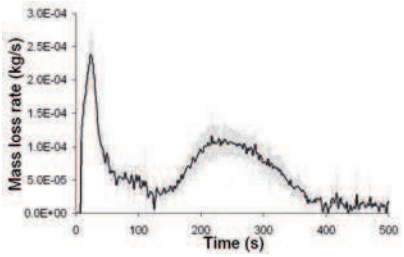

c/ Experimental MLR of the multilayer seat materials from an irradiance level of 75 $kW.m^{-2}$.

Figure 4.14: Experimental MLR of the multilayer seat materials.

before 50 seconds (mass loss of the cover and the interliner materials), then MLR peaks (due to the foam) are observed between 400 to 800 seconds, between 250 to 600 seconds and between 150 and 400 seconds at 35, 50 and 75 $kW.m^{-2}$.

The effective heat of combustion obtained from the cone calorimeter test at an external radiation of 50 $kW.m^{-2}$ is presented in figure 4.15.

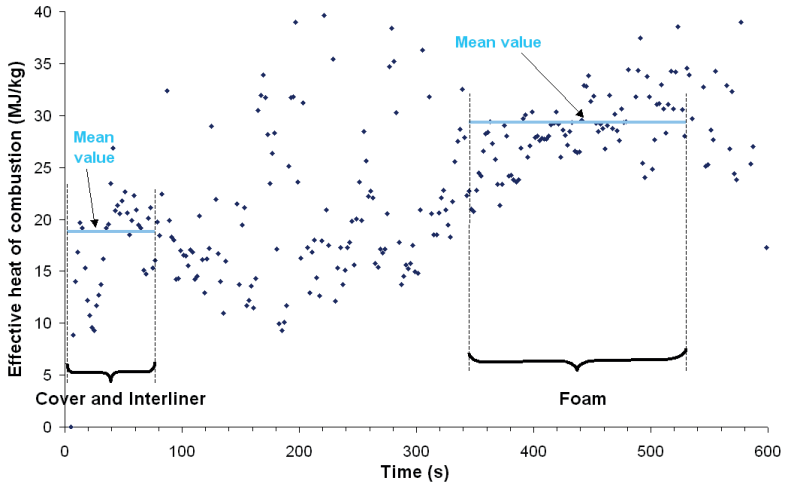

Figure 4.15: The effective heat of combustion from the cone calorimeter test under an external radiation of 50 $kW.m^{-2}$ of the multilayer seat materials, (blue lines are mean values)

The effective heat of combustion of cover and interliner corresponds to early hundred seconds of the combustion time period (like the figure 4.13b). While the effective heat of combustion time period of the foam is approximately between 350 and 550 s.

A summary of mean characteristic data for each heat flux is done on table 4.13. The mean values for the corresponding heat flux at 25 $kW.m^{-2}$ may not be representative due to the no reaction-to-fire of the foam.

Table 4.13: Multilayers seat material properties according to the heat flux

Parameters	**Unity**			**Values**		
$\dot{q}''_i$	$kW.m^{-2}$	20	25	35	50	75
$\overline{t_{ig}}$	s	59±2	24±7	8±1	4±1	2±1
$\overline{\dot{q}''_{max}}$	$kW.m^{-2}$	79±10	104±50	271±17	335 ±20	402±28
$\overline{THR}$	$MJ.m^{-2}$	3.3±0.5	20.0±6.5	65.0±1.0	76.6±4.3	89.0±1.2
$\overline{\triangle m}$	g	8.6±0.4	16.2±2.2	27.6±0.5	31.9±1.0	34.5±0.3

4.3.2 Modelling approach

The seat experimental study at material scale allows to better understand, layer by layer, the reaction-to-fire of the global seat materials .The reaction-to-fire modelling is performed by the FDS code. The simplified reaction mechanism of each seat layer and their associated pyrolysis parameters are used, as the FDS pyrolysis model input data, in order

to predict the seat thermal decomposition. Other thermodynamic and thermal properties are required to solve the heat and thermal balances at the material surface. Afterwards, a deep interaction is realised between the experimental reaction-to-fire and the limits of the FDS pyrolysis model in order to find adapted solutions. The experimental and numerical comparison is based on the heat release rate and the mass loss rate of the seat materials. When the FDS input data are validated at this scale, there are transferred at the upper scale. The modelling approach is summarized in figure 5.8.

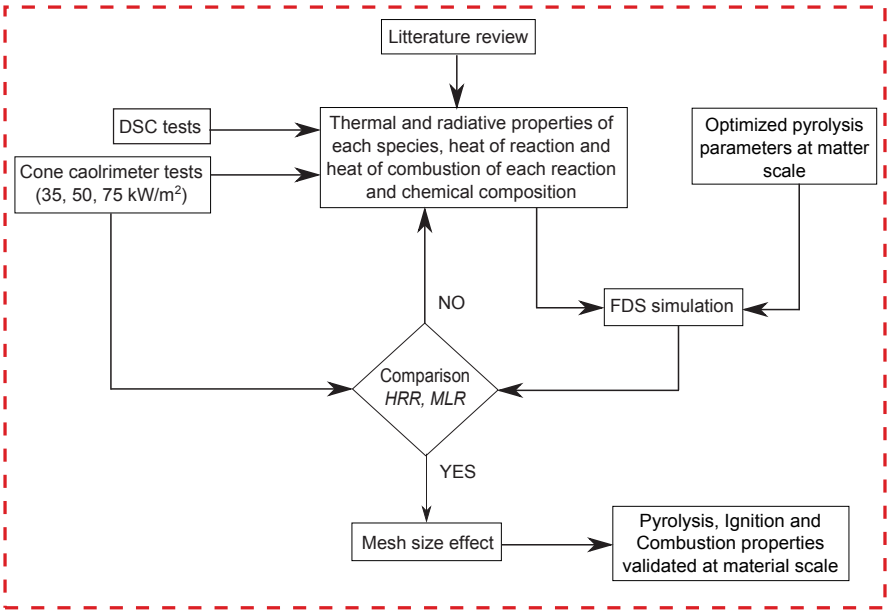

Figure 4.16: Material scale approach (Pyrolysis, Ignition and Combustion input data validation)

4.3.2.1 Mesh size

The employed mesh network in FDS is a cubic mesh network in a three dimensional Cartesian coordinate system. The choice of the mesh size for a given domain of study is not obvious and depends on the domain size as well as the physical used models. The ideal mesh size for a given study is obtained by convergence study, when the refinement of the mesh size does not influence the physical results (McGrattan *et al.* (2010)). The study domain of the cone calorimeter test is 0.25 m, 0.25 m and 0.45 m respectively in x, y and z directions. However, the study domain of a train coach is 24 m, 4 m and 3.2 m respectively in x, y and z directions. (McGrattan *et al.* (2010)) proposed to follow the Hill *et al.* (2007) criteria for the fire diameter issued from Froude Number of fire established by :

$$D^* = \left(\frac{\dot{Q}}{\rho_\infty C_p T_\infty \sqrt{g}} \right)^{\frac{2}{5}} \tag{4.20}$$

$$4 \left\langle \frac{D^*}{\triangle x} \right\langle 16 \tag{4.21}$$

$\triangle x$ represents the mesh size in each direction of the domain. In the sense of a multi scale approach, it is important to keep a coherence of a size mesh scale by scale because the same physical phenomena are caught. Thus, the train coach mesh size has to be linked to the mesh size of the finished, the semi-finished and the material scales. Concerning the train coach and the finished scale fire simulations, the chosen criteria $\frac{D^*}{\triangle x}$ is satisfied for a mesh size of 5 cm and 10 cm for a given heat flux of 230 kW. For the semi-finished scale fire simulation, the same criteria (Eq 4.21) is conserved for a mesh size of 1 cm and almost conserved for a mesh size of 2.5 cm. Like the material scale fire simulation, the criteria is satisfied for a mesh size of 1.25 cm and almost satisfied for 2.5 cm (for a given heat flux of 3 kW). Consequently, the finished scale fire simulation is tested with a mesh size of 2.5 cm to keep the link between the material, the semi-finished and the finished scales.

The numerical geometry of the conical heater and the sample holder respects the standard geometry dimensions given by the ISO 5660-1 (2002). The numerical cone calorimeter test design is represented in figure 4.17 with a mesh size of 1.25 cm in all directions of the domain.

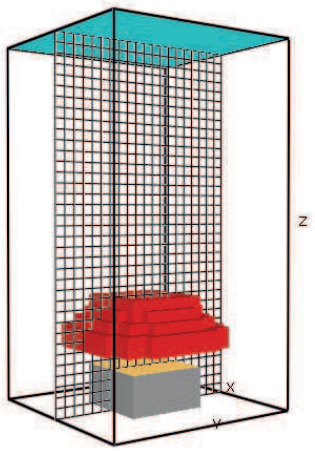

Figure 4.17: Numerical view of the cone calorimeter test geometry and the mesh network in z direction

4.3.2.2 Initial boundaries

Aerodynamic conditions

All surfaces of the domain are considered open, i.e. the initial velocities in the three directions are null and the initial pressure corresponds to the atmospheric pressure (101325 Pa). Moreover, during the simulation, the top surface of the domain (Z_{Max}) is associated to an air extraction volume flow of 24 $l.s^{-1}$ to represent cone calorimeter hood at 23°C.

Radiative and thermal conditions

The numerical conical heater is associated to a surface temperature. This temperature is

taken to be the same for each mesh of the cone and obtained by numerical calibration. It is based on a successive predicting and correcting actions through the choice of the cone temperature. A numerical gauge heat flux sensor is placed on the middle of the sample to check this incident heat flux. The net radiative heat flux from the conical heater to the material surface for each mesh is expressed as equation 5.9:

$$\dot{q}''_{r,net} = \dot{q}''_{r,in} - \dot{q}''_{r,out} \tag{4.22}$$

The incoming and outcoming radiative heat flux correspond respectively to the radiative transport equation (RTE) model and the Stefan-Boltzmann equation. The numerical heat flux distributions on the material surface at 20, 25, 35, 50 and 75 $kW.m^{-2}$ are shown in figures 4.18a, 4.18b, 4.18c, 4.18d and 4.18e according to the x and y directions corresponding to a mesh size of 1.25 cm.

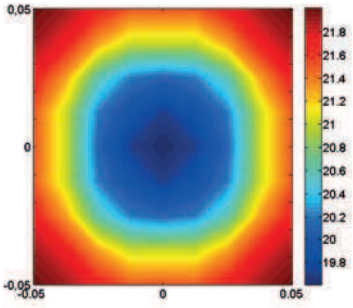

a/ Distribution of the heat flux at 20 $kW.m^{-2}$ received to the material surface.

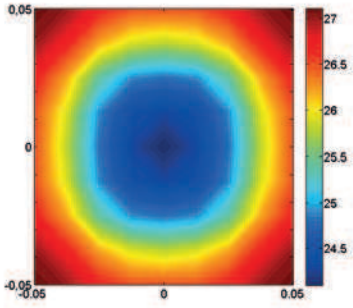

b/ Distribution of the heat flux at 25 $kW.m^{-2}$ received to the material surface.

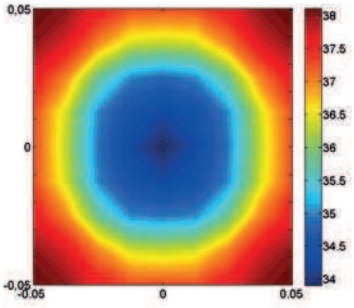

c/ Distribution of the heat flux at 35 $kW.m^{-2}$ received to the material surface.

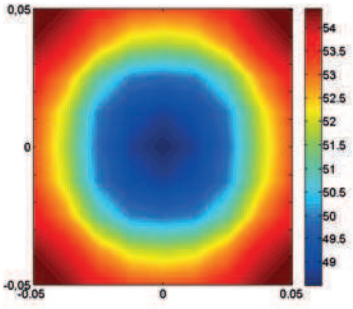

d/ Distribution of the heat flux at 50 $kW.m^{-2}$ received to the material surface.

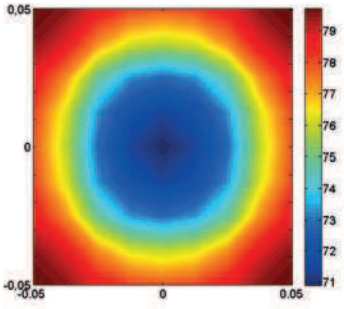

e/ Distribution of the heat flux at 75 $kW.m^{-2}$ received to the material surface.

Figure 4.18: Distribution of the incident heat flux received to the material surface in x and y directions.

All heat flux distributions are circular as the cone shape. For each distribution, the heat flux at the center of the material surface is less than the heat flux located at the edge. A heat flux ratio between the center and the edge is calculated. For each heat flux, 20, 25, 35, 50 and 75 $kW.m^{-2}$, the ratio found is the same (around 0.9). The dispersion of heat flux distribution seems to be independent of the irradiance level but dependent of the mesh size (4.19). As described in Marquis (2010) thesis, the experimental distribution of the heat flux is closer to results with the mesh size of 0.5 cm. Indeed, the experimental heat fluxes near the edges are less than the conical center ones.

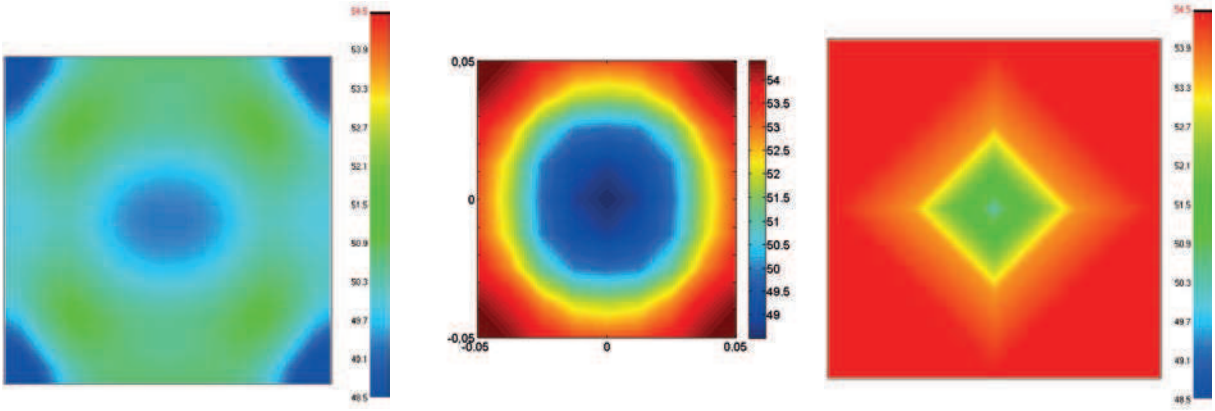

a/ Mesh size 0.5 *cm* *b/* Mesh size 1.25 *cm* *c/* Mesh size 2.5 *cm*

Figure 4.19: Distribution of the incident heat flux received to the material surface in x and y directions with three different mesh sizes

The experimental spectral distribution of the heat flux received by an uncombustible material was not performed in this study. However, Boulet *et al.* (2012) reported that the emission of the cone heater is very close to one of a blackbody in the whole wavenumbers range (between 1000 and 6000 cm^{-1}). Additionally, Boulet *et al.* (2012) presented an image of flux density at $50 kW.m^{-2}$ from IR camera. Furthermore, more information about experimental spectral distribution from the cone calorimeter test are available in Bal (2012).

According to this image, *it appears that a given sample would not receive exactly a constant density flux from all directions and on each point of its surface*. In addition to the Boulet *et al.* (2012) experimental study, the numerical surface density flux heterogeneity may come from:

- The numerical design of the conical heater (which depends on the mesh discretization)
- The number of required solid angles to solve the RTE equation.

This heat flux heterogeneity may have an influence on the numerical heating-up process of the surface material.
The initial temperature is set at $20°C$.

4.3.2.3 Numerical results

The great challenge is to use the reactions mechanism as well as the validated pyrolysis parameters for the three components of the seat, as an input data for the FDS pyrolysis models at material scale. The proposed method is to first compare numerical results with the response obtained by the cone calorimeter test at an external radiation level of 50 $kW.m^{-2}$ because:

- all the multilayer materials of the seat participate in the combustion,

- the thermal and energy balance at the surface of the seat material are modelled according to an unidirectional 1D transfer through the material.

Then, the model is tested at higher and lower external heat flux in order to check if the model in independent on the external heat flux.

With FDS models, it is important to separate the input data concerning the gas phase and the condensed phase, due to the limits of combustion model. The use of FDS implies to know for each reaction and for each condensed phase (McGrattan *et al.* (2010)):

- The thermal and radiative properties:
  - the emissivity for all initial and intermediate species,
  - the thermal conductivity as function of temperature for all initial and intermediate species,
  - the specific heat as function of temperature for all initial and intermediate species.
- The density of all initial and intermediate condensed phase.
- The heat of reaction for each pyrolysis reaction.
- The effective heat of combustion of each reaction.
- The kinetic parameters associated to the pyrolysis model.

The thermal properties and the density of each species are assessed according to literature or supplier data (table 1.13, see chapter 2). As the thermal and radiative properties (emissivity, conductivity and specific heat) of intermediate species (Char, intermediate species or Residue) are unknown, thermal properties of original materials are applied. The effective heat of combustion of each reaction associated to each intermediate species are estimated from the cone calorimeter results at an external radiation of 50 $kW.m^{-2}$. The pyrolysis parameters are supposed the same as found in the raw matter scale study (section 4.2: Simplification of the reaction mechanisms of each seat material). The heat of reaction for each reaction is one of the most difficult input data to estimate due to the thermal decomposition phenomena. For example, several reactions can occur at the same time and can result in several endothermic and exothermic phenomena or group of concomitant reactions, through the DSC measurement. Consequently, this data is fitted according to the experimental data but always in the order of magnitude of a heat of reaction found in literature (Drysdale (2011)).

The polyurethane reaction is chosen for the gas phase input data because its effective heat of combustion and its quantity of available fuel are higher than the cover and the interliner materials.

A layer of silicate wool (thickness 19 mm) is placed under the foam to compensate the space between the foam and the sample holder and to ensure the insulation of the bottom of the multilayer materials, as the cone calorimeter test required (ISO 5660-1 (2002)). The comparison between experimental and numerical HRR and MLR of the cone calorimeter test at 50 $kW.m^{-2}$ is reported in figure 4.20.

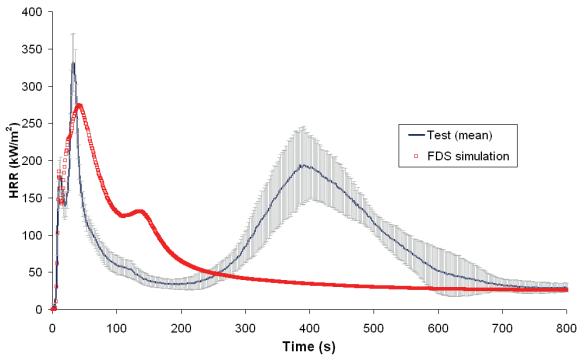

a/ Comparison of the HRR of a multilayer seat materials from an external radiation of 50 $kW.m^{-2}$.

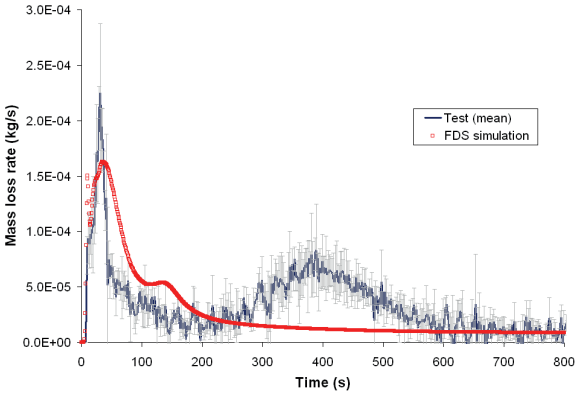

b/ Comparison of the MLR of a multilayer seat materials from an external radiation of 50 $kW.m^{-2}$.

Figure 4.20: Comparison of the HRR and MLR of a multilayer seat materials from an external radiation of 50 $kW.m^{-2}$.

The first and the second HRR and MLR peaks are quite well reproduced with FDS models. However, the combustion of the foam is not correct: the intensity of the third calculated peak is smaller than the experimental one, and the gap between the second and the third peak is not respected. The foam reaction starts earlier in the simulation.

From an experimental point of view, during the cone calorimeter test, when the top surface of the multilayer seat materials is exposed to a radiative heat flux, the cover starts to decompose. When the temperature, pressure and mix of fuel and oxygen reach the ignition conditions, the combustion starts.

Then, a char layer is formed at the surface of the virgin cover material. This char layer is an inhibitor combustion property:

- It plays a role of thermal barrier between the external radiant heat flux and foam materials.
- It reduces the available fuel mass flow of the interliner.
- It plays a role of diffusion oxygen barrier to the interliner surface: consequently, it is supposed that the interliner decomposes more under nitrogen atmosphere than under air. Thus, 50% of the initial mass of the interliner material remains into the specimen holder, as the proportion observed in TGA under nitrogen atmosphere.

Figure 4.21 summarizes the key steps of the seat thermal decomposition condensed phase during the cone calorimeter test. During the tests, the char layer is a thermal barrier between the external radiant heat flux and the foam (figure 4.21). At the same moment, according to the temperature gradient into the multilayer material, it is proposed that a certain thickness of the foam starts to decompose and to shrink between the cover protection and the virgin foam. A gas gap is then formed between the char layer and the remaining foam (figure 4.21).

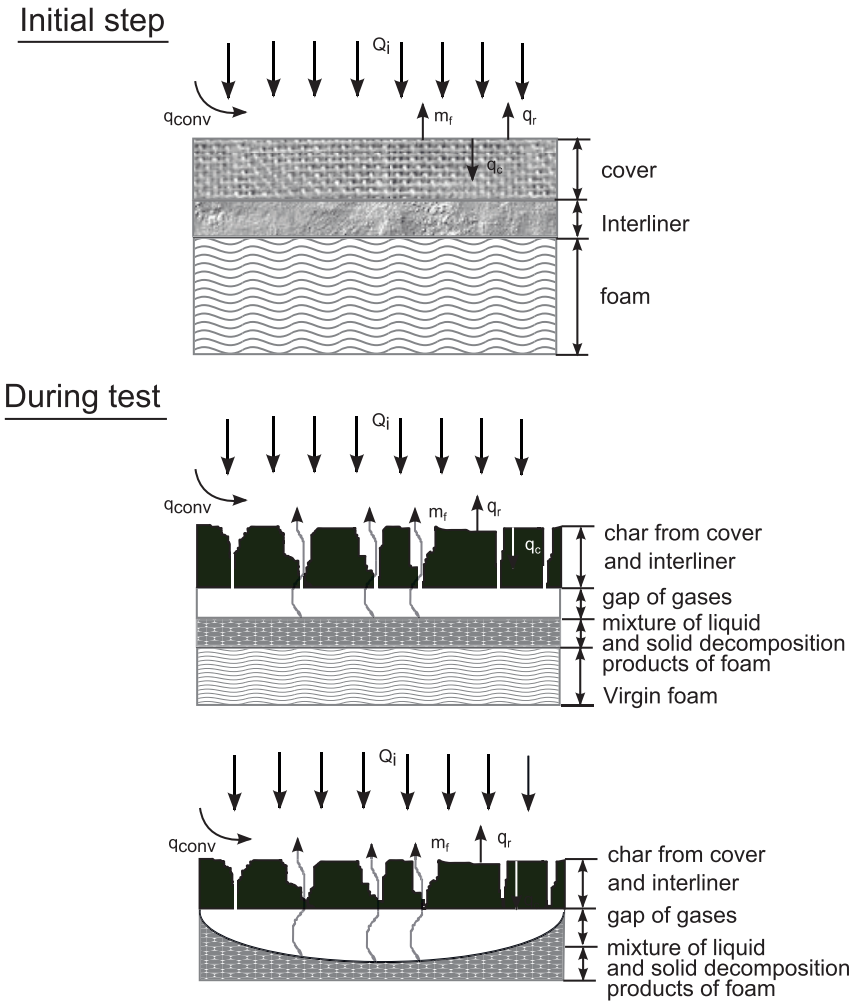

Figure 4.21: Pyrolysis phenomena of the multilayer seat material from an external radiation heat flux

Then, because of these physical changes that happen during the foam thermal decomposition, the numerical multilayer seat materials are modelled with one more layer, as an equivalent materials. This layer represents a gap of gases. The gases, from the foam decomposition, can be composed of isocyanate. These thin gas layer is blocked between the char layer and the condensed phase of the foam (figure 4.21) and plays the role of thermal barrier for the virgin foam. It is assumed that these gases (isocyanate) do not participate in the combustion because of the low concentration of oxygen and combustible gases into this gap. The oxygen diffusion is difficult through the char layer and it should be taken into account that all material sides are insulated by the sample holder.

In FDS, this extra thin layer is added between the interliner and the foam and called the *fictive layer*. Indeed, changes in the condensed phase volume can not be considered in FDS models. Moreover, the experimental HRR period time (between the second and the third peak) is associated to this fictive pyrolysis reaction (figure 4.22). Thus, in FDS, the foam initial thickness (25 mm) is separated into two materials, one thickness for the *fictive layer* and another one for the foam.

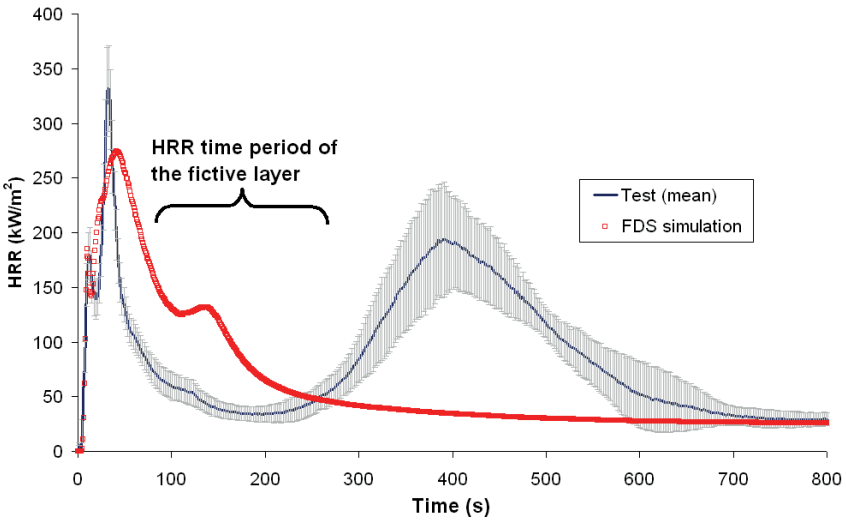

Figure 4.22: Experimental period time of the HRR between the reaction-to-fire of the cover and the interliner and the foam one, corresponding to the fictive layer.

The *fictive layer* thickness is set at 3 *mm* and the virgin foam thickness at 22 *mm* in order to keep the global thickness of the foam (25 *mm*). The new equivalent seat material is represented in figure 4.23 in FDS.

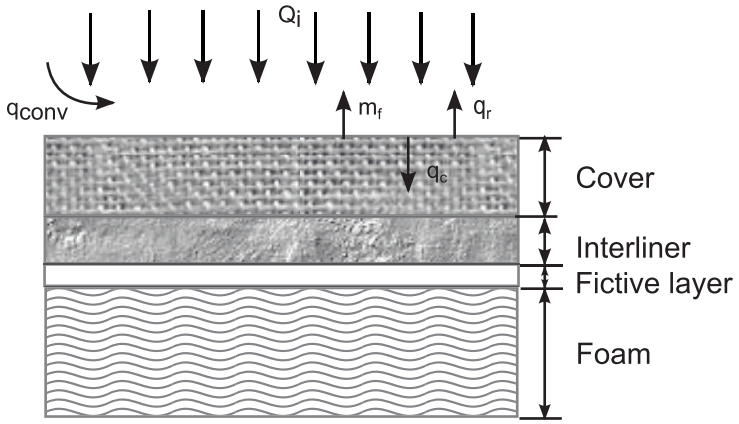

Figure 4.23: Equivalent seat material used in FDS

Then, a fictive pyrolysis reaction is associated to the *fictive layer* in order to represent the physical change of the solid foam to the gas gap. Moreover, in FDS, there are two ways to use the FDS pyrolysis model, either to define a set of pyrolysis parameters (validated at raw matter scale) or to prescribe a couple of a reference temperature and a reference rate. This type of input data ($T_{reference}$ and $r_{reference}$) are more adapted to model a decomposition reaction mechanism composed of one reaction. I should be noted that the $T_{reference}$, the $r_{reference}$ and the $\Delta H_{reaction}$ (table 4.14) are only numerical data, obtained in this case from a successive prediction and corrective actions by the author in order to represent the HRR and the MLR time period of the *fictive layer* reaction. Furthermore,

it is assumed that the fictive layer plays the role of thermal barrier between the char and the virgin foam from the incident heat flux. The fictive layer reaction does not participate to the combustion. Consequently, the $\Delta H_{combustion}$ of the fictive layer reaction is set at 0 $kJ.kg^{-1}$. Nevertheless, the effective heat of combustion of the fictive foam is assessed to a very low value (0.01 $kJ.kg^{-1}$ instead of 0 $kJ.kg^{-1}$) because the value zero is not recognized as the heat of combustion property. If $\Delta H_{combustion} = 0$, the effective heat of combustion of the gas phase is taken into account for the fictive foam combustion.

The *fictive layer* thermal properties are assumed the same as the virgin foam, except for thermal conductivity. The foam heat transfer is driven by thermal conductivity because it is a thick material ($Bi \geq 1$). The Biot number (Bi, Eq 4.23) compares the efficiency with which heat is transferred to the surface by convection from the surrounding air, and from the surface by conduction into the condensed phase (Drysdale (2011)).

$$Bi = \frac{h_c \tau}{\lambda} \tag{4.23}$$

The conductivity of a virgin polyurethane foam is around 0.03 $W.m^{-1}.K^{-1}$ (Bustamante Valencia (2009)). However, during thermal decomposition and before foam ignition, the foam condensed phase becomes a viscous material. Thermal conductivity of the shrunk foam is assessed to be close to that of a liquid fuel, such as methanol (high conductivity around 0.2 $W.m^{-1}.K^{-1}$, Pang *et al.* (2012)). Furthermore, thermal conductivity is fitted according to the third peak of the HRR experimental data and liquid fuel conductivity. This fitted new conductivity may be the result of compensation effects due to the collapse change of the foam and the thermal feedback from silica wool. Since the absorption coefficient of the cover is not known, the pyrolysis is supposed to occur at the cover surface. The optical radiative property κ was not changed and the FDS default value is used (κ = 50000 m^{-1}). The new input data corresponding to the *fictive layer* and the shrunk foam is presented in table 4.14.

Table 4.14: New thermal seat foam properties.

Properties	**Units**	**Fictive layer**	**Shrunk foam**
ε		0.9	0.9
Cp	$kJ.kg^{-1}.K^{-1}$	1.4	1.4
λ	$W.m^{-1}.K^{-1}$	0.03	0.4
ρ	$kg.m^{-3}$	76	76
$\Delta H_{combustion}$	$kJ.kg^{-1}$	0.01	30000
$\Delta H_{reaction}$	$kJ.kg^{-1}$	750	150
$T_{reference}$	$°C$	400	
$\omega_{reference}$	s^{-1}	0.0001	

According to these modifications, the new HRR and MLR comparisons between experimental and numerical results are presented in figures 4.24 with two different mesh sizes: 2.5 and 1.25 cm.

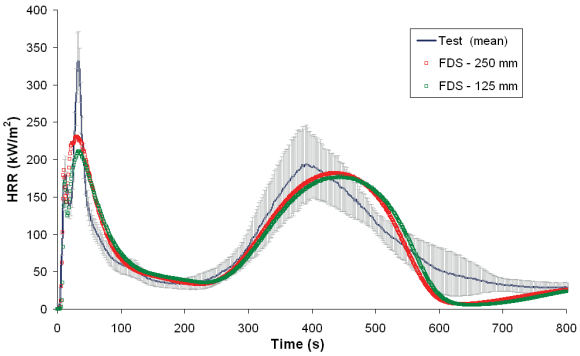

a/ New Comparison of the HRR of a multilayer seat materials from an external radiation of 50 $kW.m^{-2}$.

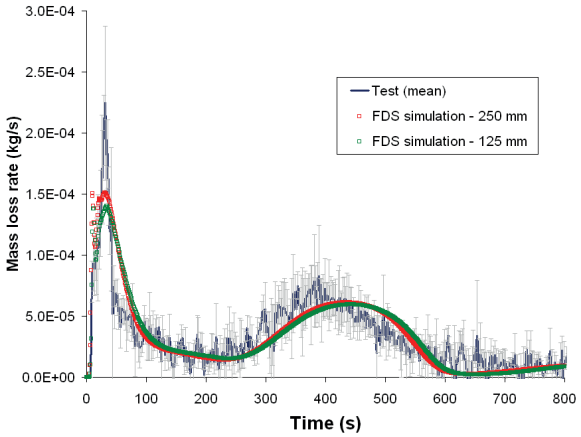

b/ New Comparison of the MLR of a multilayer seat materials from an external radiation of 50 $kW.m^{-2}$.

Figure 4.24: New Comparison of the HRR and MLR of a multilayer seat materials under an external radiation of 50 $kW.m^{-2}$.

The numerical HRR and MLR of the two first peaks are the same as the ones from previous comparisons. However, the MLR and the HRR due to the foam combustion (third peak) are in agreement with the experimental HRR and MLR. The influence of the mesh size on the MLR and HRR of the seat is negligible (same kinetic and almost same intensities). These new equivalent material input data are now tested for the external radiant heat flux of 35 and 75 $kW.m^{-2}$ in order to know if these input values are independent from the external radiation. The comparisons are presented in figures 4.25 a and figure 4.25 b for HRR results.

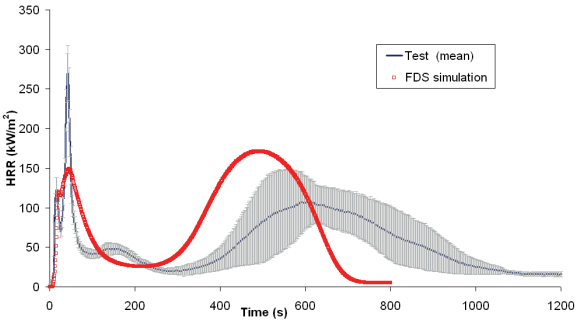

a/ New Comparison of the HRR of an equivalent multilayer seat materials from an external radiation of 35 $kW.m^{-2}$.

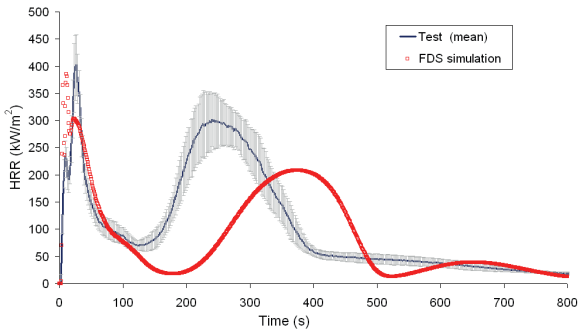

b/ New Comparison of the HRR of an equivalent multilayer seat materials from an external radiation of 75 $kW.m^{-2}$.

Figure 4.25: New Comparison of the HRR of a multilayer seat materials from an external radiation of 35 and 75 $kW.m^{-2}$.

The first two HRR peaks are correctly represented. However, the HRR and MLR of the foam are shifted for the two external radiant heat fluxes: for 35 $kW.m^{-2}$, the foam combustion occurs early unlike what happens at 75 $kW.m^{-2}$, where the HRR/MLR peak are delayed. The assumption of the *fictive layer* thus evolves: we assumed that the higher is the external radiant heat flux, the more the *fictive layer* thickness decreases and the more the shrunk foam thickness increases. The strategy is to change only the *fictive layer* thickness corresponding to each external radiant heat flux (all others input data are kept).

Table 4.15 reports the chosen thickness according to each external radiant heat flux. The new model is now tested for several external heat fluxes. It allows to validate the model from low to high heat flux. The new comparison is introduced with figures 4.26.

Table 4.15: *Fictive layer* thickness function of the external radiant level of the cone

External radiant heat flux $kW.m^{-2}$	**Fictive layer thickness** mm
20	25
25	25
35	4.5
50	3
75	1.5

Furthermore, knowing that the foam does not participate in the combustion with an external radiation level at 20 and 25 $kW.m^{-2}$, only thermal properties are associated to the third layer (the foam) of the seat materials.

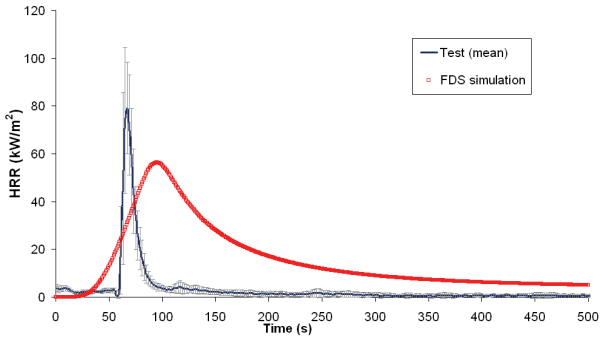

a/ New comparison of the HRR of an equivalent multilayer seat materials from an external radiation of 20 $kW.m^{-2}$.

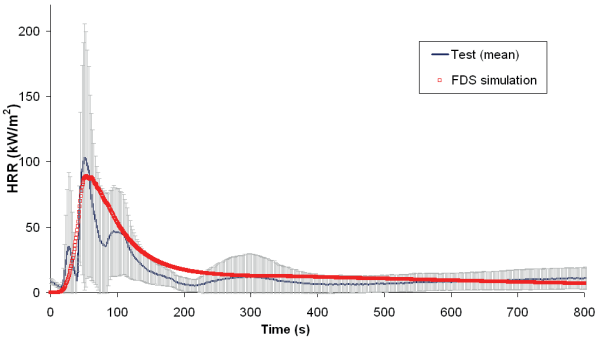

b/ New comparison of the HRR of an equivalent multilayer seat materials from an external radiation of 25 $kW.m^{-2}$.

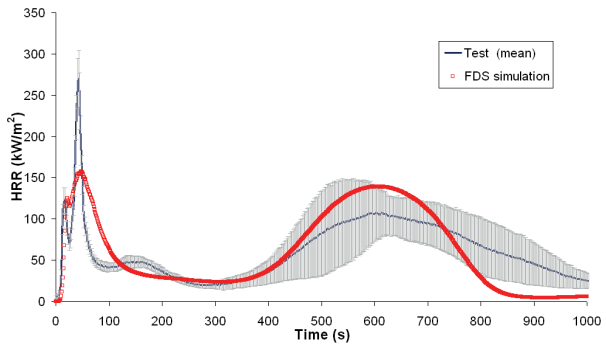

c/ New comparison of the HRR of an equivalent multilayer seat materials from an external radiation of 35 $kW.m^{-2}$.

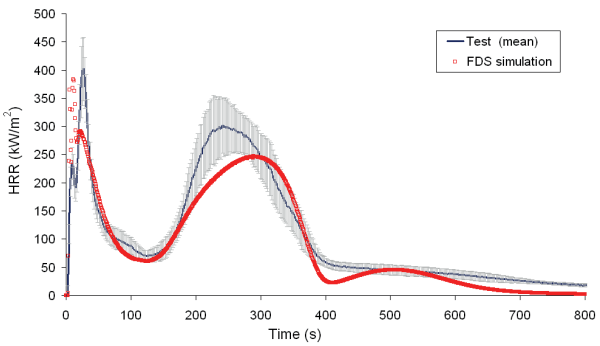

d/ New comparison of the HRR of an equivalent multilayer seat materials from an external radiation of 75 $kW.m^{-2}$.

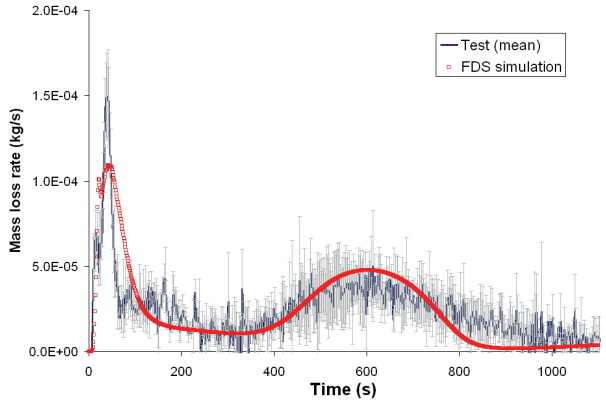

e/ New Comparison of the MLR of an equivalent multilayer seat materials from an external radiation of 35 $kW.m^{-2}$.

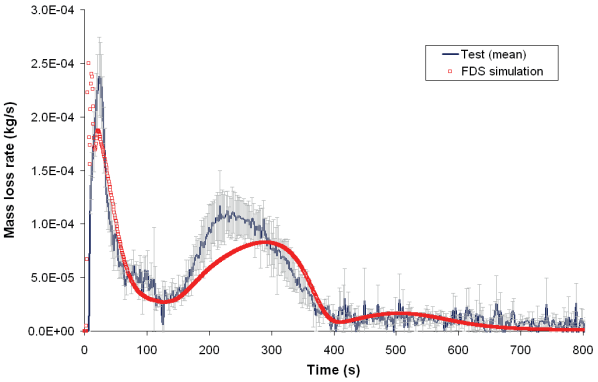

f/ New Comparison of the MLR of an equivalent multilayer seat materials from an external radiation of 75 $kW.m^{-2}$.

Figure 4.26: Experimental and numerical HRR and MLR of the equivalent multilayer seat materials from the cone calorimeter tests.

Concerning the three higher external radiation levels (35, 50 and 75 $kW.m^{-2}$), the three HRR and MLR peaks are displayed as follows: one for the cover, one for the interliner and another one for the foam. The time period and the HRR/MLR intensity between the combustion of the two covers and the foam are also respected. Concerning the external radiation level of 25 $kW.m^{-2}$, the delay ignition time and the HRR/MLR intensity is well represented. However, the number of peaks is not. For the external radiation level of 20 $kW.m^{-2}$, the kinetic and the order of magnitude of the HRR intensity are correct but the numerical ignition delay time is too low compared to the experimental one.

These visual observations confirm the comparison results obtained by an Euclidean analysis in table 4.16. Concerning the HRR results obtained under an incident heat flux of 20 $kW.m^{-2}$, the Euclidean relative deviation is high and its cosinus Θ is not satisfactory (far away from the correct value (1)). The FDS code has some weaknesses in simulating the pyrolysis and the reaction-to-fire at low heat flux. Hostikka and McGrattan (2001) showed already that the FDS model failed to predict the heat release rate at low heat flux exposure, through a pyrolysis model. They reported that this may be due to errors in the heat transfer solutions and thermal properties. Furthermore, they added that the absence of some physical phenomena, such as surface reactions and internal mass transfer, may also affect the results. However, the Euclidean relative deviation and cosinus Θ for upper incident heat fluxes are acceptable considering the uncertainties.

Table 4.16: Euclidean analysis on HRR for each external radiant heat flux

External radiant heat flux $kW.m^{-2}$	**Euclidean relative deviation** %	$cos(\Theta)$
20	88	0.45
25	21	0.95
35	10	0.93
50	0.3	0.97
75	11	0.98

The experimental and numerical mass losses are compared in table 4.17 according to each external radiant heat flux.

Table 4.17: Experimental and numerical mass loss function of the external radiant level

External radiant heat flux $kW.m^{-2}$	**Experimental mass loss (g)**	**Numerical mass loss (g)**	**Relative deviation (%)**
20	8.6±0.4	6.0	30
25	16.2±2.4	9.0	44
35	27.6±0.5	25.8	6
50	31.9±1.0	27.0	15
75	34.5±0.3	30.0	13

The relative deviation of these two results is expressed in %. Deviation results seem suf-

ficient to predict the mass loss at this scale taking into account the simplification of the reaction mechanism and experimental uncertainties (the repeatability, the cone calorimeter apparatus and the material heterogeneity) concerning the heat fluxes exposure of 35, 50 and $75kW.m^{-2}$. However, the relative deviation reaches 30% and 44% respectively for heat fluxes 20 and 25 $kW.m^{-2}$. It should be reminded that under these two incident heat fluxes, the foam combustion is not considered but the PU is used as the fuel reagent in the unique FDS gas phase combustion reaction. Thus, despite the experimental uncertainties, it is supposed that this relative deviation may come from:

- The experimental and the numerical stoechiometry combustion reaction are different.
- The foam mass loss during its decomposition that is not taken into account in FDS.

Taking into account the decomposition effect, such as the shrinking of a foam part, by the formation of an equivalent multilayer materials, the new input data depend on the external radiation level received at the surface of the material, whereas the aim of a pyrolysis model is to be independent of the external radiation heat flux. The straight line relation of the fictive foam inverse thickness as a function of the external radiation level is a linear curve (figure 4.27).

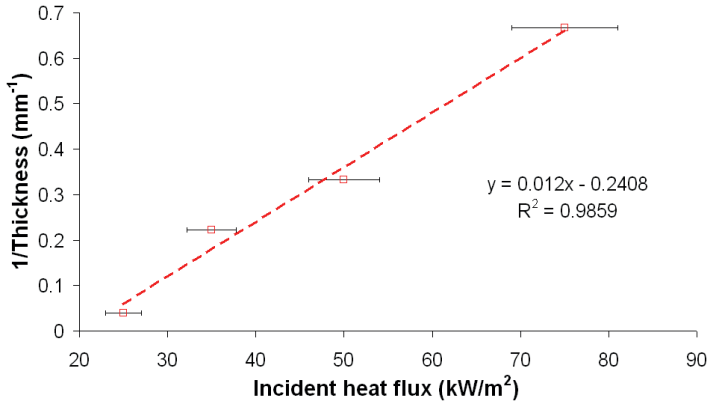

Figure 4.27: Linear relation between the fictive foam inverse thickness and the external radiation heat flux

The next challenge is to check if the validated equivalent material at upper scale (material scale) can be applied and validated at finished scale. The choice of the fictive layer thickness is explained at upper scale.

4.4 Finished product scale

This scale represents the reaction-to-fire study in the product end-use conditions. The finished product scale simulation objective is to verify the product reaction-to-fire taking into account the effect of mounting and fixing configuration (impact of the ceiling, the corner and joints) and then to confirm the material properties (thermal properties and pyrolysis parameters), used as an equivalent seat materials at material scale. Moreover,

this scale allows to compare the total experimental and numerical generation of released gases from the propane burner and from the seat itself.

4.4.1 Experimental results

Seat product

The railway seat studied is composed of the same materials as studied at the previous scale: a cover, an interliner and a foam. All these materials are shelled in polycarbonate, as seen in the following picture 4.28a. This scale follows the open calorimetry test (ISO 24473 (2006)) and represents the product in end-use conditions, i.e. the configuration, the dimension and the structural geometry of the product. The seat is located in the corner between two uncombustible panels, under an uncombustible roof. The floor is also uncombustible. All these uncombustible surfaces are made of calcium silica, with a nominal density of 680±50 $kg.m^{-3}$ (ISO 9705 (2006)). The propane burner is placed in front of the cushion seat as described in figure 4.28b.

a/ Railway seat studied placed during the finished scale test.

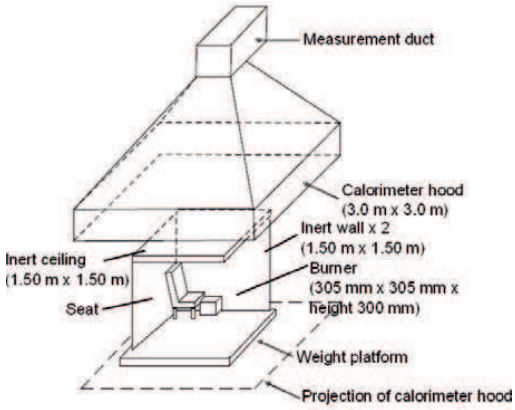

b/ Finished scales test configuration for tested seat.

Figure 4.28: Finished seat test configuration for tested seat.

Two tests are performed with a propane burner (75 kW during 2 min and 150 kW during 8 min with a surface area of 0.3 m by 0.3 m). The source used is described in ISO 9705 (2006) standard. The thermal program comes from FIRESTARR study (Briggs *et al.* (2001)a, Briggs *et al.* (2001)b and Le Tallec *et al.* (2001)) and the European standard CEN/TS 45545-1 (2009). The propane burner intensity is supposed be the same as a luggage fire placed on the floor above the seat cushion. The heat release rate, the gases released and seat temperatures from the finished product scale test are presented in figures 4.29, 4.30a, 4.30 and 4.32b.

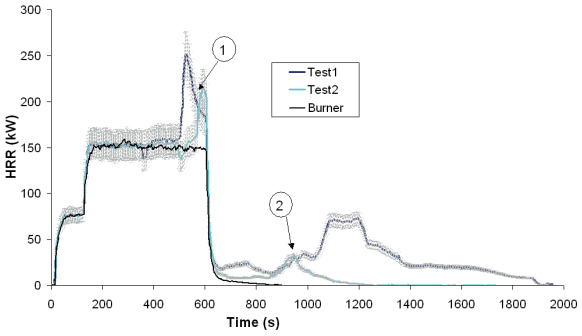

a/ Experimental heat release rate from the finished scale test

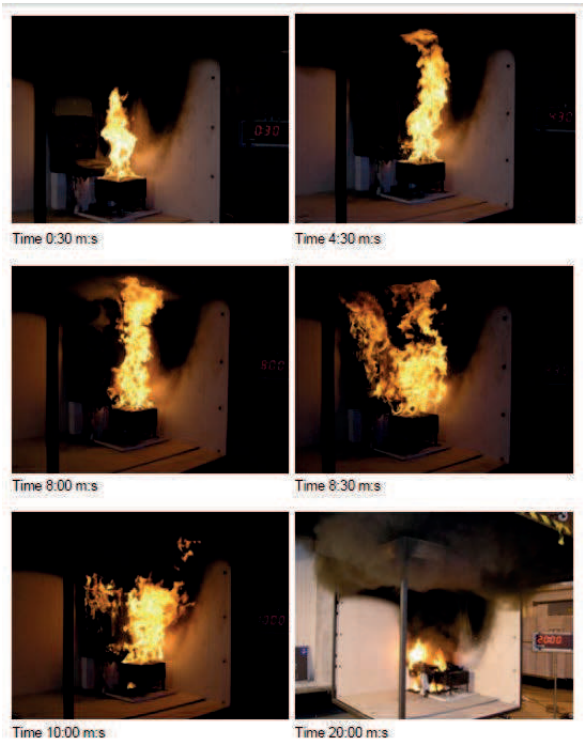

b/ Pictures taken during the test from SP laboratory

Figure 4.29: Finished seat test results.

A maximum uncertainty of 10% is estimated for individual HRR curves according to ISO 9705 (2006)). Concerning the released gases, an uncertainty of 5% is assessed on the FTIR results based on the calibration.

According to the experimental results and tests videos, around four and half minutes after the ignition of the burner, the right corner of the seat cushion (close to the burner) starts to ignite. Four minutes later, the whole cover ignites. After ten minutes, the burner stops and the seat continues to burn. It is possible then that the geometry of the back seat has been modified by the fire: the top of the seat back is not connected anymore to the bottom of the headset. The foam is not protected by the covers and burns. The second HRR peak (figure 4.29a) may be due to the combustion of the foam located on the seat back. Moreover, the second HRR peak of the first test is higher than the second one because, during the first test, at around fifteen minutes, the seat back felt down on the seat cushion.

A FTIR spectrometer was connected to the exhaust duct. Three gases were detected: carbon dioxide, carbon monoxide and sulphur dioxide (figure 4.30). The HRR has the same kinetic as the released carbon dioxide. For carbon monoxide, two major peaks are observed. The first one is due to the ignition of the seat back cover blend and seat cushion. The second one may be due to the foam combustion of the seat back. Only one peak of sulphur dioxide is detected before the extinction of the burner. As it is known, wool releases sulphur dioxide. Wool is the main component of the cover.

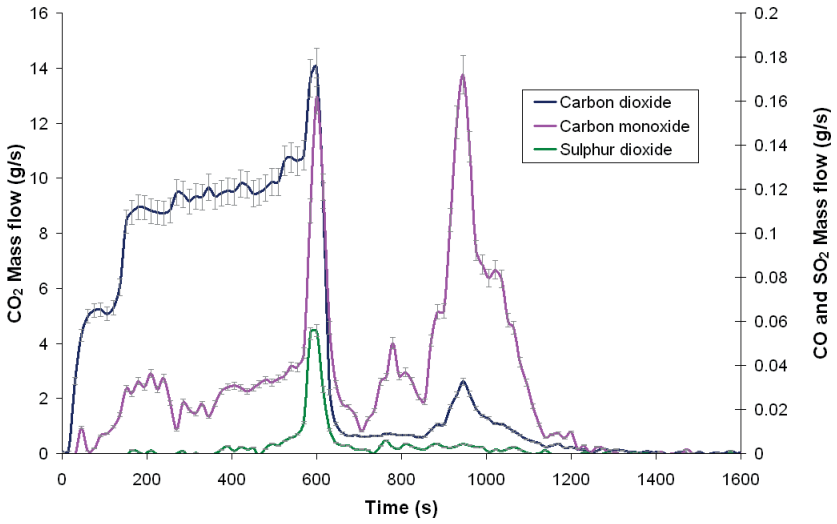

Figure 4.30: Experimental gases mass flow from the finished seat test.

This information confirms that the cover ignites mainly during the first HRR peak, between 500 and 600 seconds.

Experimental temperatures measured on the seat cushion and seat back are respectively presented in figures 4.32 a and 4.32 b. Sensors locations are introduced in figure 4.31.

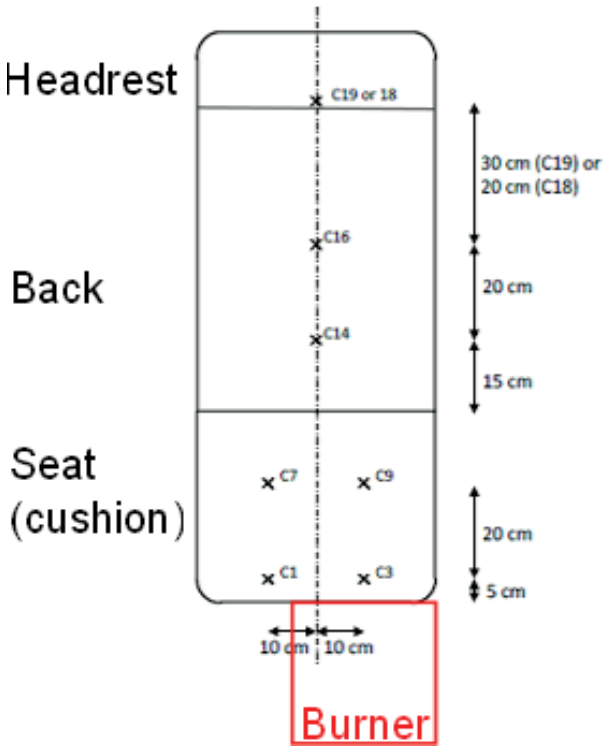

Figure 4.31: Positions of thermocouples on the tested seat

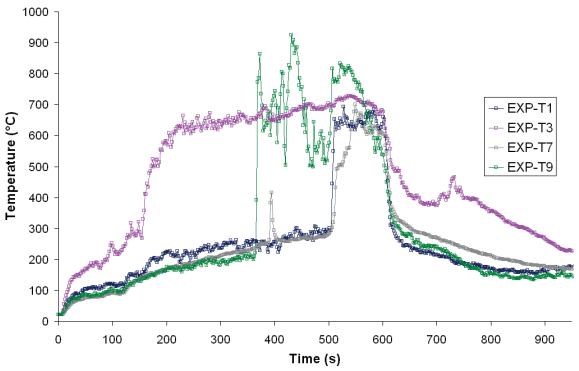

a/ Experimental temperature of the seat cushion

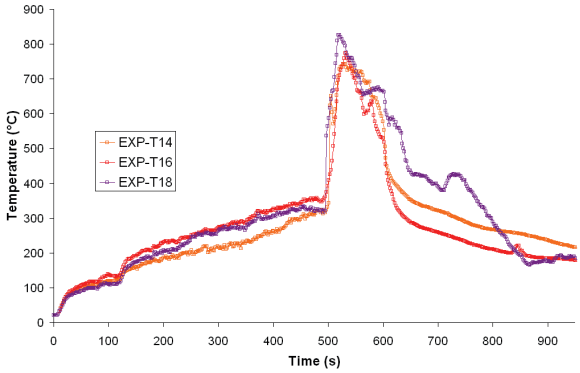

b/ Experimental temperature of the seat back

Figure 4.32: Experimental temperature of the seat.

Position *3* is the closest position to the burner. Signal of sensor *3* begins to increase from 150 seconds after the ignition of the burner. Thus, during the second phase of the burner (150 kW), sensor *3* is located inside the flame of the burner. According to sensor *3* measurements, temperature starts to raise around 370 seconds. This increase corresponds to the ignition of the cover of the seat cushion, near to the sensor *9* location. The signal of the sensors *1* and *7* records an increase at the same time, at around 500 seconds. This raise in temperature also corresponds to the ignition of the seat cushion cover, near sensors *1* and *7*. Concerning the temperature of the seat back, the three sensors (*14*, *16* and *18*) have the same kinetic and intensity of temperature. The three sensors showed a fast increase around 500 seconds after the ignition of the burner. The entire seat back and the headset ignite at the same time, at 500 seconds according to temperatures (figure 4.32a) and videos (figure 4.29b)

4.4.2 Modelling approach

The seat experimental study at finished product scale allows a better understanding of the seat product reaction-to-fire in end-use conditions. The reaction-to-fire modelling is performed with the FDS code. The aim of this scale is to test the abilities of the FDS code in order to simulate pyrolysis, ignition, combustion and flame spread over a seat from a flame propane burner. The used input data are the same as the material scale. The experimental and numerical comparison is based on the heat release rate, the temperature, the burnt areas and the released gases of the seat. When the FDS input data are validated at this scale, there are transferred at the upper scale. The modelling approach is summarized in figure 3.9.

4.4.2.1 Mesh size

For the finished product seat simulation, the domain size is 1.6, 1.6 and 2.7 m respectively in x, y and z directions. The seat cubic mesh network is complex due to its geometry and especially to the curvature of the seat back. The seat mesh network is composed of three different parts:

- cushion: 0.4 m by 0.5 m in x and y directions,

- back: 0.45 m by 0.5 m in z and y directions,
- headset: 0.2 m by 0.5 m in z and y directions.

As it is explained in the previous chapter, the ideal mesh size is given according to the criteria linked to the fire diameter (4.20 and 4.21).This criteria is satisfied for the finished test domain with a size mesh of 5 cm. In the sense of multi scale approach, a size mesh of 2.5 cm is tested too.

4.4.2.2 Initial boundaries

Aerodynamic conditions

All surfaces of the domain are considered open, i.e. the initial velocities in the three directions are null and the initial pressure corresponds to the atmospheric pressure (101325 Pa). Moreover, during the simulation, the domain top surface is associated to an air extraction volume flow of 1.5 $m^3.s^{-1}$, in order to reproduce the exhaust hood.

Radiative and thermal conditions

Propane burner

The main difference between the material scale and the finished scale, apart from the test size, is the burner. In the first scale, it is a conical radiant heater and for the finished scale, it is a propane flame burner. The heat flux received by the product depends on the fire plume intermittent (puffing flame), the burner power and the configuration factor (geometrical relationship between the flame and the product). Before studying the numerical reaction-to-fire of a seat product by a flame burner, it is important to check if the propane flame burner is well represented in FDS simulation. This validation relies on temperatures comparison. Indeed, SP has led a propane burner test with the finished scale configuration (mounting and fixing conditions and ceiling) with only uncombustible materials. The propane burner is placed in the corner configuration with two power phases: one at 75 kW during 200 seconds and then the second at 150 kW during 600 seconds. Four thermocouples are placed above the burner, as figure 4.33 shows.

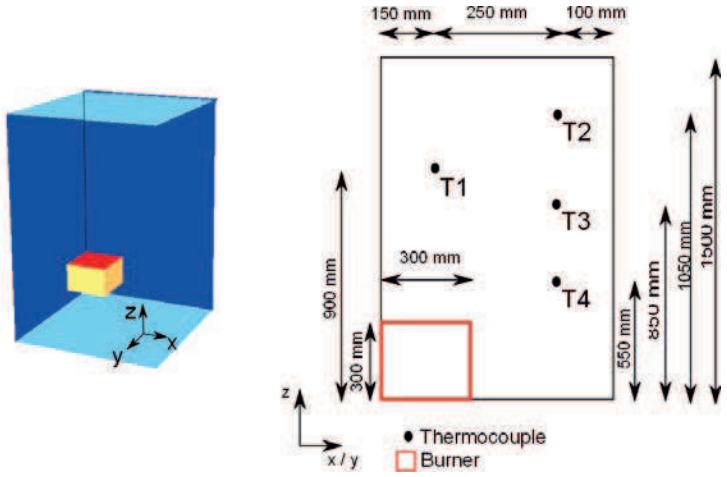

Figure 4.33: Positions of thermocouples above the propane burner

A finished scale simulation with only the burner is realised in order to compare the numerical and experimental temperatures. The burner simulation corresponds to the Transfeu fire scenario: 75 kW during 120 seconds and then 150 kW during 600 seconds. This explanation confirms the period time deviation of the burner temperatures found in figures 4.34. The initial aerodynamic conditions are the same as the the finished product scale. A HRR is prescribed to the surface burner, the same as the one used in the experimental HRR ramp. The gas phase composition and the effective heat of combustion are the ones related to the propane. The comparison results of temperature are presented in figures 4.34.

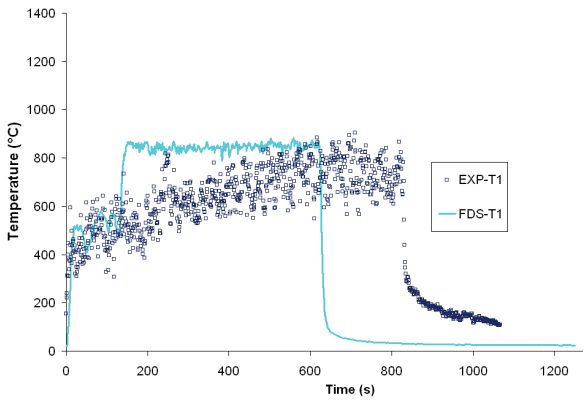

a/ Sensor T1.

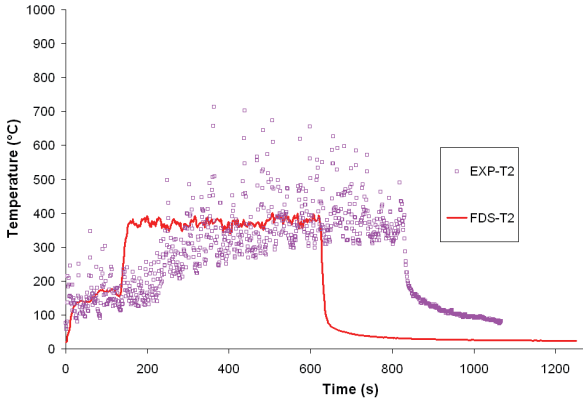

b/ Sensor T2.

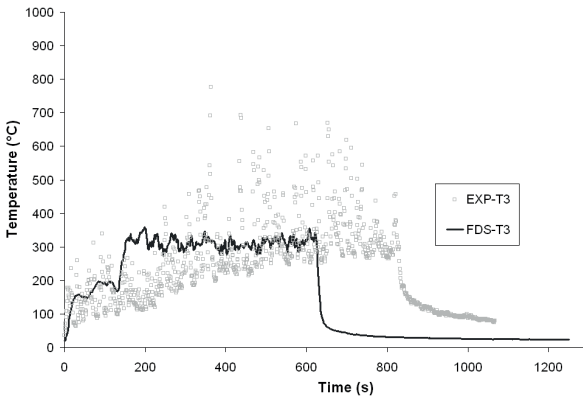

c/ Sensor T3.

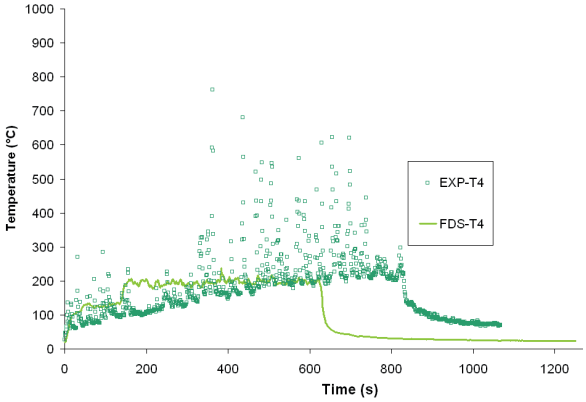

d/ Sensor T4.

Figure 4.34: Experimental and numerical temperature comparisons of the burner test only in the finished product scale configuration.

The numerical and experimental mean temperatures for each burner stage are presented in table 4.18. Considering all mean temperature values, the numerical temperatures have the same order of magnitude than experimental ones, taking into account the uncertainties due to the thermocouple itself and the position of the thermocouple into the flame. The numerical propane burner is supposed validated.

Table 4.18: Experimental and numerical mean temperature comparison for each burner stage

Thermocouple ($°C$)	**Experimental mean** 1^{st} **stage** **0 to 2** ***min***	2^{nd} **stage** 2 to 10 *min*	**Numerical mean** 1^{st} **stage** 0 to 2 *min*	2^{nd} **stage** 2 to 10 *min*
T1	500	780	565	850
T2	150	382	174	378
T3	160	350	196	340
T4	127	202	135	196

Seat

According to the results obtained from the material scale numerical simulation, the *fictive layer* thickness to be added depends on the external radiant heat flux value. In order to choose this thickness, a burner simulation is performed with the finished scale configuration but with no thermal and pyrolysis properties affected to the seat materials (figure 4.35a). The mesh size is 2.5 *cm* in all directions.

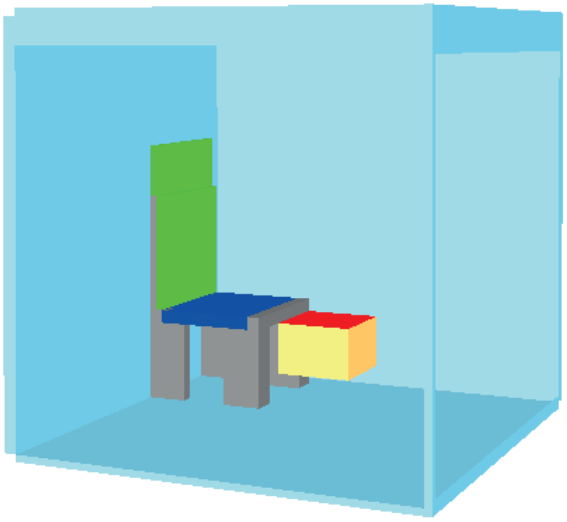

a/ Finished seat scale simulation geometry.

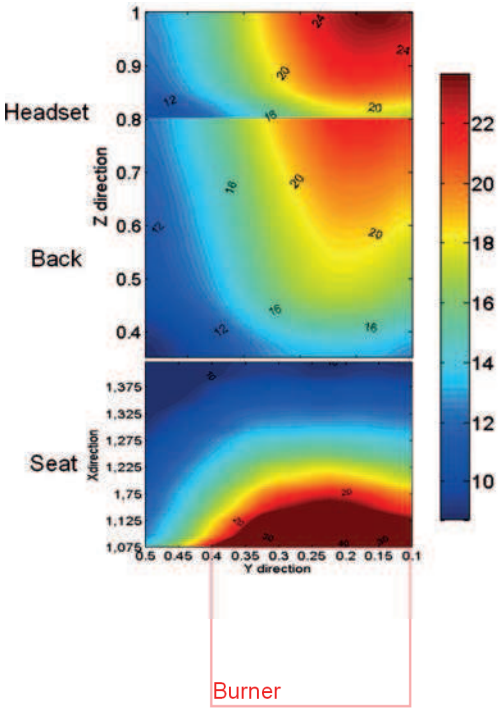

b/ Heat flux distribution of the seat from the burner.

Figure 4.35: Finished seat scale (numerical representation and heat flux distribution).

When the seat is exposed to the burner, the cushion, the back and the headset receive heat flux gradient from 10 to 40 $kW.m^{-2}$, as described by the heat flux distribution in figure 4.35b. This figure data are obtained from the beginning of the burner second phase (150 kW). It should be noted that the heat flux distribution is not continuous between

the back and the headset because they are not in the same y plan in FDS (4.35a). The burner is located in y direction from 0.1 up to 0.4 m.

At material scale, the lower external radiation heat flux, corresponding to the combustion of all materials (cover, interliner and foam), is 35 $kW.m^{-2}$. According to experimental results at finished scale and although the heat flux received by the seat are less than 35 $kW.m^{-2}$, the thickness of the fictive layer, used to reproduce gas gap during decomposition is set at 5.4 mm, equivalent to the 35 $kW.m^{-2}$ heat flux.

4.4.2.3 Input data

During Transfeu project, the real composition of the seat was investigated. In fact, the real seat back and cushion are composed of different layers:

- cover,
- protection against the vandalism,
- interliner,
- foam.

The headset is composed of a cover layer glued to the polycarbonate shell. The protection against the vandalism is composed of silicon, cotton and stainless steel wire mesh. This barrier protection material is added between the cover and the interliner layers, with a thickness which is assumed to be around 1.5 mm. Thermal properties of this barrier are estimated according to literature: it is supposed that after 350°C the cotton is entirely pyrolysed, then after 450°C the silicon is entirely pyrolysed, and only stainless steel wire mesh remains. These values (4.19) come from literature, Mc Adams (1961), ISO 10456 (2007) and Eckert *et al.* (1986) for instance. Moreover, the foam is thicker than the one tested during cone calorimeter experiments.

Table 4.19: Thermal properties of the vandalise protection material

Properties	**Units**	**Vandalise protection material**	
ε			0.9
Cp	$kJ.kg^{-1}.K^{-1}$	T(20°C)	1.25
		T(350°C)	0.88
		T(450°C)	0.44
λ	$W.m^{-1}.K^{-1}$	T(20°C)	0.53
		T(350°C)	2.87
		T(450°C)	17
effective ρ	$kg.m^{-3}$		4788

Finally, the seat is modelled as a multilayer material and shelled by a polycarbonate material:

- for the headset: a cover

- for the seat back: a cover, a protection against the vandalism and foam
- for the seat cushion: a cover, a protection against the vandalism, an interliner and foam.

The thermal properties of the polycarbonate is available in Langlais and Klarsfeld (2004) and ISO 10456 (2007). The chosen strategy is to use the validated thermal properties and the pyrolysis parameters validated at material scale. Only thermal properties are added to represent the protection against the vandalism layer, acting only as a thermal barrier one (table 4.19).

Concerning the gas phase in FDS, propane is chosen as main fuel composition and the fuel effective heat of combustion for the mixture fraction model. First, it is important to keep the combustion heat of the burner in order to accurately represent the heat flux received by the seat material. Then, the experimental total mass burnt of the finished product scale test is around 2.54 kg whose 1.76 kg is due to propane combustion. The main fuel is also propane. Moreover, it is important to keep in mind that the propane burner is also present during the real scale test. Carbon monoxide and soot mass yields are calculated from an open calorimeter test with only the burner and uncombustible materials for panels, ceiling and floor. The input data of the gas phase are summarized in table 4.20.

Table 4.20: Input data of the mixture fraction combustion model in FDS

Parameters	**Units**	
Composition		C_3H_8
$\Delta H_{combustion}$	$kJ.kg^{-1}$	46000
Y_{CO}	$kg.kg^{-1}$	0.025
Y_{Soot}	$kg.kg^{-1}$	0.009

4.4.2.4 Numerical results

Heat release rate Figure 4.36 presents the numerical and experimental HRR comparison for two different mesh sizes: 2.5 and 5 cm.

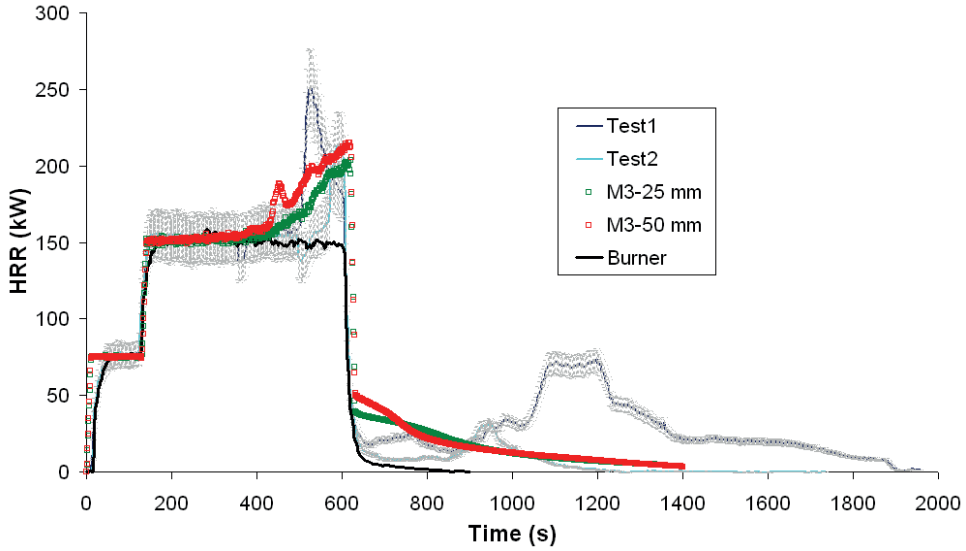

Figure 4.36: Numerical and experimental HRR comparison at finished product scale

Numerically, the top right corner of the seat cushion starts to ignites around 160 s (figure 4.36). Then, all materials burn, starting at 430 s. It should be reminded that during test 1, around 1000 seconds, the back felt down on the seat. Thus, only the HRR before 1000 seconds can to be compared with the numerical HRR for test 1. The intensity of the numerical HRR matches the experimental ones (figure 4.36). However, the kinetic of the numerical HRR is almost partially reproduced: experimentally the seat back combustion happens in two phases while numerically the combustion of seat materials is continuous. Moreover, the HRR intensity for a mesh size of 50 mm is higher than the one simulated with a mesh size of 25 mm.

Seat temperatures The comparison between experimental and numerical temperature (mesh size 5 cm) are showed in figures 4.37b, 4.37c, 4.37d, 4.37e, 4.37f, 4.37g and 4.37h. The thermocouples measure indirectly the temperatures received from the burner flame and from the seat flame. The experimental and numerical flame spread on the seat first starts to reach thermocouple T3, after the T9 and then all other thermocouples around 500 seconds. However, concerning sensors 1, 7, 16 and 18, the numerical temperatures continuously increase whereas these experimental temperatures suddenly raise at 500 seconds. The kinetic and the intensity of the experimental and the numerical temperatures have the same order of magnitude.

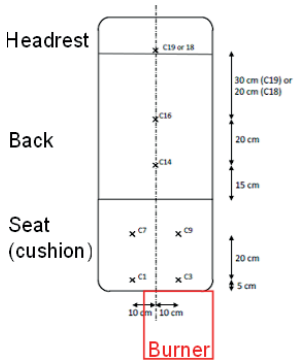

a/ Thermocouples locations on seat

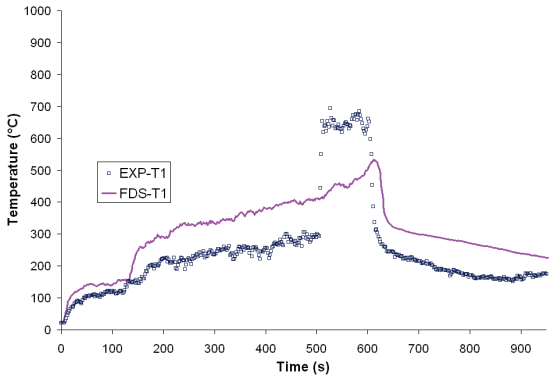

b/ Sensor T1

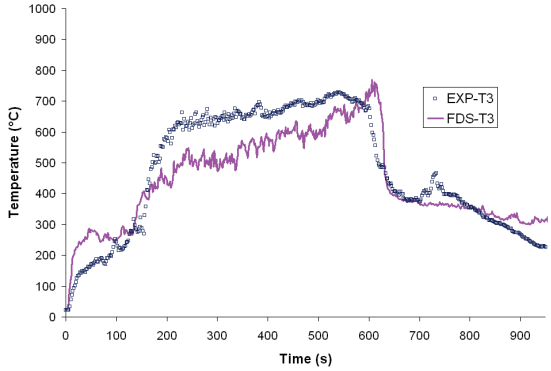

c/ Sensor T3

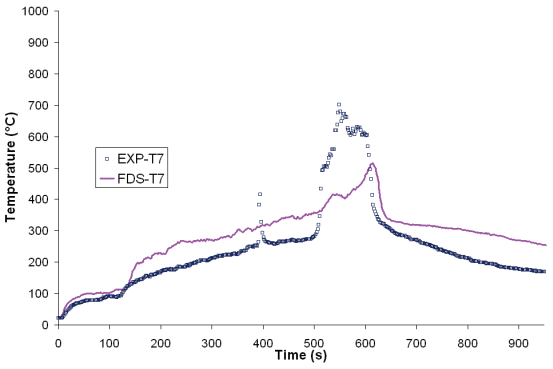

d/ Sensor T7

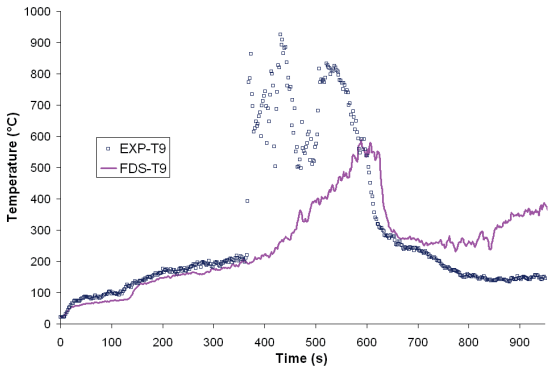

e/ Sensor T9

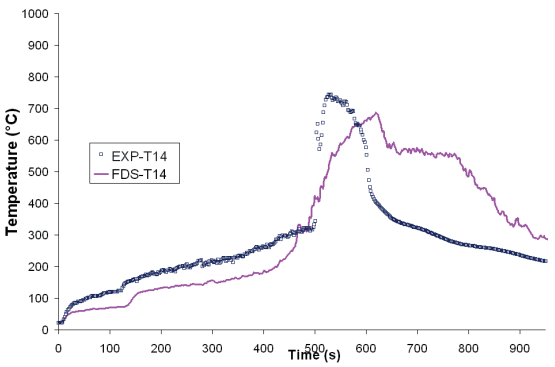

f/ Sensor T14

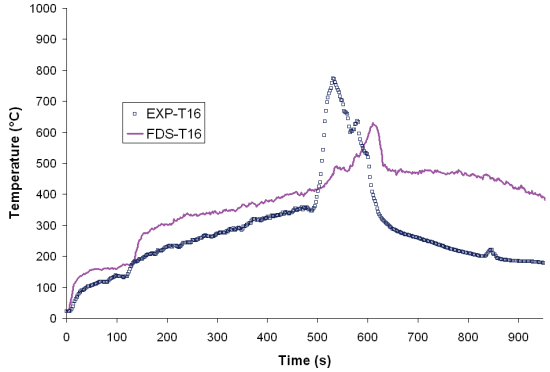

g/ Sensor T16

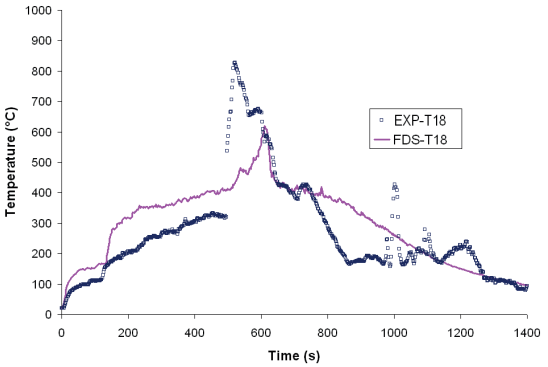

h/ Sensor T18

Figure 4.37: Experimental and numerical temperatures comparisons (mesh size 5 *cm*).

Total mass loss The numerical total mass loss of the seat product is also compared with the results of test 2 (table 4.21). The total mass loss of the seat from test 1 is not taken into account in this table because the mass is misrepresented due to the fall of the back on the seat. At 2.5 *cm*, the numerical mass loss is the same as the experimental one. Whereas, at 5 cm, the numerical mass loss is slightly higher than the experimental one.

Table 4.21: Comparison of the total mass loss of the seat product

	Total mass loss (kg)
Test 2	0.78
$FDS - 2.5\ cm$	0.78
$FDS - 5\ cm$	0.95

The effect of the mesh size on the total mass loss results is not negligible. In our case, the higher is the mesh size and the more the seat burns. Indeed, the heating up transfer of the seat arises from the burner flame. The heat transfer to the seat is a radiative and convective transfer. FDS models of radiative and convective heat transfer of the gas phase are sensitive to the mesh size.

Surface burnt area The final experimental and numerical surface burnt area of the seat are compared in figures 4.38 a and 4.38 b.

a/ Experimental surface burnt area at the end of the test, from Transfeu report.

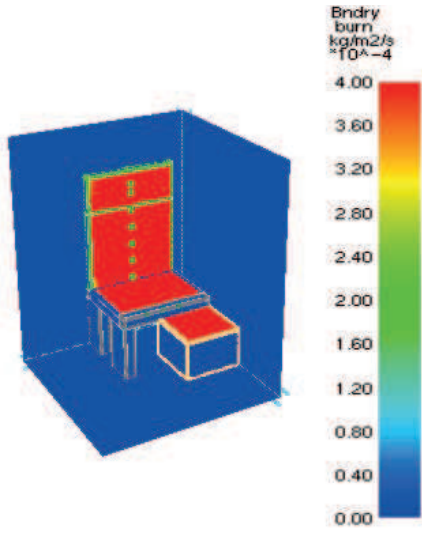

b/ Numerical surface burnt area at the end of the simulation.

Figure 4.38: Experimental and numerical surface burnt area comparisons.

For both numerical and experimental results, the seat external surfaces are completely burnt. Moreover, the experimental polycarbonate shell, located close to the burner and to the top of the headset (figure 4.38 a), has melt. For FDS simulation, the melting material can not be taken into account due to FDS model pyrolysis limits. Only the polycarbonate

thermal properties are considered in FDS, i.e. polycarbonate does not participate to the combustion.

Released gases Two different main fuels are present during the finished product seat test: one related to the propane burner and several ones released from the seat. According to the literature part, the generation of fire gases effluents are not only dependent on the type of material but also on the fire conditions. The mixture fraction combustion model, used in FDS, can only represent a well-ventilated fire with one global and infinitely fast combustion reaction: the kinetic of released gases is the same.

As explained in the section 4.4.2.3:Input data, propane is chosen as the main fuel for the combustion model. The total carbon dioxide and carbon monoxide mass flows produced by the burner alone are first compared before the comparison of the finished seat test.

The comparison results are shown in figures 4.39 a and 4.39 b respectively for the carbon dioxide and the carbon monoxide with the burner alone in an non-combustible environment.

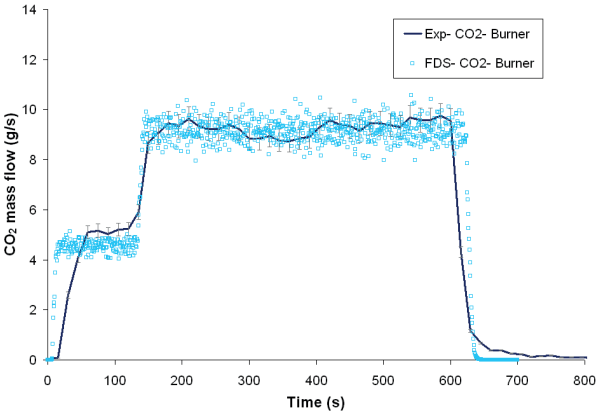

a/ Experimental and numerical comparison of the CO_2 mass flow of the burner only.

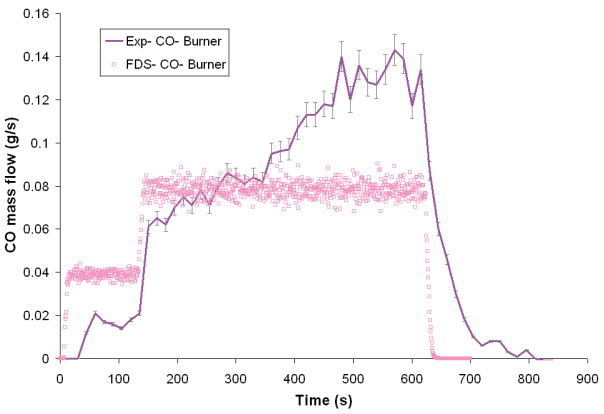

b/ Experimental and numerical comparison of the CO mass flow of the burner only.

Figure 4.39: Experimental and numerical gases mass flow comparisons.

Concerning the total quantity of carbon dioxide released by the burner, the numerical and experimental mass flow have the same kinetics and the same intensity. Whereas, the kinetic of released carbon monoxide is different for the both experimental and numerical responses. Nevertheless, the numerical carbon monoxide intensity has the same order of magnitude of the experimental one. Indeed, the input value of CO_{yield}, used in FDS, from table 4.20 is a mean of the released carbon monoxide quantity by the quantity of propane lost. Experimentally, the CO mass fraction evolves according to the type of fuel, the flame temperature and its residence time (Andzi Barhe (2004)). The flame dimension evolves due to the test configuration and temperature. Thus, the local combustion conditions changes and the CO mass fraction evolves. It means that the experimental carbon monoxide stoichiometry of the burner is not a scalar but a dynamic value, which evolves with time (figure 4.40b). Whereas in FDS, the CO production is function of the type of

the unique fuel and the mixture fraction model.

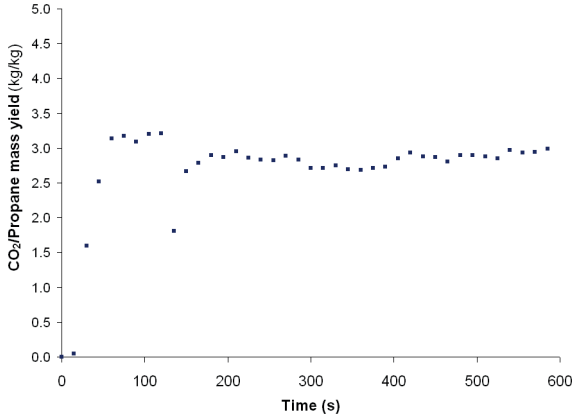

a/ Experimental mass yield of carbon dioxide on propane fuel: constant value.

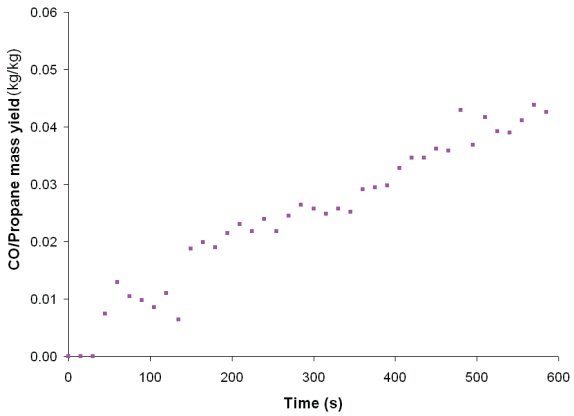

b/ Experimental mass yield of carbon monoxide on propane fuel: dynamic value.

Figure 4.40: Experimental mass yield of carbon dioxide and carbon monoxide from a propane fuel in the finished burner test condition.

Figures 4.41 a and 4.41 b present the numerical and experimental comparison of carbon dioxide and carbon monoxide from the finished seat test.

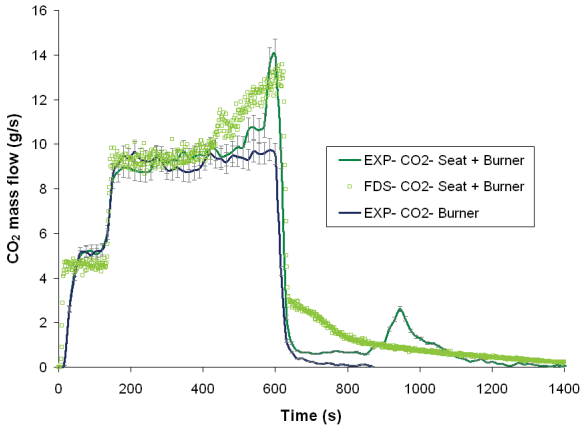

a/ Experimental and numerical comparison of the CO_2 mass flow of the finished seat test.

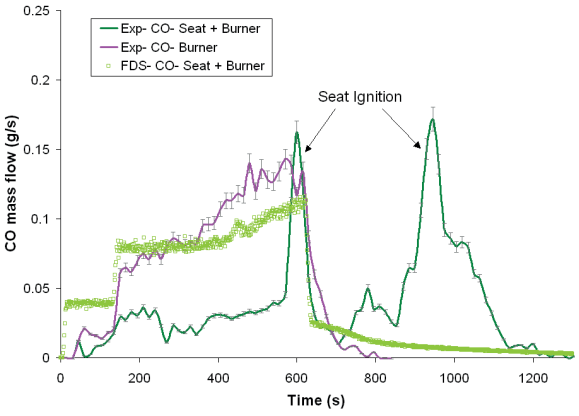

b/ Experimental and numerical comparison of the CO mass flow of the finished seat test.

Figure 4.41: Experimental and numerical comparison of the gases mass flow of the finished seat test.

In the simulation, the seat is involved in the combustion between 400 and 800 seconds approximately: only the propane burner participates to the combustion reaction before 400 seconds. Thus, before this time, the comparison between the experimental and numerical data show that they are very close (as for the previous comparison with burner only). Then, numerical carbon dioxide is released during the same combustion period with the combustion reaction stoichiometry of the propane fuel. Despite this important combustion model difference, the carbon dioxide mass flow comparison is quite good.

Concerning the release of carbon monoxide, before the seat ignition, there is a difference between the experimental burner alone and experimental finished seat test. Indeed,

before this period, the propane burner releases two times more carbon monoxide than the finished seat test one, whereas only the propane burner participates to the combustion. This mass flow difference comes from the position of the burner. In fact, when only the burner is tested (with uncombustible products), it is placed in the corner whereas when the burner and the seat are tested, it is place above the seat (figure 4.35). The burner position has an impact on the flame distribution and height. It is possible that the flame height of a burner placed in the corner is higher than the one located above the seat. Thus, the change of burner position implies a difference on the carbon monoxide production.

Then, two sudden peaks of carbon monoxide are identified in figure 4.41 b due to the seat ignition. Like the numerical released gases results from the propane burner, the carbon dioxide and the carbon monoxide mass flows have the same trend. For the finished seat test, the comparison between experimental and numerical carbon monoxide released has failed. The numerical carbon monoxide mass flow, from the seat test simulation, is closer than the experimental carbon monoxide mass flow from the propane burner test instead of the experimental seat test one. This divergence may come from the FDS combustion model (mixture fraction model and a global combustion reaction of a unique fuel).

4.5 Discussion

The first section allowed to characterise the thermal decomposition of the seat different constituents, known as the cover, the interliner and the foam. According to several TGA tests and a review of each material, a global reaction mechanism is proposed. Then, in a second step, according to the material knowledge, the position of the material in the seat product and the FDS pyrolysis and combustion model limits, the global reaction mechanism is simplified for each material. Indeed, the seat cover reaction mechanism is simplified from six to two reactions, then for the seat interliner from six to three reactions and finally for the foam from seven to two reactions. After this mechanism simplification, the pyrolysis parameters have been assessed for each chosen mechanism according to the experimental mass loss rate at a given atmosphere, an optimisation tool and the FDS pyrolysis model. Moreover, the experimental mass loss rate has been chosen according to the position of each material into the seat and the atmospheric condition hypothesis on the seat surface. In fact, it is assumed that in real condition the local atmospheric condition is composed of air on the seat cover surface. Afterwards, it is supposed that the atmospheric condition above the interliner surface (placed between the cover and the foam) is closer to the nitrogen atmosphere than air atmosphere. Concerning the foam decomposition, it is assumed that the atmospheric condition is close to air atmosphere because of the foam nature (formation of an air gap between the interliner and the decomposed foam during the reaction-to-fire of the seat). The optimized pyrolysis parameters correspond to the input data of the FDS pyrolysis model.

Then, the numerical FDS code is used to simulate the reaction-to-fire from the material to the finished scales. At material scale, the aim is to model the reaction-to-fire of

small piece (10 by 10 cm) of a seat material (from the top surface to the back: the cover, the interliner and the foam) exposed at different heat flux from 20 to 75 $kW.m^{-2}$. After a review of the required thermal and thermodynamic properties of each material, the seat reaction-to-fire is modelled and compared to experimental results, such as the mass loss rate and the heat release rate obtained from cone calorimeter tests. The first comparisons are not in accordance. Thus, according to the seat reaction-to-fire understanding, an additional fictive layer has been added between the interliner and the foam. This *fictive layer* represents the decomposition of a small area of the foam to volatiles gases. These released gases are supposed to not participate in the combustion. Furthermore, the foam conductivity has been fitted due to the physical change of the seat and the thermal feedback from the silica wool. The reaction-to-fire simulation of these equivalent seat materials is in agreement with the experimental results, taking into account the uncertainties. The main inconvenient is that the *fictive layer* thickness is dependent of the external heat flux received by the seat surface. However, this dependence is an empiric linear function between the inverse of the fictive foam thickness and the external heat flux. Afterwards, these equivalent seat materials and the validated input data are tested at the finished product scale.

The principle of the finished seat scale is to correctly simulate the burner flame in the test configuration in a first time and the reaction-to-fire of the seat in a second time. The seat heating type between the material and the finished scales is different. The first one uses a conical electrical heater and the second one applies a flame burner. The propane burner is simulated alone (without combustible materials) and compared with experimental results. The numerical propane burner is supposed validated according to the correct temperatures agreement for the two successive power phases. Then, the tested seat product was not only composed of the multilayer materials tested during the material scale. Vandalise protection materials are located between the cover and the interliner. Thus, another material layer is added into the seat back and cushion to simulate the reaction-to-fire. It is assessed that this vandalise protection material plays only a thermal barrier role and does not participate to the combustion. Moreover, due to the FDS combustion model limit, propane has been chosen as the fuel reagent of the combustion. Despite the addition of a new material into the seat (not studied at material scale) and the presence of different types of fuel during the finished seat test, the numerical results are in accordance with the experimental ones, except for the carbon monoxide mass flow response. This difference regarding carbon monoxide can come from:

- The FDS combustion reaction: indeed the stoechiometry of the reaction is different for propane and for the seat.
- The input data of the gas phase reaction: the gas phase input data (the CO yield) corresponds to the propane one. However, when the propane burner was tested alone, its position was in the corner whereas when the propane burner was tested with seat, the burner was located above the seat and not in the corner. It is well known that the corner can impact the flame spread and thus the CO quantity.

Chapter 5

Multi-scale comparison results on wall panel

Contents

5.1 Raw matter scale

The GRP composite is composed of two parts: a polyester gelcoat and a hand-laminated glass fibres/polyester/mineral fillers composite. The crucible of the TGA test was only filled with composite material because the gelcoat layer is too thin. Thus, the TGA results reported in this chapter only focus on composite and especially on the resin matrix. The TGA results of the normalised mass loss and the mass loss rate of the glass reinforced polyester (GRP) composite under air and nitrogen atmospheres for two heating rates (5 and 10 K/min) are respectively presented in figure 5.1.

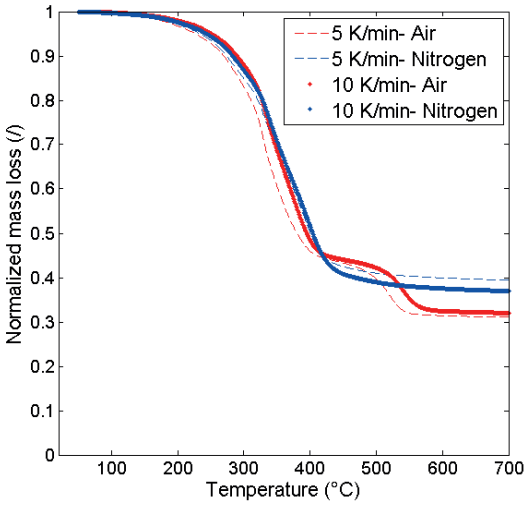

a/ Normalised mass loss results of the GRP composite.

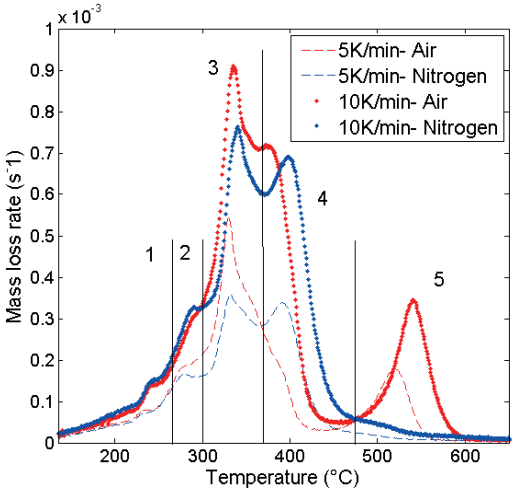

b/ Normalised mass loss rate results of the GRP composite.

Figure 5.1: Thermal decomposition of the GRP composite under air and nitrogen atmospheres for two different heating rates 5 and 10 K/min.

Under nitrogen atmosphere, four successive reactions are visually observed:

- Between 200 and 260°C: the normalised mass loss begins to decrease and inversely the mass loss rate raises until it reaches a peak at 250°C. According to Kandare *et al.* (2008), this reaction is assessed as water dehydration.
- Between 260 and 300°C: the mass loss rate suddenly increases and reaches a peak at 300°C. This mass loss is associated to the ATH decomposition in alumina oxide and water vapour (Cerin-Delaval (2010)).
- Between 300 and 380°C: the mass loss rate accelerates again and reaches an other peak at around 320°C, then the mass loss rate decreases. The polyester starts to decompose by random chain scission mechanism (Marquis (2010)) during this temperature stage.
- Between 380 and 450°C: the mass loss rate briefly increases in order to reach a peak at at around 400°C and then decreases until 430°C. The polyester finishes to decompose into a char. Around 35% of the initial mass remains into the crucible.

Five major reactions or groups of reactions occur under air atmosphere:

- Between 200 and 300 °C: the mass loss rate increases in order to reach a shoulder at around 200°C, then the mass loss rate suddenly raises and reaches another shoulder at 300°C. The first two successive steps occur under air and under nitrogen atmospheres. Oxygen has no influence on these reactions. The author assumed that this reaction is associated to dehydration, then the ATH decomposition in alumina oxide and water vapour (Cerin-Delaval (2010)).
- Between 300 and 450 °C: the mass loss rate curve accelerates and then reaches a peak at around 320°C, as under nitrogen atmosphere. Then, the mass loss rate

decreases and a shoulder is observed at around $350°C$. This shoulder is more pronounced at $10K/min$ than at $5K/min$. In this temperature range, two simultaneous reactions may occur: the polyester decomposition and oxidation in order to form a char. The oxygen presence may accelerate the second reaction. The author has chosen to gather these two reactions in order to simplify the reaction mechanism and to avoid any mistake on thermal properties estimation at material scale simulation.

- Between 450 and 600 $°C$: the mass loss rate suddenly raises until the temperature of $550K/min$ and then decreases until around $600K/min$. According to several reviews, this step corresponds to char oxidation (Kandare *et al.* (2008), Lautenberger *et al.* (2008) and Marquis *et al.* (2012))

The GRP composite is composed of ATH, polyester and glass fibres. According to the literature part, the decomposition temperature of glass fibres is around $1{,}000°C$, i.e. only ATH and polyester participate in the decomposition process in the TGA tests. Thus, three general decomposition steps or reactions are identified under air and nitrogen atmospheres, as described in figure 5.2.

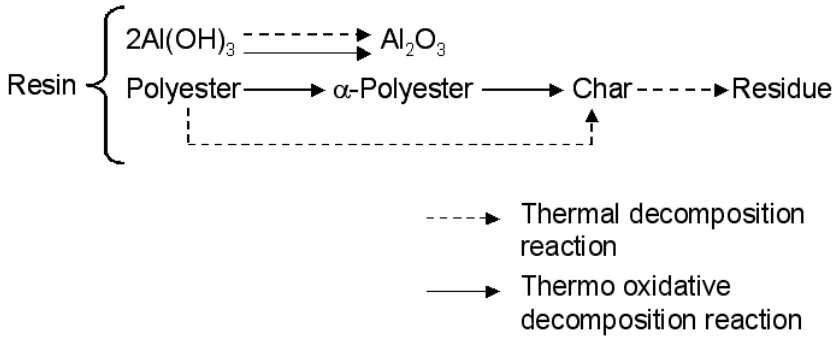

Figure 5.2: Structural unit of aramide polymer

In the multi-scale approach, FDS pyrolysis parameters are estimated with the FDS pyrolysis model used at the material scale, the semi-finished product scale, the finished product scale and the real scale. For the same reasons as those explained in the seat raw matter part, FDS pyrolysis parameters are estimated under air atmosphere. Thus, three reactions are used to define the reaction mechanism of the resin decomposition, one for ATH and two for polyester (table 5.1 where the $Y_{r,t/o,j}$ is the residual mass fraction).

Table 5.1: Reduced reaction mechanism of the thermal oxidative decomposition of the GRP composite.

Number of reaction	Type of reaction	Reagents		Products		
1	Thermal	ATH	$\rightarrow$	$Y_{r,t,ATH}$ Al_2O_3	+	$(1 - Y_{r,t,ATH})$ $3H_2O$
2	Thermo oxidative	Polyester + O_2	$\rightarrow$	$Y_{r,o,p}$ Char	+	$(1 - Y_{r,o,p})$ gases
3	Thermo oxidative	Char + O_2	$\rightarrow$	$Y_{r,o,ch}$ Residue	+	$(1 - Y_{r,o,ch})$ gases

The reduced reaction mechanism of the GRP composite is divided into two independent reaction mechanisms: the first one linked to the ATH decomposition and the second one related to the polyester decomposition. The FDS pyrolysis decomposition model (Eq 5.8 and 5.9) is applied to these reaction mechanisms (table 5.1) in order to estimate the GRP composite pyrolysis parameters. The total normalised mass loss rate is the sum of each species normalised mass loss rate:

$$\frac{dY_{tot}}{dt} = \frac{dY_{ATH}}{dt} + \frac{dY_{Al_2O_3}}{dt} \tag{5.1}$$

and

$$\frac{dY_{tot}}{dt} = \frac{dY_{Polyester}}{dt} + \frac{dY_{char}}{dt} + \frac{dY_{Residue}}{dt} \tag{5.2}$$

with

$$\frac{dY_{ATH}}{dt} = -\dot{\omega}_1 \tag{5.3}$$

$$\frac{dY_{Al_2O_3}}{dt} = Y_{r,t,ATH}\dot{\omega}_1 \tag{5.4}$$

$$\frac{dY_{Polyester}}{dt} = -\dot{\omega}_2 \tag{5.5}$$

$$\frac{dY_{char}}{dt} = Y_{r,t,p}\dot{\omega}_2 - \dot{\omega}_3 \tag{5.6}$$

$$\frac{dY_R}{dt} = Y_{r,o,ch}\dot{\omega}_3 \tag{5.7}$$

Finally we obtained:

$$MLR = \frac{dY_{tot}}{dt} = \sum_{i=0}^{N} \left(Y_{r,i} - 1\right) \dot{\omega}_i \tag{5.8}$$

with

$$\left(\dot{\omega}_i\right) = \left(Y_j\left(t\right)\right)^{n^i} A_i exp\left(\frac{-E_{a,i}}{RT}\right) \tag{5.9}$$

The unknowns of this equation system are $(Y_{r,i}, n_i, A_i, E_{a,i})_{i=1toN}$, with i the number or reaction. The input data of this system are the experimental normalised mass loss rate $\frac{dY_{exp}}{dt}$ and the boundaries:

$$\begin{cases} Y_{ATH}\,(t=0)=1 \\ Y_{Al_2O_3}\,(t=0)=0 \\ Y_{Polyester}\,(t=0)=1 \\ Y_{ch}\,(t=0)=0 \\ Y_{R}\,(t=0)=0 \\ T\,(t=0)=373K \end{cases} \tag{5.10}$$

The solution of each reaction pyrolysis parameters are optimized with the GA process, according to the explanations given in the chapter 3: Multi-scale approach.

The used strategy is to separately optimize pyrolysis parameters because there are two independent reactions and to save calculation time. The ATH reaction decomposition is the same under air and nitrogen atmospheres. Pyrolysis parameters of the ATH reaction are optimized under nitrogen atmosphere, while the ones corresponding to polyester reactions are optimized under air atmosphere at 5 and 10 K/min (figures 5.3 a and 5.3 b).

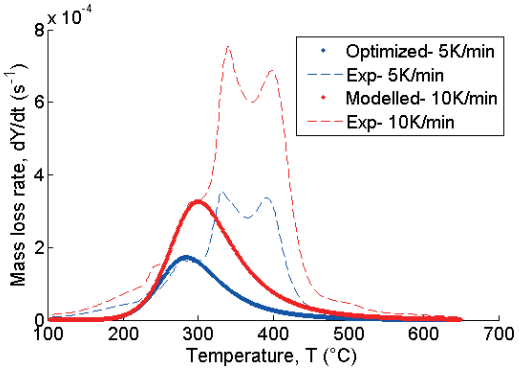

a/ Experimental and optimized mass loss rate under nitrogen atmosphere at 5 and 10 K/min of the ATH reaction (first reaction).

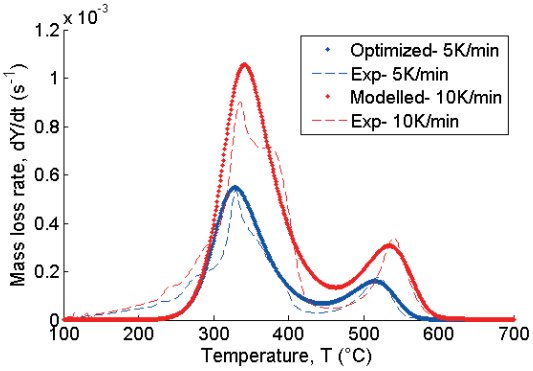

b/ Experimental and optimized mass loss rate under air atmosphere at 5 and 10 K/min of the Polyester reaction (second group of reactions and last peak).

Figure 5.3: Experimental and optimized mass loss rate of the ATH and polyester reactions.

The associated optimized pyrolysis parameters are shown in table 5.2 for each reaction.

Table 5.2: Optimized pyrolysis parameters of the GRP composite

Reaction, *i*	A_i (s^{-1})	$E_{a,i}$ $(kJ.mol^{-1}\ )$	n_i	$Y_{r,i}$ $(kg.kg^{-1})$	**Atmosphere**
1	$2.05.10^{7}$	105	2.88	0.76	Inert and Air
2	$6.60.10^{11}$	157	2.83	0.40	Air
3	$6.36.10^{9}$	176	1.06	0.65	Air

It is not necessary to gather the ATH and the polyester modelling in the same graph

because these two species are separately modelled at upper scale too. Visually, the experimental and the numerical mass loss rates of the ATH and the polyester reactions at 5 and 10 K/min are close based on their intensities and phase angles.

Table 5.3: Euclidean analysis on MLR for each heating rate

External radiant heat flux K/min	**Euclidean relative deviation** %	$cos(\Theta)$
ATH step		
5	3	0.947
10	10	0.963
Polyester steps		
5	17	0.966
10	15	0.970

The relative deviation between the experimental and the modelled mass loss rate is presented in table 5.3 for each heating rate, between 200 and 350°C for the ATH step and between 200 and 600°C for the polyester decomposition steps, according to the Euclidean comparison equation. The relative deviation is included between 3 and 17% and the $cos(\Theta)$ value is close to one. Let us remind that higher $cos(\Theta)$ result is close to one and better is the phase angle between two curves.

Deviation relative results seem sufficient to predict the MLR at this scale, taking into account the simplification of the reaction mechanism and experimental uncertainties (the repeatability, the TGA apparatus and the material heterogeneity). Thus, this reaction mechanism and the optimised pyrolysis parameters are used in the FDS pyrolysis model at upper scale.

5.2 Material scale

5.2.1 Experimental results

The experimental heat release rate (HRR) and the MLR of the GRP composite at different external heat fluxes from the cone calorimeter test (ISO 5660-1 (2002)) are presented in figures 5.4 a to e. Each test at a given external radiation heat flux is repeated three times. Figure 5.5 gathers the MLR mean from each external radiation heat flux. The relative uncertainty is added for each heat flux level. This uncertainty takes into account the repeatability and the uncertainty due to the measurement.

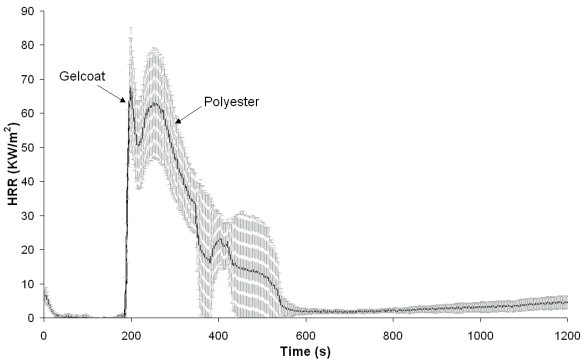

a/ Experimental HRR of the GRP composite materials from an external radiation level of 20 $kW.m^{-2}$.

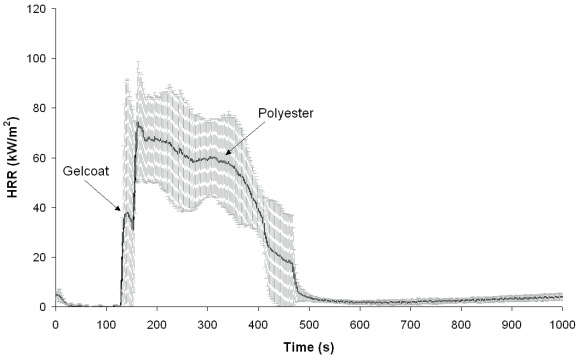

b/ Experimental HRR of the GRP composite materials from an external radiation level of 25 $kW.m^{-2}$..

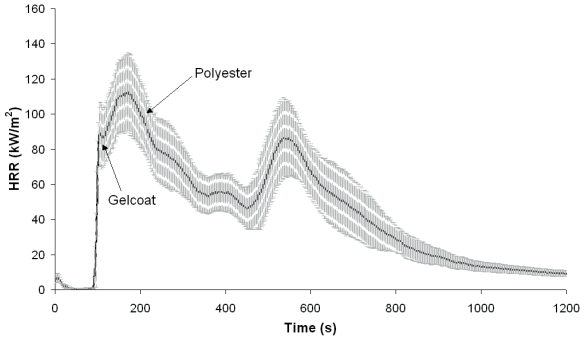

c/ Experimental HRR of the GRP composite materials from an external radiation level of 35 $kW.m^{-2}$..

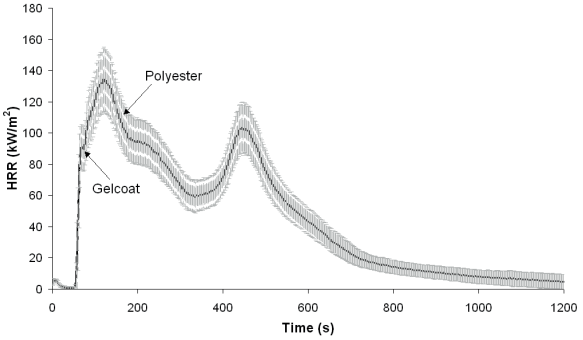

d/ Experimental HRR of the GRP composite materials from an external radiation level of 50 $kW.m^{-2}$..

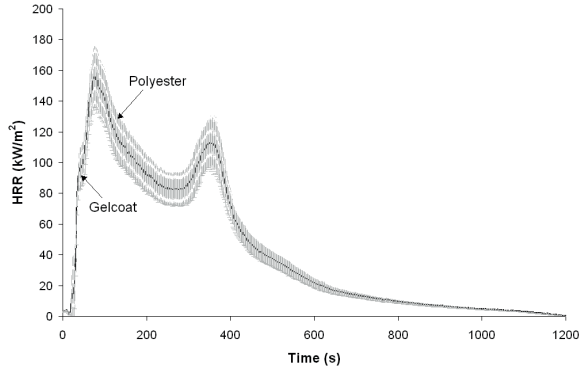

e/ Experimental HRR of the GRP composite materials from an external radiation level of 75 $kW.m^{-2}$.

Figure 5.4: Experimental HRR of the GRP composite materials from an external radiation level.

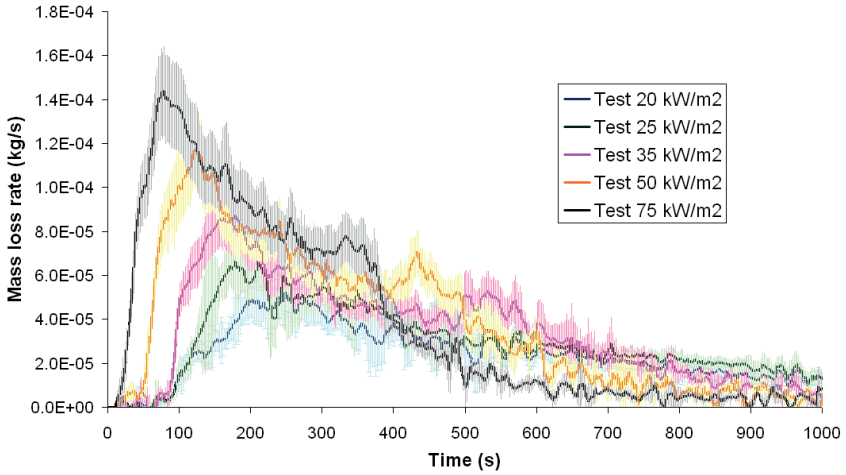

Figure 5.5: Experimental MLR of the GRP composite materials from several external radiation levels.

Concerning the HRR and the MLR results, two types of behaviour are observed, one for high incident heat flux (35 up to $75kW.m^{-2}$) and a second one for lower heat fluxes (20 and $25kW.m^{-2}$). The high external heat flux is characterised by a sudden shoulder followed by a peak, then a decreasing of HRR or MLR, and at least a second sudden peak is observed. The higher the external heat flux, the faster the second sudden peak occurs.

The HRR or MLR shoulder is due to the gelcoat, the visible part of the composite. The first HRR or MLR peak corresponds to the combustion of the composite and especially the polyester. Then the second peak is due to the backing conditions effect.
However, under lower external heat flux, two sudden HRR peaks are observed, the first one is due to the gelcoat and the second one corresponds to the composite reaction-to-fire. Moreover, for the second behaviour, the repeatability between each test is difficult due to the low heat flux and the material heterogeneity. Indeed a low external heat flux implies a bidirectional (laterally and deeply) heat transfer through the material. On the contrary, under high external heat flux, the unidirectional 1D transfer through the material controls the heat conduction. Thus, it is possible that under low external heat flux, the GRP composite decomposes and burns more on the material surface than under high external heat flux. It should be reminded that the GRP is composed of 25% of glass fibres, which remain stable until 1,000$°C$. The presence of glass fibres and of the material heat transfer orientation could explain the difference between these two types of behaviour during the first seconds:

- For high incident heat flux, the unidirectional 1D heat transfer through the material leads to the resin combustion and a rapid decrease due to the presence of glass fibres into the resin. The second peak is due to the thermal feedback received from the silica wool placed behind the material bottom (Brown *et al.* (1988) and Carvel *et al.* (2011)). The material becomes thermally thin and pyrolysis rate increases. It is not a material but a test characteristic, dependant on thermal backing conditions.
- For the lower incident heat flux, the GRP decomposes and burns through the ma-

terial surface. The heat release is reduced due to the presence of each glass fibre layer. The external heat flux is not high enough to heat up the silica wool behind the material and to suddenly rise the heat released.

To sum up, when the composite is exposed to external incident heat flux, the resin matrix starts to decompose. If volatile fuels are produced in sufficient quantity such as their concentration at material surface reaches the lower flammability limit, the fuel ignites and a charcoal layer is formed at the material surface. This char and the glass fibres:

- Protect the virgin resin matrix from the external heat remaining,
- Prevent oxygen diffusion through the material,
- Reduce the diffusion of pyrolysis gases through the material surface.

The composite reaction-to-fire is also defined in figure 5.6 at material scale.

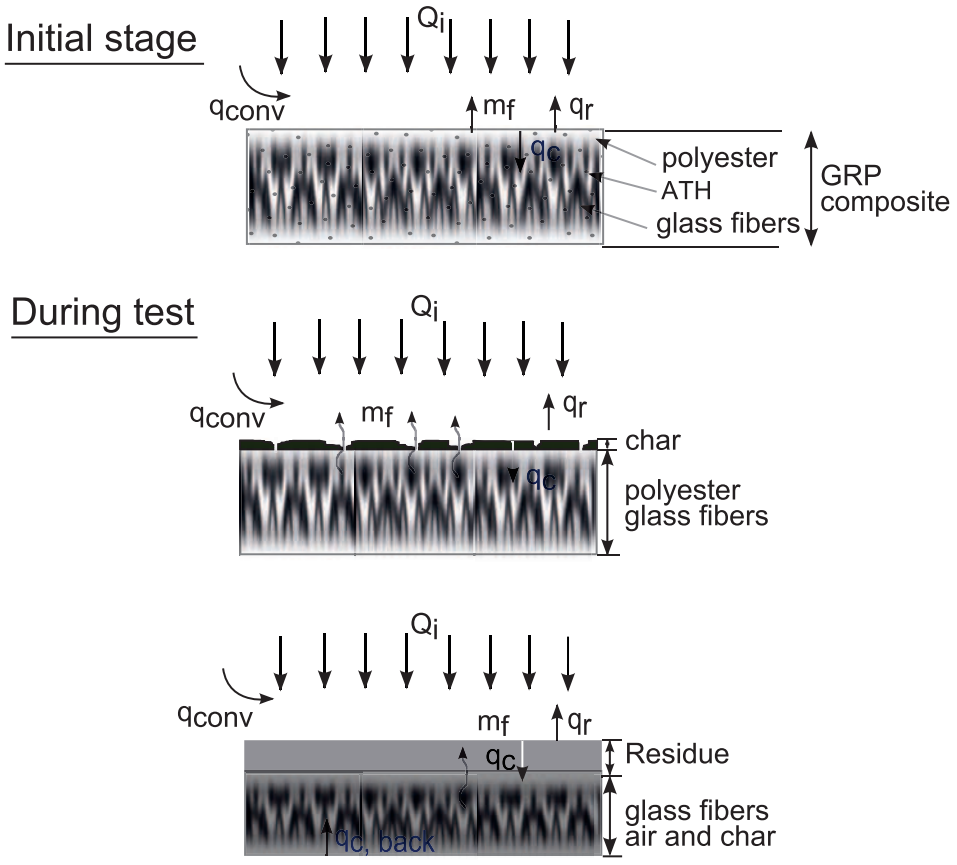

Figure 5.6: Experimental reaction-to-fire of the GRP composite at material scale

A summary of characteristic data for each heat flux is presented in table 5.4.

Table 5.4: GRP composite properties according to the heat flux

Parameters	Units	Values				
$\dot{q}_i''$	$kW.m^{-2}$	20	25	35	50	75
$\overline{t_{ig}}$	s	208±35	140±13	93±4	55±3	24±5
$\overline{\dot{q}''_{max}}$	$kW.m^{-2}$	68±8	75±12	113±11	134±10	156±10
$\overline{THR}$	$MJ.m^{-2}$	11.2±4.1	19.6±0.7	52.7±1.0	53.6±3.1	51.2±1.3
$\overline{\triangle m}$	g	20.7±1.6	29.4±1.1	35.2±1.0	39.4±0.9	40.4±0.7
$\Delta H_{combustion}$	$kJ.kg^{-1}$	4.8±1.6	6.1±0.2	13.4±0.2	12.1±0.9	11.2±0.1

The Thermal Response Parameter (TRP) is assessed according to the experimental cone calorimeter tests data (incident heat flux and ignition delay time, figure 5.7). It represents the material heating-up characteristic. The TRP equals 470±61 $kW.s^{-0.5}.m^{-2}$.

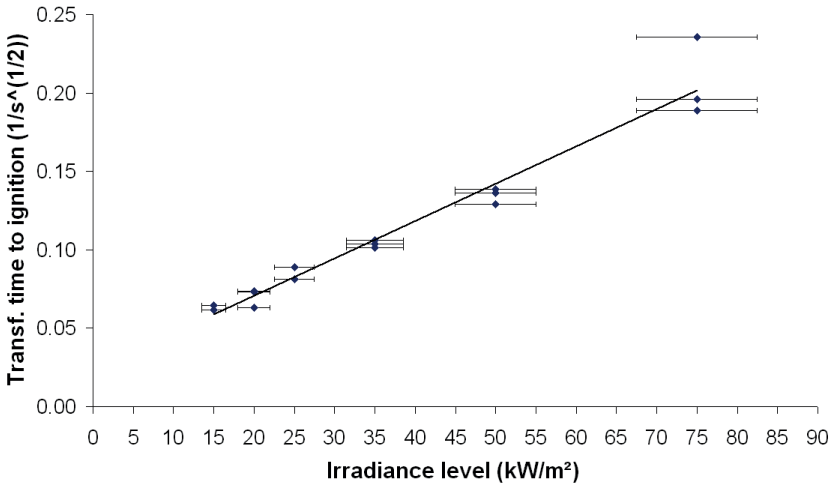

Figure 5.7: Relation between transformed ignition time and the incident heat flux of the cover

The critical heat flux (CHF) has a negative value according to the model used in figure 5.7. The CHF cannot be assessed with this model for this studied material, as boundary conditions drive its behaviour at low heat flux.

5.2.2 Modelling approach

The GRP experimental study at material scale enables to better understand the global GRP material reaction-to-fire. The reaction-to-fire modelling is performed by the FDS code. The simplified reaction mechanism and their associated pyrolysis parameters are used, as the FDS pyrolysis model input data, in order to predict the wall panel thermal decomposition. Other thermodynamic and thermal properties are required to solve the

heat and thermal balances at the material surface. The experimental and numerical comparison is based on the GRP heat release rate and mass loss rate. When the FDS input data are validated at this scale, there are transferred at the upper scale. The modelling approach is summarized in figure 5.8.

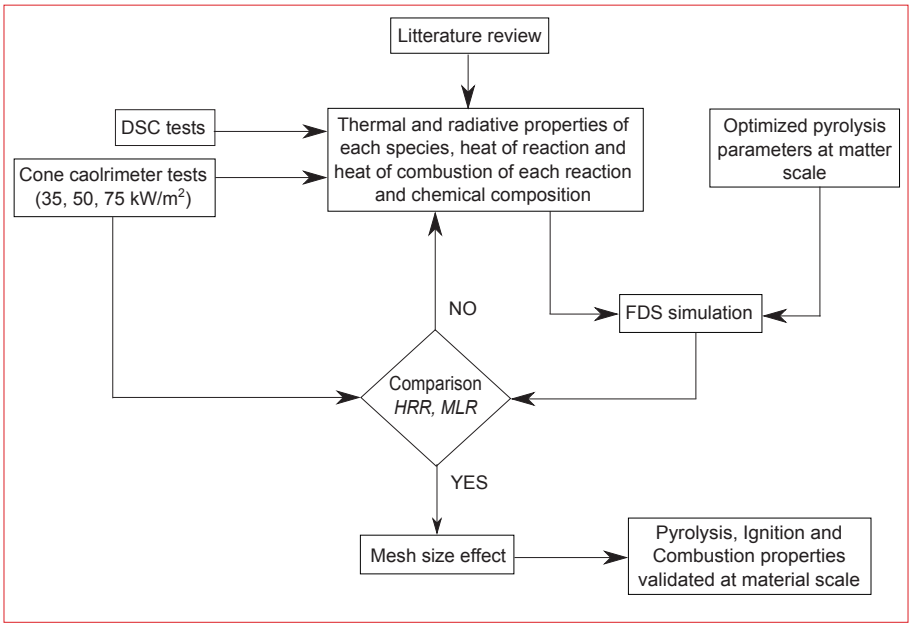

Figure 5.8: Material scale approach (Pyrolysis, Ignition and Combustion input data validation)

5.2.2.1 Mesh size

As for multilayer seat materials, criteria (Eq 64) are satisfied for a 1.25 *cm* mesh size and almost satisfied for a 2.5 *cm* one. The numerical geometry of the conical heater and the sample holder respects the standard geometry dimensions given by ISO 5660-1 (2002).

5.2.2.2 Initial boundaries

Aerodynamic, radiative and thermal conditions are the same as the multilayer seat materials, see section 4.3.2.2.

5.2.2.3 Numerical results

The GRP composite is structured as mast glass fibres linked by the resin matrix. The gelcoat, located above the composite, is associated to a thick polyester resin layer. The whole is shelled by a 5 *cm* thick sample holder. A layer of silica wool (around 4.52 *cm*) is placed under the composite to compensate the space between the composite and the sample holder.

The great challenge is to model the reaction-to-fire with pyrolysis parameters, validated

at matter scale, and thermo-radiative properties of each component, obtained by literature: the thermal properties and the density of each species are assessed according to literature or supplier data (1.13, section literature review). Since thermal and radiative properties (emissivity, conductivity and specific heat) of transient species (Char, Intermediate species or Residue) are unknown, thermal properties of virgin materials are applied. The effective heat of combustion of each material is estimated from the cone calorimeter results at an incident heat flux of 50 $kW.m^{-2}$. The heat of reaction of each reaction is one of the most difficult input data to estimate due to the thermal decomposition phenomena. For example, several reactions can occur at the same time and can result from several endothermic and exothermic reactions, through DSC measurement. Consequently, these data are fitted according to experimental data but always in the order of magnitude of a heat of reaction found in the literature (Drysdale (2011)).

The strategy used to represent the GRP composite in FDS is to separate the gelcoat and the composite in two distinct layers. The gelcoat is modelled as mixture of 11% of ATH, 35% of polyester resin and 54% of mineral compounds, as described in the literature part. The composite is also a combination of 29% of ATH, 46% of polyester resin and 25% of glass fibres. All these percentages correspond to a mass yield. The ATH decomposes in one step whereas the composite pyrolysis does in two concomitant steps. Their associated pyrolysis parameters are presented in table 5.2. However, FDS pyrolysis model aims to model fuel production. The ATH one-step reaction releases aluminium oxide and water vapour, i.e. no fuel. In FDS, the mass fuel production from surface material is corrected by a ratio of material heat of combustion by the gas phase one. Thus, ATH heat of combustion is taken close to zero in order to do not participate in gas phase combustion reaction. ATH action in condensed phase is considering while water vapour action can not be taken into account in gas phase.

The polyester is chosen for the gas phase input data because it is the only fuel involved in the combustion reaction. The data related to the polyester in the gas phase are summarized in table 5.5.

Table 5.5: Input data of the mixture fraction combustion model in FDS

Parameters	**Units**	
Composition		$C_1H_{1.039}O_{0.2}$
$\Delta H_{combustion}$	$kJ.kg^{-1}$	13000
CO_{yield}	$kg.kg^{-1}$	0.045
$Soot_{yield}$	$kg.kg^{-1}$	0.047

The comparison between experimental and numerical HRR and MLR of the cone calorimeter test from several incident heat fluxes is reported in the following figures 5.9 a to j.

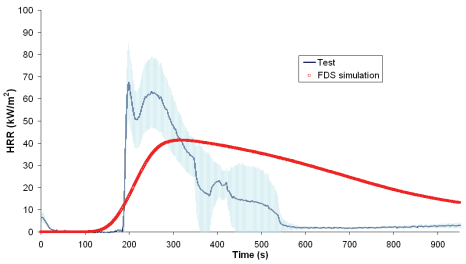

a/ Experimental HRR, 20 $kW.m^{-2}$.

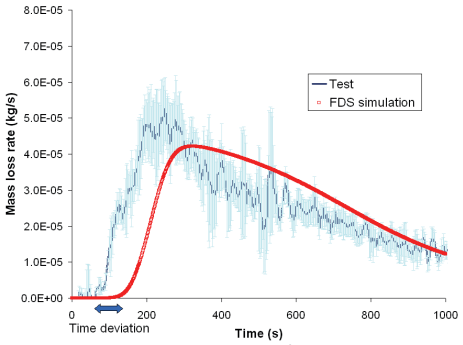

b/ Experimental MLR, 20 $kW.m^{-2}$.

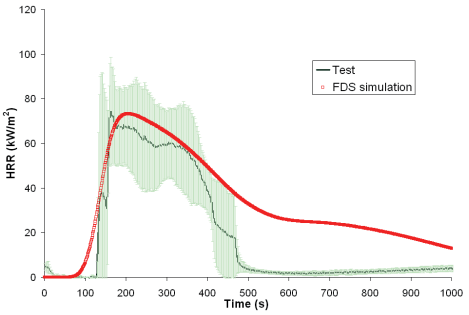

c/ Experimental HRR, 25 $kW.m^{-2}$.

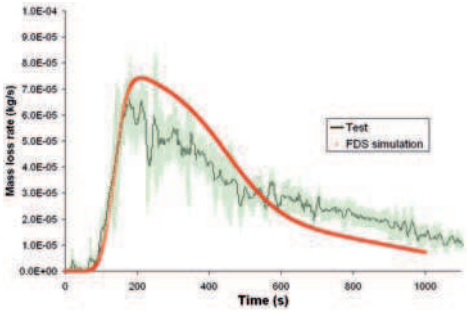

d/ Experimental MLR, 25 $kW.m^{-2}$.

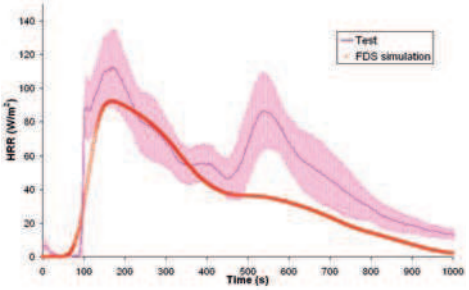

e/ Experimental HRR, 35 $kW.m^{-2}$.

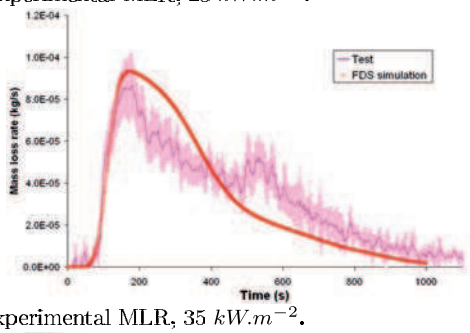

f/ Experimental MLR, 35 $kW.m^{-2}$.

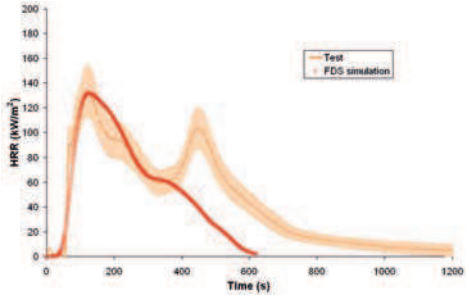

g/ Experimental HRR, 50 $kW.m^{-2}$.

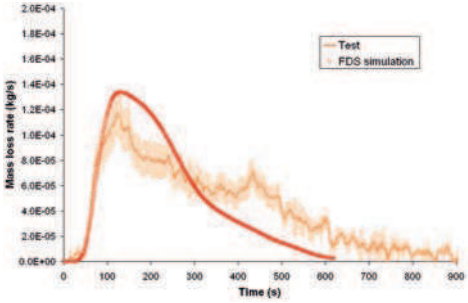

h/ Experimental MLR, 50 $kW.m^{-2}$.

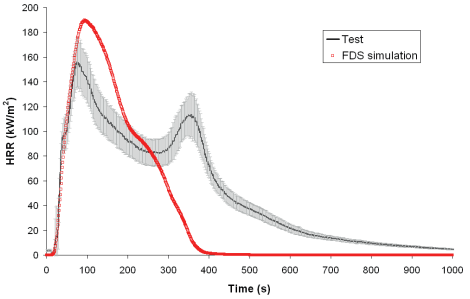

i/ Experimental HRR, 75 $kW.m^{-2}$.

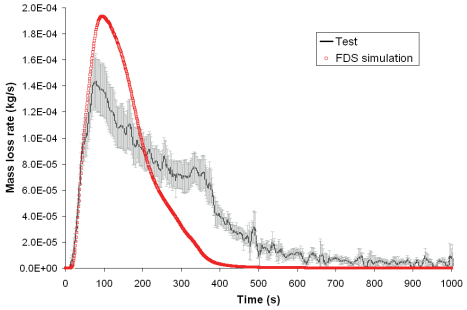

j/ Experimental MLR, 75 $kW.m^{-2}$.

Figure 5.9: Experimental HRR and MLR of the GRP composite materials from several incident heat fluxes.

Except for the numerical results obtained from $20kW.m^{-2}$, the numerical MLR and HRR have the same kinetic and order of magnitude as the experimental ones until the second sudden HRR peak occurs, taking into account the uncertainties.

Concerning the external heat flux of $20kW.m^{-2}$, the numerical MLR has the same kinetic and order of magnitude as the experimental one. However, there is a time deviation between the numerical and the experimental time delay of the mass loss rate (figure 5.9b). It is well known that the unidirectional heat transfer is favoured under a high incident heat flux. Nevertheless, at $20kW.m^{-2}$, the thermal heat transfer could be bidirectional at the material surface. The presence of glass fibres in mast may stimulate this bidirectional action.

In FDS, the thermal heat transfer is only in one direction (unidimensional). I The bidirectional heat transfer process at the material surface may be faster than a unidirectional transfer. In this case, the experimental surface material starts to decompose earlier than the numerical one. Moreover, concerning the HRR at $20kW.m^{-2}$, the numerical and experimental HRR intensities and kinetics are different (figure 5.9a). As for the MLR results, the presence of glass fibres and the lower incident heat flux favoured the surface bidirectional heat flux and the flame retardant action from the glass fibres. The own composite structure is not reproduced in FDS due to the non- quantification of the glass fibre layers.

The experimental time period before the composite starts to decompose and the experimental ignition delay period are compared with the numerical ones (table 5.6). We can notice that the numerical ignition and decomposition time periods are the same due to the assumption of the FDS combustion model. Indeed, in FDS, when the material starts to decompose (at the beginning of the material mass loss) and the conditions of the mixture fraction model are reached, then the combustion occurs at the mesh surface (the reaction is known infinitely fast). Experimental ignition and decomposition delay periods are different. Experimentally, the reaction is controlled by the fuel and oxygen mixture conditions.

Table 5.6: Comparison between experimental and numerical delay time period

External radiant heat flux $kW.m^{-2}$	$\triangle t_{MLR,exp}$ (s)	$\triangle t_{HRR,exp}$ (s)	$\triangle t_{HRR,MLR,FDS}$ (s)
20	63	185	126
25	63	127	76
35	69	89	58
50	13	53	37
75	11	17	17

For higher incident heat fluxes (35, 50 and $75kW.m^{-2}$), the second sudden HRR peak is not represented in FDS simulation. This difference comes from the unidirectional heat transfer applied in FDS. Numerically, the unidirectional 1D thermal heat transfer is ap-

plied independently of each material surface whereas experimentally a thermal feedback comes from the silica wool to the back face of the composite (figure 5.10).

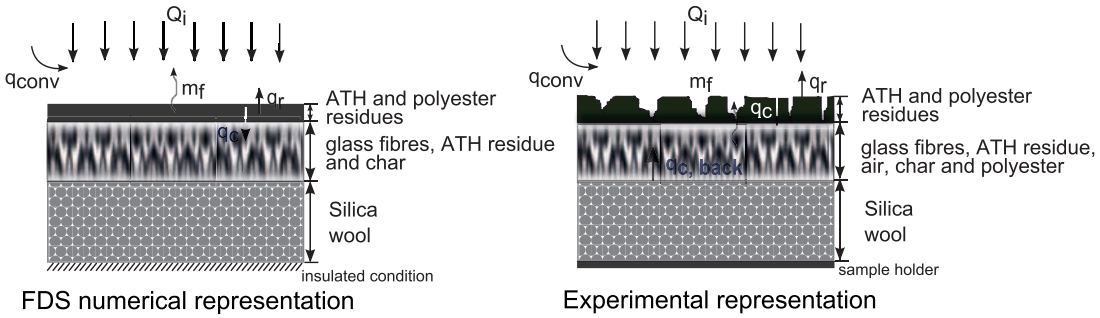

Figure 5.10: Experimental and FDS GRP composite representation at material scale

The next challenge is to verify whether the validated GRP composite material configuration and GRP properties at material scale are feasible at semi-finished product scale.

5.3 Semi-finished product scale

5.3.1 Experimental results

As explained in the methodology part, the Medium Burning Item (MBI) tests (ISO 21367 (2008)) consist in studying vertical (upward and downward) and lateral flame spread of a product placed in a vertical configuration. The tested samples measure 500 mm by 700 mm and a conical heater is placed at the bottom, facing the product (as in picture 5.13). The back face of the product is let as air. An incident heat flux of 50 $kW.m^{-2}$ has been chosen to perform the tests. The experimental results (HRR, Temperature and gases released) from the MBI tests are shown in figures 5.11, 5.12 b and 5.23 a. The two HRR tests have the same tendency: same kinetic and same order of magnitude of the heat released. Both tests are repeatable despite a small time shift.

It is important to note that the HRR kinetics between the cone calorimeter and the MBI tests are different: the second delayed HRR peak is not present in the case of an MBI test and flame spread could occur in this last test. This confirms that the second HRR peak is only caused by the cone calorimeter test configuration: a silica wool is located behind the back face of the material for the cone calorimeter test while only air is present behind the product back face during the MBI test.

The location of each thermocouple during the MBI test is presented in figure 5.12a.

Positions 107 and 108 are the ones facing the conical heater, whilepositions 104, 109

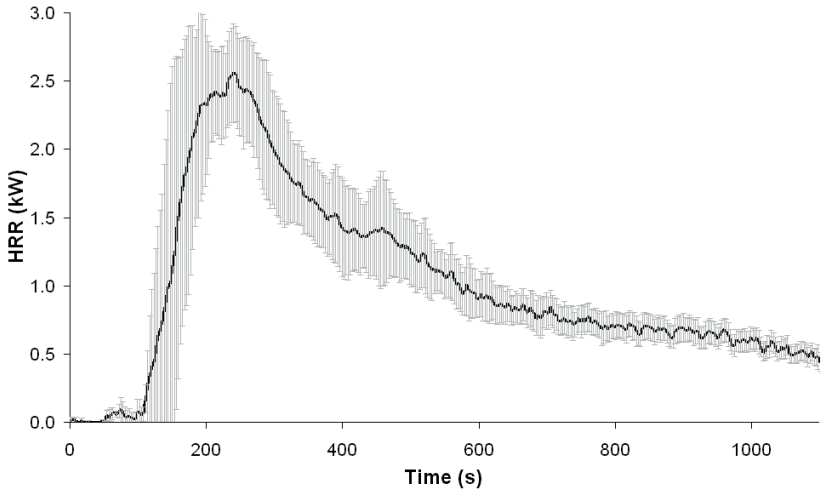

Figure 5.11: Experimental HRR of the GRP composite materials from an external radiation level of 50 $kW.m^{-2}$

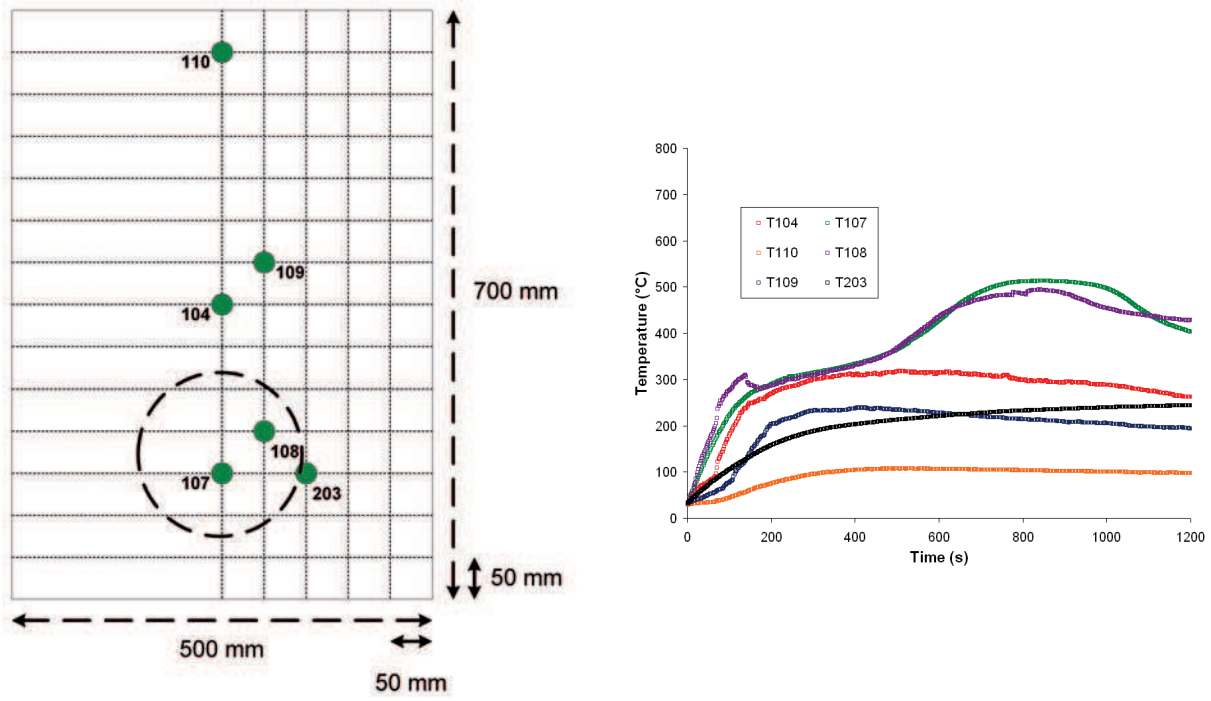

a/ Location of thermocouples on the tested wall panel during the MBI test.

b/ Experimental temperatures of the tested wall panel during the MBI test.

Figure 5.12: Experimental temperatures of the tested wall panel.

and 110 are placed above the heater. According to figure 5.12b, the thermocouple temperatures, which are located close to the heater, are higher than the ones placed far away from the heater throughout the test. This can be explained by the wall panel reaction-to-fire. Moreover, a slight decrease in temperature is observed concerning sensor 108. This temperature reduction may be the consequence of the endothermic effect of the ATH reaction. Indeed, figure 5.13 represents the final burnt surface area of the wall panel.

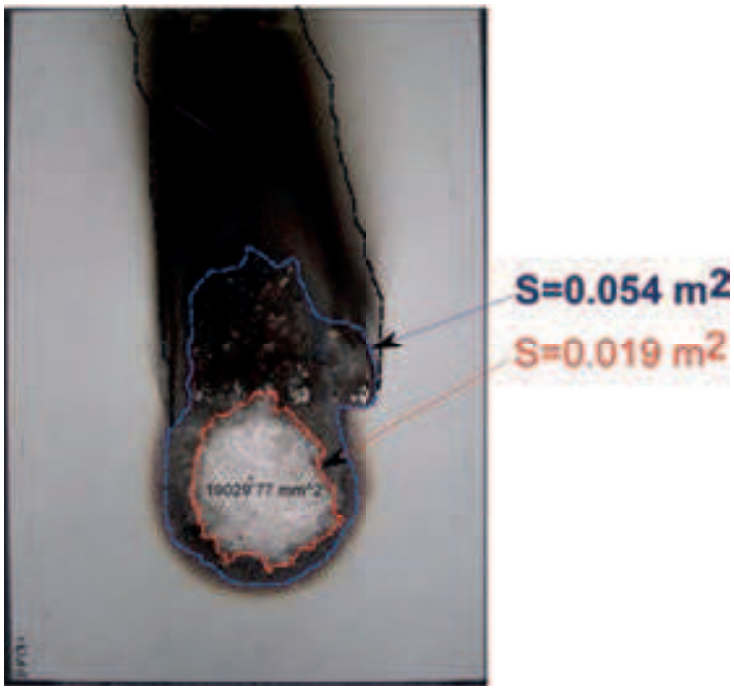

Figure 5.13: Experimental burnt area of the wall panel after a MBI test, at 50 $kW.m^{-2}$

According to figure 5.13, three different burnt areas are identified. The first one, represented by the red line, is characterised by a white color: all the available polyester is decomposed and burnt. The white color is the color of the glass fibre which remains thermally stable. The second area, represented by the blue line, is black because it remains part of a charcoal that does not participate in the combustion. The oxidation of the char had not occurred. Two causes are possible: either a lack of oxygen or the temperature are too low at the wall panel surface. The third area is also black due the soot deposit on the material surface from the flame, but the product remains almost not burnt under soot deposit. According to all these results, the product ignites face to the conical heater, then the flame spreads a little vertically upwards. No lateral and vertical downward fire spread are detected.

Moreover, during the MBI tests, four different gases are released: carbon dioxide, carbon monoxide, acetylene and hydrogen chloride (figure 5.14).

The production kinetic of carbon dioxide and carbon monoxide are visually very simi-

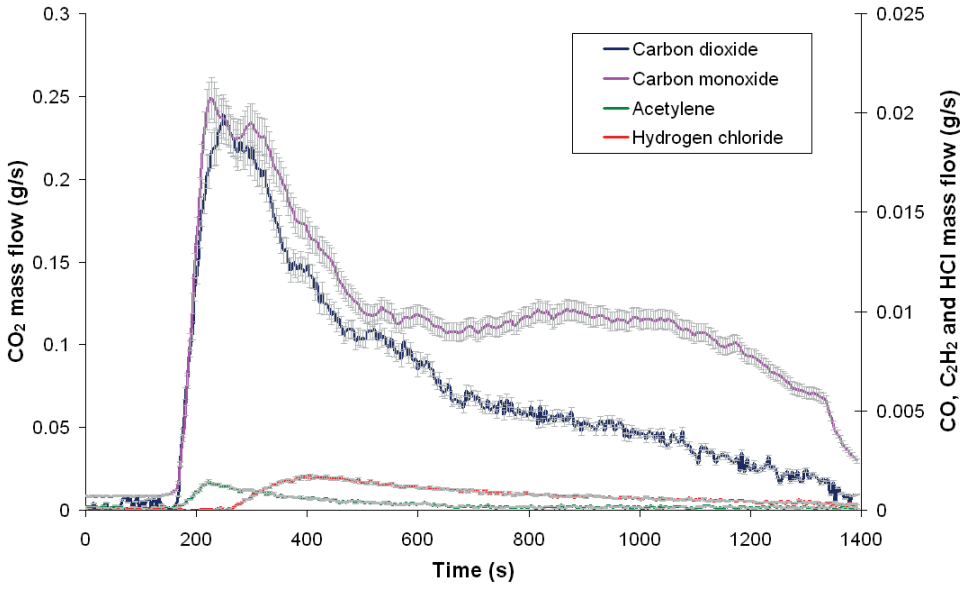

Figure 5.14: Experimental results of gases released during the MBI test from the tested wall panel with an incident heat flux of 50 $kW.m^{-2}$

lar. This kinetic is linked to the product combustion reaction. However, at around 750 seconds, the product stops burning: carbon dioxide decreases whereas carbon monoxide remains stable and then slowly increases. This slight increase of carbon monoxide could be due to an incomplete combustion on the char surface. Furthermore, a small quantity of Cl is detected into the material characterisation via an X-ray fluorescence technique. This quantity is then released in the gas phase as hydrogen chloride. There is time shift between the production of carbon dioxide and hydrogen chloride. It is possible that a product based on chlorine is presented in glass fibres. Thus, glass fibres, placed into the composite, take time to heat and to release HCl. A summary of wall panel characteristics from MBI test is given in table 5.7.

Table 5.7: Wall panel parameters according to the heat flux from MBI test

Parameters	**Units**	**Values**
$\dot{q}_i''$	$kW.m^{-2}$	50
$\overline{t_{ig}}$	s	54±6
$\overline{\dot{q}''_{max}}$	kW	2.55±0.20
$\overline{THR}$	MJ	1.125±0.015
$\overline{\triangle m}$	g	124.5±2.1
Y_{CO_2}	$kg.kg^{-1}$	0.79±7%
Y_{CO}	$kg.kg^{-1}$	0.10±7%
$Y_{C_2H_2}$	$kg.kg^{-1}$	0.004±7%
Y_{HCl}	$kg.kg^{-1}$	0.008±7%

5.3.2 Modelling approach

The GRP experimental study at semi-finished scale enables to better understand the reaction-to-fire of the GRP product in vertical position, as the end-use conditions. The reaction-to-fire modelling is performed by the FDS code. The aim of this scale enables to test the abilities of the FDS code to simulate pyrolysis, ignition, combustion and flame spread over a vertical product. The input data used are the same that at the material scale. The experimental and numerical comparison is based on the heat release rate, the temperature, the burnt areas and the released gases of the GRP. When the FDS input data are validated at this scale, there are transferred at the upper scale. The modelling approach is summarized in figure 5.15.

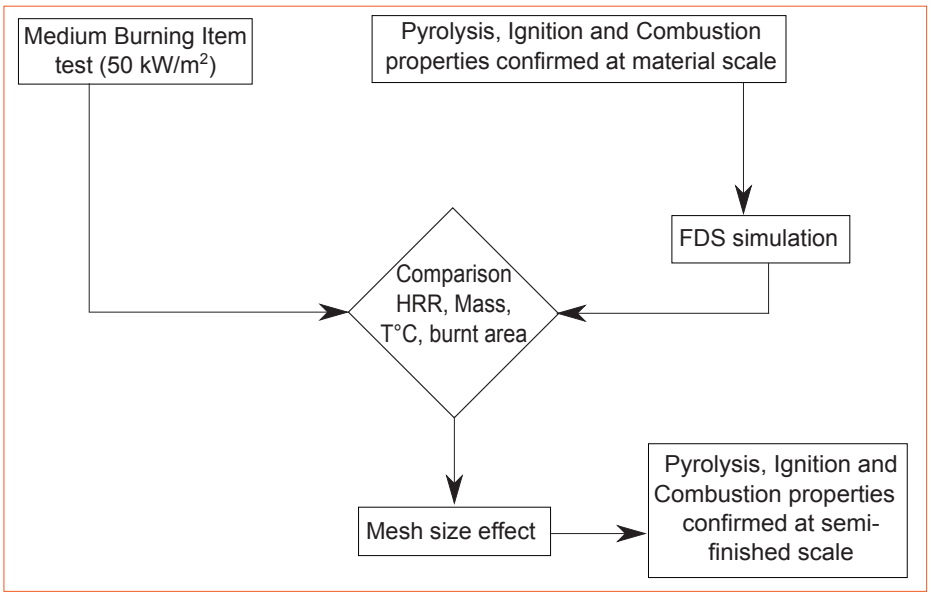

Figure 5.15: Material scale approach (Pyrolysis, Ignition and Combustion input data validation)

5.3.2.1 Mesh size

For the semi-finished product scale, the size of the domain is 0.4 m, 0.6 m and 1 m respectively in x, y and z directions. As it is explained in the previous chapter, the ideal size mesh is given according to the criteria linked to the fire diameter (Eq 4.20 and 4.21). This criteria is satisfied for the MBI test domain with a 1 cm mesh. In the multi-scale approach, a 2.5 cm mesh is tested too.

5.3.2.2 Initial boundaries

Aerodynamic conditions

All surfaces of the domain are considered open, i.e. the initial velocities in the three

directions are null and the initial pressure corresponds to the ambient pressure, or to the atmospheric pressure (101325 Pa). Moreover, during the simulation, the top surface of the domain (Z_{Max}) is associated to an air extraction volume flow of 0.0905 $m^3.s^{-1}$ to represent the exhaust duct.

Radiative and thermal conditions

The point of mutual interest of the two tests (cone calorimeter and MBI) is the usage of the same shape and type of heater: a conical radiant electrical heater. Its diameter equals 197± 0.5 mm (ISO 5660-1 (2002)). With a 2.5 or 1 cm mesh size, it is not obvious to represent a full truncated cone with cubic mesh (figures 5.16). Furthermore, like the numerical cone calorimeter configuration, a temperature is associated to each heater cubic mesh for the MBI conical heater.

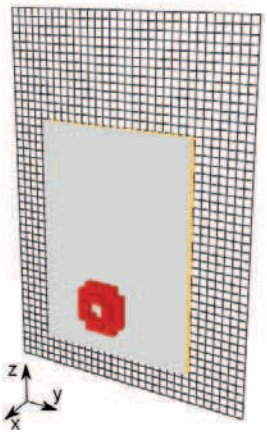

a/ Numerical discretization of the conical heater with a size mesh of 2.5 *cm*.

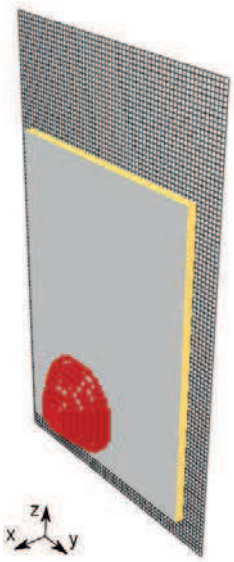

b/ Numerical discretization of the conical heater with a size mesh of 1 *cm*.

Figure 5.16: Numerical representation of the conical heater.

An experimental distribution of the heat flux received by a conical heater at 50 $kW.m^{-2}$ has been measured with a gauge heat flux and a calcium silicate backing board ($\rho = 870 \pm 50 kg.m^{-3}$), placed at the same location as the tested product. This heat flux distribution is presented in figure 5.17. The first ring (4 cm) receives a heat flux from 43.0±10 to 50.8±10 $kW.m^{-2}$. The blue ring corresponds to the conical heater diameter. Each heat flux value has an uncertainty of ±10 $kW.m^{-2}$ (ISO 21367 (2008)). According to figure 5.17, a vertical symmetry is visible. However, there is no horizontal symmetry. This could be explained by the convective movement on the calcium silicate board. Thus, each numerical conical heater (figure 5.16) has been calibrated in order to reproduce the same heat flux distribution as the experimental one (figure 5.17).

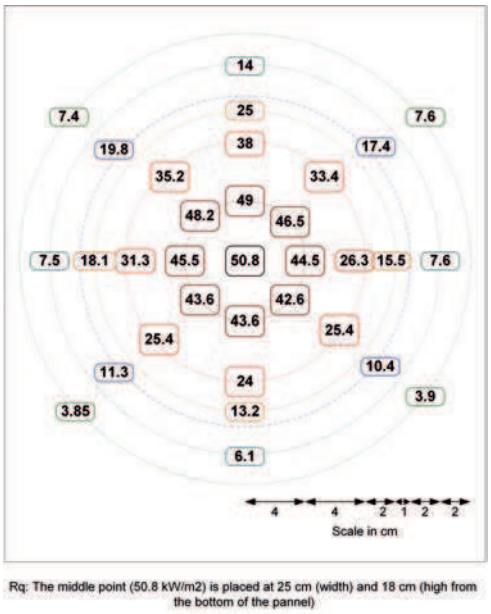

Figure 5.17: Experimental gauge heat flux received to the tested product from the conical heater.

The numerical relative errors of each external heat flux received to the calcium silica board (compared to the experimental heat flux) are presented in figure 5.18 a and in figure 5.18b respectively for mesh sizes of 2.5 and 1 cm and expressed in %.

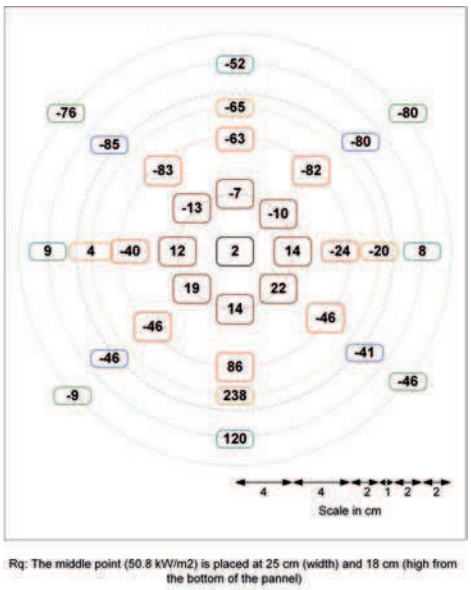

a/ Numerical relative error in % of each external heat flux received to the product compared to the experimental measurement (2.5 *cm* mesh).

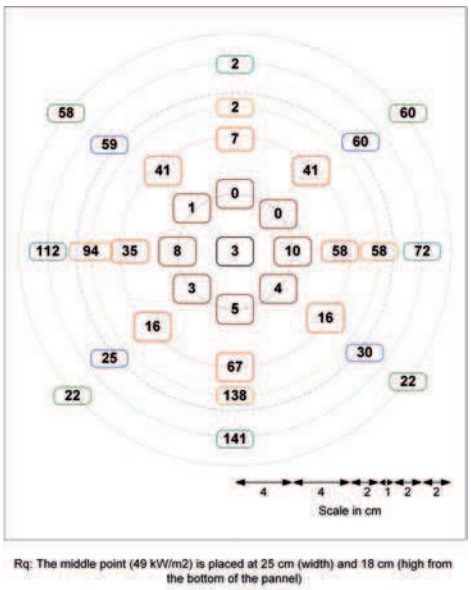

b/ Numerical relative error in % of each external heat flux received to the product compared to the experimental measurement (1 *cm* mesh).

Figure 5.18: Numerical relative error in % of each external heat flux received to the product compared to the experimental measurement.

A negative error value means that the numerical value is less than the experimental one. For both mesh sizes, the farther away the position is from the center, the higher the numerical error is. Concerning the first and second rings, the numerical relative error is reduced for the 1 cm mesh in comparison with the ones for the 2.5 cm mesh. Then, for both mesh sizes after the first ring, the FDS radiative transfer model has difficulties to represent the correct heat flux received by the calcium silicate board. The numerical heat flux distributions on the material surface from an external heat flux of 50 $kW.m^{-2}$ are shown in figures 5.19a and 5.19b according to the y and z directions. The first and the second figures represent the heat flux received by the product from the numerical heater respectively with a mesh size of 2.5 and 1 cm. The impacted surface area is more important for the mesh size at 1 cm than the mesh size at 2.5 cm.

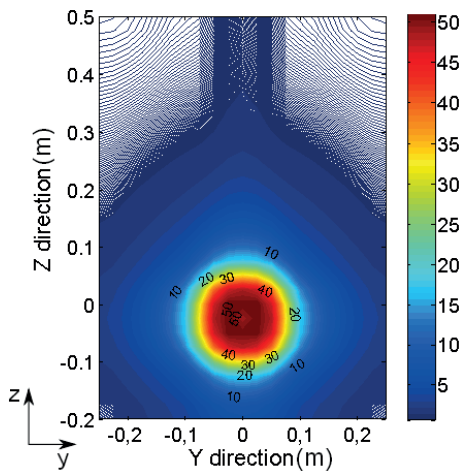

a/ Numerical heat flux distribution received by the tested product (mesh size 2.5 cm).

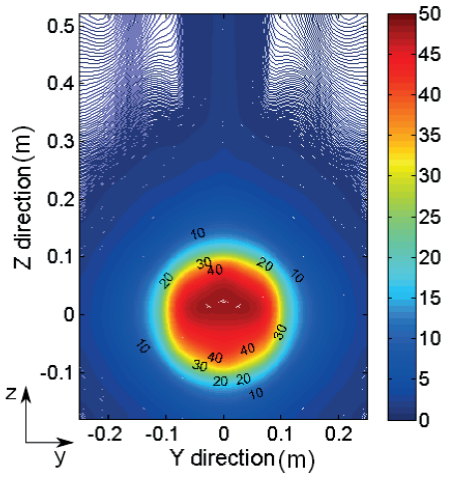

b/ Numerical heat flux distribution received by the tested product (mesh size 1 cm).

Figure 5.19: Numerical heat flux distribution received by the tested product.

5.3.2.3 Input data

The strategy chosen is to use the thermal properties and the pyrolysis parameters validated at material scale. The proportions and the composite configuration are the same as those simulated at material scale. Concerning the gas phase in FDS, the same input as the material scale are used (table 5.5), excepted for the Y_{CO} quantity calculated from the MBI test: Y_{CO}=0.10 $kg.kg^{-1}$. It is a global value. This quantity comes from the MBI test in order to avoid to take into account the thermal feedback that happened during cone calorimeter test.

5.3.2.4 Numerical results and comparison

Figure 5.20 presents the numerical and experimental HRR comparison at two different mesh sizes: 2.5 and 1 cm.

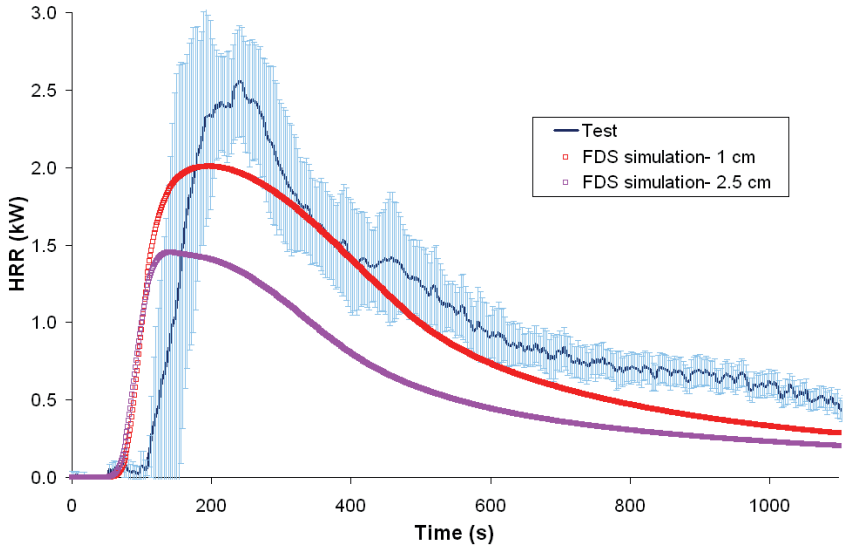

Figure 5.20: Numerical and experimental HRR comparison at semi finished product scale

The experimental and numerical HRR have the same kinetic: a sudden HRR increase and then a slow HRR decay. The experimental and numerical HRR have the same ignition delay: around 60 seconds. The difference is that the numerical sudden peak deviates a little from the experimental one. Experimentally, the polyester first ignites at the pilot flame location, then when enough polyester starts to decompose and the lean flammability limit is also reached, the combustion develops (red and pink lines in 5.13), whereas when the polyester starts to decompose in FDS, the combustion begins too. This is a limitation of FDS mixture fraction combustion model: when fuel exists in gas phase, there is a flame at the interface with air. Another difference is the HRR intensity of the peak: for both mesh sizes, the HRR intensity is lower than the experimental one.

The comparison between experimental and numerical temperatures (mesh sizes of 2.5 and 1 *cm*) are shown in figures 5.21. All experimental and numerical temperatures have the same tendency and the same order of magnitude. The numerical temperatures for a 1 *cm* mesh are generally closer to the experimental ones than for the larger mesh, except for the position 203, taking into account the experimental uncertainties on the measurements and on the sensor position.This is due to the numerical calibration of the conical heater. Indeed, the numerical calibration of the conical heater at 1 *cm* is closer to the experimental one. Nevertheless, position 203 is placed 10 *cm* from the right of the center (figure 5.12 a). For this place, the numerical relative error is less important for the 2.5 *cm* mesh (figure 5.18).

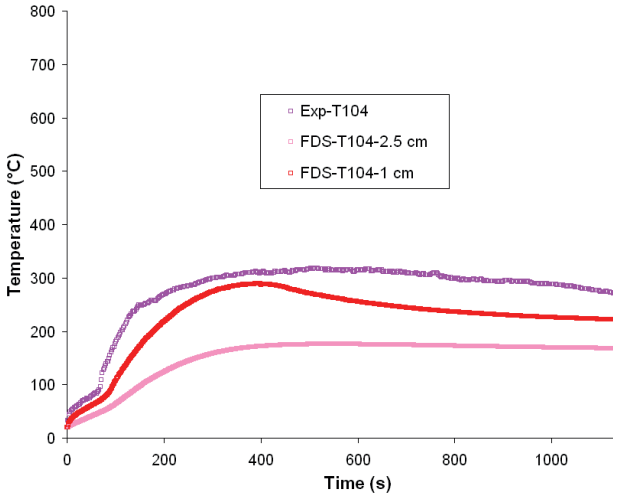

a/ Sensor 104.

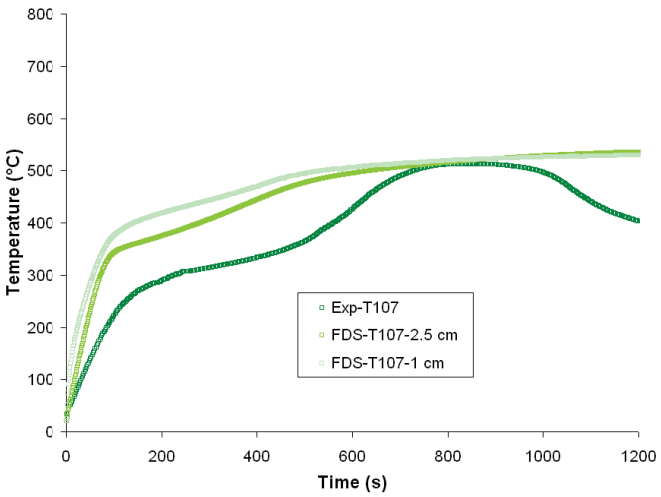

b/ Sensor 107.

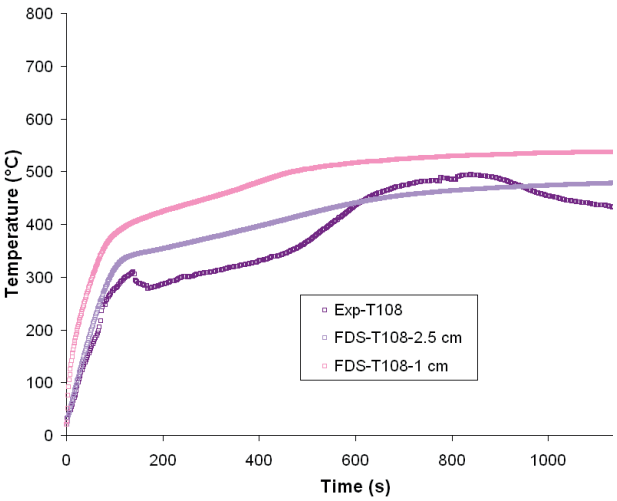

c/ Sensor 108.

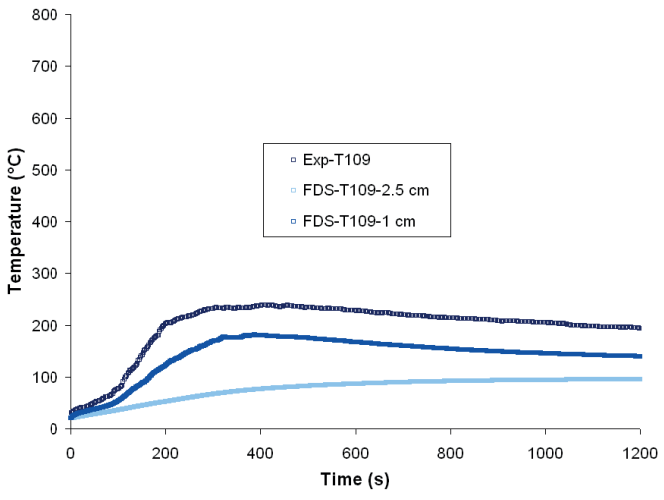

d/ Sensor 109.

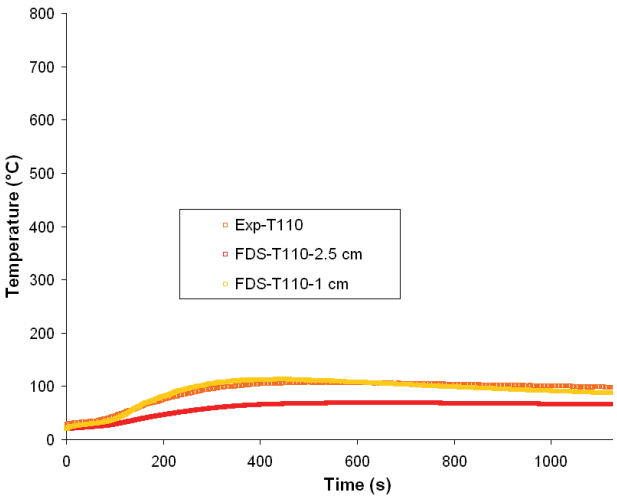

e/ Sensor 110.

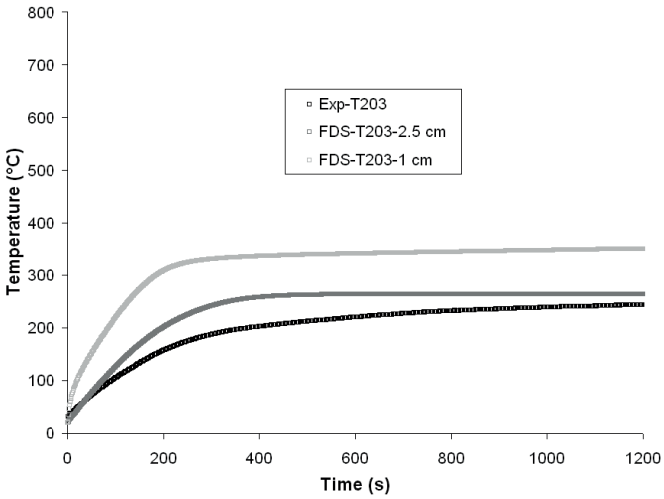

f/ Sensor 203.

Figure 5.21: Experimental and numerical temperature comparisons.

The numerical and experimental burnt surface area is compared in figure 5.22. Experimental burnt surfaces are reported on the numerical burnt surface. The numerical burnt surface is estimated with the gradient of the normalised mass loss rate (Marquis (2010)) in s^{-1}. The numerical burnt surface is higher with a 1 cm mesh than a 2.5 cm one, considering a threshold of burnt area of 2.10^{-3} s^{-1}. The numerical burnt surface is a ring. The numerical surface area is between the experimental blue and red lines (figure 5.22).

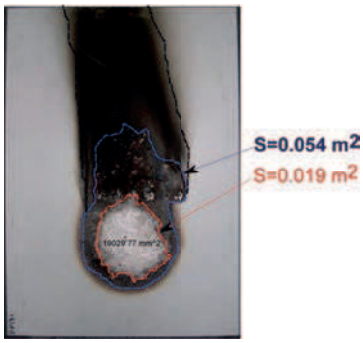

a/ Experimental burnt area of the wall panel.

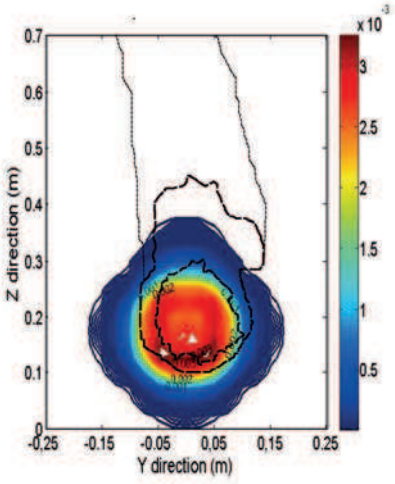

b/ Comparison between numerical and experimental burnt area of the wall panel (2.5 cm mesh).

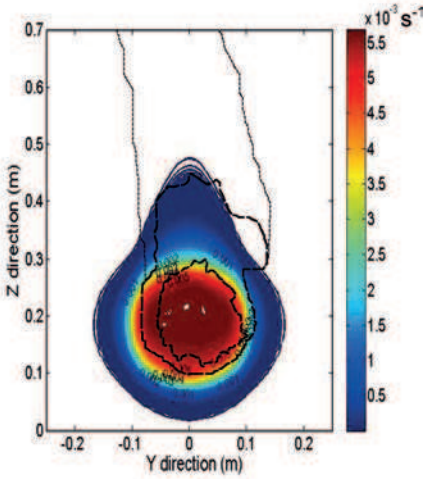

c/ Comparison between numerical and experimental burnt area of the wall panel (1 cm mesh size).

Figure 5.22: Burnt areas after the panel tests.

The experimental and numerical carbon dioxide and carbon monoxide concentration are compared in figure 5.23 a and 5.23 b.

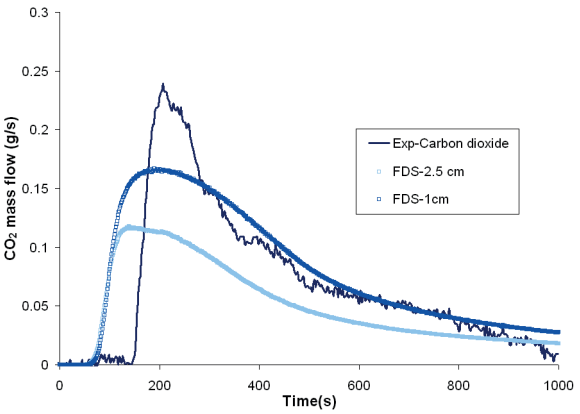

a/ Comparison between numerical and experimental of the CO_2 mass flow from the wall panel (mesh size 2.5 cm).

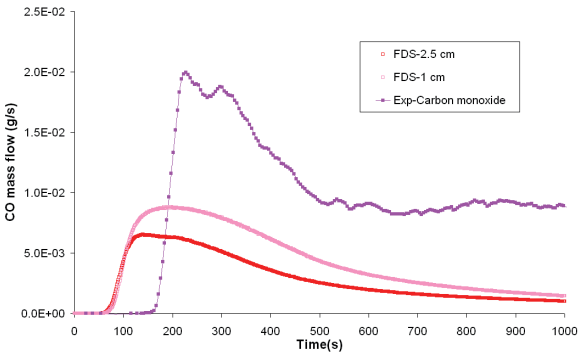

b/ Comparison between numerical and experimental of the CO mass flow from the wall panel (mesh size 1 cm).

Figure 5.23: Experimental and numerical gas mass flow comparisons.

As the HRR results, experimental and numerical gas concentration have the same tendency. However, numerical gas concentration intensities are lower than experimental ones.

The total masses of released carbon dioxide ($TRCO_2$) and carbon monoxide ($TRCO$) are compared in table 5.8. Concerning carbon dioxide, the experimental total mass released is higher than the results obtained from the numerical simulation at 2.5 and 1 cm. These numerical results are related on the total mass loss of the panel: the experimental total mass loss is also higher than the numerical ones. Meanwhile, for carbon monoxide, the experimental total mass released is not reached by the numerical simulation. The numerical estimation of carbon monoxide failed at MBI scale. Several reasons for this difference are possible: the experimental generation of carbon monoxide depends on the flame temperature, its residence time and oxygen diffusion into the flame and material (Andzi Barhe (2004)). In FDS, the CO generation is only controlled by the combustion stoechiometry and thus the type of material. The FDS combustion model does not take into account the evolution of CO formation into the flame. Moreover, the experimental GRP product releases hydrogen chloride which favours carbon monoxide production. These conditions are directly used at higher scales.

Table 5.8: Comparison of the total mass loss of the wall panel product

	THR (MJ)	**TML (g)**	**$TRCO_2$ (g)**	**TRCO (g)**
Test	1.125±0.015	124.5±2.1	96.0±2.5	13.4±0.3
$FDS - 2.5\ cm$	0.7	0.79	53.4	3
$FDS - 1\ cm$	1.0	119	82.9	4.4

5.4 Finished product wall panel scale

5.4.1 Experimental results

This finished product wall panel scale follows the open calorimetry test (ISO 24473 (2006)) and represents the product in real conditions, i.e. the product configuration, dimension and structural geometry. Two wall panels are tested which measure 1.5 by 1.5 m in a steel frame. The propane burner is located in the corner between the two tested wall panels (75 kW for 2 min then 150 kW for 8 min) at 30 cm from floor. The floor and the ceiling are non-combustible. The wall panel is considered insulated by a layer of air (10 mm), then a layer of mineral wool (25 mm) and finally a calcium silicate board (10 mm). Experimental HRR curves of both tests are shown in figure 5.24a. Some pictures during the test are illustrated in figure 5.24b (obtained from SP laboratory, Sweden). Both tests are repeatable.

The experimental temperatures are reported in figure 5.25 b and their associated locations in figure 5.25 a. Three tendencies are visually identified: each of them follows the two burner phases (black dot lines). Concerning the first group (sensors T5, T6, T7 and T8), the temperature increases rapidly until 500°C for 150 seconds then the temperature raises slowly until the burner turns off (600 seconds). For the second group (positions T3 and T4), the temperature increases up to 200°C.

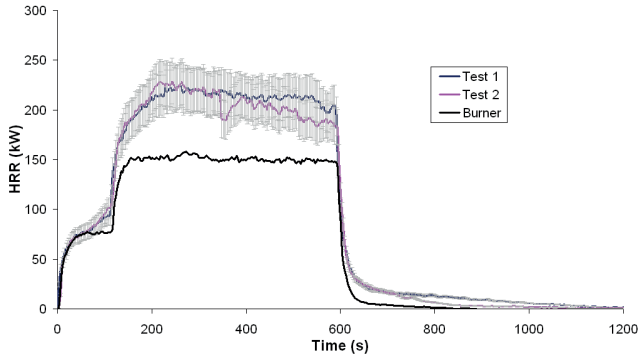

a/ Experimental HRR of the finished wall panel test

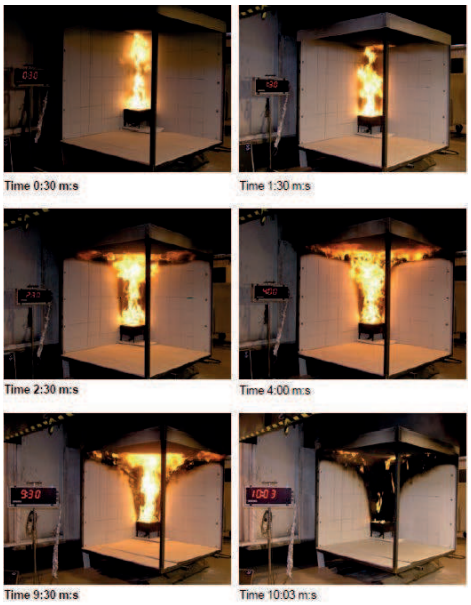

b/ Pictures of the finished wall panel test, from SP laboratory (Sweden)

Figure 5.24: Finished wall panel test.

Then, the temperature suddenly increases for a few seconds up to $500°C$ and rises slowly until the burner turns off. The same trend is observed for the third group (sensors T1 and T2) except for the reached temperature. The temperatures kinetic seems to reproduce the two phases of the burner: 75 kW for 2 min then 150 kW for 8 min.

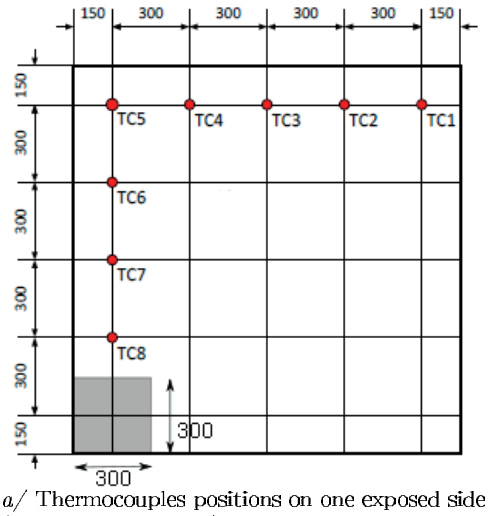

a/ Thermocouples positions on one exposed side (measurement in mm)

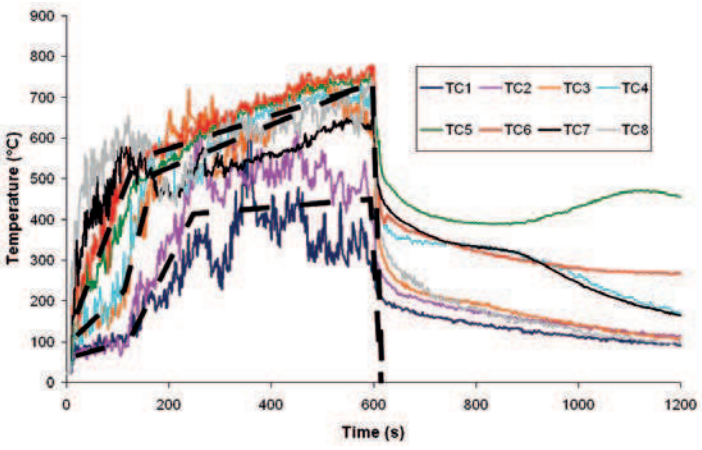

b/ Experimental temperatures from the finished wall panel test

Figure 5.25: Experimental temperatures from the finished wall panel test.

A picture and schemas of the final burnt surfaces of the wall panel are reported in figure 5.26. Two different areas are detected. The first area corresponds to the location where all the polyester resin has been consumed whereas for the second area, the polyester resin has only burnt on surface.

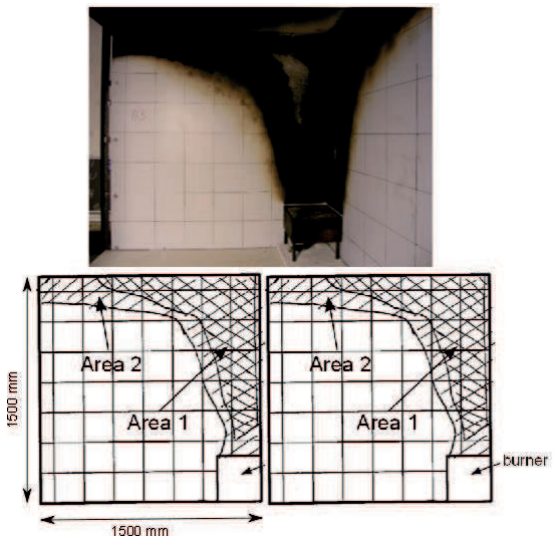

Figure 5.26: Experimental impacted surface area after the finished wall panel test, from SP laboratory (Sweden).

Three different types of gases are detected by FTIR during the finished product wall panel test: carbon dioxide, carbon monoxide and hydrogen chloride (figure 5.27). Carbon dioxide and carbon monoxide are present during both periods of the burner while Hydrogen Chloride is detected after 150 seconds. Released gases come from the burner and the wall panel product.

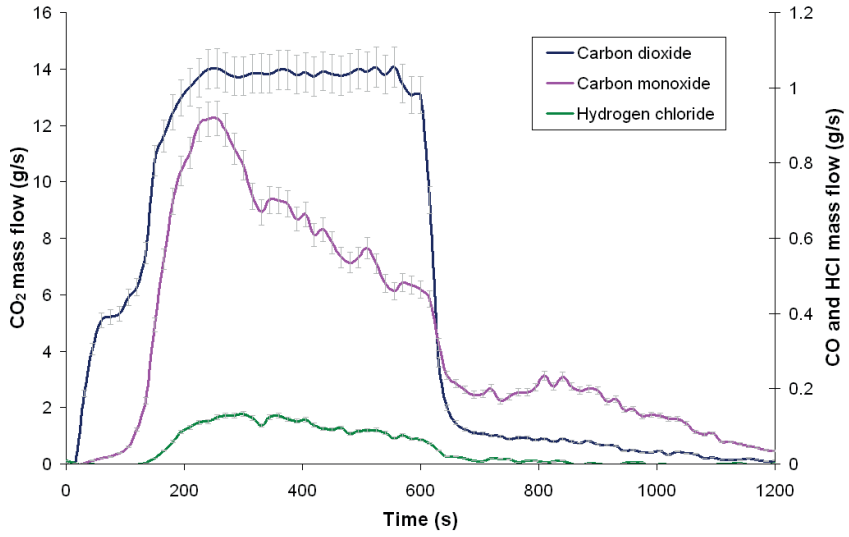

Figure 5.27: Experimental mass flow of released gases.

To sum up, the properties related to the finished product wall panel test are presented in table 5.9. The gas yields (burner excluded) are very close to the semi-finished panel test ones (see table 5.7).

Table 5.9: Wall panel parameters according to the heat flux from MBI test

Parameters	**Units**	**Values**	
$\overline{t_{ig}}$	s	63±1	
$\overline{\dot{q}''_{max}}$ *(burner included)*	kW	225.8±22.6	
$\overline{THR}$ *(burner included)*	MJ	114.1±2.3	
$\overline{\triangle m}$ *(burner excluded)*	kg	3.86±0.32	
Y_{CO_2}	$kg.kg^{-1}$	1.3±7% (burner included)	0.6±7% (burner excluded)
Y_{CO}	$kg.kg^{-1}$	0.067±7% (burner included)	0.084±7% (burner excluded)
Y_{HCl}	$kg.kg^{-1}$		0.011±7% (burner excluded)

5.4.2 Modelling approach

The GRP experimental study at finished product scale enables to better understand the reaction-to-fire of the GRP product in end-use conditions. The reaction-to-fire modelling is performed by the FDS code. This scale enables to test the abilities of the FDS code to simulate pyrolysis, ignition, combustion and flame spread over a vertical product in end-use conditions from a propane flame burner. The input data used are the same as the material and semi-finished scales. The experimental and numerical comparison is based on the heat release rate, the temperature, the burnt areas and the released gases of the GRP. When the FDS input data are validated at this scale, there are transferred at the upper scale. The modelling approach is summarized in figure 5.28.

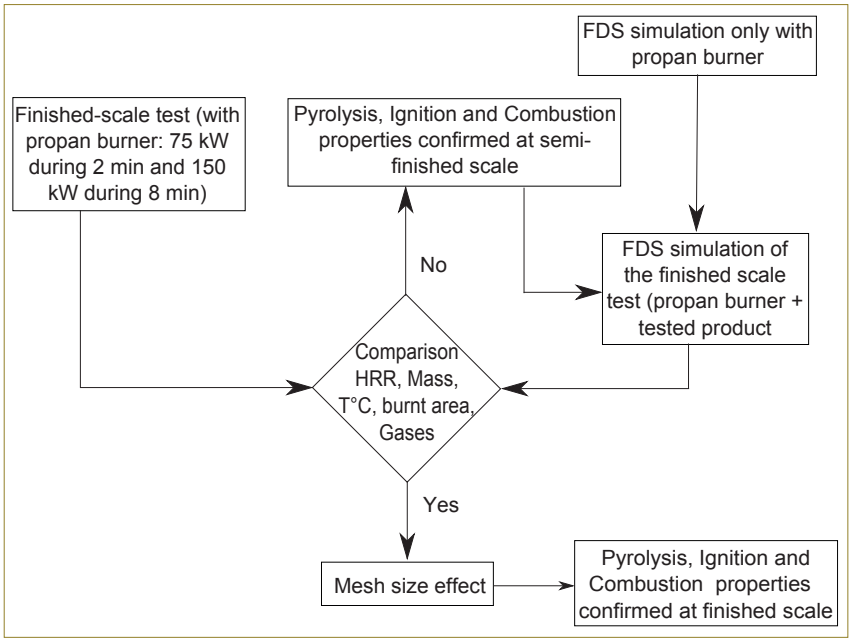

Figure 5.28: Finished product scale approach

5.4.2.1 Mesh size

For the finished product panel simulation, the size of the domain is 2.4, 2.2 and 2.7 m respectively in x, y and z directions. As it is explained in the previous chapter, the ideal size mesh is given according to the criteria linked to the fire diameter (Eq 4.20 and 4.21). This criteria is satisfied for the finished test domain with a 5 cm mesh. In the multi scale approach, a 2.5 cm mesh is tested too.

5.4.2.2 Initial boundaries

Aerodynamic conditions
All surfaces of the domain are considered open, i.e. the initial velocities in the three directions are null and the initial pressure corresponds to the ambient pressure, or to the atmospheric pressure (101325 Pa). Moreover, during the simulation, the top surface of the domain (Z_{Max}) is associated to an air extraction volume flow of 1.5 $m^3.s^{-1}$ to represent the exhaust hood.

Radiative and thermal conditions: propane burner study
The numerical propane burner is supposed to be validated. More details about the propane burner simulation are presented in the previous chapter 4: Multi-scale comparison results on a railway seat.

5.4.2.3 Input data

The wall panel is modelled as the same multilayer materials validated at the semi-finished product scale test:

- one layer of gelcoat composed of ATH, polyester and mineral compounds
- a second layer of composite (polyester, ATH and glass fibre)

Behind the back face of the wall GRP composite panel, three layers are added respectively an air gap, a layer of mineral wool and a layer of calcium silicate board, as the experimental test. The strategy used is to use thermo-radiative and thermodynamic properties, and pyrolysis parameters validated at material and semi-finished product scales.

Concerning the gas phase in FDS, the propane is chosen as a fuel composition and the fuel effective heat of combustion, for the same reasons as the finished seat simulation.

5.4.2.4 Numerical results and comparison

Heat release rate Figure 5.29 represents the HRR numerical and experimental comparison at two different mesh sizes: 2.5 and 5 cm of the finished wall panel test. For both mesh sizes, the numerical has the same kinetic and intensity compared to the experimental one. Based on the HRR results, the mesh size has no important influence in this range and for this configuration. In the following section, results from the 5 cm mesh size are studied, because it is the mesh size of the next scale.

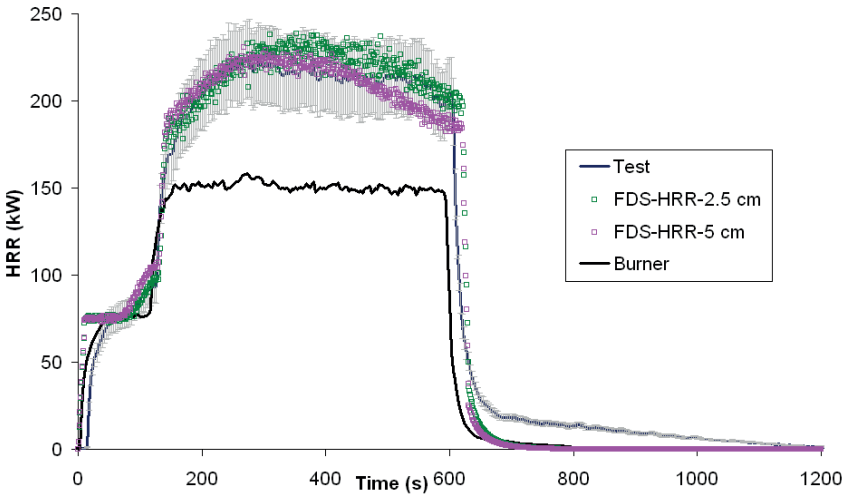

Figure 5.29: Numerical and experimental HRR comparison of the finished wall panel test

Panel temperature The comparison between experimental and numerical temperatures (5 *cm* mesh size) are shown in 5.30. The position of each thermocouple is presented in figure 5.25 a. The blue and pink curves are the temperature response of each test. For all points, they have the same tendency and approximately the same intensity. Concerning points *1, 5, 6, 7* and *8*, numerical temperatures are in line with experimental ones. Except for point 1, they are all located close to the flame burner. On the other hand, for points *2, 3 and 4*, experimental and numerical temperatures have the same kinetic but the numerical ones are lower than the experimental ones.

Pictures 5.31 a and 5.31 b respectively show the numerical mass loss rate of the wall panel at 200 and then 400 seconds. At 200 seconds, points *1, 2, 3 and 4* are located where the wall panel surface does not participate in the combustion. While at 400 seconds, positions *1, 2 and 3* are placed on the limit surface of the numerical mass loss rate. These numerical thermocouples are located on the flame limit. This limit could be defined as a transition zone. Comparing of numerical and experimental results is more difficult in this zone.

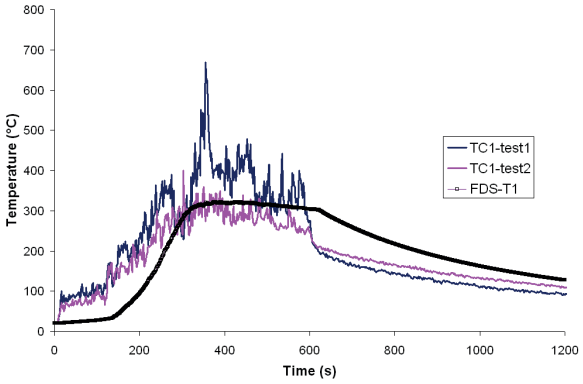

a/ Sensor TC1.

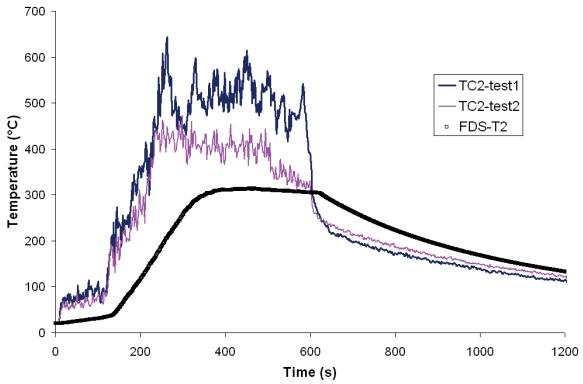

b/ Sensor TC2.

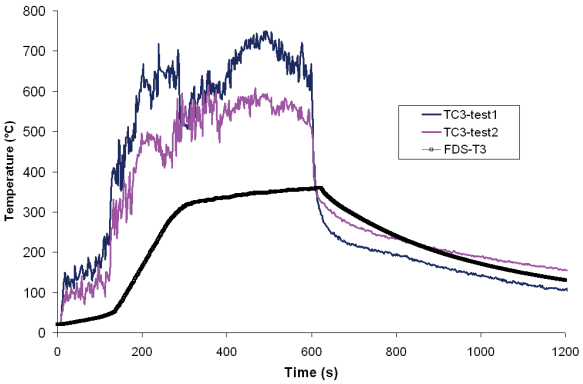

c/ Sensor TC3.

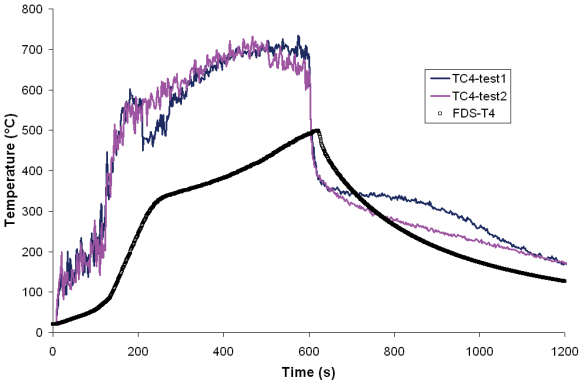

d/ Sensor TC4.

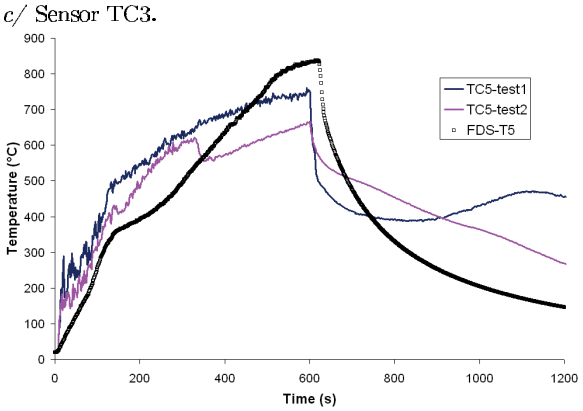

e/ Sensor TC5.

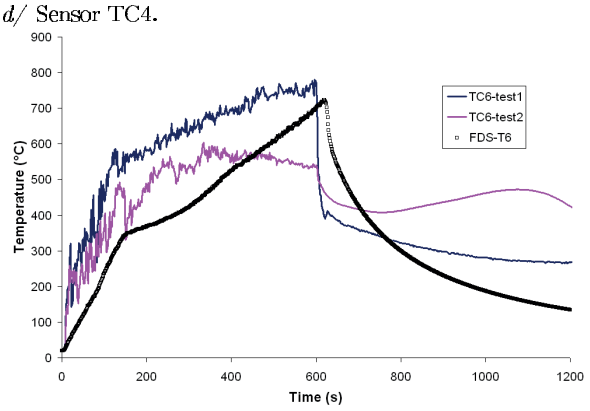

f/ Sensor TC6.

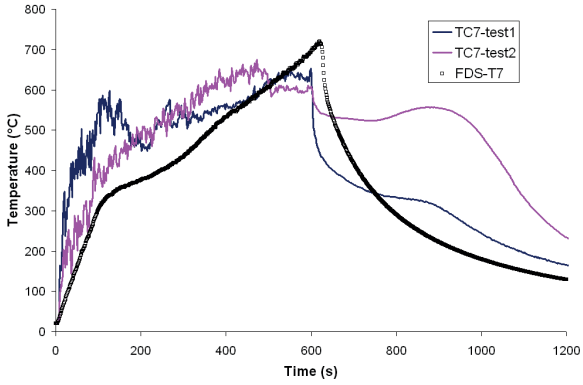

g/ Sensor TC7.

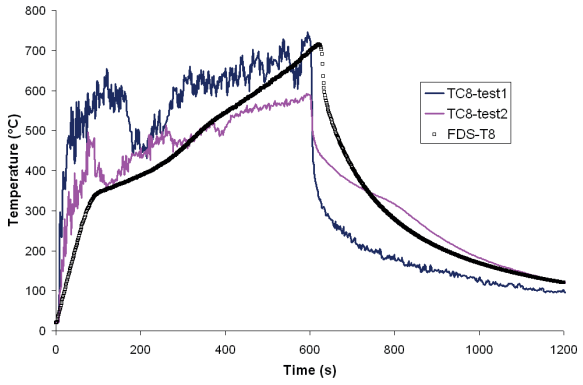

h/ Sensor TC8.

Figure 5.30: Experimental and numerical temperature comparisons (mesh size 5 *cm*).

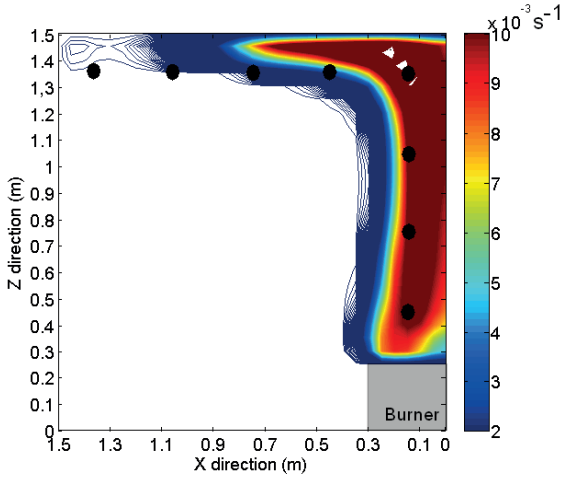

a/ Numerical impacted surface area of the wall panel product at 200 seconds.

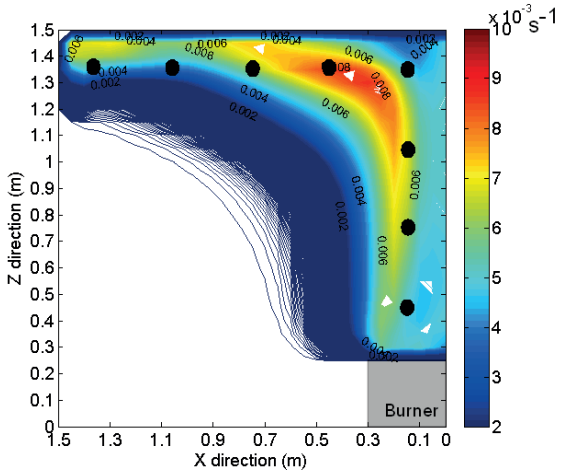

b/ Numerical impacted surface area of the wall panel product at 400 seconds.

Figure 5.31: Numerical impacted surface area of the wall panel product as represented by mass loss rate gradient. The dot represents the different thermocouples.

Total mass loss The total mass loss of the wall panel product is also compared (table 5.10).

Table 5.10: Comparison of the total mass loss of the seat product

	Total mass loss kg
Test	3.86±0.32
$FDS - 2.5\ cm$	4.01
$FDS - 5\ cm$	3.70

For both mesh sizes, the numerical total mass loss has the same order of magnitude than the experimental one. The effect of this mesh size on total mass loss results is limited.

Total impacted surface The numerical burnt surface area at the end of the simulation is reported in figures 5.32 a and 5.32 b for both wall panels (distribution of the mass loss rate). The big black dotted line represents the experimental burnt surface area (Area 2 in figure 5.26). The experimental and numerical burnt areas have the same order of magnitude.

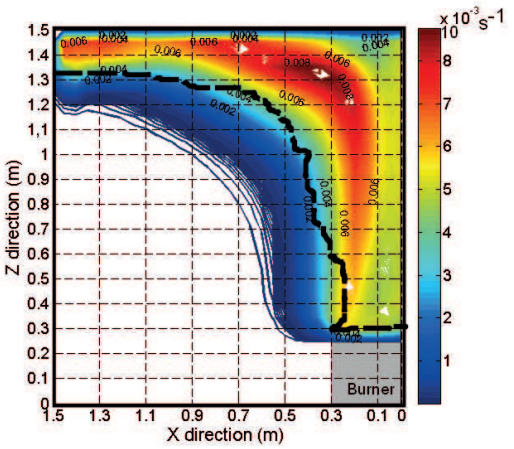

a/ Numerical impacted surface area of the wall panel product (right side).

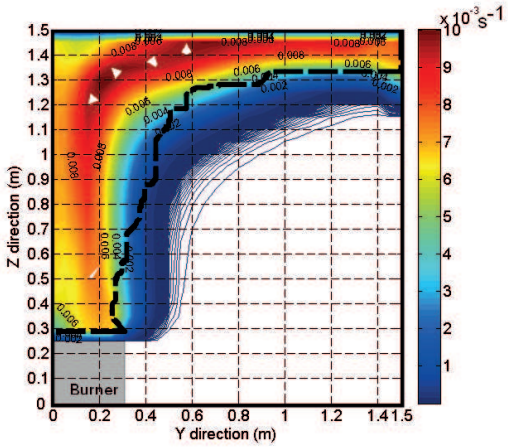

b/ Numerical impacted surface area of the wall panel product (left side).

Figure 5.32: Numerical impacted surface area of the wall panel product as represented by mass loss rate gradient. The dotted lines represent the experimental burnt area.

Gases released The experimental and numerical gases released are compared in figures 5.33 a and 5.33 b.

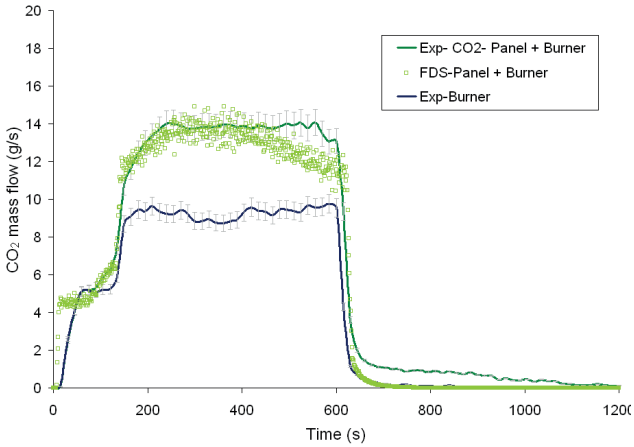

a/ Experimental and numerical CO_2 comparison of the finished panel test.

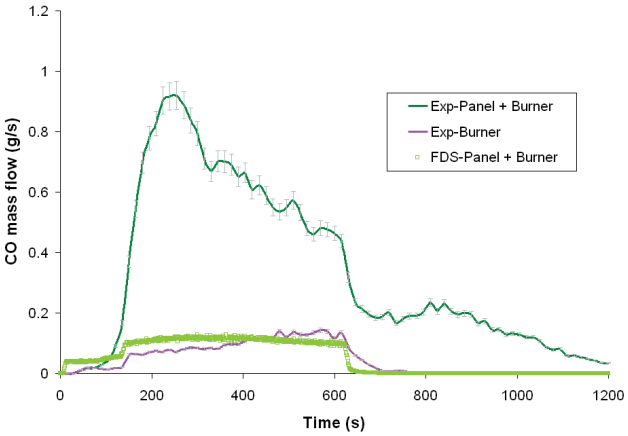

b/ Experimental and numerical CO comparison of the finished panel test.

Figure 5.33: Experimental and numerical gas mass flow comparisons.

As the HRR comparison, for the 5 cm mesh, the experimental and numerical carbon dioxide mass flows have the same kinetic and the same intensity. For released carbon monoxide and like the finished seat test results, the numerical response is close to the experimental burner. In fact, when a quantity of fuel is released from the numerical wall panel, the fuel (the propane) is oxidized in the FDS gas phase according to propane stoichiometry reaction. Moreover, the scalar mass yield of released carbon monoxide corresponds to Y_{CO}=0.025 $kg.kg^{-1}$ for the propane while the one for the composite GRP is Y_{CO}=0.045 $kg.kg^{-1}$ (according to cone calorimeter test). Thus, the comparison on the released carbon monoxide failed due to the FDS mixture fraction combustion model, as in the semi-finished product scale. However, experimentally the carbon monoxide

generation is deeply linked to the oxygen diffusion and its residence time into the flame. These experimental phenomena may control the carbon monoxide production at high scales. On the other hand, in FDS, these phenomena are not taken into account.

5.5 Discussion

At raw matter scale, the objective is to understand and to model the GRP thermal decomposition behaviour (polyester and ATH) in order to estimate pyrolysis parameters. According to several reviews on polyester decomposition and on ATH, a global reaction mechanism with five reactions has been introduced independently of the atmosphere. Then, according to material knowledge, FDS pyrolysis and combustion model limits, the global reaction mechanism is simplified to three reactions, one independent reaction linked to the ATH and two related to polyester decomposition. Pyrolysis parameters have been assessed with the experimental mass loss rate, the pyrolysis model and the optimisation tool.

At material scale, the reaction-to-fire of the GRP composite material has been simulated according to pyrolysis parameters validated at raw matter scale and thermo-radiative properties of each material component. The strategy chosen to model the GRP composite is to separate it into two layers: the gelcoat and the composite. The experimental and numerical HRR and MLR are in agreement with experimental ones considering experimental uncertainties and the limits of pyrolysis, combustion and heat transfer FDS models. Then, the FDS input data are validated and transferred at the upper scale.

The semi-finished product scale study is essential because it enables to better understand the reaction-to-fire of the GRP product in vertical position, as the end-use conditions. These simulations have shown that the numerical HRR is sensitive to the mesh size and the heater discretization in FDS. However, the numerical and experimental comparisons on the surface product temperatures, the burnt areas and the carbon dioxide generation are in good agreement. However, the comparison of the carbon monoxide mass flow failed due to the FDS mixture fraction combustion model. Some experimental phenomena, such as the carbon monoxide residence time, the local temperature and the oxygen diffusion and local concentration are not taken into account through the combustion and LES models in FDS. Despite this difficulty to simulate reaction-to-fire, FDS input data are transferred at the upper scale.

The aim of the finished product scale enables to test the abilities of the FDS code to simulate pyrolysis, ignition, combustion and flame spread over a vertical product in end-use conditions from a propane burner. The major difference between this scale and the previous ones is the type of burner used. Good agreement on HRR, total mass loss and total impacted have been proved considering experimental uncertainties. The small divergence on some numerical and experimental product surface temperatures may be due to the thermocouple position into the flame transition zone. Despite the presence of different groups of fuel, the author has chosen the propane as the only reagent in the combustion reaction in FDS. The experimental and numerical carbon dioxide generation are similar

despite the stoichiometry of the unique FDS combustion reaction. However, as for the semi-finished product scale, the numerical prediction of carbon monoxide failed for the same reasons as those explained before. In the finished product scale, carbon monoxide generation is controlled by the wall panel reaction-to-fire.

Chapter 6

Design fire scenario 1A: Comparison of products reaction-to-fire and fire effluents

Contents

According to design fire scenario 1A, described on the relative fire risk analysis chapter, the products close to the burner and thus likely to participate in the combustion are the seat and the wall panel. These two products are tested and simulated from the raw matter to the finished scale. For both products, the reaction-to-fire of the condensed phase is validated in terms of mass loss rate, heat release rate, temperature and impacted burnt surface area with some assumptions. Concerning the gas phase at the finished product scale and for the two products, the carbon dioxide concentration released matches well with experimental data despite the simple combustion model. However, the comparison failed for the released carbon monoxide concentration. This chapter describes the experiments and numerical results of scenario 1A and also the new approach to simulate the carbon monoxide released at finished product scale and real scale.

6.1 Design fire scenario 1A

6.1.1 Experimental results

The test has been performed by RATP with the contribution of all Transfeu partners. A part of this thesis work was to define the test scenario, sensors location and to participate to measurements. Design scenario 1A occurred into a single deck coach. The tested products are located on a deep down side of the coach. Four seats are placed on each side of the corridor (figure 6.1a). The wall lining panel is inserted close to the burner and below the window. The partition, the floor, the ceiling and polycarbonate strips used as light diffusers are also placed in the coach. Temperatures and gases concentrations are recorded during the test as described in figures 6.1a and 6.1b.
The key steps of scenario 1A are summarized below:

- All windows and doors were closed before beginning the test. Moreover, the ventilation which come from the strip are not stopped ($\dot{v}$= 0.3 $m.s^{-1}$).
- The burner is placed in the middle between two seats close to the wall panel.
- Time (t=0 second (t0)) starts when the burner ignited (75 kW).
- After 40 seconds, three doors are opened (blue doors in figure 6.1a)
- After 2 minutes (from t0), the burner HRR increased up to 150 kW. This intensity was maintained for 8 minutes and then the burner was turned off.
- After 22 min (from t0) the test was stopped.

6.1.1.1 Burner temperatures

The thermocouples tree position, placed above the burner, is given in figure 6.2. Thermocouples T1, T2, T3, T4 and T5 are respectively located 60 cm, 100 cm, 125 cm, 150 cm and 170 cm from the floor.

During the first phase of the burner (75 kW for 2 minutes), only thermocouples T1 and T2 reach 500 to 600°C. It means that these thermocouples are into the burner intermittent or sustained flame region. Thus, the flame height may be between 60 cm and 1 m. Then, for the second phase of the burner (150 kW for 8 minutes), thermocouples T1, T2, T3 and T4 reach 500 to 700 °C. As during the previous stage, these thermocouples may be in the burner intermittent or sustained flame region. The last thermocouple (T5) is probably into the fire plume (Drysdale (2011)). According to these information, the flame height during the second phase of the burner is located between 1.25 and 1.5 m. Moreover, according to the correlation proposed by Heskestad in 1981 (Drysdale (2011)) and based on the Froude number of fire, the burner flame height can be estimated with the following equation:

$$l_f = 0.23\dot{Q}^{2/5} - 1.02D \tag{6.1}$$

The burner flame height is assessed to 0.99 m and 1.40 m respectively for the first and second phases of the burner. This estimation of the burner flame heights matches well with the one evaluated from the flame burner temperatures (0.6 ⟨0.99⟨ 1 m and 1.25 ⟨1.40⟨ 1.50 m).

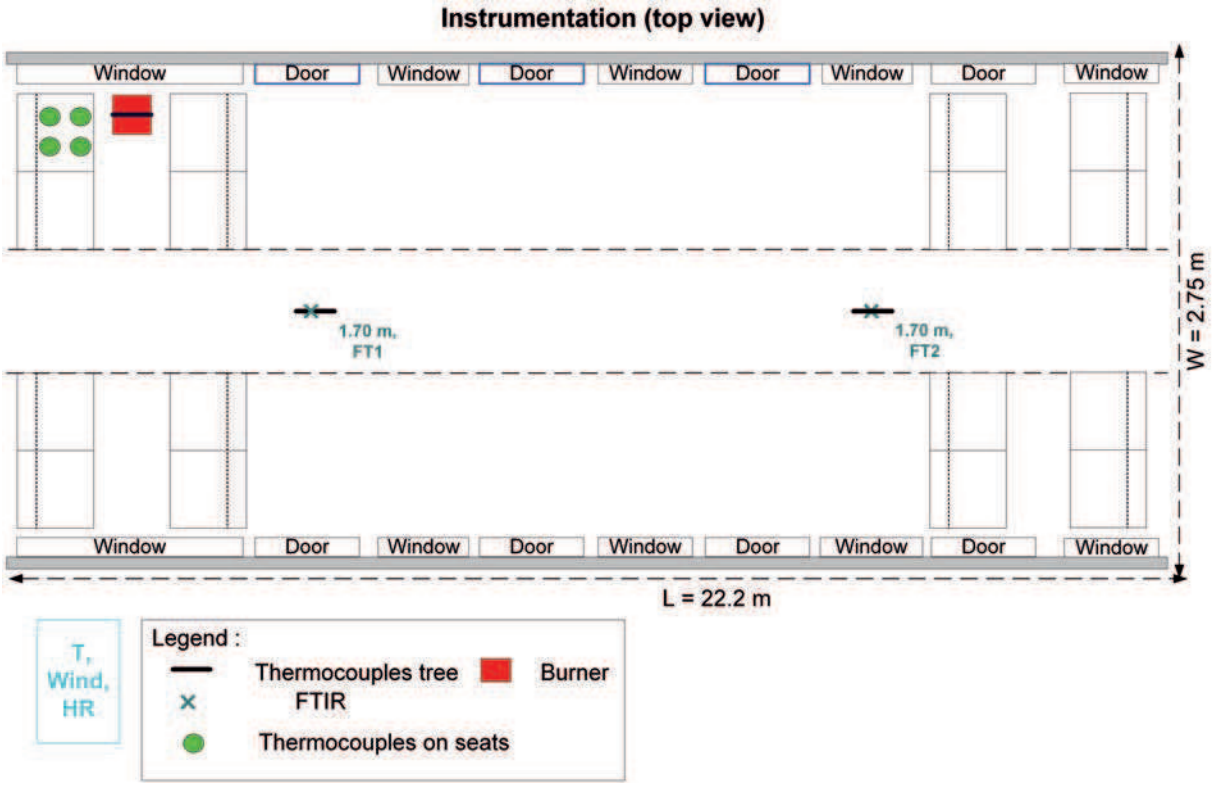

a/ Top view.

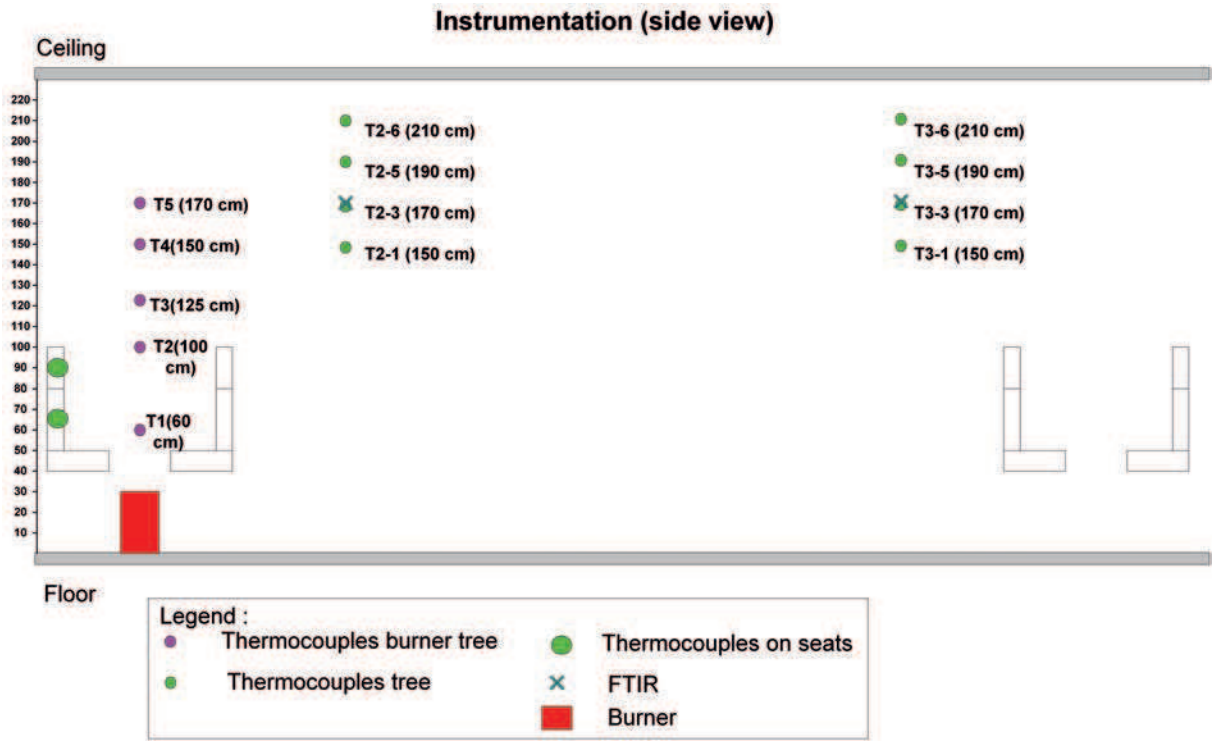

a/ Side view.

Figure 6.1: Instrumentation of scenario 1A.

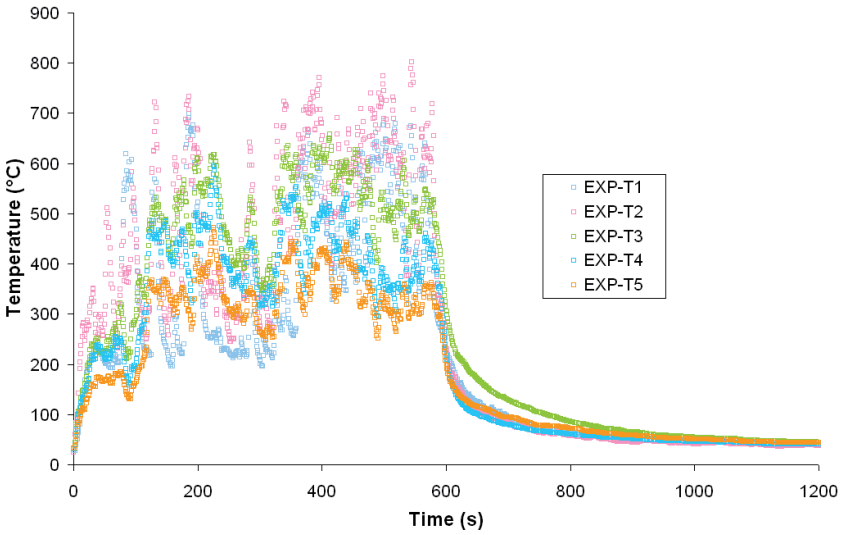

Figure 6.2: Temperatures above the burner

6.1.1.2 Seat temperatures

The seat temperatures are shown in figure 6.3b according to their positions (figure 6.3a).

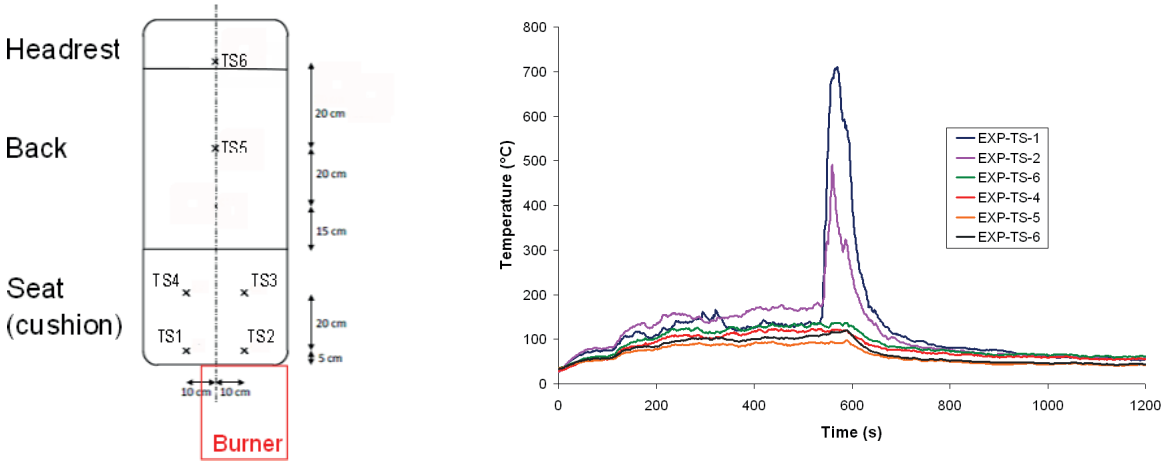

a/ Position of thermocouples on the seat

b/ Seat temperatures

Figure 6.3: Temperatures evolution of the seat during scenario 1A.

Until 475 seconds, all thermocouples have the same order of magnitude. The two phases of the burner are visible in figure 6.3b, the first one until 120 seconds and the second one from 120 to 475 seconds. Until 475 seconds, the temperature increase must only be due to the flame burner. After 475 seconds, the temperatures, related on positions TS1 and TS2, increase until reaching a peak and then shortly decrease. Thermocouples TS1 and TS2 are the ones placed close to the burner (5 *cm* from the burner surface). Thus, it is possible that the seat surface participates in the fire but only locally (near to positions 1 and 2). The other temperatures (positions 3, 4, 5 and 6) remain around

$130°C$. For all thermocouples positions, when the burner turns off, all temperatures tend to remain ambient temperatures.

6.1.1.3 Vehicle corridor temperatures

The temperatures, located in the corridor close to the fire (thermocouple tree T2) and far away from the fire (thermocouple tree T3) and distributed each 20 cm from 1.5 m to 2.1 m, are presented in figures 6.4 a and 6.4 b.

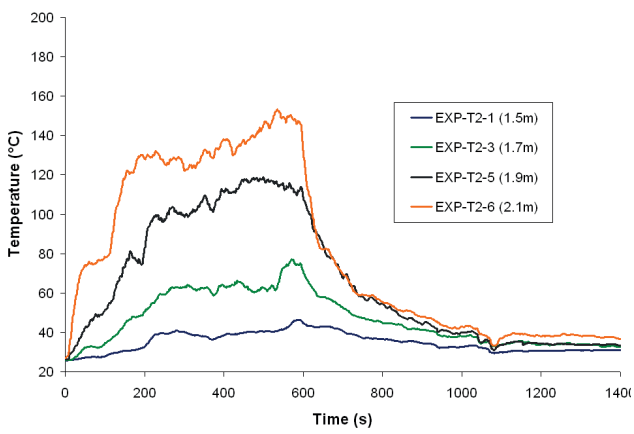

a/ Temperature evolution from 1.5 m to 2.1 m close to the fire in the corridor

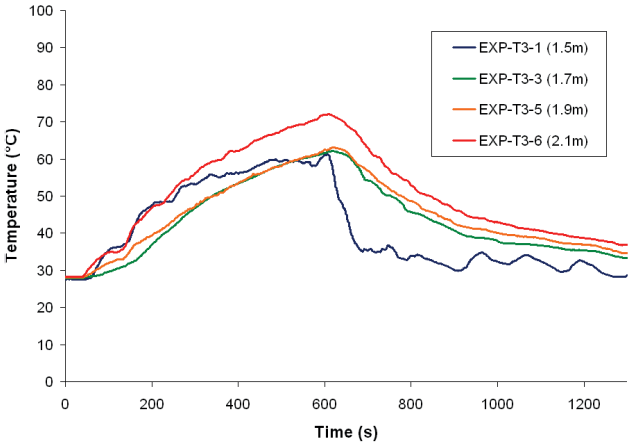

b/ Temperature evolution from 1.5 m to 2.1 m away from the fire in the corridor

Figure 6.4: Temperature evolution from 1.5 m to 2.1 m in the corridor.

During the second phase of the burner, all temperatures remain almost constant considering the thermocouple tree close to the burner. Temperatures of thermocouples T2-1, T2-3, T2-5 and T2-6 respectively reach 39, 63, 111 and $138°C$ for this time period, whereas for thermocouple tree T3, the temperature continuously increases at any height position. When all thermocouples reach around $65°C$, the temperature suddenly decreases, due to the burner which turns off. According to the two temperature graphs, temperatures seem stratified close to the fire and have a homogeneous tendency away from the fire in z direction (coach height).

6.1.1.4 Gases concentrations

Two FTIR are used to analyse (qualification and quantification) the gases from the fire effluents. A heated line is placed between the FTIR and the sampling point. Both sampling points are placed on each thermocouple tree (one close to the fire and the second one away from the fire) 1.70 m from the floor (figure 6.1 a). This height has been chosen by Transfeu partners in order to represent a critical face/nose height. Two types of gases are detected during scenario 1A: carbon dioxide and carbon monoxide. Gases concentrations of each position are presented in figures 6.5 a and 6.5 b. Positions FT1 and FT2 respectively mean the location near the fire and far from the fire.

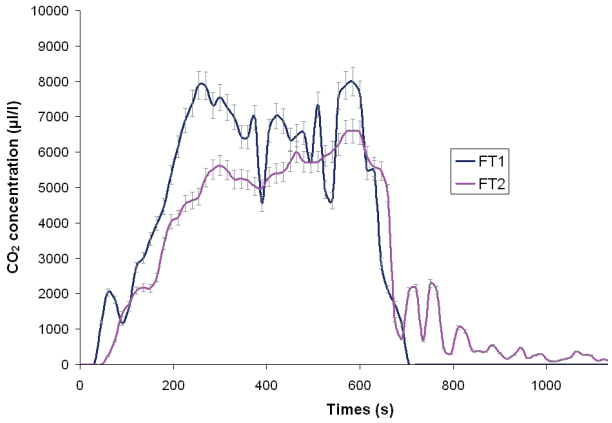

a/ Carbon dioxide concentration at the two positions during scenario 1A

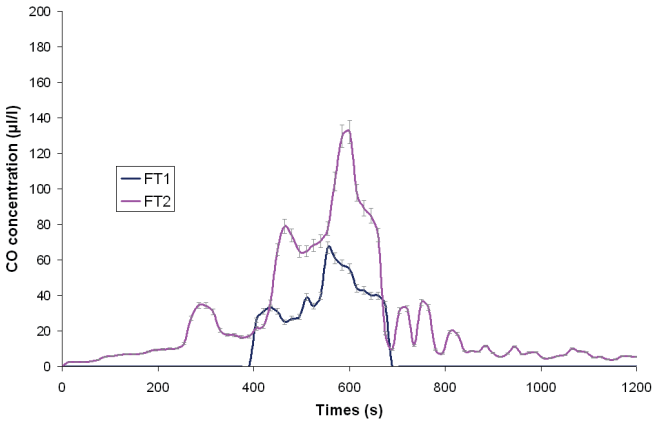

b/ Carbon monoxide concentration at the two positions during scenario 1A

Figure 6.5: Gas concentration at the two positions during scenario 1A.

Concerning carbon dioxide concentration, the two phases of the burner (75 kW for 2 min and then 150 kW for 8 min) are visually observed in the figure 6.5a (one peak at 2,000 $\mu l.l^{-1}$ until 120 seconds, then one plateau between 5,000 and 8,000 $\mu l.l^{-1}$ until 600 seconds). The plateau oscillations may be due to the position of the sampling point in the smoke layer. Indeed, smoke eddies could have an impact on carbon dioxide concentration. For the second position of the carbon dioxide concentration, a peak is also observed at around 2,000 $\mu l.l^{-1}$. This peak is a slight shift compared to the *FT1* peak due to the distance between the two sampling points (18 m). Then, during the second stage of the burner, the carbon dioxide concentration increases slowly from 4,500 to 6,000 $\mu l.l^{-1}$. This continuous increasing concentration can be due to the fact that the sampling point is close to the end of the coach and tends to homogenize. Concerning carbon monoxide concentration (position *FT1*), the gas is detected starting from 400 seconds with a direct value of 26 $\mu l.l^{-1}$. The detection of carbon monoxide may start at 25 $\mu l.l^{-1}$ and for any value lower than 25 $\mu l.l^{-1}$ the value is put to zero. Carbon monoxide concentration tendency is different between the first and second positions. Moreover, contrary to carbon dioxide concentration, carbon monoxide concentration of position *FT2* is higher than the *FT1* one. For both positions, the sample probe is placed at 1,70 m from the floor. When smoke is close to fire source, smoke thickness is thin due to its density (compared to air density). Whereas, far away from fire source, smoke tends to mix with air and its thickness increases. This can explained CO concentration difference between *FT1* and *FT2* positions.

6.1.1.5 Impacted surface

After the tests, the seat and the wall panel close to the fire have participated in the fire. Only part of the seat cushion was partially damaged (figures 6.6). This part corresponds to thermocouples position 1 and 2 (figure 6.3 a). The polycarbonate shell, located at the edge of the cushion, melted.

a/ Impacted seat surface by the burner after the test, picture from RATP

b/ Impacted seats surface by the burner after the test, picture from RATP

c/ Impacted wall panel surface by the burner after the test, picture from RATP

Figure 6.6: Impacted surfaces by the burner after the test, picture from RATP

6.1.2 Initial boundaries

6.1.2.1 Mesh size

For design fire scenario 1A simulation, the whole of the coach geometry is divided in two domains: one with a 5 cm mesh size in all directions and close to the burner, and another one with a mesh size of 10 cm in x and y directions and 5 cm in z directions. The global size of the coach domain is 24.5, 4 and 3.2 m respectively in x, y and z directions. As it is explained in the previous chapter, the ideal size mesh is given according to the criteria linked to the fire diameter and the Froude number of fire (Eq 4.20 and 4.21). This criteria is satisfied for the scenario 1A test domain with 5 cm and 10 cm size meshes. In the sense of multi scale approach and because the FDS pyrolysis model is used on the seat and on the wall panel, a 5 cm mesh size is tested close to the fire, while a 10 cm mesh size is used to transport the fluid into the coach.

6.1.2.2 Aerodynamic conditions

All surfaces of the domain are considered open, i.e. the initial velocities in the three directions are null and the initial pressure corresponds to the ambient pressure or the atmospheric pressure (101325 Pa). Moreover, during the simulation, the top surface of the strip is associated to an air input flow of 0.5 $m^3.s^{-1}$.

6.1.2.3 Radiative and thermal conditions: propane burner study

The numerical propane burner is considered validated. More details about the propane burner simulation are presented in the previous part (Multi-scale comparison results on railway seat)

6.1.3 Input data

The numerical geometry of the coach respects the dimensions obtained from the Transfeu partners (figures 6.7 a and 6.7 b):

- The internal dimension of the coach is 22.1, 2.8 and 2.4 m in x (length), y (width) and z directions (height).
- The roof is slightly curved on each side.
- Only two blocks of 4 seats are placed on each extreme side of the coach.
- The dimension of the seat is in agreement with plans provided by Transfeu partners and adjusted with the used mesh size.

a/ Numerical face view of the coach

b/ Numerical top view of the coach

Figure 6.7: Numerical views of the coach from FDS.

The products present in the simulation are:

- the roof (high pressure laminated product)
- the floor (rubber)
- the window (glass)
- the strips (polycarbonate)
- the studied seat from the raw matter to the finished product scale
- the studied wall panel from the raw matter to the finished product scale

Moreover, the whole structure is composed of steel. All thermo-physics properties are presented in table 6.1.

Table 6.1: Material properties of scenario 1A, Kakac *et al.* (1985)[a], ISO 10456 (2007)[b], Langlais and Klarsfeld (2004)[c]

Properties	**Ceiling**	**Floor**	**Strip**	**Structure**	**Window**
ρ	700^b	1200^b	1200^c	7800^b	2700^a
Cp	1.7^b	1.4^b	1.2^c	0.45^b	0.83^a
λ	0.15^b	0.17^b	0.24^c	50^b	1^a

Concerning the seat and wall panel products, all properties which are validated at the finished scale are used as input data. Moreover, the seat surface receives a maximal incident heat flux lower than $15 kW/m^2$ (figure 6.8). Consequently, all the foam thickness is replaced with the fictive layer thickness (described in the chapter 4: Multi-scale comparison results on railway seat).

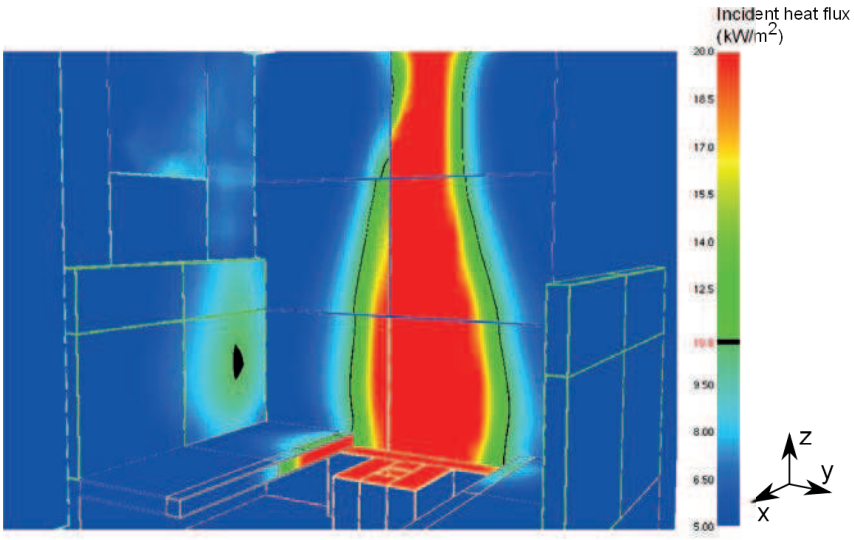

Figure 6.8: Incident heat flux received by the seat, picture from Smokeview.

Furthermore, concerning the gas phase at the finished product scale, the propane burner is chosen as the major fuel in the simulation. Thus, the composition, the carbon monoxide yield, the soot yield and also the effective heat of combustion correspond to propane.

6.1.4 Numerical results

6.1.4.1 Temperature

The comparison between experimental and numerical temperatures (5 cm mesh size) are shown in figures 6.9. Concerning the first location, experimental temperature oscillations show that the thermocouple is either in the flame or in the air, due to the flame shape. However, numerically, the temperature is constant (around 550 $°C$) and always in the flame. This difference may involve a difference on the experimental and numerical flame shapes. Concerning positions 2, 3, 4 and 5, both experimental and numerical temperatures have an oscillatory trend due to the burner intermittent flame. Moreover, they have the same temperature order of magnitude, except for sensor 5. Indeed, the experimental temperature is smaller than the numerical one. Position 5 is placed 1.5 m from the floor, while the experimental flame height is estimated at 1.4 m. The numerical flame height may be slightly higher than the experimental one. This difference may have an impact on the heating-up of products, such as the wall panel and the seat.

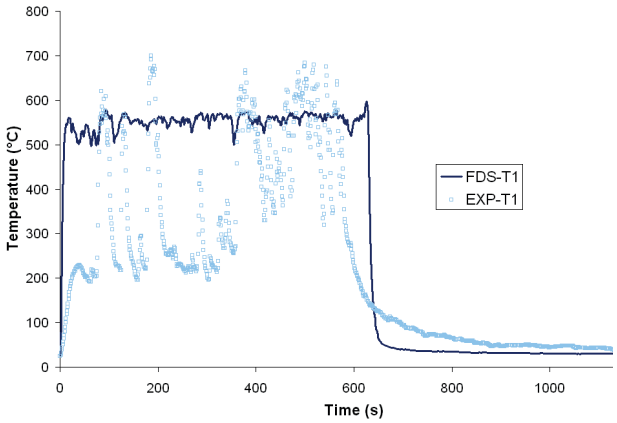

a/ Sensor 1.

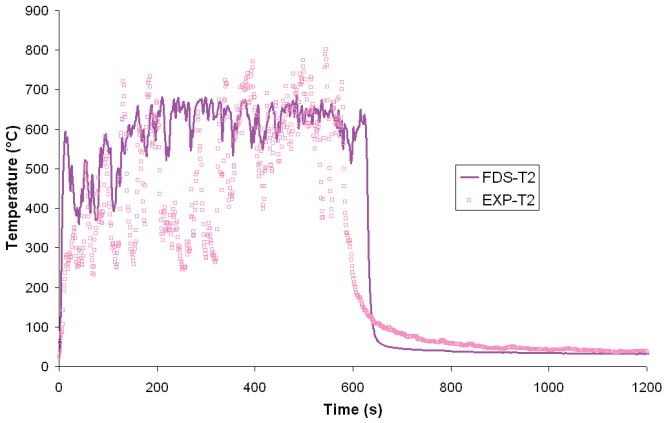

b/ Sensor 2.

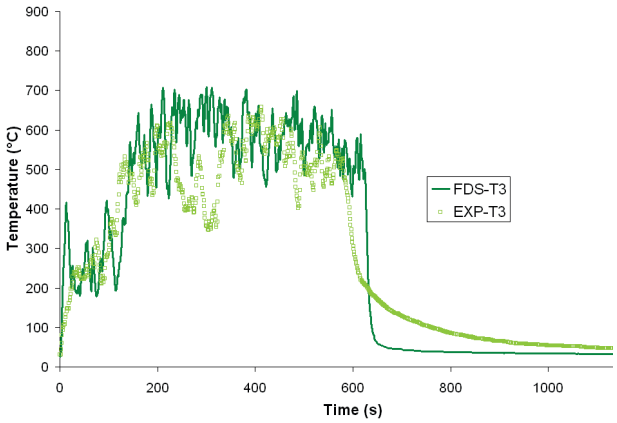

c/ Sensor 3.

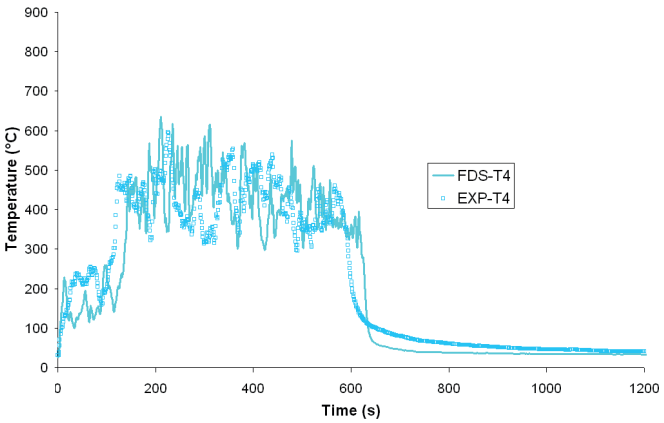

d/ Sensor 4.

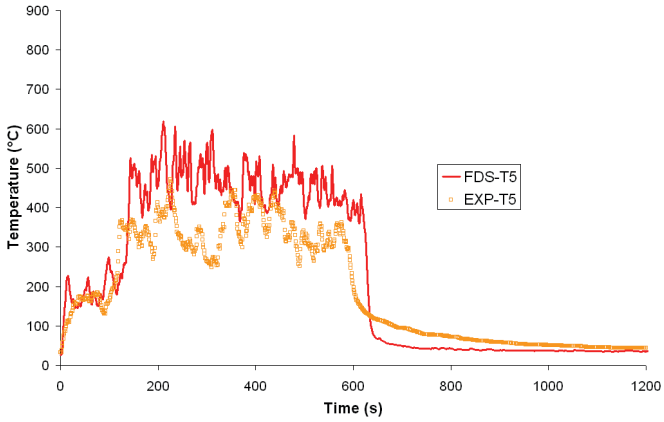

e/ Sensor 5.

Figure 6.9: Experimental and numerical temperature comparison above the burner.

Figures 6.10a and 6.10b are the experimental and numerical comparisons of the seat temperatures. During the scenario simulation the seat does not participate in the fire. All numerical temperatures remain constant between 85 and 110$°C$, whereas the experimental surface seat temperatures, located on positions 1 and 2, raise and rapidly decrease. As for positions 3, 4, 5 and 6, the numerical seat temperatures match with the experimental ones.

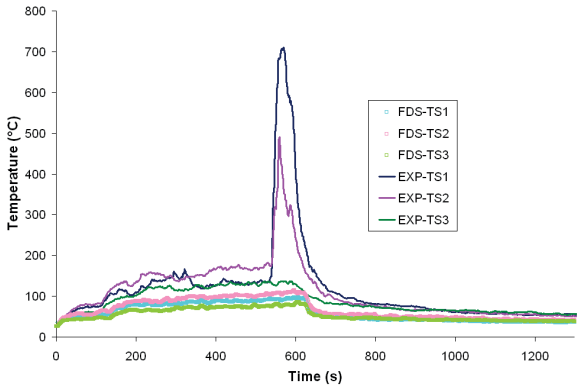

a/ Sensors 1, 2 and 3

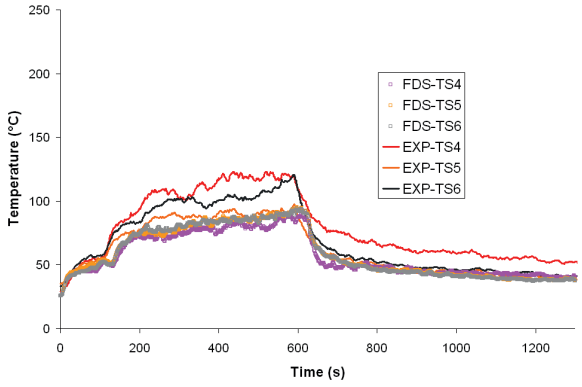

b/ Sensors 4, 5 and 6

Figure 6.10: Experimental and numerical seat temperature comparisons.

Figures 6.11a and 6.11b are experimental and numerical comparisons of the gas temperatures in the coach along the corridor, respectively close and far from the fire.

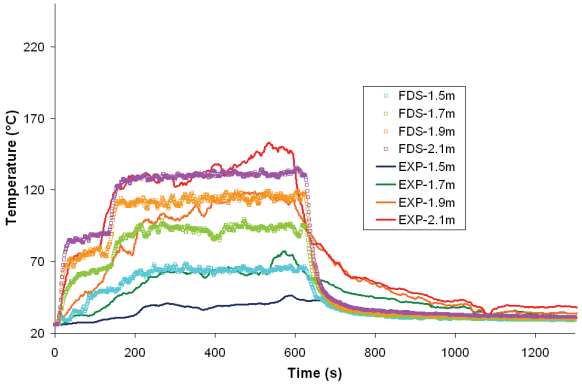

a/ Thermocouples tree 1.5 to 2.1 m from the fire.

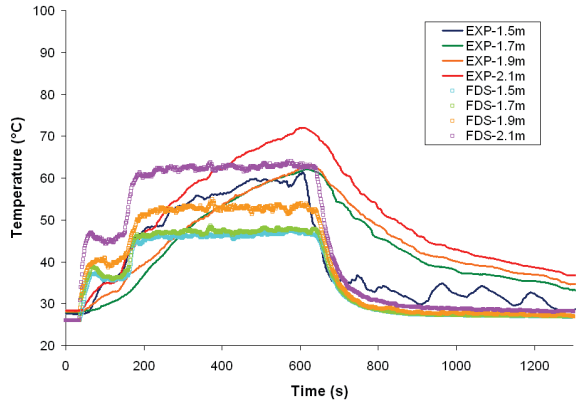

b/ Thermocouples tree 1.5 to 2.1 m far from the fire.

Figure 6.11: Experimental and numerical gas temperature comparisons in the corridor.

Concerning the thermocouples tree close to the fire, for all positions, the numerical trends follow the kinetic of the burner power (75 kW for 2 min and then 150 kW for 8 min) and have the same order of magnitude. However, for both positions at 1.5 and 1.7 m, a temperature deviation is observed during the fire scenario. This deviation oscillates between 25 and 30 $°C$. This temperature comparison is almost deciduous because the uncertainties on the measures and on the repeatability is not known. Knowing the uncertainties and the positions of both thermocouples between the air layer and the smoke layer, the comparison remains acceptable. Concerning thermocouples responses located far from the fire, the numerical and experimental temperatures kinetic are slightly different. Indeed, two numerical temperature levels are observed while the experimental temperatures continuously increase. This difference may be due to the mesh size of the coach. But, the experimental and numerical temperatures almost have the same order of magnitude.

6.1.4.2 Total impacted surface

During the simulation, the seat does not participate in the combustion. Only the wall panel has been attacked by the burner. The experimental and numerical impacted surface area of the wall panel are presented in figures 6.12a and 6.12b, knowing that the burner is placed between 0.8 and 1.1 m in the simulation. The numerical burnt surface is assessed with the burning rate gradient and considering a threshold of burnt area of 2.10^{-3} s^{-1}. According to a visual observation, the total burnt surface areas have the same order of magnitude: around 0.25 m^2.

a/ Impacted wall panel surface by the burner after the test, picture from RATP

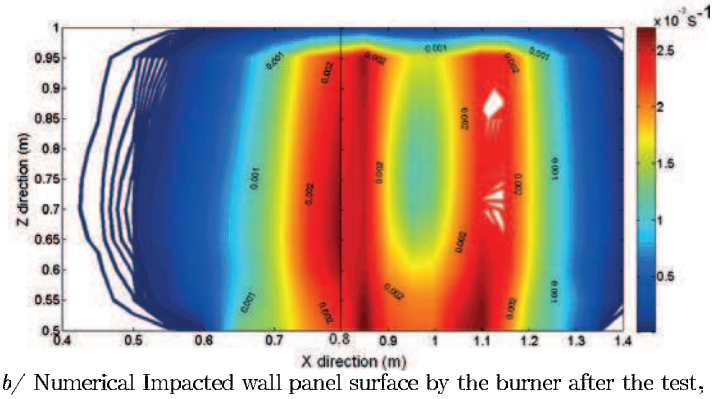

b/ Numerical Impacted wall panel surface by the burner after the test, via the gradient of the mass loss rate.

Figure 6.12: Visual comparison of impacted burnt area of the wall panel

6.1.4.3 Released gases

The experimental and numerical gases released are compared in figures 6.13. The experimental and numerical carbon dioxide and carbon monoxide concentrations have the same kinetic as the burner power (two stages are observed).

Concerning carbon dioxide results and position *FT1*, the numerical response has the same level of magnitude than the experimental one: around 2,500 $\mu l.l^{-1}$ and 6,000 $\mu l.l^{-1}$ for each plateau (figure 6.13a). For the second position, the numerical concentration is about two times lower than the experimental one (figure 6.13b). This difference could be explained by different assumptions:

- The mixture of species in the smoke layer: indeed smoke eddies can have an impact on species dilution and concentration in the coach volume.
- The numerical volume of the coach: the numerical volume may not perfectly match the real volume due to the mesh size, the mesh cubic shape and the original plan.
- Measurement uncertainties: due to the FTIR apparatus, the repeatability of the test and the sampling point position into the smoke.
- The experimental quantity of smoke species which goes out when the doors open is unknown. These data cannot be compared with numerical ones. Thus, the numerical quantity of fluid which leaves the coach could be higher than the real one.

Concerning the carbon monoxide comparison, the experimental and numerical tendencies are different from both positions. For the first position, the experimental and numerical maximum concentration have the same level of magnitude. However, for the second position, the experimental maximum concentration is two times higher than the numerical one.

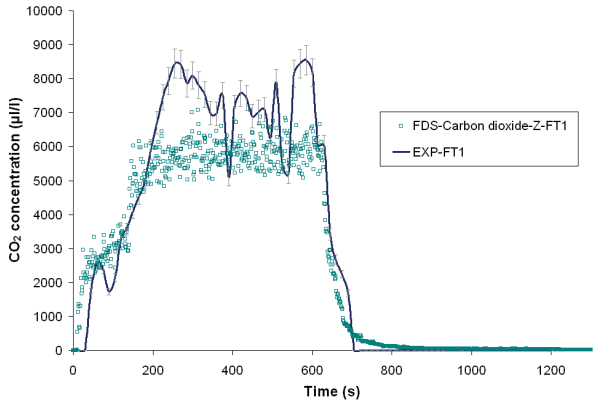

a/ CO_2 comparison of scenario 1A in position *FT1* (close to the burner).

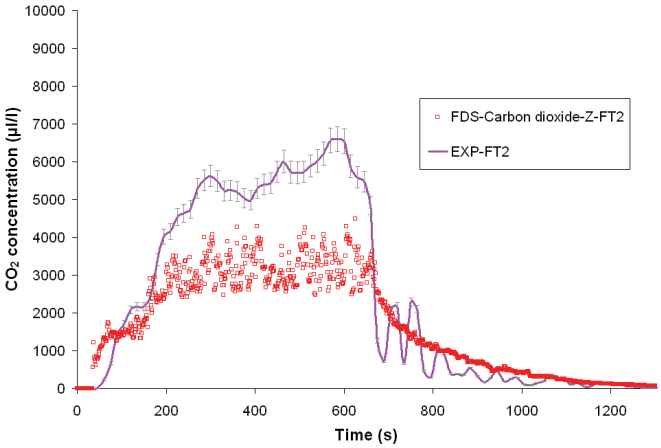

b/ CO_2 comparison of scenario 1A in position *FT2* (far from the burner).

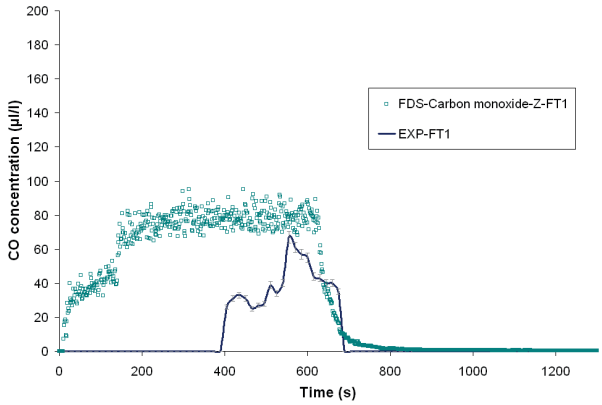

c/ CO comparison of scenario 1A in position *FT1* (close to the burner).

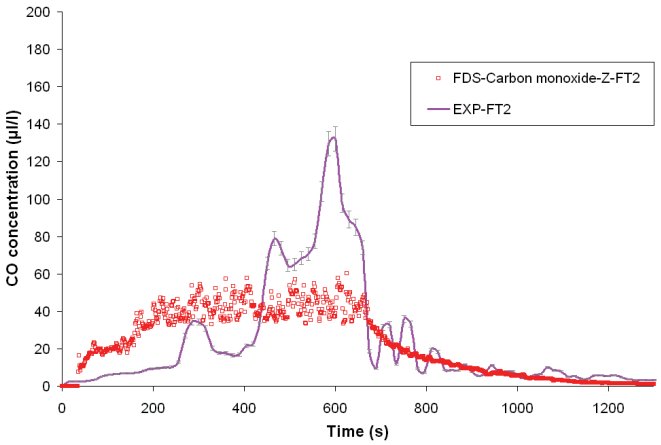

d/ CO comparison of scenario 1A in the position *FT2* (far from the burner).

Figure 6.13: Experimental and numerical gas concentration comparisons of scenario 1A.

It is important to remind that numerical carbon monoxide concentration is calculated from the FDS combustion and pyrolysis models. A unique combustion reaction and unique carbon monoxide yield (Y_{CO}=0.025 $kg.kg^{-1}$) are used in this simulation. While two different types of fuel participate in this combustion: propane and polyester. Numerical mass losses of the burner and the wall panel are respectively 1.76 kg and 0.62 kg during the scenario simulation. Propane is the unique fuel. Thus, to improve the carbon monoxide concentration comparison, a new approach has been developed. The principle is to inject the experimental mass flow of the carbon monoxide from each fire source on a surface product in the simulation. The objective is not to calculate the quantity of carbon monoxide released but only to transport it into the numerical domain in order to avoid

the error induced by the FDS combustion model. This approach is firstly tested on the finished wall panel scale, and then applied on the real scale.

6.2 Finished wall panel scale

6.2.1 Input data

The same input data as the studied finished wall panel scale are used for this new simulation: same pyrolysis parameters, thermal properties and gas phase parameters. The only difference with the previous finished wall panel scale simulation is the addition of two carbon monoxide mass flows affected in the middle of the burner surface. One mass flow is associated to the carbon monoxide released of the burner and the other one to the wall panel. Each of them are affected on the burner surface area with an area of 0.005 m^2. There are associated to this specify surface so that the released species are transported into the fire plume with the same temperature. The chosen mesh size is the same as the real scenario simulation, i.e. 5 cm.

The numerical quantity of the carbon monoxide of the burner injected (in $kg.s^{-1}.m^{-2}$) comes directly from the finished burner test. Indeed, a test was performed with only the propane burner and incombustible materials for the ceiling, the floor and the panel. The test responses are the heat release rate, the mass loss and also the released gases, such as carbon dioxide and carbon monoxide, measured into the duct. Figure 6.14 represents the total released quantity of the experimental carbon monoxide. The same carbon mass flow ramp (FDS-CO-input) is used as a prescribed FDS input data.

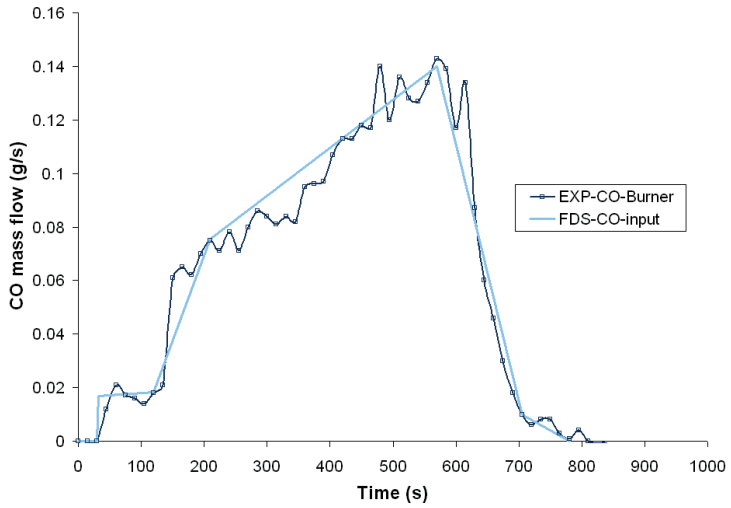

Figure 6.14: Experimental and numerical input of carbon monoxide concentration for the finished wall panel scale simulation.

Concerning the injection of the carbon monoxide mass flow from the wall panel, the first information to know is to estimate the numerical burnt surface of the wall panel. Thus, this approach is applicable in two stages. First, the mass loss rate, the heat release rate

and the temperature of the finished wall panel test during the first simulation have to be validated. Secondly, the numerical burnt area of the wall panel is assessed and a carbon monoxide mass flow quantity is injected. This quantity is also derived from a small wall panel material test, which is supposed to be more cost-effective than the finished scale test.

For the wall panel product, there are two possible choices: either the CO mass flow quantity from the cone calorimeter test (ISO 5660-1 (2002)), or from the medium burning item test (ISO 21367 (2008)). This choice is made according to the test conditions and the end-condition of the wall panel product.

Nevertheless and as demonstrated previously (in the wall panel multi scale results), the reaction-to-fire of the wall panel material is affected by thermal feedback by the back face level of the material. This thermal effect implies an additional released quantity of CO due the cone calorimeter tests conditions. Moreover, the tested product during the cone calorimeter tests is placed horizontally, whereas the end-condition of the wall panel product is vertical. However, during the MBI test, the wall panel is tested vertically and no thermal feedback is observed due to the lack of back condition material. The numerical released carbon monoxide ramp (from MBI test) is injected when the second phase of the burner begins because the numerical pyrolysis and the combustion of the wall panel material starts at this moment. The maximum quantity of carbon monoxide released from the MBI test is 0.03 $g.s^{-1}$. Then, this quantity is corrected by ratio R of the burnt surface area at finished product scale by the MBI one. The panel burnt areas are estimated with figure 5.32 for the finished product test and figure 5.13 for the MBI test (blue curve). The burnt areas are assumed as 0.055 m^2 and 1.5 m^2, respectively for the MBI and the finished tests.

The related assumptions on this approach are:

- All numerical surface units must release the same carbon monoxide quantity.
- The thermal attack of the MBI test is 50 $kW.m^{-2}$ on the panel. The numerical quantity of released carbon monoxide corresponds to this thermal attack. Consequently, the injected carbon monoxide mass flow depends on the exposure fire source.
- The numerical simulation of the finished product scale is supposed to have the same fire conditions as the MBI test (fire well-ventilated).
- The numerical injected carbon monoxide species is defined by its molar mass (28 $g.mol^{-1}$) and does not interact with other species. It is considered as a no-reactive species.
- No scale effects on flame size. This is known as false but assumption is made here.

6.2.2 Numerical results

Before analysing the gas phase, the pyrolysis and the combustion of the wall panel have been checked in order to ensure the additional injected species do not disturb fire ignition and fire spread on the wall panel. No changes have been detected between this new simulation and the previous simulation results on the mass loss, the heat release and the temperature. Furthermore, as the numerical reaction-to-fire of the panel is the same, the

carbon dioxide mass flow has also the same response as the first finished panel simulation (figure 5.33 a). Thus, only the carbon monoxide mass flow differs from the first simulation.

Figure 6.15 shows the experimental carbon monoxide mass flows from the burner and from the finished panel tests (respectively green and pink curves). Moreover, the figure presents the numerical carbon monoxide mass flows from the previous simulation (from the multi-scale chapter - light green square) and from these new input data (injected species - grey square).

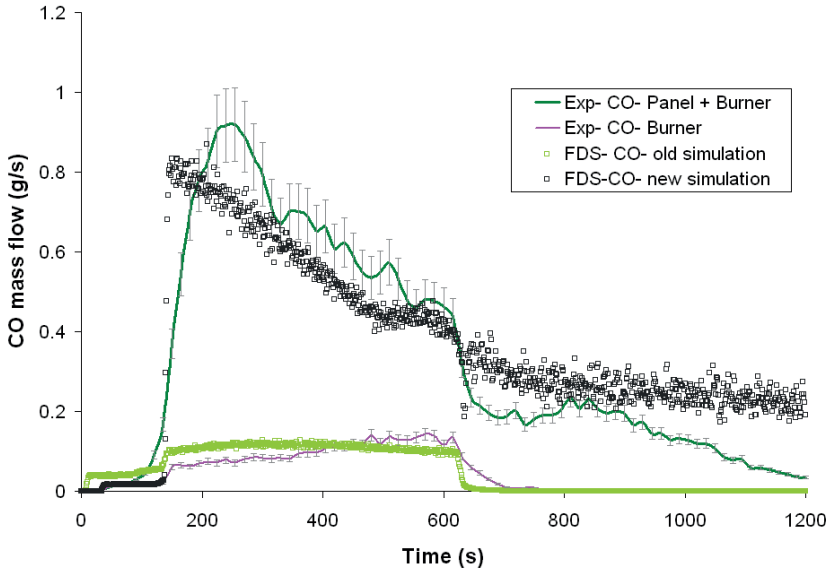

Figure 6.15: Experimental and numerical comparison of carbon monoxide mass flow for the finished wall panel scale simulation- old and new results simulation

The new numerical carbon monoxide mass flow matches well with the experimental one (curve green and grey square). The trend and the intensity are similar. This new approach to prescribe carbon monoxide seems effective for this test. This approach is thereafter tested on scenario 1A.

6.3 Design fire scenario 1A: New approach on carbon monoxide concentration estimation

6.3.1 Input data

The same input data as for the previous design fire scenario 1A simulation are used. Furthermore, the new approach to compare the CO concentration and validated on finished panel scale, is tested on scenario 1A. The carbon monoxide mass flow input data related on the burner is the same as the previous scale (figure 6.14). Concerning the injected CO mass flow of the panel in the numerical scenario, it comes from the MBI test and the new ratio between the burnt surface area at real scale by the MBI one. The panel burnt areas are estimated with figures 6.12a for the real test and figure 5.13 for the MBI test (blue

curve). The burnt areas are assumed as 0.055 m^2 and 0.25 m^2 respectively for the MBI and the real tests.

6.3.2 Numerical results

As the finished scale, no more changes have been detected between this new and the previous simulations results on the temperatures. Furthermore, the carbon dioxide mass flow has also the same response as the first scenario 1A simulation because the numerical reaction-to-fire of the panel is equivalent and the mixture fraction model is used to estimate the carbon dioxide concentration. Thus, only the carbon monoxide mass flow is different from the first scenario simulation.

Figures 6.16 a) and 6.16 b) represent the new comparisons of carbon monoxide concentrations of scenario 1A for both positions *FT1* (close to the fire) and *FT2* (far from the fire).

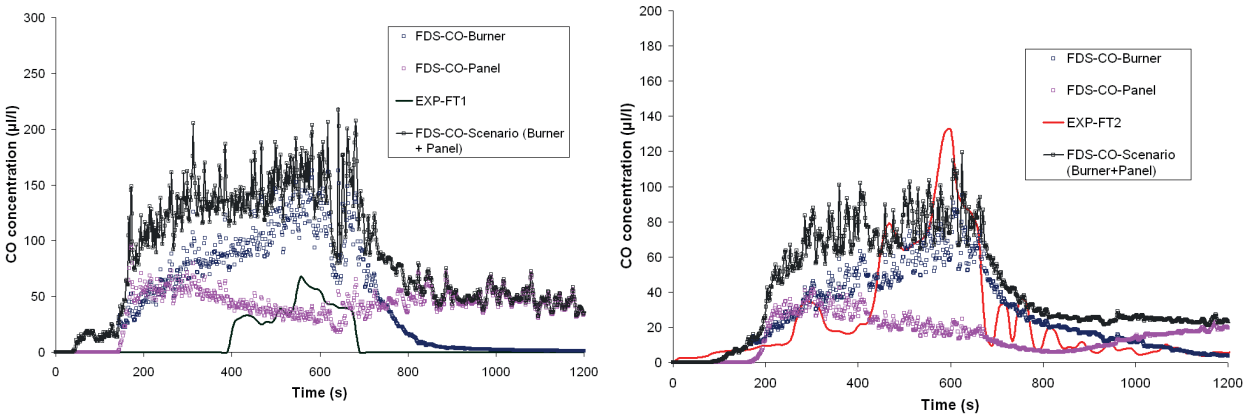

a/ New comparison of experimental and numerical *CO* of the scenario 1A in position *FT1* (close to the burner).

b/ New comparison of experimental and numerical *CO* of the scenario 1A in position *FT2* (far from the burner).

Figure 6.16: New experimental and numerical carbon dioxide concentration comparisons of scenario 1A.

As a carbon monoxide track has been injected for each fire source (burner and wall panel), it is possible to separate the numerical concentration which comes from the panel (pink square) and the burner (blue square). The addition of these two track species gives the total carbon monoxide concentration of scenario 1A (grey square) for each position.

Concerning the first position, the numerical CO concentration has a longer and earlier kinetic than the experimental one. Indeed, the numerical CO starts to be released from 145 seconds (CO concentration higher than 25 ppm) while experimentally it is around 390 seconds. Moreover, the maximal numerical CO concentration is around two times higher than the experimental one. According to figure 6.16a , the intensity of the CO concentration, which comes only from the panel, has approximately the same order of magnitude as the experimental one. Thus, the numerical CO concentration which comes from the burner may be overestimated when it is injected in FDS. Remains that the numerical CO injected comes from the experimental finished product scale with only the

burner (figure 6.14). Even if the fire is well-ventilated in both situations (finished product and real scales), it is possible that the effect of the corner, wall and ceiling configurations have a considerable influence on the CO production. Indeed, the flame may be different between these two scales and it implies a divergence on the oxygen diffusion processes and the CO residence time into the flame.

Concerning the second position, the numerical CO concentration has the same intensity and almost the same kinetic as the experimental one (figure 6.16b).

6.4 Discussion

The fire risk analysis used enables to identify four risky design fire scenarios on a high number of probable and hazard fire scenarios in the context of the Transfeu project. One of them, named Scenario 1A, is studied according to a multi-scale approach. The reaction-to-fire of two products (a seat and a wall panel) located close to the fire source are carefully analysed from the raw matter to the finished product scales.

The numerical and experimental comparison is based on the HRR, MLR, mass loss, temperature, impacted surface area and released gases. For the seat and the wall panel, the comparison is satisfactory considering the experimental uncertainties and the FDS code limitations. However, a difference on the production kinetic and intensity at the finished product scale persists on the carbon monoxide emissions. This experimental and numerical difference can be explained by the generation processes of carbon monoxide from a flame. Indeed, experimentally, the CO formation depends on the type of fuel, the oxygen diffusion, its time residence and the temperature into the flame and the surrounding factors which can influence the flame. These parameters are not taken into account in the FDS Mixture fraction combustion model applied to multiple fuels. Thus a new approach with FDS is tested in order to improve this comparison on the released carbon monoxide.

The objective of this real scale is to validate the reaction-to-fire of the seat and the wall panel designed in a real test and through the pyrolysis input data associated to a reaction mechanism and also the thermo-radiative properties of the materials. The fire source of scenario 1A is placed in the middle, between two seats. It is a different situation from the finished product test where the burner is located very close to the seat and the wall panel. The incident heat flux received on the seat is lower during the real scale test than during the finished product test. The incident heat flux received by the seat is around $11 kW.m^{-2}$ according to figure 6.8. According to the FDS simulation of scenario 1A, the seat does not participate in the combustion, only the panel does. As it is known, FDS models have some limits to predict the heat release rate at low heat flux exposures (Hostikka and McGrattan (2001)).

Several temperatures at different locations (seat, burner and coach corridor) are compared with numerical ones. Despite the experimental uncertainties and the FDS code limits, good correlations have been found. Concerning the impacted surface area com-

parison, the one corresponding to the wall panel is satisfactory, taking uncertainties into account. As for gases released, only carbon dioxide and carbon monoxide are detected by the FTIR spectrometer. Indeed, contrarily to the carbon dioxide concentration, CO concentration of the position *FT2* is higher than the position *FT1*. The carbon dioxide volume concentration comparison is acceptable knowing the experimental and numerical uncertainties (sample position into the smoke layer, the FTIR itself and the discretization of the coach volume), and regarding FDS limitations (presence of multiple fuels). However, the comparison between experimental and numerical emissions of CO is more complex. The experimental and numerical kinetic of CO concentration is different.

Thus, only for the CO production, the FDS Mixture fraction combustion model is not used any more. The CO source is not predicted but prescribed from experimental tests. The transport FDS equation models are used to disperse the CO in the domain. A CO ramp-time function is introduced in FDS from the finished burner test and from the MBI test for the wall panel. It is admitted that the seat does not release CO because it does not participate in the combustion. This approach is tested firstly at the finished product test (burner + wall panel). Using this approach, the experimental burnt surface has to be known.

The comparison of CO production is better with the prescriptive approach than with the FDS combustion model at finished product scale. Indeed, a good correlation is found between the experimental and numerical CO generation. Let us remind that the proportion of CO production comes from the panel. This approach is then tested at upper scale.

For the first position in the vehicle corridor (close to the fire source), the numerical CO production is overestimated compared to the experimental one, whereas for the second position in the corridor far away from fire source, the comparison shows the same order of magnitude. At this scale, CO formation is controlled by the burner combustion, contrary to the previous scale. Thus, even if the fire is supposed to be globally well ventilated in both scales (finished burner and real scales), it is possible that the fire conditions evolve locally during the finished test due to its configuration and have an influence on the CO production. The injected CO from the finished burner test in FDS code may not be adapted to the simulation of this real scenario. This prescriptive approach is interesting when a fuel is dominating. Nevertheless, it requires data from the experimental tests.

Conclusion and future works

This thesis deals with European railway transport fire safety of in a project named Transfeu. European research project Transfeu studied the fire behaviour and toxic gas generation of different train products in order to predict the fire impact during passenger evacuation. The toxic potential from fire effluents was studied at material, semi-finished product, finished product and real scales. Moreover, one of the major Transfeu objectives was to develop a fire safety methodology to simulate fire growth and gas dispersion in a train coach in order to estimate life expectancy for a given design fire scenario.

Transfeu works aimed to improve European regulation (European Directive 2008/57/EC (2008)) and railway standard (FprEN 45545-2 (2012)), which will soon be published, and especially the fire safety engineering methodology. The objective of this approach is to prove that the design fire scenario reaches fire safety levels according to several fire scenarios. Eventually, toxic potential is not estimated product by product with fire safety criteria but for a complete design scenario. The experimental fire safety study of a design fire scenario is feasible but expensive. Thus, a fire safety methodology is developed through a strong interaction between experimental tests and numerical fire models. The thesis objective aims to predict the fire growth of a specific design fire scenario of a train coach considering the CDF fire code limits. The code used in this thesis is FDS version 5.5.3. The principle is to understand the FDS abilities to simulate a fire. When the FDS models are validated, the product fire growth and gas dispersion are assessed according to different types of design fire sources, for instance. However, this validation is not obvious and required a multi-scale approach on each studied product. The multi-scale approach comprises three phases:

- Experimental tests from raw matter to real scales: all individual tests and the coupling between two increasing scale tests provide essential information to try to understand the involved phenomena.
- Numerical FDS simulations of these experiments: this step requires the comprehension of FDS models and their limits. Additionally, a model needs input values (constant or temperature dependent) to work. These input values depend on the model itself and on the type of studied phase (gas or condensed). Which ones and how can we find these input data ?
- Experimental and numerical comparison and feedback corrective actions regarding input data used for the simulation (if necessary). This step is fundamental because it couples the experimental tests comprehension and the evaluation of FDS limits.

A fire risk analysis is conducted in order to select one of the most hazardous design fire scenarios and to study their fire performance through a multi-scale approach.

The objective of this relative fire risk analysis is to compare a few design fire scenarios, selected by Transfeu railway fire safety experts, with the overall possible scenarios in a risk matrix. Each design fire scenario of the matrix is obtained from a global event tree and quoted with its own probability and severity. The selected design fire scenario is finally classified in the "Serious Risk" category. This ranking is questionable because it depends on the type of probabilities and severities used. These values are difficult to obtain due to the rarity of these kinds of events nowadays in the European railway transport. Consequently, the sensitivity analysis is carried out. The results show that:

- The occurrence probability of the selected scenario (1A) is controlled by the ventilation event.
- No particular event controls the severity of scenario 1A.

Moreover, scenario 1A is still a hazardous scenario compared to the global matrix considering the uncertainties due to the sensitivity analysis.

Scenario 1A corresponds to a flame burner source placed close to the seat and a wall panel in a standard train coach. The burner ignites for 2 minutes at 75 kW and then at 150 kW for 8 minutes. Three doors open after 40 seconds in order to represent the delay time between the ignition and the station arrival. Scenario 1A is studied according to a multi-scale approach. The two products (a seat and a wall panel) located close to the fire source and likely to burn, follow this approach.

The thermal decomposition of each layer of the seat and the wall panel is studied at raw matter scale. Four layers (cover, interliner, foam and composite resin) are analysed through TGA/DSC tests. A reaction mechanism is assessed for each layer according to the MLR and the mass loss curves, obtained from TGA tests and an overview of each component decomposition. The reaction mechanism is supposed to be independent of the heating rate and the ambient atmosphere and proper to each material. The influence of the heating rate and the oxygen atmosphere is studied. For certain components, the presence of oxygen accelerates thermal decomposition. The objective of this scale is to model the potential fuel production via the MLR model. The decomposition MLR model of a condensed phase depends on the material temperature, the heating rate, atmospheric conditions (nitrogen or air) and pyrolysis parameters. These constant values are associated to one reaction or group of reactions and independent of the heating rate and the atmospheric conditions knowing this MLR pyrolysis model.

Then, each reaction mechanism of each component is simplified for various reasons related to the MLR pyrolysis model used (the FDS one), the FDS mixture fraction combustion model, the feedback experiments at material scale and the comprehension of the component decomposition mechanism. The estimation of pyrolysis parameters is widely studied in the fire community. Various methods exist to solve them from the simplest to the most sophisticated one. This choice of method depends on the type of component studied and the pyrolysis model used. The method used in this thesis is optimization. The principle is to optimize pyrolysis input data until an acceptable accordance between the experimental and the modelled MLR curve. This approach must be performed on the whole MLR results for the whole of the heating rates. It is important to perform optimization considering experimental uncertainties.

The reaction-to-fire of a multilayer seat material and a GRP composite is studied at material scale. The interaction between the previous and this scale is fundamental concerning the thermal decomposition process comprehension between each layer. The experimental test used is the cone calorimeter. The experimental understanding of thermal decomposition and the reaction-to-fire enables to create equivalent materials taking into account FDS pyrolysis model limits. These equivalent materials, for the seat, considered an extra

fictive layer as a gas gap which comes from the foam decomposition. This numerical strategy has made the replacement of the experimental evolution of the foam thickness possible when the seat is exposed to an incident heat flux. Furthermore, the matter flow movement into the solid is not taken into account in FDS. This leads to the record that with FDS code, it is easier to simulate a thermoset pyrolysis than a thermoplastic material. However, FDS limits, such as the unidirectional thermal heat transfer cannot be avoided. Indeed, the thermal feedback received on the back face of the composite, from the silicate wool, is not modelled in FDS. Nevertheless, this phenomenon is not a material property but a parameter which depends on the test configuration.

For both materials studied, FDS pyrolysis and combustion models have difficulties to simulate reaction-to-fire at lower incident heat fluxes. Indeed, at low heat flux levels, the experimental ignition may be more controlled by reaction or diffusion, it occurs on and in materials, then by thermal surface budget on material. Another issue at this scale is to find all radiative and thermo-physical properties of each intermediate species. The best way to estimate them is to derive there value from experimental tests whenever possible. For similar cases, several authors have chosen to optimize them, such as pyrolysis parameters. In this thesis, these properties are estimated according to literature reviews on the virgin material. Finally, the numerical and experimental reaction-to-fire of multilayer seat materials and the GRP composite are in agreement taking into account experimental uncertainties and FDS model limits.

The aim of the semi-finished product scale is to study reaction-to-fire and flame spread over a vertical product. For this scale, only the GRP composite is tested due to its end-use conditions. These associated simulations have shown that numerical HRR is sensitive to the mesh size and to the heater discretization in FDS. The numerical and experimental comparisons are in good agreement taking into account experimental uncertainties. However, the comparison of carbon monoxide mass flow failed due to the limitation of FDS mixture fraction combustion model. Nevertheless, the numerical and experimental flame spread seems equivalent, knowing that the incident heat flux (received on the product surface) is distributed between radiative and convective heat flux.

The objectives of the finished product scale are to test the abilities of FDS to simulate pyrolysis, ignition, combustion and flame spread of a product in end-use conditions from a propane burner. The major difference between this scale and the previous ones is the type of burner used. It is essential to correctly reproduce the burner flame, especially the heat flux received by the product, and also the released gases only from the propane burner. When the finished burner scale (only burner and non-combustible products) is validated in FDS, the two finished product tests are modelled with the input data from the material or the semi-finished product scale. For both studied products, numerical results are in accordance with experimental ones considering experimental uncertainties and the FDS combustion model applied to one fuel. However, a difference is highlighted for the release of carbon monoxide. This divergence on kinetic and intensity comes from:

- The FDS combustion reaction: a unique reaction and stoechiometry exists in FDS even if multiple fuels are present.

- The FDS mixture fraction combustion model: a constant yield value of carbon monoxide is produced in FDS if ignition conditions are gathered, whereas the carbon monoxide production depends on the type of fuel, the oxygen concentration and diffusion and its residence time in the flame.
- Gas phase input data correspond to propane characteristics in order to reproduce the quantity and distribution of exposure heat flux on products. This chosen carbon monoxide yield is obtained from a precise test configuration (in the corner). This position can have an impact on the flame shape over a vertical non combustible panel and change the quantity and kinetic of released carbon monoxide (compared to the finished product scale test).

Thus a new approach in FDS is tested in order to improve this carbon monoxide mass flow comparison.

The objective of this real scale is to validate the reaction-to-fire of the seat and the wall panel designed in a real tests and through the pyrolysis input data associated to a reaction mechanism and also the thermo-radiative properties of the materials, validated at previous scales. The seat does not burn during the simulation whereas experimentally a small part of the seat cushion ignites. This simulation shows that FDS models have some limitations to predict the heat release rate at low heat flux exposure.

Furthermore, the experimental and numerical comparisons are in accordance considering experimental uncertainties and FDS limits, excepted for the release of carbon monoxide. Thus, another simulation is performed but the FDS mixture fraction combustion for carbon monoxide is not used this time. The carbon monoxide source is not predicted but prescribed from experimental tests. This approach is tested firstly at finished product scale and then at real scale. The addition of a non reactive species such as carbon monoxide on the burner surface has no influence on the combustion and the flame spread of the wall panel. A good correlation is obtained between the experimental and numerical carbon monoxide generation. For scenario 1A, the comparison of carbon monoxide production for the second position is better than for the first one in the coach corridor. At this scale, CO formation is controlled by the burner combustion, contrary to the previous scale. Thus, even if the fire is supposed to be globally well ventilated in both scales (finished burner and real scales), it is possible that fire conditions evolve locally during the finished scales test due to their configuration, and have an influence on the CO production. The CO injected from the finished burner test in FDS code may not be adapted to the simulation of the real scale scenario.

Despite FDS models limits, the combustion process prediction of the two different products (thermoplastics and thermoset) with two different structures (multilayer materials and composite) and two different designs (seat and wall panel) is performed according to a multi-scale approach. The fire safety level of several scenarios can be estimated tanking into account the products studied in this thesis (only for fire well ventilated condition).

In view of these elements, several future works on experimental and numerical parts can be planned, such as:

- The influence of oxygen concentration in the ambient atmosphere on the condensed phase at raw matter and at material scales via the TGA test and the controlled atmosphere cone calorimeter. What is the influence of oxygen mass fraction on the MLR models and on pyrolysis parameters ? The coupling of TGA+FTIR spectrometer lacks in this thesis and should be recommended for a thermal decomposition study of a material.
- The test repeatability at finished product and real scales is questionable. Moreover, in case of FTIR analysis, the position of the sampling probe during the scenario test is also debatable.
- Considering the future FDS gas phase model, adding a combustion reaction for each fuel in order to represent a combustion of multiple fuels will lead to change from mixture fraction model to a most sophisticated, but also more computation expensive approach.
- A finite-rate chemistry is available in FDS but it requires fine grid resolution and a Direct Numerical Simulation of the flow. This model is not conceivable due to the domain size, the misreading of gaseous fuel and calculation time.
- The mixture fraction model is well adapted for gases which do not locally evolve into the flame. This prescriptive approach tested should be tested with other gases, such as hydrogen halide.
- Two-step reactions exist in FDS for the infinitely fast combustion reaction. These combustion reactions should be tested in order to know whether it affects carbon monoxide production.
- A new version of FDS 6.0 is available as test version until the end of 2012. It should be interesting to investigate combustion and pyrolysis models of this version.

Résumé

La sécurité incendie est un domaine de recherche majeur dans le milieu ferroviaire. En cas d'incendie dans une voiture de train, le danger est d'autant plus sérieux que le nombre de passagers est important et que l'évacuation de la voiture n'est pas directe et immédiate. Le type et la quantité de combustible proviennent soit des produits propres au train (siège et paroi) ou propres aux passagers (bagages). Ce dernier ne peut pas être contrôlé car il dépend de chaque personne présente dans le train. Inversement, la nature de chaque produit propre à l'intérieur d'une voiture de train est supposée connue. Ces produits doivent répondre à un niveau de sécurité satisfaisant en fonction de la catégorie d'exploitation et du type de voiture.

Dans ce contexte, ce travail de thèse s'inscrit dans le cadre d'un projet de recherche européen, dénommé Transfeu. L'objectif est de prédire la croissance et le développement d'un incendie dans une voiture de train, en prenant en compte les limites de l'outil numérique utilisé. Ces travaux sont alors basés sur une étude multi-échelle d'un scenario précis, choisi suite à la réalisation d'une analyse de risques. La performance au feu de deux produits est étudiée. Il s'agit d'un siège et d'une paroi verticale composite de voiture de train.

L'approche multi-échelle est basée sur une comparaison expérimentale et numérique du comportement au feu des matériaux, de l'échelle matière à l'échelle réelle. A l'échelle de la matière, un mécanisme de décomposition simplifié a été établi en fonction des données de la littérature et d'essais réalisés en Analyseur Thermo-gravimétrique. Ensuite, des constantes cinétiques associées à un modèle de pyrolyse ont été estimées via l'outil d'optimisation des algorithmes génétiques. Ces constantes correspondent aux données d'entrée du modèle de pyrolyse incorporé au code Fire Dynamics Simulator (FDS) aux échelles supérieures. Le comportement au feu des matériaux du siège et du composite a été simulé à l'échelle du matériau grâce à l'analyse des essais réalisés en cône calorimètre. Les limites du code FDS ont été incluses dans l'analyse. Le développement du feu d'un siège de train et d'une paroi verticale composite a été simulé avec succès en prenant en compte les limites de FDS. Les données d'entrée utilisées sont les mêmes, de l'échelle du matériau à l'échelle réelle du scénario dans le véhicule ferroviaire.

Les résultats obtenus soulignent les limites et la capacité du code FDS à prédire le développement du feu à grande échelle compte tenu des incertitudes expérimentales, des modèles de FDS et des solutions alternatives proposées. Cependant, des variations importantes existent entre les résultats expérimentaux et numériques sur le dégagement de monoxyde de carbone. Ces écarts sont dus aux limites du modèle de combustion à

fraction de mélange utilisé dans le code FDS. Une approche prescriptive du dégagement de monoxyde de carbone est proposée à l'échelle du produit fini et du scénario réelle. Cette approche est intéressante, néanmoins, elle nécessite des données expérimentales nombreuses et précises.

Cette analyse expérimentale du comportement au feu des matériaux et des produits étudiés a permis de simuler la pyrolyse, la combustion et la génération des effluents gazeux à l'échelle d'un scénario dans des conditions de feu bien ventilé.

Nomenclature

Gaseous species

CO	Carbon monoxide
CO_2	Carbon dioxide
H_2O	Water vapour
NO	Nitric oxide
NO_2	Nitrogen dioxide
NH_3	Ammonia
SO_2	Sulphur dioxide
HBr	Hydrogen bromide
HCN	Hydrogen cyanide
HCl	Hydrogen chloride
CH_4	Methane
CH_3CH_2CHO	Propionaldehyde
$C_8H_6O_4$	Isophtalic acid
C_8H_8	Styrene
$H^\bullet$	Hydrogen radical
$OH^\bullet$	Hydroxyl radical
CH_2O	Formaldehyde
C_3H_4O	Acrolein
$C_8H_4O_3$	Phtalic anhydride
C	Carbon
$Cl^\bullet$	Chlorine radical
H_2	Dihydrogen
$Al(OH)_3$	Aluminium hydroxide
Al_2O_3	Aluminium oxide
CS_2	Carbon disulphide
C_6H_6	Benzene
C_3H_8	Propane
C_7H_8	Toluene

Roman letters

A	$[s^{-1}]$	Arrhenius pre-exponential factor
c_p	$[J.kg^{-1}.K^{-1}]$	Mass specific heat at constant pressure
D	$[m]$	Fire diameter
D_i	$[m]$	Diffusion coefficient of the species i
E	$[kJ.mol^{-1}]$	Activation energy
h_c	$[W.m^{-2}.K^{-1}]$	Heat transfer coefficient
Δh_{comb}	$[kJ.kg^{-1}]$	Combustion enthalpy
$\Delta h_{reaction}$	$[kJ.kg^{-1}]$	Reaction enthalpy
Δh_s	$[kJ.kg^{-1}]$	Sensible enthalpy
k	$[s^{-1}]$	Rate constant of the condensed phase
l_f	[m]	Flame height
m	$[kg]$	Mass
$\dot{m}_f$	$[kg.s^{-1}]$	Mass flow
$\triangle m$	$[kg]$	Total mass loss
n	$[kg]$	Reaction order
p	[Pa]	Pressure
p		Event or failure probability of the SDFS
P		Occurrence probability of the SDFS
$\dot{q}$	$[W]$	Flux
q_r	$[W.m^{-2}]$	Radiative heat flux vector
q_c	$[W.m^{-2}]$	Conductive heat flux vector
q_{conv}	$[W.m^{-2}]$	Convective heat flux vector
$\dot{Q}$	[W]	Heat release rate
Q_i	$[W.m^{-2}]$	Incident heat flux
Q		Occurrence probability of the DFS
R		Risk of the DFS
s		Severity of the SDFS
S		Severity of the DFS
S_i		1^{st} Order Sobol coefficient
S_{ij}		2^{nd} Order Sobol coefficient
S_T		Total Sobol coefficient
t	[s]	Time
T	[K]	Temperature
u	$[m.s^{-1}]$	Fluid rate vector
V	$[m^3]$	Volume
W	$[g.mol^{-1}]$	Molar mass
x		Variable
y		Variable
y	$[kg.kg^{-1}]$	Mass fraction
Z		Mixture fraction

Dimensionless quantity

Bi	Biot Number
Pr	Prandtl Number
Re	Reynolds Number

Greek letters

α		Component or species
α_s		Absorption coefficient
β		Reaction
β	$[K.min^{-1}]$	Heating rate
γ		Reaction
δ		Extent of reaction
ε		Emissivity
κ	$[m^{-1}]$	Absorption coefficient of the solid phase
λ	$[W.m^{-1}.K^{-1}]$	Thermal conductivity
μ^t	$[[kg.m^{-1}.s^{-1}]$	Turbulent viscosity
ν		Stoechiometric coefficient
ρ	$[kg.m^{-3}]$	Density
τ	$[m]$	Thickness
τ	$[kg.m^{-1}.s^{-2}]$	Stress factor
ϕ		Fitness function
$\dot{\omega}$	$[s^{-1}]$	Reaction rate
Δ	$[m]$	Characteristic size of mesh
Ω		Number of sample

Abbreviation

ABS		Acrilonitrile Butadiene styrene
ATH		Aluminium Trihydrate
CC		Cone calorimeter
CEN		European Committee for Standardization
CFD		Computational Fluid Dynamics
CFL		Courant-Friedrichs-Lewy
CHF	$[W.m^{-2}]$	Critical Heat Flux
DFS		Design Fire Scenario
DNS		Direct Numerical Simulation
DSC		Differential Scanning Calorimetry
E		Integrity barrier
EI		Integrity and Insulation barrier
EXP		Experiment
EW		Integrity and Radiation transfer barrier
FDS		Fire Dynamics Simulator
$FT1$		First Position of FTIR in the coach
$FT2$		Second Position of FTIR in the coach
$FTIR$		Fourier Transformed Infra-red spectrometer
$F1$		Fitness function 1
$F2$		Fitness function 2
$F3$		Fitness function 3
GC		Gas Chromatography
GRP		Glass Reinforced Polymer
HRR	$[kW]$	Heat release rate
IR		Infra-red
LES		Large Eddy Simulation
LNE		Laboratoire National de Métrologie et d´ Essais
LPA		Lumped approach parameter
LFL		Lower Flammability Limit.
MBI		Medium Burning Item
ML	$[kg]$	Mass Loss
MLR	$[s^{-1}]$	Mass Loss Rate
MS		Mass Spectrometer
$NIST$		National Institute of Standards and Technology
NUM		Numerical
OC		Operation Category
PE		Polyethylene
PP		Polypropylene
PS		Polystyrene
PU		Polyurethane
$PTFE$		Polytetrafluoroethylene
PVC		Polyvinyl chloride
PVF		Polyvinyl fluoride
RTE		Radiative Transfer Equation

Abbreviation

$SDFS$		Sub-Design Fire Scenario
$S1A$		Scenario 1A
$S1B$		Scenario 1B
SP		Scientific Partner
SRC		Standardized Regression Coefficient
TGA		Thermogravimetric Analyser
THR	$[MJ.m^{-2}]$	Total Heat Release
$TRCO$	$[g]$	Total release Carbon monoxide
$TRCO_2$	$[g]$	Total release Carbon dioxide
TRP	$[W.s^{0.5}.m^{-2}]$	Thermal Response Parameter
TSI		Technical Specification Interoperability
Var		Variance

Physical constants

$\sigma = 5,6704.10^{-8} W.m^{-2}.K^{-4}$	Stephan Boltzmann constant
$c_0 = 2,998.10^{-8} m.s^{-1}$	Speed of light
$p_0 = 101325 Pa$	Reference Pressure
$R = 8,314 J.K^{-1}.mol^{-1}$	Ideal gas constant
$g = 9,81 m.s^{-2}$	Gravitational force

Exponents

$\cdot$	Time unit
$'$	Length unit
$''$	Area unit
$'''$	Volume unit
$-$	Mean value

Subscripts

∞	Ambient air
c	Cover
ch	Char
eff	Effective
f	Final
f	Foam
F	Fuel
g	Gas
ig	Ignition
i	Reaction
In	Interliner
j	Species
max	Maximal
min	Minimum
0	Initial
o	Thermo-oxidative
pyr	Pyrolysis
r	Residual
R	Residue
s	Solid
st	Stoechiometrique
t	Time
t	Thermal

Bibliography

Accuratus, Aluminium oxide, material characteristic. *http://accuratus.com/alumox.html*, accessed on December 2012, 2002.

Allard, A., Fischer, N., Didieux, F., Guillaume, E., Iooss, B., Evaluation of the most influent input variables on quantities of interest in a fire simulation. *Journal de la Société Française de Statistique*, Vol 152, 2011.

Almaz Optics, Titanium dioxide (Rutile) properties. *http://www.almazoptics.com/index.html*, accessed on January 2012, 1993.

Andersona, H., Kemmlera, A., HoEhneb, G., Heldta, K., Streya, R., Round robin test on the kinetic evaluation of a complex solid state reaction from 13 European laboratories. Part 1. Kinetic TG-analysis. *Thermochimica Acta*, Vol 332, pp 33-53, 1999.

Andzi Barhe, T., Etude expérimentale et numérique de l'influence des paramètres opératoires sur les mécanismes de formation des oxydes d'azote lors de la combustion de mélanges de matériaux cellulosiques et plastiques. *PhD-Thesis of Ecole Nationale Supérieure de Mécanique et d'Aérotechnique, Université de Poitiers, France*, 2004.

Arrêté du 1^{er} Juillet 2004 relatif aux exigences applicables aux matériels roulants circulant sur le reseau ferré national et modification par Arrêté du 28 février 2006, 2004.

Bal, N., Uncertainty and complexity in pyrolysis modelling. *PhD-Thesis of University of Edinburgh, UK*, 2012.

Barnett, J., Fire Safety Sea Road Rail. *International Conference on Fire Safety - Sea, Road, Rail*, Melbourne, Australia, November 2005.

Batiot, B., Collin, A., Richard, F., Luche, J., Rogaume, T., Sensitivity analysis of solid degradation mechanism with the Arrhenius law under inert atmosphere. *Proceeding of the international congress on Fire Computer Modelling*, GIDAI on Fire computer modelling, University of Cantabria, Santander, Spain, October 2012.

Biotechnology learning hub, Wool fibre structure and properties. *http://www.biotechlearn.org.nz*, University of Waikato, New Zealand, accessed on December 2012, 2005.

Bolland, J., Kinetic studies in the chemistry of rubber and related materials. I. The thermal oxidation of ethyl linoleate. *Proceedings of the Royal Society of London. Series A, Mathematical and Physical Sciences*, pp 218-236, 1946.

Bolland, J. & Gee, G., Kinetic studies in the chemistry of rubber and related materials. II. The kinetics of oxidation of unconjugated olefins. *Transactions of the Faraday Society*, pp 236-243, 1946(a).

Bolland, J. & Gee, G., Kinetic studies in the chemistry of rubber and related materials. III. Thermochemistry and mechanisms of olefin oxidation. *Transactions of the Faraday Society*, pp 244-252, 1946(b).

Boulet, L., Parent, G., Acem, Z., Rogaume, T., Fateh, T., Zaida, J., Richard, F., Characterization of the radiative exchanges when using a cone calorimeter for the study of the plywood pyrolysis. *Fire Safety Journal*, Vol 51, pp 53-60, 2012.

Bourbigot, S. & Le Bras, M., Flame retardant Plastics. *In: Plastics Flammability Handbook*, 3^{rd}*Ed.*, Munich, Troitzsch J., Hanser, ISBN 1-56990-356-5, pp 133-157, 2004.

Braun, E. A Fire Hazard Evaluation of the Interior of WMATA Metrorail Cars, Final Report. *Prepared for Washington Metropolitan Area Transit Authority*, NBSIR 75-971, National Bureau of Standards (NBS), 1975.

Braun, E. 1978 Fire Hazard Evaluation of BART Vehicles. *Prepared for Urban Mass Transportation Administration (UMTA), now Federal Transit Administration (FTA)*, NBSIR 78-1421, National Bureau of Standards (NBS).

Briggs, P., Metral, S., Tallec, Y., Troïano, D., Messa, S., Breulet, H., FIRESTARR - Final Report. *FIRESTARR Consortium*, Contract SMT4-CT97-2164, 2001(a).

Briggs, P., Le Tallec, Y., Sainrat, A., Métral, S., Messa, S., and Breulet, H., 2001 The FIRESTARR Research Project on the Reaction-To-Fire Performance of Products in European Trains. *Proceedings of the* 9^{th} *International Interflam Conference*, Edinburgh, Scotland, pp 925-936, 2001(b).

Briggs, P., Developments in fire safety engineering methodology for classifying products on European trains. *Proceedings of the* 12^{th} *International Conference and exhibition on fire science and Engineering*, United Kingdom, AM3237, ISBN: 978-0-9541216-5-5, pp 995-1008, 2010.

Brossas, J., Retardateurs de flammes. *Techniques de l'Ingénieur*, Traité Sécurité, AM3237, p 14, 1999.

Brown, J., Braun, E., Twilley, W., Cone calorimeter evaluation of the flammability of composite materials. *Technical report NBSIR 88-3733*, National Bureau of Standards, Center for fire research, 1988.

BS 6853, Code of production for fire precautions in the design and construction of passenger carrying trains, 1999.

Bustamante Valencia, L., Experimental and numerical investigation of the thermal decomposition of materials at three scales: application of polyether polyurethane foam used in upholstered furniture. *PhD-Thesis of Ecole Nationale Supérieure de Mécanique et d Aérotechnique, Université de Poitiers, France*, 2009.

Camillo, A., Rogaume, T., Guillaume, E., Marquis, D., Chivas-Joly, C., Relative risk analysis methodology of fire and evacuation events in European railway transport. 12_{th} *International Conference Fire and Materials*, San-Francisco, USA, pp 13-25, January 2011.

Camillo, A., Rogaume, T., Guillaume, E., Marquis, D., Methodology of fire growth and toxic gases production simulation - Application to an European train vehicle. 2_{nd} *International Conference on Fire in vehicles*, Chicago, USA, pp 133-145, September 2012.

Capote, J., Alvear, D., Lazaro, M., Espina, P., Heat release rate and computer fire modelling vs real scale fire tests in passenger trains. *Fire and Materials Journal*, Vol 32, pp 213-229, 2008.

Carvel, R., Steinhaus, T., Rein, G., Torero, J., Determination of the flammability properties of polymeric materials:A novel method. *Polymer Degradation and Stability*, Vol 96, pp 314-319, 2011.

Cerin-Delaval, O., Development and characterisation of a novel flame retardant EVM-based formulation: investigation and comprehension of the flame retardant. *PhD-Thesis of University of Lille 1, France*, 2010.

Chaos, L., Khan, M., Krisnamoorthy, N., De Ris, J., Dorofeev, S., Materials properties for CFD Fire models. *FM Global Open Source CFD Fire Modelling Workshop*, Norwood, USA, April 29-30, 2010.

Chern, Y., Twua, J., Chen, J., High Tg and high organosolubility of novel polyimides containing twisted structures derived from 4-(4-amino-2-chlorophenyl)-1-(4-aminophenoxy)-2,6-di-tert-butylbenzene. *European Polymer Journal*, Vol 45, pp 1127-1138, 2009.

Chiam, B. Numerical simulation of metro train fire. *Master thesis*, University of Canterbury, New Zealand, p 303, 2005.

Chivas, C., Guillaume, E., Sainrat, A., Barbosa, V. Assessment of risks and benefits in the use of flame retardant in upholstered furniture. *Fire Safety Journal*, Vol 44, pp 801-807, 2009.

Collin, A. and Anstett-Collin, F. Analyse de sensibilité appliquée à un model de propagation de feux de forêts: Influence de la charge et de l'humidité de la végétation au sol. *Congrès Français de thermique*, Le Touquet, 2010.

Corlett, R., Velocity distribution in fires. *In: Heat transfer in Fires*, New York, John Wiley & Sons, P.L. Blackshear ed., pp 239-255, 1974.

Costa, L., Camino, G., Cartemiglia, L., Mechanism of thermal degradation of fire retardant melamine salts. *Fire and Polymers*, Chapter 15, ISBN 9780 841217799, pp 211-238, 1990.

Crews, G., Melamine expands fire retardants uses. *Plastics Compounds*, Vol 15, pp 41-43, 1992.

Desanghere, S., Determination des conditions d´ échauffement de structure extrieure à un batiment en situation d'incendie. *PhD-Thesis of INSA, Rouen, France*, 2006.

Di Blasi, C., Modelling and simulating of combustion processes of charring and non-charring solid fuels. *Progress in Energy and Combustion Science*, Vol 19, pp 71-104, 1993.

Di Blasi, C., Transition between regimes in the degradation of thermoplastic polymers. *Polymer Degradation and Stability*, Vol 64, pp 359-397, 1999.

DIN 5510-2, Fire test to railway components, 2009.

European Directive, Directive 2008/57/EC on the interoperability of the rail system within the Community. *Official Journal of the European Union*, 2008.

Drysdale, D., Fire science and combustion. *In: An introduction to fire dynamics*, chapter 1, 3^{rd}*Ed.*, John Wiley & Sons, ISBN: 9780470319031, pp 1-34, 2011.

Drysdale, D., 2011 Diffusion flames and fire plumes. *In: An introduction to fire dynamics*, chapter 4, 3^{rd}*Ed.*, John Wiley & Sons, ISBN: 9780470319031, pp 121-178, 2011.

Drysdale, D., Steady burning of liquids and solids. *In: An introduction to fire dynamics*, chapter 5, 3^{rd}*Ed.*, John Wiley & Sons, ISBN: 9780470319031, pp 181-283, 2011.

Drysdale, D., Ignition: the initiation of flaming combustion. *In: An introduction to fire dynamics*, chapter 6, 3^{rd}*Ed.*, John Wiley & Sons, ISBN: 9780470319031, pp 225-275, 2011.

Drysdale, D., Spread of flame. *In: An introduction to fire dynamics*, chapter 7, 3^{rd}*Ed.*, John Wiley & Sons, ISBN: 9780470319031, pp 277-315, 2011.

Eckert E., Drake R., Analysis of heat and mass transfer, McGraw-Hill New edition, CRC Press, ISBN-13: 978-0891165538, 1986.

FprEN 45545-2, Railway applications - Fire protection on railway vehicles - Part 2: Requirements for fire behaviour of materials and components, 2012.

CEN/TS 45545-1, Railway application, Fire protection on railway vehicles, part 1: General, 2009.

EN 45545-2, Railway application, Fire protection of railway vehicles - Part 2:Requirements for fire behaviour of materials and components, 2009.

EN 45545-6, Railway application, Fire protection of railway vehicles - Part 6: Fire control and management systems, 2009.

EN 60812 Analysis techniques for system reliability - Procedure for failure mode and effects analysis (FMEA), 2006.

Eurostat, European commission Railway transport accident database. *http://epp.eurostat.ec.europa.eu/portal/page/portal/transport/data/database*, accessed on December 2012.

Fardell, P. and Guillaume, E. Sampling and measurement of toxic fire effluent. *In: Fire Toxicity*, chapter 11, Cambridge, Stec A. and Hull R., Woodhead Publishing CRC ed., ISBN 978-1-84569-502-6, pp 385-423, 2010.

Fateh, T., Etude expérimentale et numérique de la cinétique de décomposition thermique de contreplaqués en bois. *PhD-Thesis of Ecole Nationale Supérieure de Mécanique et d'Aérotechnique, Université de Poitiers, France*, 2011.

Flambard, X., Bourbigot, S., Koslowski, K., Muzyczek, M., Mieleniak, B., Ferreira, M., Vermeulen, B., Poutch, F., Progress in safety, flame retardant textiles and flexible fire barriers for seat in transportation. *Polymer Degradation and Stability*, Vol 88, pp 98-105, 2005.

Friedman, R., Ignition and burning of solids. *In: Fire standard and safety*, ASTM STP 614, A.F. Robertson ed., American Society for Testing and Materials, Philadelphia, pp 91-111, 1977.

Goransson, U. & Lundqvist, A., Fires in buses and trains, fire test methods. *SP Report 1990:45*, SP Swedish National Testing and Research Intitute, Fire Technology, Boras, Sweden, 1990.

Guillaume, E. & Chivas, C., Fire models used in toxicity testing. *In: Hazards of combustion Products*, London, Grayson, Babrauskas and Gann editors, Interscience communications, ISBN 978-0-9556548-2-4, pp 59-72, November 2008.

Guillaume, E. Essais de comportement au feu dans les transports. *Technique de l'ingénieur*, Traité Sécurité, SE 3 255, p 14, 2010.

Guillaume, E., Toxicité des fumées d´ incendie. *Techniques de l'Ingénieur*, Traité Sécurité, SE 2 060, p 14, 2012.

Guillaume, E., La modélisation de la décomposition thermique des matériaux en cas d'incendie. *Techniques de l'Ingénieur*, Traité Sécurité, SE2066, p 14, 2013.

Guillaume, E., Marquis, D., Saragoza, L., Yardin, C., Uncertainty on heat release rate measurement with cone calorimeter. *Revue Française de métrologie*, Submitted.

Hall, J., Characteristics of home fire victims. *NFPA, Fire analysis and research, Appendix D: fatal effects of fire*, 2008.

Hartzell, G., Criteria and methods for evaluation of toxic hazard. *Fire Safety Journal*, Vol 12, pp 179-182, 1987.

Hartzell, G., Engineering analysis of hazards to life safety in fires: the fire effluent toxicity component. *Safety Science*, Vol 38, pp 147-155, 2001.

Hilbert, D., Neumann, J., Nordheim, L., Über die Grundlagen der Quantenmechanik. *Mathematische Annales*, Vol 98, pp 1-30, 1928.

Hill, K., Dreisbach, J., Joglar, B., Najafi, K., McGrattan, R., Peacock, M., Hamins, A., Verification and Validation of Selected Fire Models for Nuclear Power Plant Applications-Fire Dynamics Simulator. *United States Nuclear Regulatory Commission*, Vol 7, NUREG-1824, Washington, 2007.

Hirschler, M. & Morgan, A., Thermal decomposition of polymer. *In: The SFPE Handbook of Fire Protection Engineering*, chapter 1-7, 4^{th} Ed., National fire protection association, Quincy, USA, ISBN-10: 0-87765-821-8, pp 112-143, 2008.

Höcker, H., Fibre morphology. *In: Wool: Science and Technology*, Cambridge, ed. Simpson, W.S and Crawshaw, G.H, Woodhead Publishing Limited, pp 60-79, 2002.

Horrocks, R., Developments in flame retardant for heat and fire resistant textiles. the role of char formation and intumescence. *Polymer Degradation and Stability*, Vol 54, pp 142-154, 1996.

Horrocks, A. & Kandola, B., Textiles. *In: Plastics Flammability Handbook*, 3^{th} Ed., Munich, Troitzsch J., ISBN 1-56990-356-5, pp 133-157, 2004.

Houck, C. & Joines, J., A genetic algorithm for function optimization, a Matlab implementation, *Report NCSU-IE TR 95-09.*, North Carolina State University, 1996.

Hostikka, S. & McGrattan, A., Large Eddy Simulations of Wood Combustion. *Proceedings of the 9^{th} International Interflam Conference*, Vol 1, London, Interscience Communications Ltd, Edinburgh, Scotland, the 17-19^{th} September 2001.

Hu, X., Wang, Z., Jia, F., Galea, ER., Numerical investigation of fires in small rail car compartments. *Journal of Fire Protection Engineering*, Vol 22, pp 245-270, 2012.

Hugett, C., Estimation of rate of heat release by means of oxygen consumption measurements, *Journal of Fire and Materials*, Vol 12, pp 61-65, 1980.

Huggett, A., Combustion conditions and exposure conditions for combustion product toxicity testing. *In: Combustion Toxicology*, chap 14, 1^{st} Ed., CRC Press, ISBN-13: 978-0849388026, pp 220-239, 1989.

Hudson, S., Train fires - Special topic report. *Controller, Safety and Risk railway safety*, 66 p, 2001.

Hull, R. & Stec, A., Polymers and Fire. *In: Fire Retardancy of Polymers, New strategies and Mechanisms*, Cambridge, Hull R. and Kandola B. ed., Royal Society of Chemistry, ISBN 978-0-85404-149-7, pp 1-14, 2009.

Hull, R. & Stec, A., 2010 Introduction to fire toxicity., *In: Fire Retardancy of Polymers, New strategies and Mechanisms*, Cambridge, Hull R. and Kandola B. ed., Royal Society of Chemistry, ISBN 978-0-85404-149-7, pp 3-23, 2009.

Iddir, O., Principes d évaluation de la probabilité de défaillance des Mesures de Maitrise des Risques (MMR). *Techniques de l'Ingénieur*, Traité Sécurité, SE1057, p 18, 2009.

Initiating event frequency working group, Initiating event frequency and availability of safety barriers. *Les cahiers de la sécurite industrielle*, 21 p, 2009.

Iooss, B. Review of global sensitivity analysis of numerical model. *Journal de la Société Française de Statistique*, Vol 152, pp 3-25, 2011.

ISO/CEI GUIDE 98-3/S1, Uncertainty of measurement - Part 3: guide to the expression of uncertainty in measurement (GUM: 1995) - Propagation of distributions using a Monte Carlo method, 2008.

ISO/CEI GUIDE 98-3, Uncertainty of measurement - Part 3: guide to the expression of uncertainty in measurement (GUM: 1995), 2008.

ISO 5659-2, Smoke generation, Part 2: Determination of optical density by a single chamber test), 2012.

ISO 5660-1, Reaction-to-fire tests, Heat release rate, Smoke production and Mass loss rate- Part 1: Heat release rate (cone calorimeter method), 2002.

ISO 5660-2, Reaction-to-fire tests, Heat release rate, Smoke production and Mass loss rate- Part 2: Smoke production rate (dynamic measurement), 2012.

ISO 9705, Fire tests - Full scale room for surface products, 2006.

ISO 10456, Building materials and products - Hygrothermal properties - Tabulated design values and procedures for determining declared and design thermal values. Hygrothermal properties. Tabulated design values, 2007.

ISO 13571, Life threatening components of fire, Guidelines for the estimation of time to compromised tenability in fire, 2012.

ISO 13943, Fire safety vocabulary., 2011.

ISO 16730, Fire safety engineering Assessment. Verification and validation of calculation methods, 2007.

ISO 16732-1 Fire safety engineering - Fire Risk Assessment - Part 1: General, 2012.

ISO 11357-5, Plastics - Differential scanning calorimetry (DSC) - Part1: determination of characteristic reaction-curve temperatures and times, enthalpy of reaction and degree of conversion, 1999.

ISO 11358-1, Plastics - Thermogravimetry (TG) of polymers - Part1: General principles, 1997.

ISO 11358-12, Plastics - Thermogravimetry (TG) of polymers - Part1: determination of activation energy, 2005.

ISO 19701, Methods for sampling and analysis fire effluents., 2013.

ISO 19702, Toxicity testing of fire effluents - Guidance for analysis of gases and vapours in fire effluents using FTIR analysis, 2006.

ISO 197013, Generation and analysis of toxic gases in fire - Calculation of species yields, equivalence ratio and combustion efficiency in experimental fires, 2010.

ISO 19706, Guidelines for assessing the fire threat to people, 2011.

ISO 21367, Reaction to fire, Test method for flame spread and combustion product release from vertically oriented specimens, 2008.

ISO 23932, Fire safety engineering - General principles, 2009.

ISO 24473, Fire tests Open calorimetry : Measurement of the rate of production of heat and combustion products for fire up to 40 MW, 2006.

Janssens, M. & Parker, W., Oxygen consumption calorimetry., *In: Heat release in Fires*, London, Babrauskas V. and Grayson S. eds., Interscience Communications Ltd, ISBN 978-0-9556548-4-8, pp 31-60, 1992.

Janssens, M., Improved method of analysis for the LIFT apparatus, Part I : Inflammation. *Proceeding of the 2nd Fire and Material Conference*, London, Interscience communication, 1993.

Jiang, Y., Decomposition, Ignition and Flame spread on furnishing materials. *PhD-Thesis of Centre for Environment Safety and Risk Engineering, Victoria University, Australia*, 2009.

Kakac, S., Yener, Y., *Heat Conduction*, 2nd Ed., Washington, Hemisphere Publishing Corp., p 411, 1985.

Kandare, E., Balijinder, K., Kandola, K., Price, D., Nazaré, S., Horrocks, R., Study of the thermal decomposition of flame retarded unsaturated polyester resins by thermogravimetric analysis and Py-GC/MS. *Polymer Degradation and Stability*, Vol 93, pp 1996-2006, 2008.

Kaplan, H., Grand, A., Hartzell, G., Toxicity and the smoke problem. *Fire Safety Journal*, Vol 7, pp 11-24, 1984.

Kashiwagi, T., Polymer combustion and flammability role of the condensed phase. *Proceeding of the 25th Combustion Institute. Symposium (International) on Combustion*, Combustion Institute, Pittsburgh, USA, pp 1423-1437, 1994.

Konig, A., Fehrenbacher, U., Kroke, E., Hirth, T., Thermal decomposition behaviour of the flame retardant melamine in slab-stock flexible polyurethane faom. *Journal of Fire Science*, Vol 27, pp 87-211, 2009.

Kirchsteiger, C., On the use of probabilistic and deterministic methods in risk analysis. *Journal of Loss Prevention in the Process Industries*, Vol 12, pp 399-419, 1999.

Krisnamoorthy, N., Wang, Y., Krisnamoorthy, N., Dorofeev, S., Pyrolysis models in FireFoam. *FM global Open Source CFD Fire Modelling Workshop*, Norwood MA, USA, April 16-17, 2009.

Langlais, C. & Klarsfeld, S., Isolation thermique temperature ambiante - Applications. *Techniques de l'Ingénieur*, Traité Sécurité, BE9861, p 13, 2004.

Lattimer, B. & Ouellette, J., Properties of composite materials for thermal analysis involving fires. *Composites Part A: Applied Science and Manufacturing*, Vol 37, pp 1068-1081, 2006.

Lautenberger C., Gpyro,A generalized pyrolysis model for combustible solids. *PhD-Thesis of the University of California, Berkeley, USA*, http://code.google.com/p/gpyro/, 2007.

Lautenberger, C., Kim, E., Dembsey, N., Fernandez-Pello, C., The role of decomposition kinetics in pyrolysis modelling - Application to a fire retardant Polyester composite. *Fire Safety Science - Proceedings of the 9th International Symposium*, Germany, Vol 9, p 12, 21-26 September 2008.

Lautenberger, C. & Fernandez-Pello, C., Generalized pyrolysis model for combustible solids. *Fire Safety Journal*, Vol 44, pp 919-839, 2009.

Lautenberger, C. & Fernandez-Pello, C., 2011 Optimization algorithms for material pyrolysis property estimation. *Fire Safety Science*, Vol 10, pp 751-764, 2011.

Le Tallec, Y., Sainrat, A., Métral, S., Briggs, P., Messa, S., and Breulet, H., The FIRESTARR Project - Fire Protection of Railway Vehicles. *Proceeding of the 7th Fire and Material Conference*, San Francisco, USA, January 2001.

Levin, B. Combustion toxicology., *In: Inhalation Toxicology.*, chapter 10, New York, Salem H. and Katz S. ed., CRC Press Taylor & Francis Group, ISBN 0-8493-4049-7, pp 205-230, 2006.

Magee, R. & McAlevy, R., The mechanism of flame spread. *Journal of Fire and Flammability*, VoL 2, pp 271-297, 1971.

Marquis, D., Projet MP08: Tenue au feu des composites - Etat de l´ art de l´ utilisation des matériaux composites sandwichs dans le milieu naval. *Rapport Projet MP08*, MS1: LNE-R1-1, p 61, 2007.

Marquis, D., Caractérisation et modélisation multi-échelle du comportement au feu d' un composite pour son utilisation en construction navale. *PhD-Thesis of Ecole des Mines de Nantes, France*, 2010.

Marquis, D. & Guillaume, E., Modelling reaction-to-fire of polymer-based composite laminate. *Nanocomposites with properties and applications in medicine and industry*, chapter 9, Croatia, Cuppoletti J. Ed., INTECH publishing, ISBN 978-953-307-351-4, pp 175-204, 2011.

Marquis, D., Guillaume, E., Camillo, A., Pavageau, M., Rogaume, T., Usage of controlled-atmosphere cone calorimeter to provide input data for toxicity modelling. *Proceeding of the 13th Fire and Materials International Conference*, San Francisco, USA, pp 121-134, January 2011.

Marquis, D., Guillaume, E., Camillo, A., Rogaume, T., Richard, F., Existence and uniqueness of solution of a differential equation system modelling the thermal decomposition of polymer materials. *Combustion and Flame*, 2013.

Marquis, D., Pavageau, M., Guillaume, E., Chivas-Joly, C., Modelling decomposition and fire behaviour of small samples of a glass-fibre-reinforced polyester/balsa-cored sandwich material. *Fire and Materials*, 2012.

Matala, A. & Hostikka, S., Fire modelling of fire retardant electrical cable. *Proceeding of the 12th International Conference Fire and Materials*, San Francisco, USA, pp 583-595, 2011.

Matala, A., Lautenberger, C. and Hostikka, S., Generalized direct method for pyrolysis kinetic parameter estimation and comparison to existing methods. *Journal of Fire Sciences*, Vol 30, pp 338-356, 2012.

Mc Adams, W., Transmission de la chaleur, Ed. Dunod, 1961.

McGrattan, K., Hostikka, S., Floyd, J., Baum, H., Rehm, R., Mell, W., McDermott, R., Fire Dynamics Simulator (Version 5) - Technical Reference Guide. Volume 1: Mathematical Model. *NIST Special Publication 1018-5*, 2010(a).

McGrattan, K., McDermott, R., Hostikka, S., Floyd, J., Fire Dynamics Simulator (Version 5) - User Guide. *NIST Special Publication 1019-5*, 2010(b).

Mehrabian, R., Scharler, R., Obernberger, I., Effects of pyrolysis conditions on the heating rate in biomass particles and applicability of TGA kinetic parameters in particle thermal conversion modelling. *Fuel*, Vol 93, pp 567-575, 2012.

Mouritz, A. & Gibson, A., 2006 Thermal decomposition of composite in fire. *Fire properties of polymer composite materials*, chapter 2, Springer Ed., Solid mechanics and its applications, ISBN-10 1-4020-5355-X, pp 19-56, 2006.

Mortureux, Y., Analyse préliminaire des risques. *Techniques de l'Ingénieur.*, Traité Sécurité, SE4010, p 10, 2002.

NF X70-100-2, Analysis of gaseous effluents, Part 2: Tubular furnace thermal degradation method, 2006.

NF ENV 13005, Guide to the expression if the uncertainty in measurement, 1999.

NF T70-368, Determination of physical characteristics by DSC, 2012.

NF F 16-101, Railway rolling stock Fire behaviour Choice of materials, 1988.

NF F 16-102, Railway rolling stock Fire behaviour Material choosing application for electric system, 1992.

NF F 16-103, Railway rolling stock Fire protection and fire fighting - Design arrangements, 1989

NFPA 130, Standard for fixed guide way transit and passenger rail systems, 2010.

Nikolaeva, M. & Karki, T., A review of fire retardant processes and chemistry, with discussion of the case of wood plastic composites. *Baltic Forestry*, Vol 17, pp 314-326, 2006.

OpenFoam, the open source CFD toolbox. *http://www.openfoam.com/*, accessed on December 2012.

Pang, C., Jung, J., Lee, J., Kang, Y., Thermal conductivity measurement of methanol-based nanofluids with Al_2O_3 and SiO_2 nanoparticles. *International Journal of Heat and Mass Transfer*, Vol 55, pp 5597-5602, 2012.

Paul, S. & Welch, S., 2010 Prediction of CO formation in Fires. *Proceeding of the 6^{th} International Seminar on Fire and Explosion Hazards*, University of Leeds, UK, 11-16 April 2010.

Peacock, R. & Braun, E., Fire Tests of Amtrak Passenger Rail Vehicle Interiors. *Prepared for FRA*, Technical Note 1193, National Bureau of Standards (NBS), 1984.

Peacock, R. & Braun, E., Fire Safety of Passenger Trains; Phase I: Material Evaluation (Cone Calorimeter). *NISTIR 6132, National Institute of Standards and Technology (NIST)*, 1999.

Peacock, R., Reneke, P., Davis, W., Jones, W., 1999 Quantifying fire model evaluation using functional analysis. *Fire Safety Journal*, Vol 33, pp 167-184.

Peacock, R., Reneke, P., Averill, R., Bukowski, R., Klote, J., Fire Safety of Passenger Trains, Phase II: Application of Fire Hazard Analysis Techniques. *NISTIR 6525, National Institute of Standards and Technology (NIST)*, 2002.

Peacock, R., Averill, R., Madrzykowski, D., Stroup, D., Reneke, P., Bukowski, R., Klote, J., Fire Safety of Passenger Trains; Phase III: Evaluation of Fire Hazard Analysis Using Full-scale Passenger Rail Car Tests. *NISTIR 6563, National Institute of Standards and Technology (NIST)*, 2004.

Perilhon, P., MOSAR - Présentation de la méthode. *Techniques de l'Ingénieur*, Traité Sécurité, SE4060, p 18, 2002.

Popescu, C., Segal, E., Iditoiu, C., A kinetic model for the thermal decomposition of wool. *Journal of Thermochimica Acta*, Vol 256, pp 419-427, 1995.

Powell, R., Ho, C., Liley, P., Thermal conductivity of selected materials. *National Bureau of StandardS report*, 1966.

Purser, D. Assessment of hazards to occupants from smoke, toxic gases, and heat. *In: The SFPE Handbook of Fire Protection Engineering*, chapter 2-6, 4^{th} Ed., National Fire Protection Association, Quincy, USA, ISBN-10: 0-87765-821-8, pp 96-193, 2008.

Purser, D., Stec, A., Hull, R., 2010 Fire scenarios and combustion conditions. *In: Fire Toxicity*, chapter 2, Cambridge, Stec A. and Hull R., Woodhead Publishing CRC ed., ISBN 978-1-84569-502-6, pp 26-50, 2010.

Ravey, M. & Pearce, E., Flexible polyurethane foam. Thermal decomposition of polyether-base, water-blown commercial type of flexible polyurethane foam. *Journal of Applied Polymer Science*, Vol 63, pp 47-74, 1997.

Rehm, R. & Baum, H., The equation of motion for thermally driven buoyant Flows. *Journal of Research of the National Bureau of Standards*, Vol 83, pp 297-308, 1978.

Rein, G., Computational model of forward and opposed smoldering combustion with improved chemical kinetics. *PhD-thesis of the University of California, Berkeley, USA*, 2005.

Rippon, J., The structure of wool. *In: Wool Dyeing*, Bradford, Lewis D Ed., Society of Dyers and Colourists, pp 1-51, 1992.

Rocaboy, F., Comportement thermique des polymères synthétiques, Tome 1 polymère à chaîne carbonées, Paris, Ed. Masson and cie., ISBN 2-85599-442-X, p 281, 1972.

Rogaume, T., Décomposition thermique - Mécanisme de formation des polluants gazeux. *Synthèse des activités de recherche, Habilitation à Diriger les Recherches, Université de Poitiers, France.*, 2010.

Rogaume, T., Bustamante Valencia, L., Guillaume, E., Richard, F., Luche, J., Rein, G., Torero, J., Development of the Thermal Decomposition Mechanism of Polyether Polyurethane Foam Using Both Condensed and Gas-Phase Release Data. *Combustion Science and Technology*, Vol 183, pp 627-644, 2011.

Rogers, F. & Ohlemiller, T., Pyrolysis kinetics of a polyurethane foam by thermogravimetry; a general kinetic method. *Journal of Macromolecular Science*, Vol 15, pp 169-185, 1981.

Royer, M., Une méthode d'analyse des risques - Principe et Mise en oeuvre. *Techniques de l'Ingénieur*, Traité Sécurité, SE4031, p 19, 2009.

Salpin, F., Laine et colorants: fixation, quantification et vieillissement. Etude par spectrométrie de Raman. *PhD-thesis of University Pierre et Marie Curie, Paris 6, France*, 2008.

Saragoza, L., Yardin, C., Guillaume, E., Analyse des effluents de combustion par spectrométrie Infra rouge a Transformée de Fourier (IRTF) - Incertitude sur les spectres étalons du dioxyde de soufre (SO_2). *Congrès Francais de Métrologie*, Poster, the 14^{th} ed., Paris, the 22-25 June 2009.

Snegirev, A., Talalov, V., Stepanov, V., Harris, J., 2012 A new model to predict multi-stage pyrolysis of flammable materials in standard fire tests. *Proceeding of the 6^{th} European Thermal Sciences Conference (Eurotherm 2012)*, p 10, 2012.

Stec, A.A., Estimation of toxicity during burning of common materials. *In: Fire Toxicity*, chapter 15, Cambridge, Stec A. and Hull R., Woodhead Publishing CRC Ed., ISBN 978-1-84569-502-6, pp 26-50, 2010.

Stec, A., Fardell, P., Blomqvist, P., Guillaume, E., Quantification of fire gases by FTIR: Experimental characterisation of calibration systems. *Fire Safety Journal*, Vol 46, pp 225-233, 2011.

Shafizadeh, F., Thermal deterioration of wood. *In: Wood Technology: Chemical Aspects*, American Chemical Society, ACS Symposium Series, Vol 43, pp 57-81, 1977.

SNCF group, *http://www.sncf.com/fr/portrait-du-groupe/histoire-sncf*, accessed on December 2012.

Stoliarov, S. & Lyon, R., Thermo-kinetic model of burning. *Technical report of the Federal Aviation Administration*, DOT/FAA/AR-TN08/17, 2008.

Tewarson, A., Flammability parameter of material - Ignition combustion and fire propagation. *Journal of Fire Science*, Vol 12, pp 329-356, 1994.

Tewarson, A., Generation of Heat and Gaseous, Liquid, and Solid Products in Fires. *In: The SFPE Handbook of Fire Protection Engineering*, section 3, chapter 4, 4^{th} Ed., National fire protection association, Quincy, USA, ISBN-10: 0-87765-821-8, pp 109-194, 2008.

Torero, J., Flaming ignition of solid fuels. *In: The SFPE Handbook of Fire Protection Engineering*, chapter 2-11, 4^{th} Ed., National Fire Protection Association, Quincy, USA, ISBN-10: 0-87765-821-8, pp 260-278, 2008.

Thornton, W., 1917 The relation of oxygen to the heat of combustion of organic compounds. *Philosophical magazine and Journal of Science*, Vol 33, pp 196-203, 1917.

TSI 2008/232/EC, Technical specification for interoperability of the Trans-European High speed rail system - Rolling stock sub system. *Official Journal of the European Union*, 2008.

TSI 2011/291/EC, Technical specification for interoperability related on the Rolling stock sub system - Locomotives and passenger rolling stock of the Trans-European conventional rail system. *Official Journal of the European Union*, 2011.

Tuovinen, H. & Simonson, M., Incorporation of detailed chemistry in CFD modelling of compartment fires. *Proceeding of the* 3^{rd} *International Seminar on Fire and Explosion Hazards*, University of Leeds, UK, ISBN-1-901-902-17-2001, pp 307-318, April 2001.

Troitzsch, J., Plastics 2007: Flame retardants, Fire safety, Environment Aspects. *Study report*, p 227, 2007.

UNI CEI 11170-3, Guidelines for railway vehicle protection for tramways and with guided rail - Part 3: Assessment of fire behaviour of materials, acceptance limits, 2005.

Wang, Z., Jia, F., Galea, E., A generalized relationship between the normalized yields of carbon monoxide and hydrogen cyanide. *Fire and Materials*, Vol 35, pp 577-591, 2011.

Welsh, S., Paul, S., Torero, J., Modelling fire growth and toxic gas formation. *In: Fire Toxicity*, chapter 20, Cambridge, Stec A. and Hull R., Woodhead Publishing CRC ed., ISBN 978-1-84569-502-6, pp 637-662, 2010.

White, N. & Dowling, V., Conducting a full-scale experiment on a rail passenger car. *Proceedings of the* 6^{th} *Asia-Oceania Symposium on Fire Science and Engineering*, Korea, pp. 591 to 601, 2004.

White, N. Fire development in passengers trains. *Master thesis*, Centre for Environment Safety and Risk Engineering, Victoria University, Australia, 2010.

Wichman, I., Material flammability, Combustion, Toxicity and Hazard in transportation. *Journal of Energy and Combustion Science*, Vol 29, pp. 247-299, 2003.

Wilkie, C. & Mckinney, M., Thermal properties and burning behavior of the most important plastics. *In: Plastics Flammability Handbook*, chapter 4-2, 3^{rd}*Ed.*, Munich, Troitzsch J., Hanser, ISBN 1-56990-356-5, pp 58-76, 2004.

List of Figures

List of Tables

Titre Etude multi-échelle du comportement au feu d'un siège et d'une paroi types issus d'un système de transport ferroviaire Européen.

Résumé Cette thèse s'inscrit dans le cadre d'un projet de recherche européen (Transfeu), composé de 21 partenaires, dédié à l'estimation des effets du feu sur les personnes présentes dans un train et basée sur une méthodologie de sécurité incendie. L'objectif est de modéliser le comportement au feu d'un siège (matériaux multicouches) et d' un panneau vertical (composite) d' une voiture de train indépendamment de la source de feu et du design de la voiture. Le principe est basé sur l'étude de la réaction au feu de deux produits par une approche multi-échelle (de l'échelle de la matière à l'échelle réelle). A chaque échelle, les données expérimentales et numériques sont comparées et valident les processus de décomposition thermique et de combustion mis en jeu. Les données d'entrée sont estimées selon des essais normalisés ou à partir de la littérature et sont identiques pour toutes les échelles. Les phénomènes de décomposition thermique et de combustion sont simulés à partir d'un modèle de pyrolyse et d'un modèle de combustion à fraction de mélange. Cette comparaison, à complexité croissante, permet d'observer la capacité des modèles de FDS de reproduire des simulations réalistes. Les résultats permettent de souligner les limites des modèles et de les dépasser en proposant des solutions alternatives.

Mots-clés Effets du feu, Train, Réaction au feu, Matériaux multicouches, Composite, Essais et Simulations.

Title Multi-scale investigations of fire behaviour of a seat and a wall panel from European railway transport system.

Abstract This thesis work comes within the framework of a collaborative European research program (Transfeu), dedicated to estimate the fire effects on people into a train coach, based on fire safety methodology. The objective is to model the fire behaviour of a multilayer seat materials and a composite wall panel in a coach independently of the fire source in order to estimate the safety level of a coach design scenario. The principle is based on a multi-scale approach of the reaction-to-fire of two products from the raw matter to the real scale. At each scale, experimental and numerical data are compared and then validated on the thermal decomposition and the combustion processes. The used input data are the same for all scales and estimated according to standard experimental tests or literature reviews. The thermal decomposition and the combustion phenomena are simulated from a pyrolysis and a mixture fraction combustion models. This comparison at increasing complexity allows observing the ability of the models to reproduce realistic simulations. The results allow to highlight the limits of the models and then to propose better solutions in order to overcome them.

Keywords Fire effects, Train coach, Reaction-to-fire, Multilayer materials, Composite, Experimental tests and Simulations.